



DOTTORATO DI RICERCA IN CHIMICA

Convenzione tra
UNIVERSITÀ DEGLI STUDI DI TRIESTE
e
UNIVERSITÀ CA' FOSCARI DI VENEZIA

CICLO XXX

**Advanced polymeric and nanostructured coatings for Cultural
Heritage conservation and restoration.**

Settore scientifico-disciplinare: CHIM 03

DOTTORANDA

Giulia Gheno

COORDINATORE

Prof. Mauro Stener

SUPERVISORE DI TESI

Prof. Renzo Ganzerla

CO-SUPERVISORE DI TESI

Prof. Marco Bortoluzzi

ANNO ACCADEMICO 2016/2017

Abstract

Development of techniques and research on plastic and nanostructured materials have provided a wide variety of formulations with versatile uses, such as binding and retouching media, adhesives, consolidants, coating materials, varnishes, or fillers for missing parts. However, the compatibility between artwork and applied products and their durability are tested only in very limited cases before application. In recent years, the awareness of the fact that conservative treatments applied without preliminary tests can cause damages or promote degradations processes, had leads to a growing interest towards the stability and durability of the materials used in conservation practices.

In this work were studied and compared the degrading mechanisms occurring in different polymeric and nanostructured commercial products, in particular two acrylic co-polymers (*Acril33* and *Acril ME*), two synthetic resins (*Aquazol 500* and *Laropal A81*), a silicate consolidant (*Estel 1000*) and two nanoparticles dispersions (*NanoEstel* and *NanoRestore*), chosen for their widespread use and different physical-chemical characteristics and applications. The potentiality as consolidants or retouching materials was determined by means of Thermogravimetric Analysis (TGA), Dynamic Light Scattering (DLS), Centrifugal Separation Analysis (CSA), Viscometry, Size Exclusion Chromatography (SEC) and Fourier Transform Infrared Spectroscopy (FT-IR). Afterwards, thermal (80, 100, 120 and 140°C up to 15000 hours) and photo-oxidative (UVA $\lambda=254$ nm, UVC $\lambda=366$ nm up to 2000 hours) accelerated aging tests allowed to define behaviours, long-lasting performances, degradation kinetic parameters as well as degradation mechanisms of each commercial product by means of SEC, FT-IR, colorimetric and gloss measurements.

Finally, luminescent materials were synthesized and tested with the aim to discriminate between original and retouched or consolidated areas. The visible emitting lanthanide complexes $\text{Eu}(\text{NO}_3)_3(\text{phen})_2$ and $\text{Tb}(\text{NO}_3)_3(\text{phen})_2$ were prepared and embedded in the commercial polymeric and nanostructured products herein tested. Appreciable photoluminescence was observed for the complexes once dispersed in the different matrices and after photo-oxidative aging (UVA $\lambda=254$ nm up to 2000 hours) tests.

Sommario

La ricerca e lo sviluppo di nuove tecnologie riguardanti materiali plastici e nanostrutturati ha fornito un'ampia varietà di formulazioni le quali possono essere utilizzate, da parte di Restauratori e Conservatori, in modo versatile come leganti pittorici e da ritocco, adesivi, consolidanti, materiali di rivestimento, vernici o riempitivi per parti mancanti. Tuttavia, le prestazioni e la durata dei trattamenti a lungo termine, nonché la compatibilità tra l'opera d'arte e il prodotto applicato, sono state testate solo in casi molto limitati prima che il prodotto sia utilizzato nell'intervento conservativo. Negli ultimi anni, invece, la consapevolezza che trattamenti conservativi effettuati senza test preliminari possono causare danni o accelerare processi di degradazione, ha portato a un crescente interesse verso lo studio della stabilità e della durabilità dei materiali.

In questo lavoro sono stati studiati e confrontati i meccanismi di degrado di diversi prodotti commerciali polimerici e nanostrutturati, in particolare due copolimeri acrilici (*Acril33* e *Acril ME*), due resine sintetiche (*Aquazol 500* e *Laropal A81*), un consolidante a base di silice (*Estel 1000*) e due dispersioni di nanoparticelle (*NanoEstel* e *NanoRestore*), scelti per il loro diffuso utilizzo e per le loro diverse caratteristiche fisico-chimiche e applicazioni. Le potenzialità come consolidanti o materiali da ritocco sono state determinate in seguito alla caratterizzazione dei prodotti commerciali mediante Analisi Termogravimetrica (TGA), Dynamic Light Scattering (DLS), Analisi in Campo Centrifugale (CSA), Viscosimetria, Cromatografia ad Esclusione Dimensionale (SEC) e Spettroscopia Infrarossa in Trasformata di Fourier (FT-IR). Successivamente, gli invecchiamenti accelerati di tipo termo-ossidativo, effettuati alle temperature di 80, 100, 120 e 140°C per un massimo di 15000 ore e gli invecchiamenti di tipo foto-ossidativo UVA ($\lambda=254$ nm) e UVC ($\lambda=366$ nm), effettuati per un massimo di 2000 ore, hanno permesso, mediante analisi SEC, FT-IR, misure colorimetriche e di gloss, di definire i comportamenti prestazionali a lungo termine nonché i parametri cinetici e i meccanismi di degradazione di ciascun prodotto commerciale studiato.

Infine, sono stati sintetizzati e testati materiali luminescenti con lo scopo di ottenere una facile discriminazione tra aree originali e ritoccate o consolidate del manufatto. A tale fine, i complessi luminescenti $\text{Eu}(\text{NO}_3)_3(\text{phen})_2$ e $\text{Tb}(\text{NO}_3)_3(\text{phen})_2$ sono stati preparati e dispersi nei prodotti commerciali polimerici e nanostrutturati qui studiati. Apprezzabile fotoluminescenza è stata osservata per entrambi i complessi dispersi nelle singole matrici e in seguito a loro invecchiamento foto-ossidativo UVA ($\lambda=254$ nm) per un massimo di 2000 ore.

Contents

Aim	7
1. Introduction	8
1.1 Artificial aging.....	8
1.2 Kinetics of degradation	11
1.3 Mechanisms of degradation.....	12
1.3.1 Thermal degradation.....	12
1.3.2 Photo-oxidative degradation.....	14
2. Acrylic Emulsion and Microemulsion: Chemistry and Degradation	17
3. Aquazol 500: Chemistry and Degradation	20
4. Laropal A81: Chemistry and Degradation	22
5. Inorganic commercial products: Chemistry and Degradation	25
6. Lanthanide complexes	26
7. Materials and Methods	28
7.1 Materials and preparation of films samples.....	28
7.2 Natural and accelerated ageing tests.....	29
7.3 Colorimetric measurements.....	30
7.4 Gloss measurements.....	30
7.5 Thermogravimetric (TGA) analyses.....	31
7.6 Dynamic Light scattering (DLS) and Centrifugal Separation Analysis (CSA).....	31
7.7 Viscometric analyses.....	32
7.8 Size Exclusion Chromatography (SEC).....	33
7.9 Fourier Transform Infrared Spectroscopy (FT-IR).....	36

7.10 Synthesis of Ln(NO ₃) ₃ (phen) ₂ (Ln= Eu; Tb) complexes and preparation of luminescent films.....	36
7.11 Photoluminescence measurements.....	37
8. Results and Discussion.....	40
8.1 Colorimetric measurements.....	40
8.2 Gloss measurements.....	49
8.3 Thermogravimetric analyses.....	51
8.4 Dynamic Light Scattering (DLS) and Centrifugal Separation Analysis (CSA).....	54
8.5 Viscometric measurements.....	59
8.6 Size Exclusion Chromatography (SEC) measurements.....	62
8.7 FT-IR analyses.....	70
8.8 Photoluminescence measurements.....	90
9. Concluding Remarks.....	105
Appendix A.....	109
Appendix B.....	118
Appendix C.....	120
Appendix D. Scientific publications and conferences papers.....	130
References.....	131

Aim

While the progress in Materials Science furnished engineering polymers and nanostructured materials for different applications, the preservation of Cultural Heritage is still based on traditional methodologies and conventional products usually characterized by a low compatibility with the substrates that constitute the original works of art. Synthetic organic materials have been widely applied by Conservators, but their presence on artistic substrates has often shown to be detrimental because of the different physic and chemical properties of polymers with respect to the original materials. On the other hand, inorganic nanomaterials exhibit high compatibility with many artistic and architectonics substrates and thus represent a suitable alternative to organic coatings. For example, calcium and barium hydroxide nanoparticles dispersions are used with success for the deacidification and/or consolidation of paper, wood and wall paintings, but the restorers found many technical problems in their use. In particular, their usage is often unsatisfactory due to the poor penetration inside the porosity of the material and its inability to achieve complete consolidation of the damaged area. These drawbacks are due, as reported from Dillmann P. and Bellot-Gurlet L. in its book *Nanoscience and Cultural Heritage* (Atlas Press, 2016), to chemical, petrological and mineralogical incompatibility or to the specific environmental conditions they are applied and exposed. Therefore, the use of synthetic polymers is usually the only way to obtain a good restoration intervention.

In this context, seven different polymeric and nanostructured commercial products have been chosen and studied for their different physical-chemical characteristics and applications: two acrylic copolymers (*Acril33* and *Acril ME*), two synthetic resins (*Aquazol 500* and *Laropal A81*), a silicate consolidant (*Estel 1000*) and two nanoparticles dispersions (*NanoEstel* and *NanoRestore*). Their potentiality as consolidants or retouching materials was determined by means of physico-chemical characterizations and thermal and photo-oxidative accelerated aging tests. In particular, the latter allowed to define behaviours, long-lasting performances, degradation kinetic parameters as well as degradation mechanisms of each commercial product.

Moreover, the possibility to visually discriminate between original and retouched or consolidated areas was investigated. Visible-emitting lanthanide complexes with well-designed antenna-ligand, easily detectable with a common Wood lamp, were used as dopants for the commercial products to obtain luminescent materials. Coordination compounds with general formula $\text{Ln}(\text{NO}_3)_3(\text{phen})_2$ ($\text{Ln}=\text{Eu}; \text{Tb}$), were added in different concentrations (from 0.25 to 10% w/w) and the luminescence features of the samples were thus evaluated as a function of the dopants concentration and after UVA aging.

1. Introduction

Since the last decades of the '800, novel polymeric materials have been developed and introduced in the market thus being quickly adopted in both production and conservation/restoration of artworks [1] thanks to their excellent physical properties and special functionalities. The wide variety of formulations available made these materials very versatile as binding and retouching media, adhesives, consolidants, coating materials, varnishes, or fillers for missing parts. Unfortunately, no preliminary tests were done beforehand to ensure their efficacy and long-lasting behaviour, and several drawbacks, adverse effects or even complete deterioration were recorded shortly after their application or use. In the last years, despite more attention has been given to compatibility and durability between artworks and applied products, just few materials have been tested before being applied [2].

Inappropriate use of commercial products can produce irreversible damages to the treated surfaces, leading to modification of several characteristics of the material, such as colorimetric parameters and porosity, and speeding up specific degradation processes such as cracking and powdering.

It is a well know principle in conservation that materials used must not change or cause damages to the original objects. Therefore, a proper approach would require to analytically characterize every material that is going to be used in conservation and restoration. The knowledge of the mechanisms of alteration allows for better understanding of purposes and limits of the different conservation treatments and for their proper application. Chemical reactions triggered by light, heat, oxygen, water and pollutants may induce changes which make these materials unsuitable for conservation purposes. Yellowing, bleaching, changes in colour, embrittlement, loss of gloss, softening, increasing in solubility are just some of the physical alterations that materials can undergo. These changes are caused by chemical modifications of the materials which include cross-linking between chains, chain scission, volatilization of low molecular weight fractions and oxidation of the main chain or of the side groups.

1.1 Artificial aging

Degradation is defined as any process which leads to deterioration of the physical properties of a material [3]. Degradation is affected by many factors, the most important being:

- chemical composition. For example, linear saturated polyolefins are resistant to oxidative degradation while unsaturated structures are not; amorphous regions are more susceptible to thermal oxidation as compared to crystalline areas because of their higher permeability to molecular oxygen;
- molecular weight. Generally, the higher the molecular weight, the lower the rate of degradation;
- hydrophobic character;
- presence of specific functionalities. The presence of chromophores, for example, generally causes an increase in the rate of photodegradation;

- additives [4], fillers and pigments affect the resistance to degradation. Photo-stabilizers decrease the chances of photodegradation of plastic materials and can be distinguished in light absorbers or antioxidants (such as benzotriazoles, benzophenones, and phenyl esters) and hindered amine light stabilizers (HALS);
- synthesis. The size of the molecules in the polymers affects their mechanical and thermal degradation as well as the biodegradation and it is worth noting that an increase in molecular weight of the plastic material decreases the rate of degradation. Moreover, the linkage affects the degree of degradation. Thermoplastic polymers obtained by addition polymerization head-to-head or tail-to-tail are susceptible to degradation. On the other hand, cross-linking decreases the rate of degradation by locking the polymer structure. The lamellar unfolding is prevented, together with the separation of photo-produced radicals, while the radical-radical combination is favoured;
- environmental conditions (e.g. moisture, temperature, oxygen, and biotic presence) during storage and use.

In most of the cases, physical and chemical changes due to natural aging are recordable in very long periods and are considerably slower in hot dry climates than in hot wet climates. Weathering is a degradation process and it is temperature dependent, i.e. it occurs faster at higher temperatures. The rule of thumb is that a 10°C-increase in temperature causes the reaction rate to double [5]. Therefore, to evaluate the long-term behaviour and stability of materials in opportunely short times, accelerated artificial aging is usually performed by speeding up the natural aging. Deterioration processes can hence be artificially induced in the laboratory to elucidate chemical reactions and mechanisms involved in the degradation and their effects on the materials. Surprisingly, to the best of knowledge, up to now only few studies concerning the permanence and chemical mechanisms of deterioration of protective coatings and painting materials have been published [2].

Accelerated aging tests allow to estimate the potential long-term serviceability of materials, defined as “the maintenance of performance above a threshold level that is regarded as acceptable” [6]. First of all, it is important to distinguish between *stability* and *durability*. *Stability* is defined as the resistance of a material to environmental factors such as oxygen, ozone, moisture, heat, and light, which primarily bring about chemical changes. *Durability* is commonly regarded as the physical resistance to degradation with respect to the stress imposed. Anyhow, it is generally held that changes in the chemical structure of materials are usually responsible for the physical disintegration and failure of materials. Hence, monitoring the changes in chemical properties of materials is by far the most common approach associated with accelerated aging tests [7].

Nevertheless, it is worth remembering that all predictions of long-term behaviour are essentially a simply rank of the relative stability of one material with respect to another under a given set of conditions. Feller R.L. suggested three classes of photochemical stability (Table 1) [6]. Unstable

materials (Class C) are those that would seriously degrade in less than 20 years of normal usage in a museum. Class A materials, of excellent quality, e.g. suitable for use in conservation practice, are materials that might give at least 100 years of satisfactory service. Class B materials are those falling between the two and guaranteed from 20 to 100 years of service.

Table 1. Classification of useful lifetimes for conservation materials as proposed by Feller R.L. (1978).

<i>Class</i>	<i>Classification</i>	<i>Proposed lifetime</i>
<i>A1</i>	Excellent	> 500 years
<i>A2</i>	Excellent	> 100 years
<i>B</i>	Intermediate	20-100 years
<i>C</i>	Unstable	< 20 years
<i>T</i>	Temporary	< 6 months

The wide range of stability of materials makes it impossible to specify a standard accelerated-aging test that can effectively evaluate both highly fugitive and highly stable materials. Standard test procedures for artificial aging have been published only for commercial products such as paper, thermosetting powder coatings for architectonic surfaces, dyes, pigments [8] and, in most of the cases, they represent the basis for procedures used to evaluate the long-term stability of other types of materials applied in the conservation practice.

In order to design the optimum accelerated aging test, chemical and physical properties (e.g. tensile strength, adhesion, brittleness and colour) to be controlled during aging have to be in principle defined beforehand. Unfortunately, it is usually not possible to decide ahead which property is going to be the most significant to monitor the aging process. The most commonly employed approach relies on measuring several chemical and physical properties and on recording changes that, collectively interpreted, may explain the relative stability of one material with respect to another.

It is worth considering that in real practice, aging processes may be far more complex. Firstly, opposite reactions, such as yellowing and bleaching or cross-linking and chain cleavage, can take place concurrently during aging. Secondly, often it is not easy to define whether the property chosen and monitored represents an appropriate indicator of the point at which unacceptable changes occur.

There are two main methods to artificially accelerate the aging processes: (1) changing/stressing only one environmental parameter at a time (e.g. light or temperature) while maintaining the others constant; (2) stressing several environmental conditions at once (i.e. climatic chamber). These experiments may reproduce the physical decay effects caused by natural aging, such as colour and gloss changes, change in the degree of polymerization and loss of hydrorepellence. Even though techniques have been improved, artificially accelerated aging processes are just approximations to the natural situation. Thus, the results of artificial and natural aging tests should always be compared for the same material.

1.2 Kinetics of degradation

The kinetic of degradation is defined as the study of the rate at which deterioration reactions occur and the influence of conditions such as temperature, humidity, concentration of reactants on the rate [9]. The rate of reactions can be assessed by monitoring the change in the properties of the material, e.g. yellowing, over time [10]. When only one chemical process is responsible for the degradation, and hence for the change monitored, the interpretation in terms of chemical kinetics is usually easy. However, in most of the cases, two or more degradation processes occur simultaneously during aging and data might seem contradictory because the overall effect most likely depends on which chemical process is the dominant one under the specific aging conditions tested.

In solution and gaseous mixtures (homogeneous conditions), the rate at which a chemical process takes place is related to the concentration of the substances undergoing the reaction. In the study of chemical kinetics, reactions can be interpreted according to the molecularity, i.e. the number of atoms or molecules taking part to each specific chemical reaction, or according to the order of the reaction. The latter refers to the number of atoms or molecules whose concentration determines the velocity of the process.

Deterioration processes are generally the result of a series of reactions. Thus, if one measures the change in concentration of a chemical specie, the kinetic represents the result of the overall set of chemical reactions rather than of one specific chemical step. Materials generally tend to deteriorate not according to a first-order reaction, but following kinetics such as those illustrated in Figure 1.

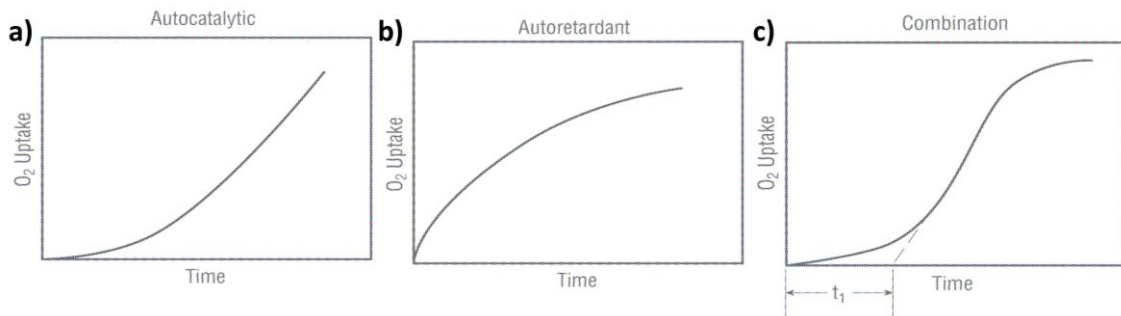


Figure 1. Models of chemical kinetics.

Therefore, when accelerated-aging tests are designed and carried out, it is necessary to evaluate changes in physical and chemical properties up to the point of failure (or the point at which changes are no longer acceptable) and to determine whether the system follows one of the paths shown in Figure 1. If chemical properties tend to follow one of the principal kinetic processes, the respective mathematic model can be used to predict the progress of the accelerated aging as well as the course of aging under natural conditions.

1.3 Mechanisms of degradation

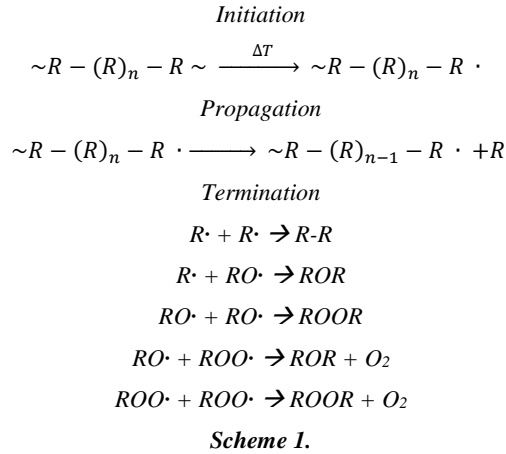
The mechanism of degradation is the series of chemical reactions involved in the deterioration processes of a specific material. Depending upon the nature of the degrading agents, degradation have been classified as thermal-oxidative, photo-oxidative, ozone-induced, mechanochemical, catalytic and biodegradation [11]. In their review, Singh B. and Sharma N. [12] well described the different mechanisms of deterioration and discussed the methods used to study these degradations as well as the various influencing factors. Nevertheless, the mechanism of degradation depends firstly on the type of material. Polymeric materials can be synthesized via polyaddition or polycondensation of small molecules (monomers) and they are in general classified into two groups, thermoplastics and thermoset plastics [13]. Thermoplastics are linear chain macromolecules, obtainable from the reaction of the double bond of vinyl monomers, where the atoms and molecules are joined end-to-end (addition polymerization) into a series of long carbon chains. On the other hand, thermoset plastics are formed following step-growth polymerization allowing bi-functional molecules to condense inter-molecularly with the liberation of small products such as H₂O, HCl, etc. at each reaction step. During these reactions, monomers condense and irreversibly convert into a no longer workable mass.

1.3.1 Thermal degradation

Both photochemical and thermal degradation processes are classified as *oxidative mechanisms*, with the main differences being the sequence of initiation steps leading to auto-oxidation cycle and the extent of degradation. In fact, while thermal degradation occurs throughout the bulk of the material, photochemical degradation concerns only the surface [15].

Thermal degradation of polymers occurs through random chain depolymerization (or fragmentation) initiated by a thermal stress and consists of two distinct reactions which may occur simultaneously. The first is a chain-end scission of C-C bonds (known as unzipping route) generating volatile products, and the other is the random scission of chemical linkages (i.e. random degradation route or depolymerization) causing a reduction in the molecular weight of the polymer.

The type and composition of pyrolysis products could give useful information about the mechanism of thermal degradation of polymers [12]. The chain-end degradation, for example, successively releases the monomer units and often this is the opposite of the propagation step in an addition polymerization. In fact, it occurs through a free radical mechanism (Scheme 1). In this type of degradation, the molecular weight of the polymer decreases slowly, and large quantity of the monomer is released. In general, chain-end degradation occurs when the backbone bonds are weaker than the side groups bonds and only to polymer molecules carrying active chain ends with a free radical, a charged fragment, etc. On the other hand, random degradation occurs arbitrarily at any point along the polymer chain and it is the reverse of the polycondensation process, because the polymer degrades to lower molecular weight fragments, but no monomer is released.



The most common method to induce thermal degradation in a material is by increasing the environmental temperature inside a ventilated oven or in a thermo-cycling system [16]. During a thermo-oxidative aging, samples are exposed to moderately or extremely high temperatures in an air-circulating heating system where the volatile deterioration products possibly formed are continuously removed and further degradation induced by the released volatiles is avoided.

The rate of a chemical reaction (k) can be determined from the activation energy (E) of the reaction and the temperature (T) using the Arrhenius equation Eq. (1):

$$Eq. (1) \quad k = Ae^{-E/RT}$$

where A is the pre-exponential factor and R is the gas constant (8.31 KJ/mol). According to this equation, an increase in the temperature implies an increase of the reaction rate. However, if more than one reaction occurs during the thermal degradation process, the increase in the temperature may change the relative importance of the different reactions.

Another common method for investigating the thermal stability of the polymers is by means of thermogravimetric analysis (TGA) [17]. The rate of degradation in TGA (da/dt) is defined as the rate of change of the degree of conversion and it is calculated in terms of mass as shown in Eq. (2):

$$Eq. (2) \quad \alpha = W_0 - W / W - W_f$$

where W_0 , W and W_f are respectively the initial weight, the weight at each point of the curve, and the final weight measured at the end of the degradation process [18].

Thermogravimetry signals (TG) provide the weight losses W of the samples as a function of time and temperature, while the respective derivative thermogravimetry signals (DTG) are obtained by taking the time derivative, $d(W/W_0)/dt$, of the ratio W/W_0 . The method allows to study the decomposition pathway of materials, i.e. the loss of volatile components such as moisture, the presence of retained solvents or unreacted monomers, the combustion of carbon black, and the presence of possible final residues (ash, fillers, glass fibers) and hence to draw conclusions about their individual constituents. TGA experiments can be additionally used to evaluate the apparent activation energy of the degradation process by

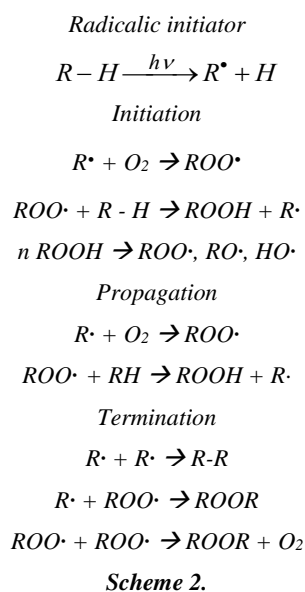
applying different equations and calculation methods [19], the most common being the Kissinger [19a, 19l], Friedman [19l] and the modified Kissinger–Akahira–Sunose (KAS) [19 g] models. It was shown [20] that in the case of complex processes involving the overlapping of TG signals, the KAS and Friedman methods provide good qualitative information about the activation energy of the single processes. However, data are not easy to interpret and deconvolution procedures are necessary. On the other hand, in most of the cases the apparent activation energy determined by the Kissinger equation for the overlapped dominant peak is in agreement with the true value determined for the single process [19n]. This suggests that the Kissinger method is an advantageous approach to evaluate complex kinetic degradation processes.

1.3.2 Photo-oxidative degradation

Photo-oxidative degradation is a process initiated by UV and visible light. Most of the synthetic polymers are susceptible because photons, especially in the UV range, have sufficient energy to cleave C-C bonds. The damage induced depends, for each material, on the specific UV wavelength and on the chemical bonds present. Visible light causes slightly changes in properties as it provides just the minimum amount of energy sufficient to activate the breakage.

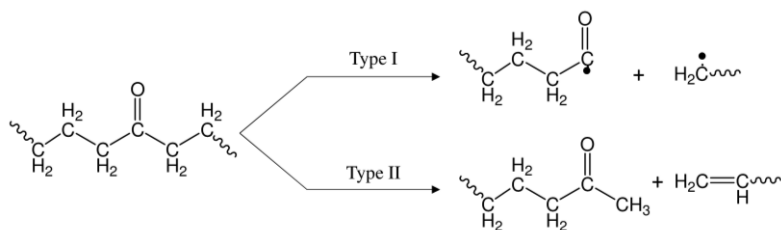
Photo-oxidative reactions can be additionally triggered simply by extraneous groups and/or impurities in the polymer, which absorb light quanta and form excited states.

Photodegradation generally changes the physical, chemical and optical properties of the materials. Common damages result in visual phenomena such as yellowing or opacification, as well as in the loss of mechanical properties and changes in molecular weight and molecular weight distributions [14]. Although some specific photo-aging chambers are available on the market, aging conditions and methods have not been yet standardized and thus results available in the literature are often not directly comparable.



In most of the cases, photo-oxidative degradation mechanism involves auto-oxidation cycle (Scheme 2) and it is determined by the groups and/or impurities in the polymer, which absorb light quanta and form excited states. Initiation is due to the absorption of UV light having sufficient energy to break C-C (375 kJ/mol) and C-H (420 kJ/mol) bonds in the polymer chain.

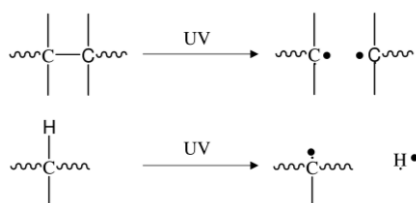
Under UV irradiation, the initial short-lived singlet state is transformed into long-lived triplet excited state which may cleave the polymer chains and form either (a) radical pairs according to a Norrish Type I reaction or (b) pairs of saturated and unsaturated chain ends by hydrogen transfer (Norrish Type II reaction) as shown in Scheme 3.



Scheme 3.

Free radicals formed by photon absorption act as initiator by reacting with oxygen to produce a polymer peroxy radical (ROO•) which reacts with a polymer molecule to generate polymer hydroperoxide (ROOH) and a new polymer alkyl radical (R•).

Other sources of radicals initiator are peroxides, C=C sites and carbonyl groups eventually presented, as shown in Scheme 4.



Scheme 4.

Propagating reactions in auto-oxidation cycle are common in all carbon-backbone polymers and lead to the generation of hydroperoxide species which are responsible for the polymer degradation through the cleavage of the hydroperoxide O-O bond. Polymer backbone cleavage occurs through Norrish Type I and II reactions following β -scission mechanism, which is the main route for photo-oxidative degradation. Specifically, polymer-derived radicals formed during the initiation can add molecular oxygen (oxidation reactions) to form peroxy radicals which abstract hydrogen and form hydroperoxide groups. In the latter, following the absorption of UV light or energy transfer, the weak O-O bonds break forming pairs of alkoxy and hydroxyl radicals. These new radicals can react in different ways such as hydrogen abstraction, chain scission, rearrangement, etc. and accelerate the photodegradation.

Finally, termination reactions occur by free radicals coupling to create inert products.

Although light and heat represent important factors to initiate degradation, the greatest damages to polymers are caused by oxygen. Oxidation occurs in all organic materials, but their resistance can be greatly variable. For example, polymers that contain oxygen in their backbone, like acrylates and cellulose derivatives, are far less stable to oxidation than saturated polyolefins [21]. Oxidation reactions may result in an increase of the molecular weight by incorporation of oxygen, as in the case of drying oils, or in a loss of weight [22]. Four stages were identified during the oxidation processes [23]:

- *inception*, adjustment of the material at the exposure conditions;
- *induction*, formation of peroxides groups (in many cases this represents the maximum shelf life of a material which can be extended by adding antioxidants and/or UV stabilizers and/or absorbers);
- *propagation*, reactions of the reactive groups in the polymer;
- *termination*, reactions of radicals with formation of neutral species.

2. Acrylic Emulsion and Microemulsion: Chemistry and Degradation

Acrylic resins, derived from the polymerisation of different esters monomers of acrylic and methacrylic acids, have been largely used in conservation practices. The most prominent polymers in the field of conservation as well as in modern and contemporary artworks are the so-called *acrylics* thanks to the possibility of developing a wide variety of resins, with specific molecular weights and tailored physico-chemical characteristics, by simply varying the ratio of constituting monomers [7].

In the early 1940s, the acrylic commercial products *Lucite 44* and *Lucite 45* based on poly(butyl methacrylate) (*PBMA*) started to be used as picture varnishes because of their optical clarity, mechanical properties, adhesion and chemical stability [1]. In particular, the first acrylic paints were formulated by *Bocur and Golden* as solutions of poly(*n*-butyl methacrylate) in organic solvent. Unfortunately, these resins have been found unsuitable for long-term use due to unexpected cross-link reactions, cracking and yellowing exhibited when the polymers were exposed to different natural environments [24].

At the end of the 1960s, more stable acrylic resins were introduced in the market with the generic name *Paraloid*. These resins, applied in an organic solvent with variable solid content, were recommended for a wide range of applications, such as textile, wood, pigments consolidant, as adhesives for paper, mosaics, amber, fossil, ceramic and glass and as consolidants and water repellent for stones thanks to their hydrophobicity [7, 25]. Considering the wide range of monomers used over time to produce acrylic resins, extensive studies have been conducted to define the aging behaviours of each acrylic and methacrylic monomer and of the different commercial *Paraloids*. The structural and molecular changes occurring under artificial aging were evaluated from different authors by means of UV-Vis, FT-IR Spectroscopy and by Size Exclusion Chromatography (SEC) [26]. The main aging behaviours observed are summarized in Table 2.

Under photodegradative conditions, acrylate units are generally more reactive towards oxidation as compared to the methacrylate ones, but for both monomeric units scission reactions prevail over cross-linking when the ester side group is short [26b, 26f]. When a butyl ester group is present the behaviour changes dramatically, and the polymer undergoes fast and extensive cross-linking [26g]. The overall stability of the acrylic polymers is strongly influenced by the presence of long alkyl side groups, such as butyl or isobutyl, whose oxidation is favoured by the presence of relatively labile hydrogen atoms. The *Paraloid* resins containing only ethyl and methyl esters showed a good stability towards oxidation, reaching an equilibrium between scission reactions and macromolecular coupling which allows maintaining their molecular characteristics during ageing [26b].

Lazzari M. and Chiantore O. studied the mechanisms of thermal degradation of different acrylic resins and highlighted as chain scissions prevail over cross-linking in the systems where most of the alkyl side groups are short [26d]. FT-IR analyses revealed that the first step of aging involves the thermal decomposition of labile structures formed during synthesis. For longer times of treatment, the oxidative

decomposition of side groups may occur and it is favoured for longer esters containing isobutyl and butyl groups [27].

Table 2. Aging behaviour of acrylic and methacrylic polymers evaluated by SEC.

<i>Sample</i>	<i>Chemical composition</i>	<i>Eluent</i>	<i>Mw (KDa)</i>	<i>Aging conditions</i>	<i>Degradation mechanism</i>	<i>Ref</i>	
<i>PMA</i>	<i>PMA</i>	THF	82	UV aging	Mainly cross-linking	[26b]	
<i>PEMA</i>	<i>PEMA</i>		328	T=25°C	Mainly chains scission		
<i>P(MA-EMA)</i>	<i>P(MA-EMA)</i>		69	RH=50%	Mainly chains scission		
<i>B72</i>	<i>P(MA-EMA)</i>		105	Up to 600 hours	Mainly chains scission		
<i>PMA</i>	<i>PMA</i>	THF	28	UV aging	Chain scission	[26c]	
<i>PEA</i>	<i>PEA</i>		110	($\lambda > 295\text{nm}$)	Initial bimodal distribution but prevails extensive chain scission		
<i>PEMA</i>	<i>PEMA</i>		310	T _{max} 45°C	Prevails chain scission but in competition with cross-linking reactions		
<i>PnBMA</i>	<i>PiBMA</i>		220	Up to 1550 hours	Cross-linking		
<i>B44</i>	<i>EA/MMA/BMA (28/70/1)</i>	CHCl ₃	105	Thermal aging T ₁ =110°C T ₂ =135°C T ₃ =150°C	Initial Cross-linking followed by chain scission	[26d]	
<i>B82</i>	<i>EA/MMA/BMA (43/56/1)</i>		96		Chain scission		
<i>B48N</i>	<i>MMA/BMA (74/25)</i>		184		Initial cross-linking followed by chain scission		
<i>B66</i>	<i>MMA/BMA (48/52)</i>		55		Tendency to form cross-linking structures with initial formation of low weight products		
<i>B72</i>	<i>MA/EMA/BMA (32/66/2)</i>		88		Up to 200 hours		Chain scission
<i>B67</i>	<i>PiBMA</i>		48		Simultaneous cross-linking and fragmentation but branching reaction prevails in the long term or high temperature aging		
<i>PMMA</i>	<i>PMMA</i>		58		UV aging		Random chain scission
<i>PEMA</i>	<i>PEMA</i>	THF	39	($\lambda = 254\text{nm}$)	[26e]		
<i>PBMA</i>	<i>PBMA</i>		73	T=25°C		Simultaneous chain scission and increase of molecular weight	
<i>PHMA</i>	<i>PHMA</i>		63				
<i>B66</i>	<i>MMA/BMA (48/52)</i>		55	UV aging		Strong tendency to give cross-linking reactions	[26f]
<i>B72</i>	<i>MA/EMA/BMA (32/66/2)</i>	88	($\lambda > 295\text{nm}$)				
<i>B82</i>	<i>EA/MMA/BMA (43/56/1)</i>	96	T _{max} 45°C				
<i>B67</i>	<i>PiBMA</i>	48	Up to 2500 hours				
<i>B67</i>	<i>PiBMA</i>	THF	50.3	UV aging	Competition between cross-linking reactions and chain scission	[26i]	
<i>B72</i>	<i>MA/EMA (30/70)</i>		103.1	T _{max} 40°C	Initial prevailing of fragmentation with respect to cross-linking		
				Up to 2000 hours			

The influence of the ester groups size in the photochemical stability of some poly(alkyl methacrylate)s has also been estimated by Kaczmarek H. *et al.*. They revealed as *PMMA* undergoes slower photooxidation but faster photodegradation with respect to higher poly(alkyl methacrylate)s and as the different behaviours of degradation is caused by the different reactivity of the macroradicals, depending mainly on the flexibility and mobility of macro chains at room temperature [26e].

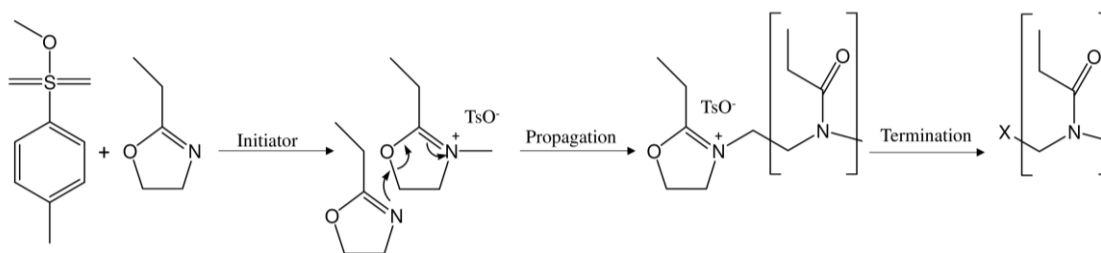
On the other hand, only few studies have been reported on the chromatic stability upon artificial aging of the different *Paraloid* types [26b, 26i, 26h]. It has been demonstrated that photodegradation causes acrylates to yellow because of the formation of conjugated double bonds systems [28]. Melo M.J. *et al.* [26b] have highlighted also as the very fast yellowing is followed by discolouration due to the loss of polymer on the treated surface.

Acrylic latexes, i.e. dispersions of acrylic polymers in water, became commercially available around 1950, and quickly became the preferred materials for artist's paints [29]. Learner T. has characterized by Pyrolysis–Gas Chromatography–Mass Spectroscopy (Py-GC/MS) a large number of modern paintings stored at the Tate Gallery (London), revealing a wide variety of compositions, including acrylic/styrene copolymers, vinyl/acrylic copolymers, poly(vinyl acetate), and vinyl acetate/vinyl neodecanoate copolymers [30]. Among paints based only on acrylic polymers, Learner revealed as poly(ethyl acrylate/methyl methacrylate) and poly(*n*-butyl acrylate/methyl methacrylate) copolymers are the most common types used.

Moreover, the growing attention towards human health and environment has led water-based emulsions (safer than the initial solvent-based formulations) to become the most common acrylic products available on the market. However, despite these products are available from several years, just a limited literature concerns their long-term stability [31]. Furthermore, the mechanisms and the kinetics of their degradation have not yet been defined.

3. *Aquazol 500*: Chemistry and Degradation

Aquazol is a class of hydrophilic-thermoplastic polymers manufactured by *Polymer Chemistry Innovations Inc.* *Aquazol (PEOX)* is the commercial name of the tertiary amide polymer made by cationic ring opening polymerization of 2-ethyl-2-oxazoline [32]. The synthesis is typically initiated by an electrophilic initiator, such as methyl tosylate, and terminated by nucleophiles [33]. The molecular structure of the polymer is characterized, as showed in Scheme 5, by a backbone in which two carbon atoms are alternated with one nitrogen atom with a pendent propionyl group.



Scheme 5. Methyl tosylate initiated cationic ring-opening polymerization of 2-ethyl-2-oxazoline.

Aquazol is available in four different molecular weights, three of which (50, 200 e 500 g/mol) are suitable for conservation purposes. The polymers differ only in the chain size and they are completely miscible in one other. Moreover, thanks to this wide range of molecular weights, *Aquazol* is a versatile material that can be used as consolidant (in a 5-20% range of concentration (w/v)), as adhesive, as inpainting medium (thanks to its high flexibility and reversibility with deionised water or polar solvents) and as a barrier or filler [34].

Aquazol was introduced in conservation in the early 90's, right after the first scientific studies on its chemical properties [35]. The polymer was well accepted because since 1930s conservators attempted to replace the natural water-soluble glue adhesives that suffer from embrittlement and yellowing [35]. The resin is an off-white solid with a glass transition temperature (T_g) of 69-71°C [36]. However, a T_g of 55°C is reported for a dried film of *Aquazol 500* made from aqueous solution [32, 37]. *Aquazol* has unusual physical and chemical properties compared to conventional polymers, one of the most interesting being its high solubility in water and its miscibility with a wide range of other polymeric materials. Polar and non-polar domains facilitate the interaction of *Aquazol* with a wide range of polar organic solvents, such as alcohols and ketones, and enable it to adhere to various surfaces [32, 38]. The long polymer chains have unusually low viscosity, heat stability, excellent flexibility and a high, glass-like refractive index. Other interesting features of *PEOX* are the relatively good stability at room temperature and pressure, the neutral pH in aqueous solution, the compatibility with a broad range of materials, the non-toxicity and its biodegradability [32, 34g, 39].

Wolbers R.C., McGinn M. and Duerbeck D. carried out accelerated photo-ageing tests on samples of *Aquazol 50* and *500* and they detected a good stability of these two products [37]. They found that after

280 KJm⁻² total radiant exposure, (corresponding to 24 years of exposure in a museum environment), the FT-IR spectra of the polymer do not change significantly, and no yellowing or discolouration are detectable. Moreover, viscosity and Size Exclusion Chromatography (SEC) measurements were performed revealing a decrease of the molecular weights of the polymers during the aging tests. However, despite depolymerization reaction occurs, the solubility of the aged material remains unchanged as compared to the fresh one samples. Finally, Thermogravimetric Analysis (TGA) confirmed the thermal stability of *Aquazol*, with Differential Thermal Analysis (DTA) yielding similar results before and after ageing [32].

On the other hand, Camaiti M. *et al.* revealed as *Aquazol 200* and *Aquazol 500*, aged in a solarbox with UV light ($\lambda > 280$ nm) and irradiation of 500 W/m² up to 3000 hours, exhibited extensive oxidation and depolymerization reactions with evident changes in the FT-IR spectra, in the molecular weights distributions and in the chromatic properties [40]. Thus, they concluded that *Aquazol* is too sensitive to UV light for outdoor use and its only acceptable use is as adhesive. Moreover, Ackroyd P. [41] revealed that *Aquazol* is very sensitive to water sorption especially at elevated humidity levels. In particular, relative humidity over 50% affects its mechanical behaviour and the induced dimensional variation can produce distortion of the treated materials.

Orsini S. *et al.* characterized *Aquazol* using Pyrolysis coupled with Gas Chromatography and Mass Spectrometry (Py-GC/MS) and Direct Exposure Mass Spectrometry (DEMS) techniques [42]. The analyses allowed to determine that the pyrolytic degradation of *Aquazol 500* is not based on unzipping mechanism, but it occurs by chain scissions of the polymer backbone followed by loss of side chains.

4. *Laropal A81*: Chemistry and Degradation

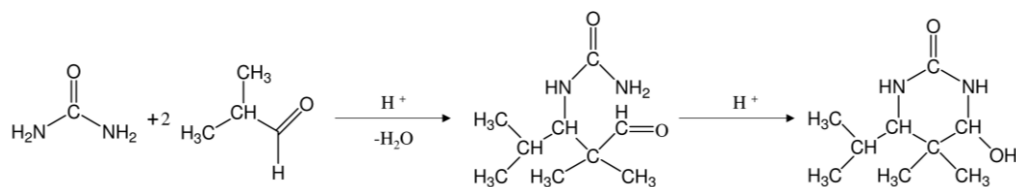
Synthetic low molecular weight (LMW) resins have found wide applications as varnishes (or protective layers) and binding materials for paintings thanks to their excellent optical characteristics and chemical stability. Final varnishes modify microscopically the roughness of the paint surfaces by reducing surface scattering and by increasing gloss and colour saturation [43]. The main reason for the use of a varnish is, in fact, to unify and generally increase the gloss. The general rule is that colours become darker when a varnish, with a refractive index (RI) significantly higher than that of air is applied [44].

Having excellent optical characteristics, low molecular weight resins are used in substitution for the traditional natural terpenoid varnishes, such as gum, dammar and mastic that are chemically unstable and over time may undergo yellowing and cracking or become difficult to remove. LMW resins appear good alternative to natural resins thanks to their comparable molecular weight distributions [45].

LMW varnish resins can be divided into three broad groups: ketone resins, hydrogenated hydrocarbon resins and urea-aldehyde resins. Maines C.A. *et al.* [45a] determined the molecular weights distributions and glass transition temperatures of the three groups of resins, as well as changes in their molecular weights distributions during exposure to a xenon-arc lamp for approximately 3000 hours. Although some of these LMW resins, such as ketone resins (e.g. *Laropal K-80*) and reduced ketone resins (e.g. *MS2A*) are known to be unstable, hydrogenated hydrocarbon (HHC) resins (e.g. *Arkon P-90* and *Regalrez 1094*) and some aldehyde resins (e.g. *Laropal A81*) exhibit high stability to aging as compared to the natural terpenoids varnishes [45a, 46].

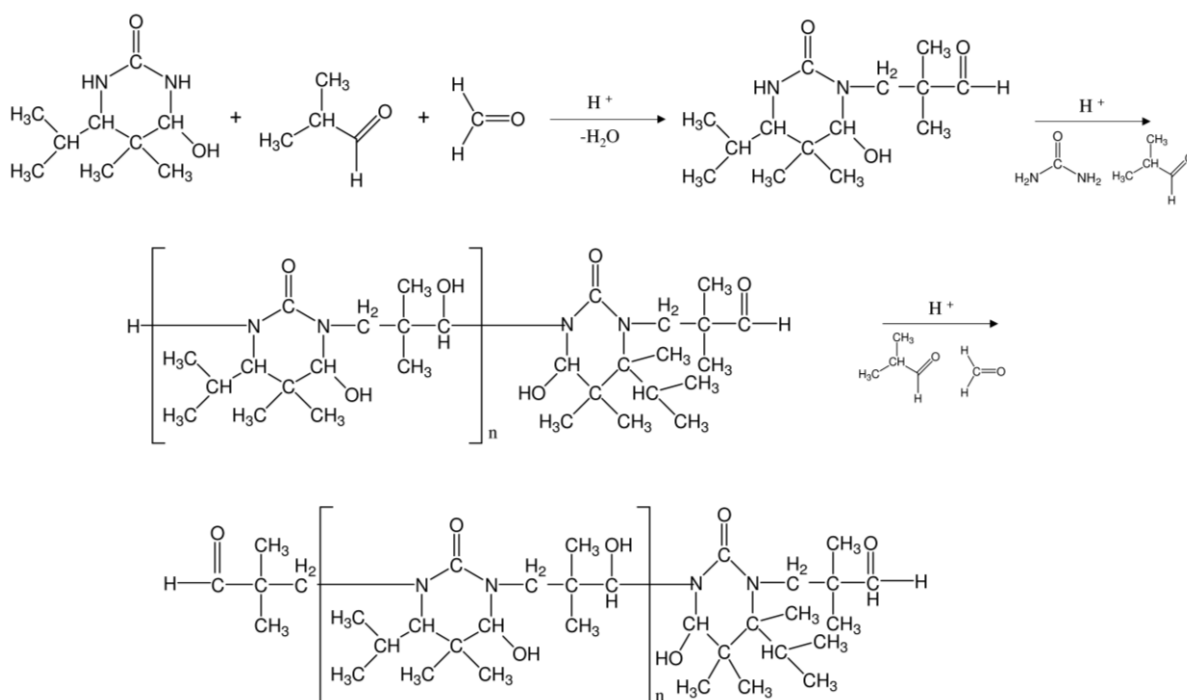
Urea-formaldehyde (UF) resins are the most important type of the so-called aminoplastic resins and are based on the manifold reaction of two monomers, urea and formaldehyde. By using different conditions of reaction, a variety of condensed structures can be obtained. After hardening, UF resins form an insoluble, three-dimensional network that cannot be melted or thermoformed again [47]. In particular, *Laropal A81* is a low molecular weight urea-aldehyde resin made by condensation of urea and aliphatic aldehydes, formaldehyde and isobutyraldehyde. It is soluble in most of the solvents, except water and aliphatics. It is commercialized by BASF and it was just only recently introduced in the field of conservation as varnish, consolidant and binding material. *Laropal A81* was also investigated in binary mixtures with *Paraloid B72* [48] and with different ethylene copolymers [49] to obtain specific characteristics of the final conservation blend product.

A urea–isobutyraldehyde–formaldehyde (UIF) resin can be synthesized in two steps [50]. In the first, an α -ureidoalkylation reaction occurs between urea and isobutyraldehyde to give 4-hydroxy-6-isopropyl-5,5-dimethyl-tetrahydro-pyrimidin-2-one (HIDTPO) as reported in Scheme 6 [51].



Scheme 6. Reaction between urea and isobutyraldehyde to give HIDTPO.

In the second step, HIDTPO reacts with formaldehyde and isobutyraldehyde to gradually produce the UIF resin, as reported in Scheme 7.



Scheme 7. Reaction of HIDTPO with formaldehyde and isobutyraldehyde to produce the UIF.

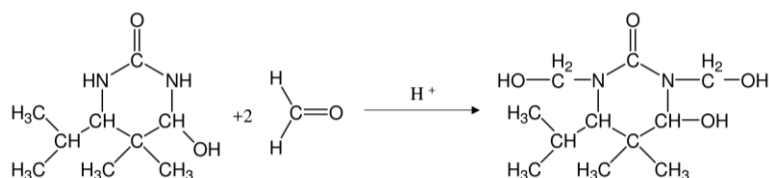
Although the nature of the monomers used in the synthesis of UIF is known, the specific molar ratio of urea, isobutyraldehyde and formaldehyde as well as the synthetic pathway are patented and therefore some data are not publicly available.

Zhang Y. *et al.* [51a] have shown the changes in the yield of reaction and on the properties of UIF resins obtained from different molar ratio of U/I/F. The main results are listed in Table 3.

Table 3. Effect of molar ratio of U/I/F on yield and properties of final resin.

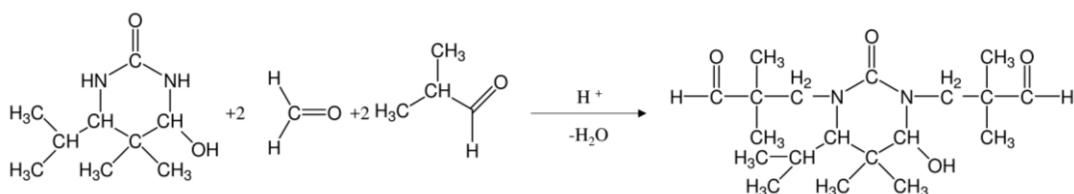
<i>U/I/F (mol/mol/mol)</i>	<i>Yield (wt%)</i>	<i>Softening point</i>	<i>Hydroxyl value (mg KOH/g)</i>
1.0/2.0/4.0	43.4	116	28
1.0/3.0/3.0	70.1	102	38
1.0/3.6/2.4	76.5	90	32
1.0/4.0/2.0	73.2	83	30

As seen in Table 3, the yield of the reaction significantly depends on the ratio of urea, isobutyraldehyde and formaldehyde. Therefore, Zhang Y. *et al.* have hypothesized deviations from the scheme of reaction reported above (Scheme 7). In the specific, the low yield obtained for the reaction with molar ratio of 1.0/2.0/4.0 is explained considering that only HIDTPO and formaldehyde are present in the reactive mixture of the second step thus, in this case, the reaction tends to proceed according to Scheme 8, producing water soluble units easily removed during the washing. Moreover, they have hypothesized that cross-linking condensation reactions might occur between HIDTPO units during distillation.



Scheme 8. Reaction between HIDTPO and formaldehyde.

On the other hand, Zhang Y. *et al.* observed as the softening points of the resins decrease on increasing the amount of isobutyraldehyde. For increasing amount of isobutyraldehyde, the secondary product of the reaction is the one reported in Scheme 9.



Scheme 9. Reaction between HIDTPO, formaldehyde and isobutyraldehyde.

Peris-Vicente J. *et al.* [52] have described only partially the pyrolysis profile of *Laropal A81*, detecting methyl-2,2-dimethyl-3-hydroxypropionate, ethylbutanal and isobutanal as main pyrolytic products. Only Bonaduce I. *et al.* [53] have completely characterized the molecular structure of *Laropal A81* using FIA-ESI-Q-ToF, revealing a dimeric-like structure whose repeating unit is the cyclic structure 4-hydroxy-6-isopropyl-5,5-dimethyltetrahydropyrimidin-2(1H)-one (186 uma) and confirming a structure like the one reported in Scheme 7.

The structure of the final polymer was investigated also by FT-IR and NMR Spectroscopy [51] and by Direct Temperature Resolved Time of Flight Mass Spectrometry (DTMS) [54].

T_g values reported in literature range from 48°C [45a] to 59 [55] depending on the thermal history, purity of the sample, and eventually changes in formulation.

SEC analysis performed on *Laropal A81* revealed a molecular weight of 3.6 KDa [44a] for the unaged resin and little or no change in the molecular weight distributions after up to 3000 hours of accelerated photo-oxidative aging [45a]. On the other hand, Maines C.A. *et al.* [45a] reported a number-average molecular weight of 13 KDa for the fresh *Laropal A81*.

5. Inorganic commercial products: Chemistry and Degradation

In the last years, engineering nanoparticles have been widely applied in the field of Cultural Heritage thanks to their compatibility with the artistic substrates, that reduces the possibility of drawbacks and negative effects of the conservative treatments. Inorganic nanoparticles (NPs) are mainly used as consolidants thanks to their precipitation into the porosities, as a consequence of the chemical reaction between the NPs and carbon dioxide in the air, the water or some components of the treated materials. Dispersions of $\text{Ca}(\text{OH})_2$ nanoparticles in water or short-chain alcohols have been largely studied to establish their potential use for consolidation of limestone and carbonatic painted surfaces [56], wood [57], paper and canvas deacidification [58], as well as for archaeological bones treatment [59]. Several methodologies for $\text{Ca}(\text{OH})_2$ NPs synthesis have been reported [60], and the related formulations showed different features such as the degree of dispersibility, the particle size distribution and the structure, which are expected to affect the consolidation process. Literature studies showed that $\text{Ca}(\text{OH})_2$ NPs dispersed in short-chain alcohols exhibit a higher colloidal stability than using water as dispersant, significantly improving the degree of consolidation by decreasing the rate of particles agglomeration [56d, 61].

As far as silica-based consolidants are concerned, commercial products containing alkoxy silanes, such as tetraethylortosilicate (*TEOS*), are commonly used [62]. These products, by polymerizing in situ via a sol-gel process within the porous structure of the materials to be consolidated, increase the mechanical properties of the material. However, they can form a dense microporous network of gel that tends to become brittle and susceptible to cracking. Moreover, this network can obstruct the pores of the materials promoting a significant reduction of water permeability [63]. To improve consolidation performances, nanosilica-based products were synthesized by a template synthesis in which a surfactant was used as structure-directing agent during the polymerization process [64]. Following this procedure, silica nanoparticles with uniform size and ordered mesopores were obtained. Moreover, the presence of surfactants avoids the cracking of the gel during the drying phase because of a coarsening of the gel network that reduces the capillary pressure [65]. Furthermore, the advantage of using nanosilica-based product with respect to the traditional solvent-based *TEOS* is the non-hazardous solvents employed and the reduced time necessary to obtain the gel network (3-4 days instead of 28) [66]. On the other hand, the capability of silica nanoparticles to penetrate porous materials with respect to the solvent-based silica products have not been yet deeply investigated [67].

6. Lanthanide complexes

The use of luminescent lanthanide complexes as dopants in retouching materials for restoration has been little studied, while their application in many frontier technology fields is well known. For example, these compounds are currently studied for optical amplifiers and laser materials and for efficient lighting devices and monitors [68]. Moreover, these species are successfully used as luminescent probes for biological and medicinal applications [69]. Luminescence studies in the field of works of art are instead limited to fluorescent organic pigments sometimes containing transition metal elements [70] or to novel non-toxic or high-temperature resistant pigments [71]. In previous papers [72], the possibility to visually discriminate between original and retouched areas by the use of photoluminescent lanthanide complexes was evaluated. The homoplectic scorpionate complexes $\text{Ln}(\text{Tp})_3$ ($\text{Ln}=\text{Eu}; \text{Tb}$) allow a facile recognition of the restored parts because these species are easily detectable with a common Wood lamp. Moreover, their high resistance towards thermal and photo-oxidative aging was highlighted.

The major advantages of lanthanide complexes as luminescent species are the long emission lifetimes, narrow bandwidths and large Stokes shifts [73]. However, the photoluminescence of the common salts of lanthanides is very weak, primarily due to the very low absorption coefficients of these ions. To overcome the low emission efficiency stemming from the forbidden intra- $4f$ transitions, it is common practice to select organic ligands that behave as antennae and can increase the Ln^{3+} luminescence efficiency. Thus, complexes with well-designed ligands, having broad and intense absorption band, are synthesized. An intense metal-centred luminescence can be observed if the excitation energy is transferred from the organic ligands to the excited states of the lanthanide ion by intramolecular mechanism. The efficiency of the energy transfer depends on the relative energies of the ligands excited states with respect to resonant levels of the metal centre. The excited state of the ligands must have energy greater than the emission level of the Ln^{3+} ion to reduce the back-energy transfer. However, a too high energy separation makes competitive other radiative decay processes such as fluorescence or phosphorescence. The radiative decay of the excited Ln^{3+} ion to the ground state causes an emission dependent upon its electronic structure (antenna effect). Several $\text{Ln}(\text{III})$ ions give emission in the visible range, such as $\text{Eu}(\text{III})$ and $\text{Pr}(\text{III})$ (red emitters), $\text{Sm}(\text{III})$ (orange emitter), $\text{Dy}(\text{III})$ (yellow emitter), $\text{Tb}(\text{III})$ (green emitter) and $\text{Tm}(\text{III})$ (blue emitter). Near infrared (NIR) emissions can be instead obtained from lanthanide ions such as $\text{Yb}(\text{III})$, $\text{Nd}(\text{III})$ and $\text{Er}(\text{III})$. However, non-radiative decay of the excited lanthanide ions can occur in the presence of high-frequency oscillators, such as the O-H bonds in water, or by concentration quenching phenomena. Thus, to avoid the quench of the luminescence, the ligands should keep water molecules outside the inner coordination sphere of the metal centre [69i, 69m, 69n, 69r]. Moreover, concentration quenching, caused by excessive amounts of chromophore, can be avoided by dispersing the luminescent species in a matrix. These matrices can be identified among inorganic, usually silica- or alluminosilica-based materials, and organic polymers. Furthermore, the embedding of a lanthanide complex in a matrix improves some physical properties of the complex like the optical and

thermal stability.

In the last years 1,10-phenanthroline (phen) ligand has aroused growing interest thanks to its ability to coordinate in a bidentate fashion to form stable complexes with many different transition and rare-earth metal ions [74]. Phenanthroline has been used as an excellent antenna to sensitize lanthanide ions by absorbing light in the UV region and transfer it, usually from the triplet state, to the lanthanide ion [75]. Moreover, Taha Z.A. *et al.* [76] highlighted as Ln-phen complexes can be considered thermally stable and how the structure of the complexes is free of lattice or coordinated water or solvent molecules.

7. Materials and Methods

7.1 Materials and preparation of films samples

After detailed research, the most commonly used but so far scarcely investigated consolidants and binding media were selected to be tested in this project. The commercial products were chosen for their different physical-chemical characteristics and are:

- *Acril 33*, an aqueous emulsion (solid content 46%) of ethylacrylate and methylmethacrylate (*EA-MMA* 70:30) co-polymer;
- *Acril ME*, a water based micro emulsion (solid content 41%) of poly(butyl methacrylate) (*PBMA*);
- *Aquazol 500*, the tertiary amide made by cationic ring opening polymerization of the monomer 2-ethyl-2-oxazoline (*PEOX*);
- *Laropal A81*, a urea-aldehyde resin;
- *Estel 1000*, tetraethylortosilicate in white spirit D40;
- *NanoEstel*, an aqueous colloidal dispersion of nano-sized silica (solid content 30%) stabilized with sodium hydroxide ($\text{NaOH} < 0.5\%$);
- *NanoRestore*, a 2-propanol dispersion of $\text{Ca}(\text{OH})_2$ nanoparticles (5 g/L solid concentration).

Films samples were prepared using a silk-screen frame obtaining, onto microscope glass slices, averaged film thicknesses of about 60 μm . The main characteristics of the applied products are reported in Table 4.

Table 4. Chemical composition, glass transition temperature (T_g) (experimental data), solid content, solvent, and concentration of applied product (% w/w).

<i>Product</i>	<i>Chemical composition</i>	T_g	<i>Solid content (%)</i>	<i>solvent</i>	<i>Conc. (% w/w)</i>
<i>Acril 33</i>	<i>P(EA/MMA)</i> (70/30)	27.8	46	Water	50
<i>Acril ME</i>	<i>PBMA</i>	29.8	41	Water	50
<i>Aquazol</i>	2-ethyl-2-oxazoline	49.4	--	Water	20
<i>Laropal A81</i>	Urea aldehyde resin	65.5	--	Butyl acetate	50
<i>Estel 1000</i>	<i>TEOS</i>	--		White spirit D40	
<i>NanoEstel</i>	SiO_2 NPs	--	30	Water	30
<i>NanoRestore</i>	$\text{Ca}(\text{OH})_2$ NPs	--	0.5	2-propanol	0.5

Moreover, to evaluate the influence of the porosity on the aging behaviour of the consolidants, solutions of the consolidants *Acril 33*, *Acril ME*, *Estel 1000*, *NanoEstel* and *NanoRestore* were applied on Vicenza white limestone, Arenaria and Istria stone specimens, by brushing until complete saturation. In fact, it is well known that the objects supporting the testing materials can make an enormous difference on the

aging behaviour of the applied polymers [7]. Before consolidating stone specimens, the supports were carefully washed and brushed to remove all the soluble salts. After, they were dried in a ventilated oven and kept in a desiccator until the application of the products. Samples stones 5 x 5 x 2 cm³ were provided by Laboratorio Morseletto (Vicenza, Italy). Vicenza stone is a light ivory calcareous rock, principally composed by calcite and dolomite, with total porosity of 27.8% [77], extracted from the Oligocene horizons in Colli Berici (Vicenza, Italy). It is the result of the sedimentation of innumerable minute fossils, which create its texture. Arenaria, characterized by a total porosity of 5.10% with a specific surface of 1.06 m² g⁻¹ and average pore radius of 0.06 μm (experimental data), is a clastic sedimentary rock composed mainly by sand-sized minerals or rock grains with a dark grey colour. Instead Istria stone is a sedimentary compact rock (total porosity of 0.7% with a specific surface of 0.2 m² g⁻¹ and pore radius ranging from 7 to 20 nm [78]) with a micritic structure and a whitish colour, formed during the lower Cretaceous. All the types of stones used in this study were chosen because they were commonly used as building architecture materials in Venice. Some examples of their use can be seen in the architectural decorative apparatus of numerous palaces and churches, such as the Basilica of S. Marco and Palazzo Ducale. Beside the consolidation effectiveness, the knowledge of the aesthetic variations occurring on historic surfaces treated with the different consolidants after aging is of interest for a large community of end-users (e.g. architects, curators, conservators). Moreover, only few studies have been focused on the effect of venetian environment on weathering of the stone investigated [79], with still a lack of knowledge about their consolidation and aesthetic surface variations before and after aging tests. The results concerning the influence of the porosity on the aging behaviour of the consolidants, and the effect of venetian environment on weathering of the stone, were published in a scientific paper [80] reported in the appendix A.

The effective potential as consolidants or retouching materials of the commercial products were evaluated by physical-chemical characterizations and through thermal and photo-oxidative accelerated aging tests.

7.2 Natural and accelerated ageing tests

Ageing of materials used for conservation purposes may affect their original macroscopic properties as a result of the alteration of optical properties (like changes in colour and brightness) and changes in solubility, due to chemical alterations including cross-linking and depolymerization [81]. Therefore, the long-lasting stability is of great interest because it is closely related to the chemical stability.

Aging tests allowed to define the long-lasting performances and behaviours, the kinetic degradation parameters and the degradation mechanisms of each commercial product. Samples have been submitted to a systematic investigation of their chemical and physical stability under different thermal (T=80, 100, 120 and 140°C, up to 15000 hours in a ventilated oven) and photo-oxidative (UVA λ=254 nm and UVC λ=366 nm, 28 ± 2°C, relative humidity of 45%, up to 2000 hours) artificial aging conditions. The temperatures of the thermo-oxidative aging were chosen accordingly to the glass transition temperatures

of the different commercial products, while the two photo-oxidative wavelengths are the most common employed in artificial aging tests. The aging behaviours were followed at incremental times of aging by colorimetric and gloss measurements, Gel Permeation Chromatography (SEC) and FT-IR analyses. Thus, the results obtained were compared with the ones obtained from the natural aging of the same samples. Natural aging was performed, for the glass slides samples, by exposing the films at the natural light in normal indoor conser

vative environment (25°C, UR%= 30, up to 670 days), while for the stone samples by exposing the treated supports over two years to Venice-Mestre (Italy) outdoor conditions using rigid plastic supports with an inclination of 60°. In Appendix B are collected the environmental parameters (ARPAV data, Favaro Veneto station) at which the stone samples were exposed during the outdoor natural aging. In particular are reported the monthly average and maximum and minimum values recorded for the parameters temperature (°C) and relative humidity (%), while for the parameters rainfall (mm/month) and total solar irradiation (MJ/m²) are reported only the values of the monthly average.

7.3 Colorimetric measurements

The colour variation of aged samples was monitored at increasing time intervals, monthly for natural aging and every 100 hours for the thermal and photo-oxidative aging.

The colour measurements were carried out by a Konica Minolta spectrophotometer CM-2600d according to CIE Lab colour space method [82]. The parameters L*, a*, b* were simultaneously collected. L* stands for the lightness (L*=0 corresponds to black, L*=100 corresponds to white), while a* and b* are the colour-opponent dimensions: a* is the red/green balance (-a* corresponds to green and +a* corresponds to red) and b* is the yellow/blue balance (-b* corresponds to blue and +b* corresponds to yellow). The total variation of colour (ΔE^*) was calculated by the equation Eq. (3) [83]:

$$Eq. (3) \quad \Delta E = \sqrt{(\Delta L^*)^2 + (\Delta a^*)^2 + (\Delta b^*)^2}$$

where the parameters ΔL^* , Δa^* and Δb^* refer to the difference between the aged samples at each aging time and the unaged ones ($\Delta L^* = L^*_{t=x} - L^*_{t=0}$; $\Delta a^* = a^*_{t=x} - a^*_{t=0}$; $\Delta b^* = b^*_{t=x} - b^*_{t=0}$) [84].

7.4 Gloss measurements

The specular gloss, i.e. the ratio of the luminous flux reflected from the sample in the specular direction for a specified source and receptor angle, was determined with a Picogloss 503 instrument (Erichsen) at the beginning and at the end of each aging test at the incident angles of 60° with a resolution of 1 GU (Gloss Unit), according to ASTM D523-08:2004 [85]. The gloss retention ($\Delta_{gloss} \%$) was calculated between the fresh (gloss_{t=0}) and aged (gloss_{t=x}) gloss values as indicated in Eq. (4).

$$Eq. (4) \quad \Delta_{gloss} \% = \frac{gloss_{t=0} - gloss_{t=x}}{gloss_{t=0}} \times 100$$

7.5 Thermogravimetric (TGA) analyses

TGA analyses were performed with a STA 409 PC Luxx Simultaneous thermal analyzer (Netzsch) to evaluate the decomposition pathway of materials, i.e. the loss of volatile components and moisture, the presence of restrain solvents or unreacted monomers, the combustion of carbon black, and the presence of eventual final residues (ashes, fillers, glass fibers) [86]. Moreover, by imposing different heating rates, the thermal stability of the polymers *Acril 33*, *Acril ME*, *Aquazol 500* and *Laropal A81* was evaluated.

The emulsion *Acril 33* and the micro emulsion *Acril ME* were diluted in distilled water (50% w/w), applied as thin films (60 μm) and, after drying, cut in small squares of 2x2 mm of width. The same method was followed for *Aquazol 500* diluted at 20% in distilled water and for *Laropal A81* diluted at 50% in butylacetate. Before measurements the temperature scale was calibrated using an indium reference and the instrument was purged with nitrogen in the range temperature 25-700°C with a heating rate of 30°C min⁻¹. Between 25 and 30 mg of bulk sample were weighed and analysed in an open alumina standard pan. The characterization analyses were performed by heating the samples from 25 to 700°C at heating rate of 25°C min⁻¹ in controlled mixed gases (air and nitrogen in the ratio 70:30) atmosphere. The studies of thermal stability were carried out at different heating rates [87], from 5 to 25°C min⁻¹, in mixed atmosphere of nitrogen and air (70:30). TG signals give the weight losses W of the samples as function of time and temperature, meanwhile the derivative thermogravimetry (DTG) signals were obtained by taking the time derivative, d(W/W₀)/dt, of the ratio W/W₀, where W₀ is the initial weight of the sample.

Among the different methods that can be used [19], data were processed by means of the Kissinger's method which requires only the temperature at the maximum rate of weight loss to determine the activation energy (E) value according to the Eq. (5)

$$\text{Eq. (5)} \quad \ln\left(\frac{\phi}{T_m^2}\right) = \ln\left(\frac{nRAW_m^{n-1}}{E}\right) - \frac{E}{RT_m}$$

where ϕ is the heating rate in the TG experiment, T_m is the temperature at the maximum rate of weight loss, R is the universal gas constant, A is the pre-exponential factor, W_m is the weight of the sample at the maximum rate of weight loss and n is the apparent order of the reaction with respect to the weight of the sample. The activation energy values E were determined for each polymer from the slope of linear interpolations of ln(ϕ/T_m^2) versus 1/T_m at various heating rates.

7.6 Dynamic Light Scattering (DLS) and Centrifugal Separation Analysis (CSA)

The stability of the dispersions of *Acril 33*, *Acril ME*, *NanoEstel* and *NanoRestore* was evaluated by Dynamic Light Scattering (DLS) and Centrifugal Separation Analysis (CSA). Analyses were made both

on fresh, diluted as well as on one-year aged samples and the overall results from DLS and CSA were reported as average of three independent measurements.

Hydrodynamic particles diameter was measured by DLS by means of a multi-angle Nicomp ZLS Z3000 instrument (Particle Sizing System, Port Richey, FL, USA) with an optical fiber set at 90° scattering angle ($W=25$ mW, $\lambda=639$ nm, 25°C). Particles size diameter was calculated by Nicomp PSS software after imposing viscosity, density and refractive index values of both continuous and dispersed phases. Particles sedimentation velocity was calculated by CSA, employing the Multiwavelength Dispersion Analyzer LUMiSizer 651 ($\lambda=470$ nm). The samples were analysed in polycarbonate cuvettes with 10 mm optical path every 50 seconds (25°C). Different Rotation Per Minute (RPM) values were selected to prove the linearity of the method. RPM values have been converted to Relative Centrifugal Force (RCF) by the Eq (6)

$$\text{Eq. (6)} \quad \text{RCF}=1.1179 \cdot 10^{-3} \cdot \text{RPM}^2 \cdot R$$

where R [m] is the radius, calculated from the centre of the rotor to the point at which the transmittance values were considered.

The variations of the transmission profiles over time and space provide information on the kinetic of the separation/sedimentation process and on the particles size distribution [88]. The transmission profiles, which are the raw data generated by CSA, moved from the lowest values of transmittance (indicating the highest number of particles in suspension) to the maximum transmittance, corresponding to the total sedimentation of particles in the cuvette (i.e. plateau). SEPView software was used to obtain sedimentation velocities distributions data at 1300, 1500, 1700, 2000, 2300, 2500 and 2800 RPM to finally extrapolate sedimentation velocity value at gravity. Moreover, SEPView software was employed to obtain particles size distribution of the fresh, diluted and one-year aged samples, imposing viscosity, density and refractive index values of both continuous and dispersed phases.

7.7 Viscometric analyses

The viscometric properties of the diluted polymeric solutions provided the rheological behaviour and the influence of the different aging tests on the degree of polymerization. Viscometric analyses were performed in a water bath ($25 \pm 0.1^\circ\text{C}$) using Ostwal-glass capillary viscometers. Each sample solution has been analysed three times and the values reported are the average of the repetitions.

The determination of the intrinsic viscosity (η , mg ml^{-1}) of *Acril 33*, *Acril ME*, *Aquazol 500* and *Laropal A81* was obtained by the measure of the flow time of the polymer solutions at different concentrations through a glass capillary [89]. Thus, polymer films obtained from the solutions described in Table 4 were dried (25°C), cut into small pieces, weighted and solubilised under magnetic stirring (25°C). The characteristics of the analysed solutions and the conditions used for the viscometric analyses are reported in Table 5.

Table 5. Characteristics of the investigated solutions and conditions used for the viscometric analyses.

<i>Sample</i>	<i>Solvent</i>	<i>Conc. range (g dL⁻¹)</i>	<i>T(°C)</i>	<i>Ostwald Type</i>
<i>Acril 33</i>	Acetone	0.25 - 1.25	25	100/200
<i>Acril ME</i>	Acetone	0.25 - 1.25	25	100/200
<i>Aquazol</i>	MilliQ Water	0.1 – 0.8	25	200/300
<i>Laropal A81</i>	Butylacetate	1 - 10	25	100/200

The reduced viscosity was calculated for each sample as reported in Eq. (7)

$$\text{Eq. (7)} \quad \eta_{red} = \frac{\frac{t}{t_s - 1}}{c}$$

where t and t_s are the flowing times of the solvent and of the solution, respectively, and c is the concentration of the solution. A plot of the reduced viscosity versus concentration gives the intrinsic viscosity from the extrapolation to $c = 0$.

Viscometric measurements were additionally carried out on the aged polymer samples solutions in order to investigate the degradation mechanisms by comparing their flowing time with respect to the fresh sample.

7.8 Size Exclusion Chromatography (SEC)

SEC analyses have been performed during the doctoral internship at *Universität für Bodenkultur Wien*, BOKU (University of Natural Resources and Life Sciences, Vienna) at the Biopolymer and Paper Analytics Laboratory, under the supervision of Univ. Prof. Dipl.-Chem. Dr. Antje Potthast. Analyses have been performed on selected samples of *Acril 33*, *Acril ME*, *Aquazol 500* and *Laropal A81* and allowed to evaluate the molecular masses values (M_n , M_w and M_z) and the molecular weight distributions (*MWD*).

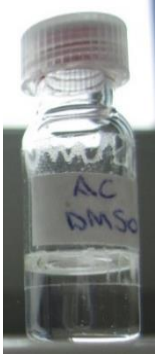
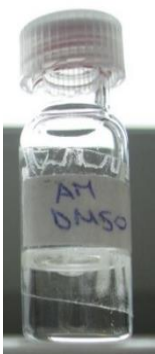
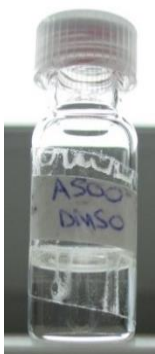
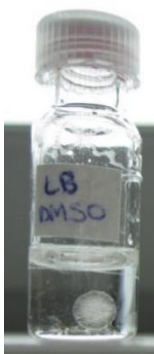
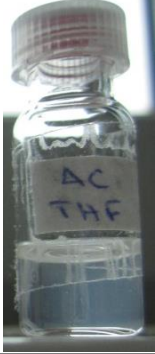
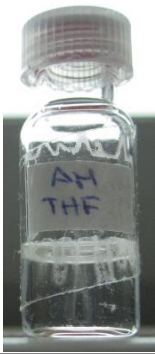

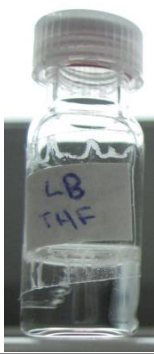

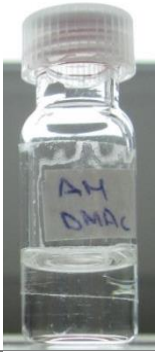
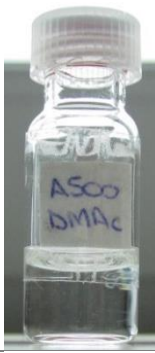
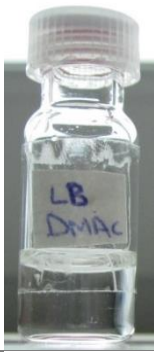

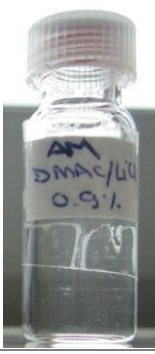
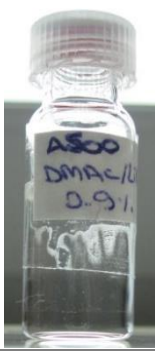
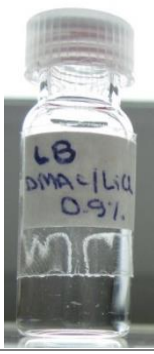
Firstly, the best solvent to dissolve the samples was investigated by evaluating the dissolution of the polymers *Acril 33*, *Acril ME*, *Aquazol 500* and *Laropal A81* (around 15 mg) in 1 mL of DMSO, THF, N,N-dimethylacetamide (DMAc) and 0.9% (w/V) lithium chloride/N,N-dimethylacetamide (DMAc/LiCl). As shown in Table 6, the solvents that provided a complete dissolution of all the polymers studied are DMAc and DMAc/LiCl 0.9% (w/V). It was chosen DMAc/LiCl 0.9% because it can be either used as solvent and as SEC mobile phase.

Samples were dissolved in 0.9% (w/V) lithium chloride/N,N-dimethylacetamide at room temperature and filtrate through 0.45 µm PTFE filters prior injection. Measurements were performed with a SEC/MALLS system equipped with: a pump (Bio-Inert 1260 Infinity II, Agilent, Waldbronn, Germany), an autosampler (HiP-ALS 1200, Agilent, Waldbronn, Germany), a column oven (Gynkotek STH 585), a multiple-angle laser light scattering detector (MALLS, Wyatt Dawn HELEOS II, Wyatt Inc. Santa Barbara, USA) with argon ion laser ($\lambda=663.6$ nm), and a refractive index detector (RI, Shodex RI-71, Showa Denko Europe GmbH, Munich, Germany). Four serial SEC columns (Polymer Laboratories,

currently Varian/Agilent) PLgel mixedA LS, 20 μm , 7.5 X 300 mm were used as the stationary phase. Operating conditions: 1.00 ml/min flow rate, 100 μl injection volume, 45 minutes run time. DMAc/LiCl (0.9%, w/V) filtered through a 0.02 μm Anopore inorganic membrane (Anodisc Sigma Aldrich) was used as eluent.

Unfortunately, both fresh and aged samples of *Laropal A81* exhibited quite lower molecular masses values and MDW, resulting unfit to be analysed with this instrument set up.

Table 6. Dissolution tests of polymer samples in DMSO, THF, DMAc and DMAc/LiCl 0.9% (w/V).

<i>Solvent</i>	<i>Acril 33</i>	<i>Acril ME</i>	<i>Aquazol</i>	<i>Laropal A81</i>
<i>DMSO</i>				
<i>THF</i>				
<i>DMAc</i>				
<i>DMAc/LiCl 0.9% (w/v)</i>				

The specific refractive index, i.e. the ratio of change of the refractive index with the concentration of a solution of polymer at a given temperature, wavelength, and a given solvent, was evaluated for the polymers *Acril 33*, *Acril ME* and *Aquazol 500* samples in DMAc/LiCl 0.9% (w/V) at 25°C and $\lambda=663.6$ nm. The $\delta n/\delta c$ values were calculated on assuming that 100% of the injected analyte elutes from the columns and that integration of the chromatogram encompasses all the contributions from the analyte [90]. The $\delta n/\delta c$ values used to evaluate the molecular masses values are reported in Table 7.

Table 7. $\delta n/\delta c$ values calculated for the polymer samples in DMAc/LiCl 0.9% (w/V) at 25°C and $\lambda=663.6$ nm.

<i>Sample</i>	$\delta n/\delta c$
<i>Acril 33</i>	0.0306
<i>Acril ME</i>	0.0351
<i>Aquazol</i>	0.0775

Together with the distribution of molar masses (*MMD*), given by the plot of the molar mass (g mol^{-1}) against the differential weight fraction, MALLS detector allows the determination of the molar masses averages M_n , M_w and M_z (representing three moments of the distribution) and the number n_i of molecules of molar mass M_i in each slice of the resulting chromatogram. The following parameters were considered.

The number average molar mass (M_n) is defined as the total molecular mass of n polymer molecules divided by the number n of polymer molecules, according to Eq. (8).

$$\text{Eq. (8)} \quad M_n = \frac{\sum n_i M_i}{\sum n_i}$$

M_n is sensitive to the presence of low molecular weights fractions and corresponds to the value for which there are equal numbers of molecules with lower and higher molecular weight.

Weight average molar mass (M_w) is large-molecule sensitive and influences the bulk properties and toughness of the polymer. M_w reflects changes in the high-MM components and is defined as reported in Eq. (9).

$$\text{Eq. (9)} \quad M_w = \frac{\sum n_i M_i^2}{\sum n_i M_i}$$

Z-average molar mass (M_z) is sensitive to very high-MM components and influences viscoelasticity and melt flow behaviour. It is defined according to Eq. (10).

$$\text{Eq. (10)} \quad M_z = \frac{\sum n_i M_i^3}{\sum n_i M_i^2}$$

The polydispersity index (\mathcal{D}) represents the width of molecular mass distribution and is calculated by the Eq. (11). The larger is the \mathcal{D} , the broader is the distribution (a monodisperse polymer is characterized by $\mathcal{D} = 1$).

Eq. (11)
$$\mathfrak{D} = \frac{M_w}{M_n}$$

MALLS detector provided also the averaged root mean square radius (rms, or radius of gyration R_z) in the range between 10 to several hundred nm, independently from the shape of the scattering particles. Moreover, the conformation plot slope was evaluated. This parameter was calculated from the slope of the plot of logarithm of radius (rms) as a function of the logarithm of the molar mass. The slope values give a good estimation of the shape: sphere corresponds to conformation slope plot in the range 0-0.33 (0 corresponds to a compact sphere), random coil to 0.5-0.6, rod to 1 and 1.8 to very stiff chain.

Finally, the average number of chain scission (S) per macromolecules was calculated according to Eq. (12) [91]

Eq. (12)
$$S = [M_n(0) - M_n(t)] - 1$$

where $M_n(0)$ and $M_n(t)$ are respectively the number-average molecular weight of the polymer before and after t hours of aging.

The weight- and number-average molar masses (M_w , M_n) and the molar mass distribution (MMD) were evaluated using Astra 6 (Wyatt Technologies) software. The relative standard deviation for M_w is below 5% and around 10% for M_n .

7.9 Fourier Transform Infrared Spectroscopy (FT-IR)

In an effort to follow the changes occurred in the samples, Fourier Transform Infrared Spectroscopy (FT-IR) spectra were recorded before and during artificial and natural aging tests.

FT-IR has been successfully employed to identify synthetic polymers in artworks and their degradation pathways [for some examples see: 26b, 26c, 26d, 26g, 26h, 26i, 31e, 32, 92]. In fact, this technique allows to detect characteristic absorption bands and their modifications due to degradation.

Analyses were performed with a Perkin Elmer Spectrum One FT-IR spectrometer. Spectra were acquired with the software Spectrum (Perkin Elmer) in the spectral range between 4000 and 400 cm^{-1} performing 64 scans at 4 cm^{-1} resolution. The resulting spectra were processed by Origin 8.0 software. Analyses were performed on films cast from one drop of polymer or of NPs solution directly on a KBr disks. Before being subjected to aging, the disks were held in a desiccator for one month (dark conditions) to allow the complete polymerization and formation of solid films.

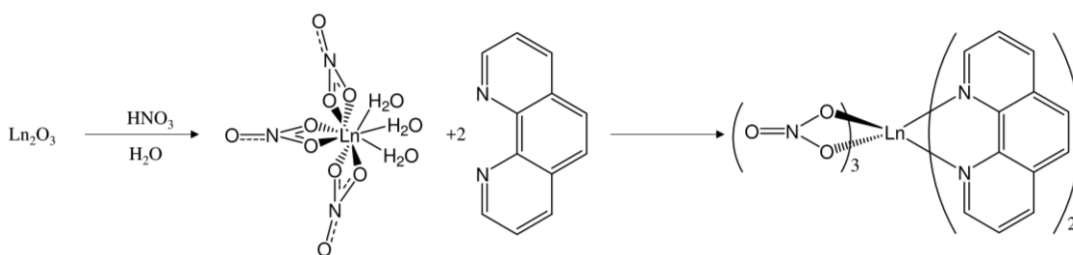
7.10 Synthesis of $\text{Ln}(\text{NO}_3)_3(\text{phen})_2$ (Ln= Eu; Tb) complexes and preparation of luminescent films

$\text{Eu}(\text{NO}_3)_3(\text{phen})_2$ was synthesized from a dispersion of 0.2 g of Eu_2O_3 in 2 mL of H_2O to which were added 6 equivalents of HNO_3 (65% in water). The reaction mixture was heated at 80°C until the solution became clear. 30 mL of absolute ethanol were then added, and the solution was concentrated by heating

to ca. 3 mL. This step was repeated two times. Under stirring were added once again 30 mL of absolute ethanol and the solution was allowed to cool. The phenanthroline ligand (4 equivalents with respect to Eu_3O_3) was solubilized in 6 mL of absolute ethanol and then added drop by drop to the stirred solution of $\text{Eu}(\text{NO}_3)_3(\text{H}_2\text{O})_3$ obtaining the pale-yellow $\text{Eu}(\text{NO}_3)_3(\text{phen})_2$ complex, which was collected by filtration.

To prepare the analogous Tb(III) derivative, in a closed reflux system 0.2 g of Tb_4O_7 were allowed to react with 20 mL of concentrated aqueous HCl and 20 mL of CH_3COOH for 2 hours. The solution was then filtered and taken to dryness. The solid was treated with 5 mL of distilled water and the resulting solution was filtered. An excess of NaOH (0.130 g) was then added to precipitate Tb(III) hydroxide, which was then filtered, washed with water and dried. The remaining part of the synthesis is identical to that affording the previously described Eu(III) derivative.

The scheme of reaction and the chemical structure of the lanthanide $\text{Ln}(\text{NO}_3)_3(\text{phen})_2$ ($\text{Ln}=\text{Eu}$; Tb) complexes obtained is shown in Scheme 10.



Scheme 10.

The X-ray structural analyses indicate that $\text{Ln}(\text{NO}_3)_3(\text{phen})_2$ complexes crystallize in the monoclinic space group $C2/c$ (no. 15) [93]. Zeng Y.Q. *et al.* [93c] reported values of cell dimension, for $\text{Ln}=\text{Eu}$, of $a=11.165 \text{ \AA}$, $b=17.972 \text{ \AA}$, $c=13.052 \text{ \AA}$, $\beta=100.57^\circ$, $V=2574.5 \text{ \AA}^3$, $Z=4$. On the other hand, Mirochnik A.G. *et al.* [93d] reported, for the same complex, cell values of $a=11.168 \text{ \AA}$, $b=17.976 \text{ \AA}$, $c=13.053 \text{ \AA}$, $\beta=100.57^\circ$, $Z=4$. In the mononuclear complex, the rare earth atoms are coordinated by four N atoms of two phenanthroline ligands and six O atoms of three nitrate groups to complete a 10-fold coordinated polyhedron. The Eu-O bond distances vary in the range $2.495\text{-}2.540 \text{ \AA}$ and are slightly shorter than the Eu-N bond distances, which range between 2.541 and 2.593 \AA [93c, 93d].

A weighted and variable quantity (from 0 to 10%) of the pure $\text{Ln}(\text{NO}_3)_3(\text{phen})_2$ ($\text{Ln}=\text{Eu}$; Tb) complexes have been added to the polymers/NPs solutions prepared as described in Table 4 and the dispersions were kept under stirring until obtaining homogeneous systems suitable for the depositions. Samples have been spread by brushing on glass slides and let to dry in laboratory conditions.

7.11 Photoluminescence measurements

Photoluminescence emission (PL), excitation (PLE) and luminescence lifetimes measurements on solid-state samples have been performed during the doctoral internship period at the Department of

Engineering Sciences and Mathematics (Luleå University of Technology) in Luleå, Sweden, under the supervision of Univ. Prof. Dr. Alberto Vomiero.

Photoluminescence excitation (PLE) and emission (PL) spectra were recorded by an Edinburgh Instruments FLS980 Photoluminescence Spectrometer. A continuous-wave xenon lamp or a microsecond xenon flash lamp were used as excitation sources for steady-state or time-resolved measurements respectively, coupled to a double-grating monochromator for wavelength selection. The light emitted from the samples was also collected by a double-grating monochromator and recorded by a photon counting R928P photomultiplier tube.

The intrinsic quantum yield (Q_i) allows to evaluate the influence of the non-radiative decay processes between the radiative ones and can be calculated from the Eq. (13)

$$Eq. (13) \quad Q_i = \frac{k_r}{k_r + k_{nr}}$$

where k_r and k_{nr} are, respectively, the rate constant of the radiative and non-radiative decays. The reciprocal of the rate constant is a lifetime. τ_{rad} is the radiative lifetime while the reciprocal of the sum of the rates constant is the observed lifetime, τ_{obs} . The intrinsic quantum yield of the Ln ion has been estimated on the basis of Eq. (14), where τ is the measured luminescence lifetime.

$$Eq. (14) \quad Q_i = \frac{\tau_{obs}}{\tau_{rad}}$$

τ_{rad} has been obtained for the europium-based samples from Eq. (15)

$$Eq. (15) \quad \frac{1}{\tau_{rad}} = 14.65n^3 \frac{I(^5D_0 \rightarrow ^7F_1)}{I(^5D_0 \rightarrow ^7F_1)}$$

where n indicates the refractive index of the sample (value of 1.5 is assumed in this work for comparative purposes) and $I(^5D_0 \rightarrow ^7F_1)/I(^5D_0 \rightarrow ^7F_1)$ is the ratio between the total integrated emission from the $Eu(^5D_0)$ level to the 7F_1 manifold ($J=0-6$) and the integrated intensity of the transition $^5D_0 \rightarrow ^7F_1$ [94].

On the other hand, the intrinsic quantum yield (Q_i) for the terbium-based samples was calculated, as suggested by Kaback R.H. *et al.* [95], on the basis of the Eq. (16), where τ_{obs} is expressed in ms.

$$Eq. (16) \quad Q_i = \frac{\tau_{obs}}{4.75}$$

The chromaticity coordinates x and y were estimated from the PL spectra of the pure and dispersed $Ln(NO_3)_3(phen)_2$ ($Ln=Eu; Tb$) complexes as indicated by the International Commission for Illumination (Commission Internationale de l'Eclairage, CIE) which has standardized the measurements of colour by means of colour-matching functions and by the chromaticity diagram (CIE, 1931) [96]. The CIE 1931 colour-matching functions individuate three functions $x(\lambda)$, $y(\lambda)$, and $z(\lambda)$ which reflect the fact that human colours vision is trichromatic. For a given spectral density $P(\lambda)$, the degree of stimulation required to match the colour of $P(\lambda)$ is given by the tristimulus values X (red), Y (green), and Z (blue) as

reported in Eq. (17-19).

$$\text{Eq. (17)} \quad X = \int_{\lambda} x(\lambda) P(\lambda) d\lambda$$

$$\text{Eq. (18)} \quad Y = \int_{\lambda} y(\lambda) P(\lambda) d\lambda$$

$$\text{Eq. (19)} \quad Z = \int_{\lambda} z(\lambda) P(\lambda) d\lambda$$

The chromaticity coordinates x and y are calculated as the stimulation of each primary light divided by the entire stimulation ($X + Y + Z$) from the tristimulus values according to Eq. (20) and Eq. (21).

$$\text{Eq. (20)} \quad x = \frac{X}{X+Y+Z}$$

$$\text{Eq. (21)} \quad y = \frac{Y}{X+Y+Z}$$

z chromaticity value can be obtained from x and y values, then no useful chromaticity information is provided from this coordinate.

The (x, y) chromaticity diagram shows a detailed attribution of colours: reddish and greenish colours are found for respectively large values of x and y , while bluish colours are found for low values of x and y , or near the origin of the chromaticity diagram. Moreover, all colours can be characterized in function of their position in the chromaticity diagram: monochromatic or pure colours are located on the perimeter, while white is at the centre of the diagram. Thus, the colour purity is the relative distance of the sample under test from the centre of the chromaticity diagram.

8. Results and Discussion

8.1 Colorimetric measurements

The degree of colour can give useful information in following the changes in the properties of materials. Therefore, colour parameters in aged samples was monitored at increasing time intervals, monthly for natural aging and every 100 hours for the thermal and photo-oxidative aging. The results obtained are reported as plots of total variation of colour (ΔE parameter calculated as in *Eq. (3)*) over the time of thermo- (T=80, 100, 120 and 140°C up to 15000 hours) and photo-oxidative (UVC $\lambda=366$ nm and UVA $\lambda=254$ nm up to 2000 hours) as well as natural aging (up to 670 days). However, ΔE shows only the total colour change magnitude but does not specify in what way colour varies. Therefore, colour parameters L^* , a^* and b^* of fresh and aged samples are reported as average of three independent measurements, together with the colour graph (plot of a^* vs b^*) and the histogram of L^* values.

The results of colorimetric analyses obtained for increasing times of thermo- and photo-oxidative aging as well as during natural aging of *Acril 33 (P(EA-MMA))* are shown in Figure 2.

As shown in Figure 2a, only the thermo-oxidative aging of *Acril 33* at 120 and 140°C induces a variation of colour higher than 5, thus detectable by naked eye. In particular, at the end of the thermo-oxidative aging at 120 and 140°C of *Acril 33*, ΔE values of 11.53 and 42.24 were determined respectively for the two temperatures. As shown in Figure 2e, the colour variation is due to a shift towards orange shade due to a contemporary increment of the parameter a^* (green-red opponent coordinate), which implies a shift towards reddish shade, and of b^* (blue-yellow opponent coordinate) value, which determines a shift towards yellowish shade. Moreover, it is important to note that the high standard deviation associated to the a^* and b^* values highlights wide inhomogeneity of the colour of the acrylic film aged at 140°C. Instead, as shown in Figure 2f, the L^* parameter (brightness) slightly influences the total variation of colour.

On the other hand, the thermo-oxidative degradation at 80 and 100°C, the photo-oxidative aging conditions, as well as the natural aging, do not affect significantly the colorimetric parameters (Figures 2a, 2b, 2c and 2d) of the polymeric films of *Acril 33*. At the end of the experiments the ΔE values determined are 0.67 and 3.12 for the samples subjected to thermal degradation at 80 and 100°C, 0.47 and 1.54 for the samples subjected to UVC and UVA radiations and 1.16 for the sample aged under natural conditions.

The high resistance in terms of colour variation of the polymeric films of *Acril 33* with respect to the UV aging herein reported, is in contrast with the high instability reported in literature for the acrylic resin *Paraloid B72 (P(EA-MMA))*. In the specific, Melo M.J. *et al.* [26b] accordingly with Bracci S. and Melo M.J. [26h], reported fast yellowing since the first hours of UV or accelerated (climatic chamber) aging of the acrylic resin. Therefore, is herein revealed as the films obtained from the solubilization of

P(EA-MMA) resin in solvent show a higher instability with respect to the films deriving from the water-based emulsion.

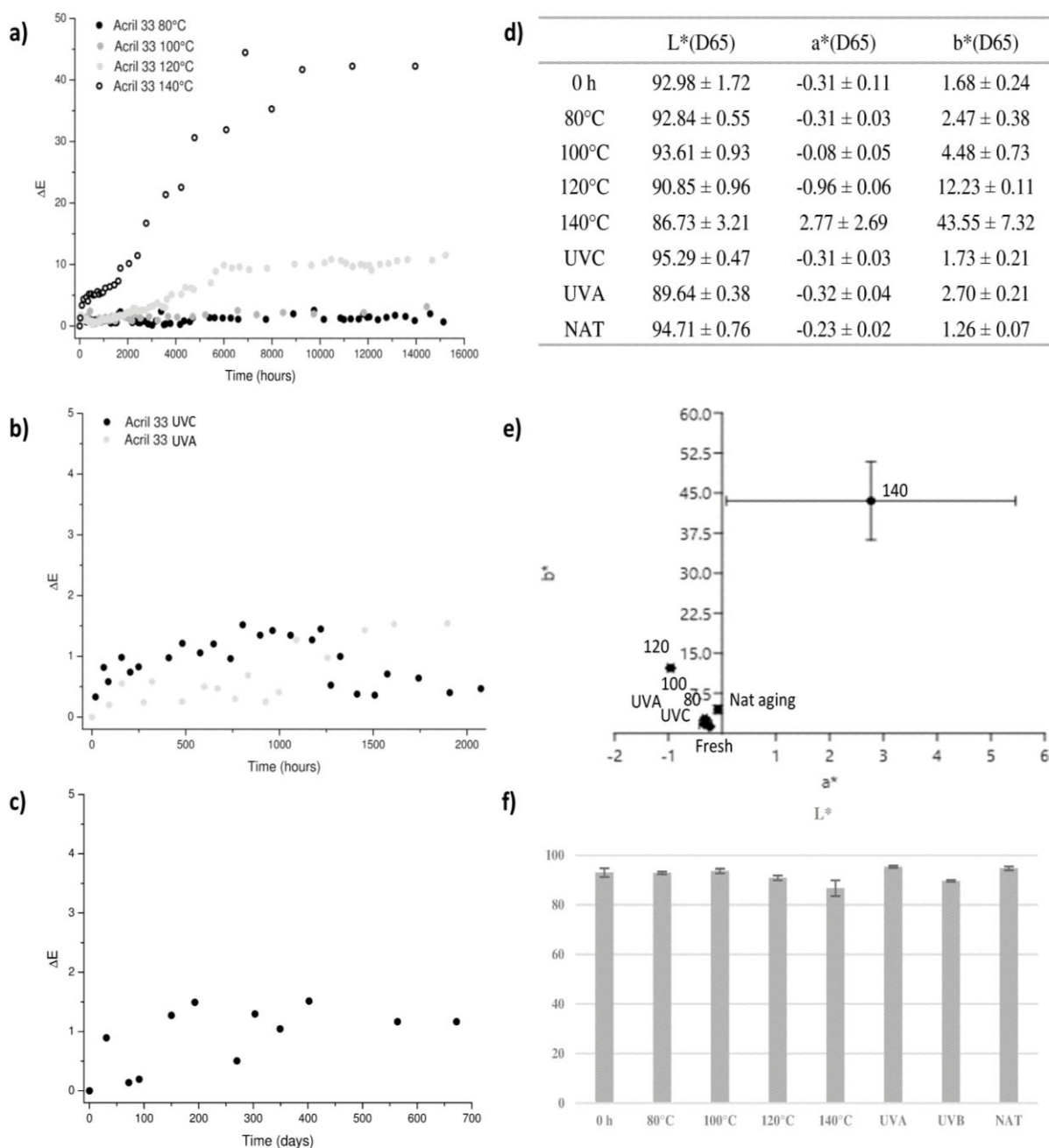


Figure 2. ΔE parameters determined for *Acril 33* subjected to (a) thermal aging at 80, 100, 120 and 140°C, (b) photo-oxidative aging (UVC and UVA) and (c) natural aging; (d) colour parameters L^* , a^* and b^* of fresh and aged *Acril 33* films; (e) plot of a^* vs b^* values (colour graph) of unaged and aged samples; (f) plot of L^* values of fresh and aged samples.

As for *Acril 33*, only the thermo-oxidative aging at 120 and 140°C induces significant variations in the colour of *Acril ME (PBMA)* films (Figure 3a). More specifically, the two aging temperatures induced total variation of colour of, respectively, 4.60 and 10.23. The colour changes are caused by a shift towards yellow-green shades (Figure 3e), while the L^* parameter remains substantially unchanged during thermal aging (Figure 3f). Also in this case, the high standard deviation associated to a^* and b^* parameters of the sample aged at 140°C can be attributed to inhomogeneity of the colour of the

polymeric film.

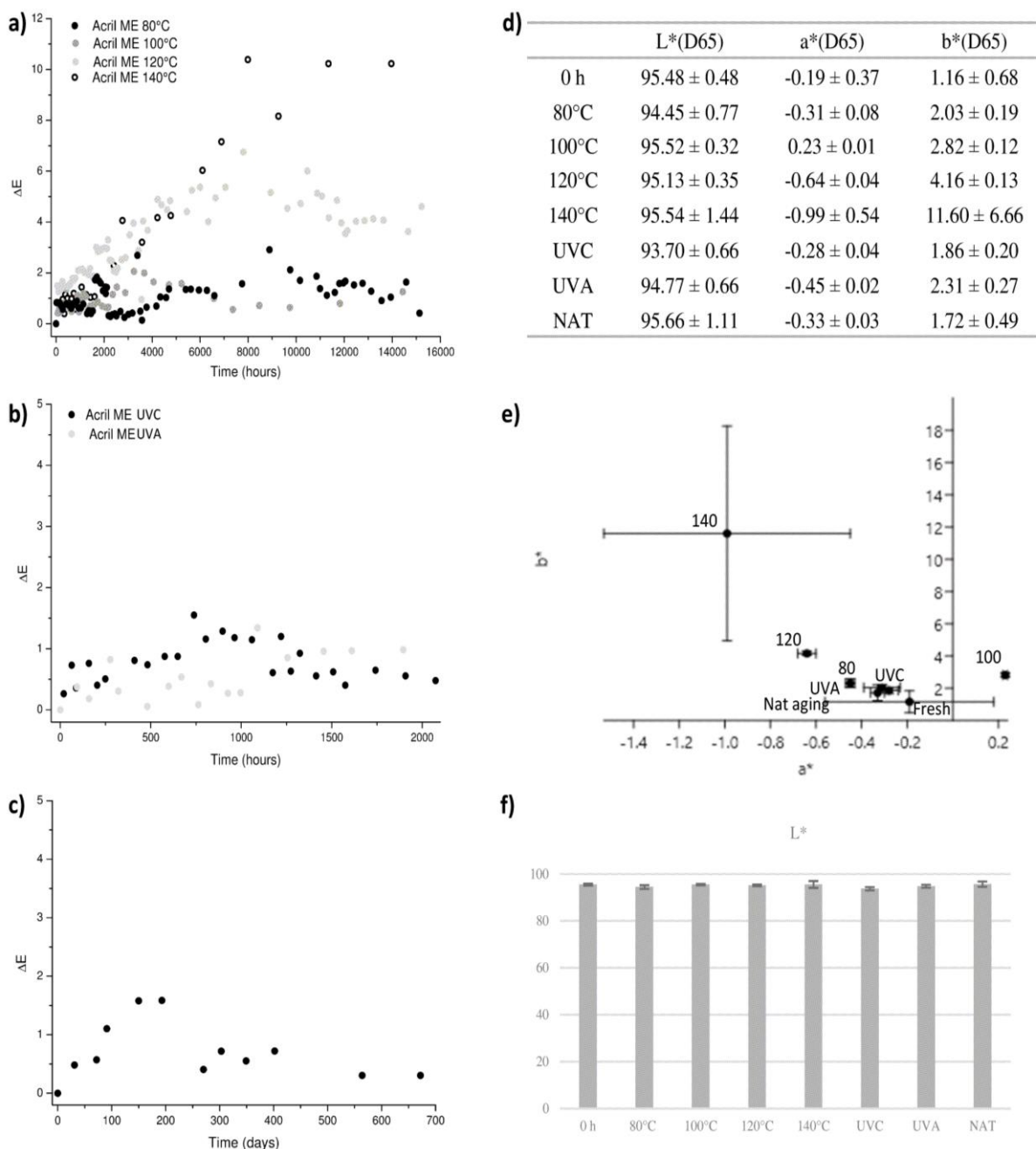
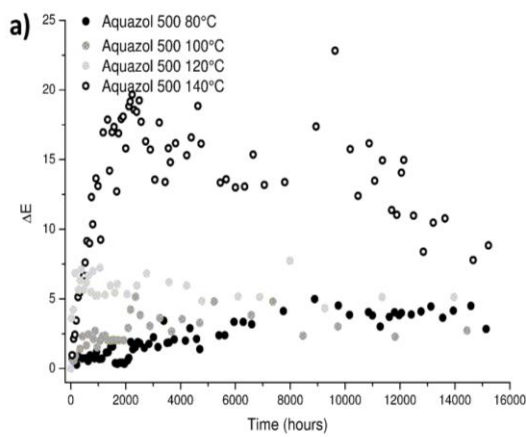


Figure 3. ΔE parameters determined for *Acril ME* subjected to (a) thermal aging at 80, 100, 120 and 140°C, (b) photo-oxidative aging (UVC and UVA) and (c) natural aging; (d) colour parameters L^* , a^* and b^* of fresh and aged *Acril ME* films; (e) plot of a^* vs b^* values (colour graph) of unaged and aged samples; (f) plot of L^* values of fresh and aged samples.

Also for *Acril ME*, the thermo- and photo-oxidative aging as well as the natural aging did not induce significant variations in the colour parameters. In fact, ΔE values determined at the end of the tests are 0.42, 1.26, 0.48, 0.98 and 0.30 respectively for the aging at 80°C, 100°C, UVC, UVA and natural aging. Anyway, higher stability in terms of colour changes was herein demonstrated for *Acril ME* with respect to *Acril 33*, in good agreement with the results reported in literature [31e]. It is important to note that the transition between solvent-based to microemulsion not only improves the human and environmental

safety, but also increases the stability of the *PBMA*. In fact, differently from the low values of ΔE reported in this work and by Camaiti M. *et al.* [31e], Favaro M. *et al.* [26i] determined colour variation close to 10 for Paraloid B67 sample exposed to 2000 hours of UV radiation.

Aquazol 500 appears more susceptible to thermal aging with variations of colour slightly detectable at naked eyes also for the samples aged at low temperatures (Figure 4a). More specifically, at the end of the thermo-oxidative aging at 80, 100, 120 and 140°C were determined ΔE values of, respectively, 2.72, 4.49, 5.12 and 8.84. These changes in colour are due to a slight shift to yellow-greenish shades (Figures 4d) but also to a darkening of the surfaces detectable as decrease of L^* values (Figure 4f).



	$L^*(D65)$	$a^*(D65)$	$b^*(D65)$
0 h	96.84 ± 0.77	-0.35 ± 0.04	1.48 ± 0.30
80°C	93.32 ± 0.59	-0.31 ± 0.03	2.87 ± 0.24
100°C	95.19 ± 0.79	-0.44 ± 0.12	6.68 ± 1.67
120°C	92.06 ± 1.01	-0.17 ± 0.08	10.47 ± 1.80
140°C	95.66 ± 0.52	-1.26 ± 0.07	4.49 ± 0.25
UVC	96.08 ± 0.60	-0.29 ± 0.02	1.98 ± 0.12
UVA	96.02 ± 0.35	-0.38 ± 0.02	2.42 ± 0.13
NAT	97.18 ± 0.53	-0.23 ± 0.04	1.2 ± 0.26

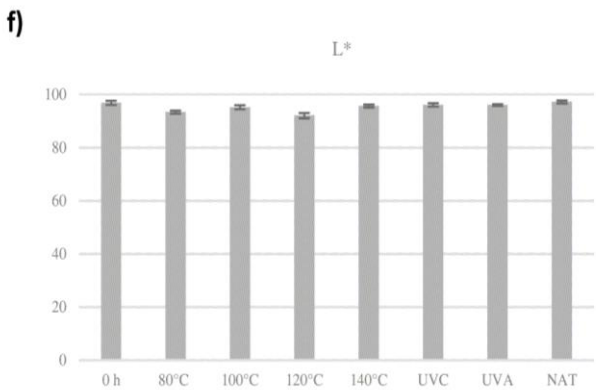
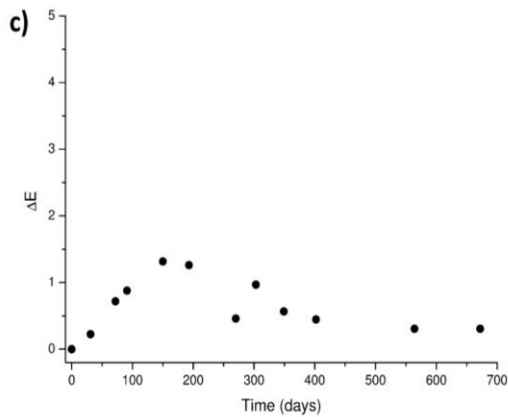
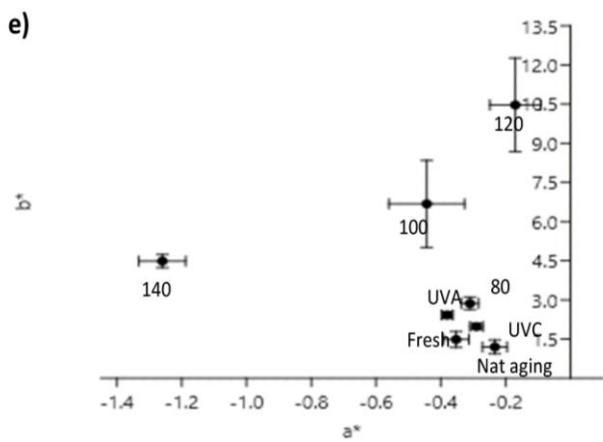
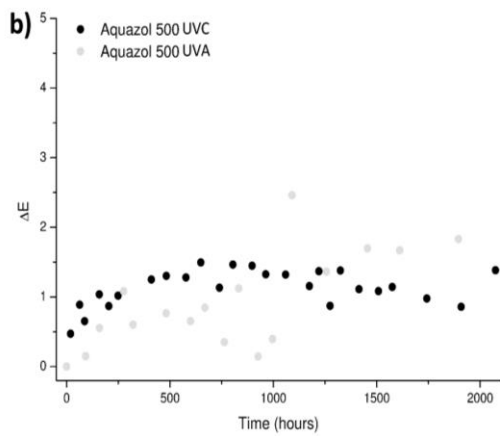


Figure 4. ΔE parameters determined for *Aquazol 500* subjected to (a) thermal aging at 80, 100, 120 and 140°C, (b) photo-oxidative aging (UVC and UVA) and (c) natural aging; (d) colour parameters L^* , a^* and b^* of fresh and aged *Aquazol 500* films; (e) plot of a^* vs b^* values (colour graph) of unaged and aged samples; (f) plot of L^* values of fresh and aged samples.

As the acrylic samples, *Aquazol 500* exhibits high stability in terms of colour changes on considering the UVC, UVA and natural aging, with total colour variation of, respectively 1.38, 1.83 and 0.31 at the end of the experiments. Even if the ΔE values of the samples aged at 80, 100 and 120°C are higher with respect to those determined for *Acril ME*, *Aquazol* guarantees better performance (lower ΔE) for the aging at high temperature. These results are in contrast with those reported by Camaiti M. *et al.* [31e], which determined high values of ΔE (30-40) also after short time of exposure of *Aquazol* to UV radiation. Nevertheless, also Wolbers R.C. *et al.* [37] reported that no significant variation in terms of discolouration occurs during UV aging of *Aquazol 500* with a xenon lamp.

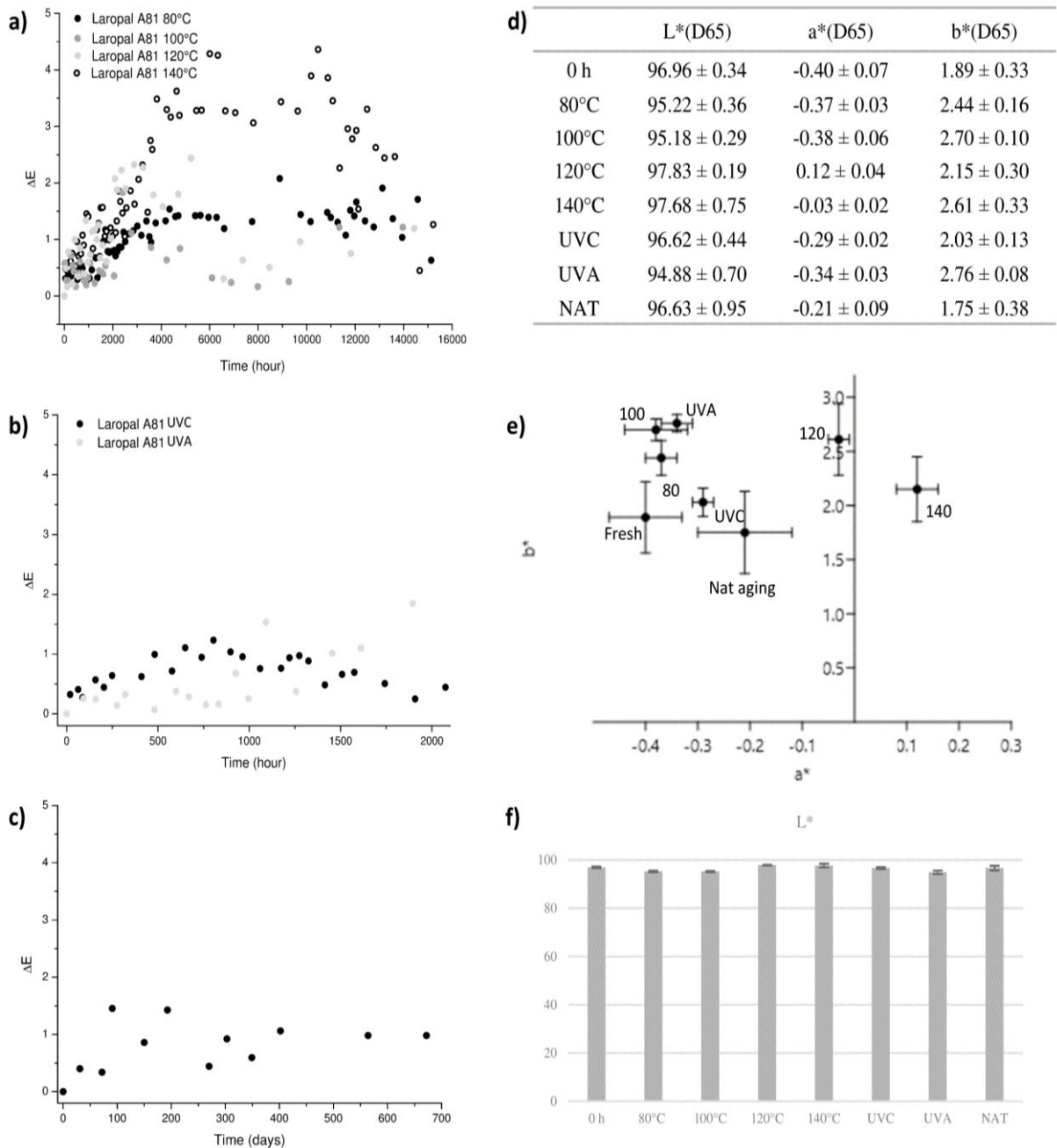


Figure 5. ΔE parameters determined for *Laropal A81* subjected to (a) thermal aging at 80, 100, 120 and 140°C, (b) photo-oxidative aging (UVC and UVA) and (c) natural aging; (d) colour parameters L^* , a^* and b^* of fresh and aged *Laropal A81* films; (e) plot of a^* vs b^* values (colour graph) of unaged and aged samples; (f) plot of L^* values of fresh and aged samples.

Laropal A81 revealed high resistance not only towards the photo-oxidative conditions, but also towards thermal aging, with ΔE values always lower than 5 (Figures 5a, 5b and 5c). Values of a^* , b^* and L^* parameters remain practically unchanged during the different aging tests (Figures 5d and 5f) and finally ΔE values are 0.63, 1.19, 1.26 and 1.21 for the samples subjected to the thermal degradation at 80, 100, 120 and 140°C, 0.44 and 1.44 for the samples subjected to UVC and UVA aging and 0.98 for the sample aged under natural conditions. Anyway, the low changes of colour imply a shift towards yellow-orange shades (Figures 5e) while, as shown in Figure 5f, the L^* values remain practically unchanged along the aging. These data allowed to individuate in *Laropal A81* the polymer with the higher stability in terms of colour retention under the aging conditions investigated.

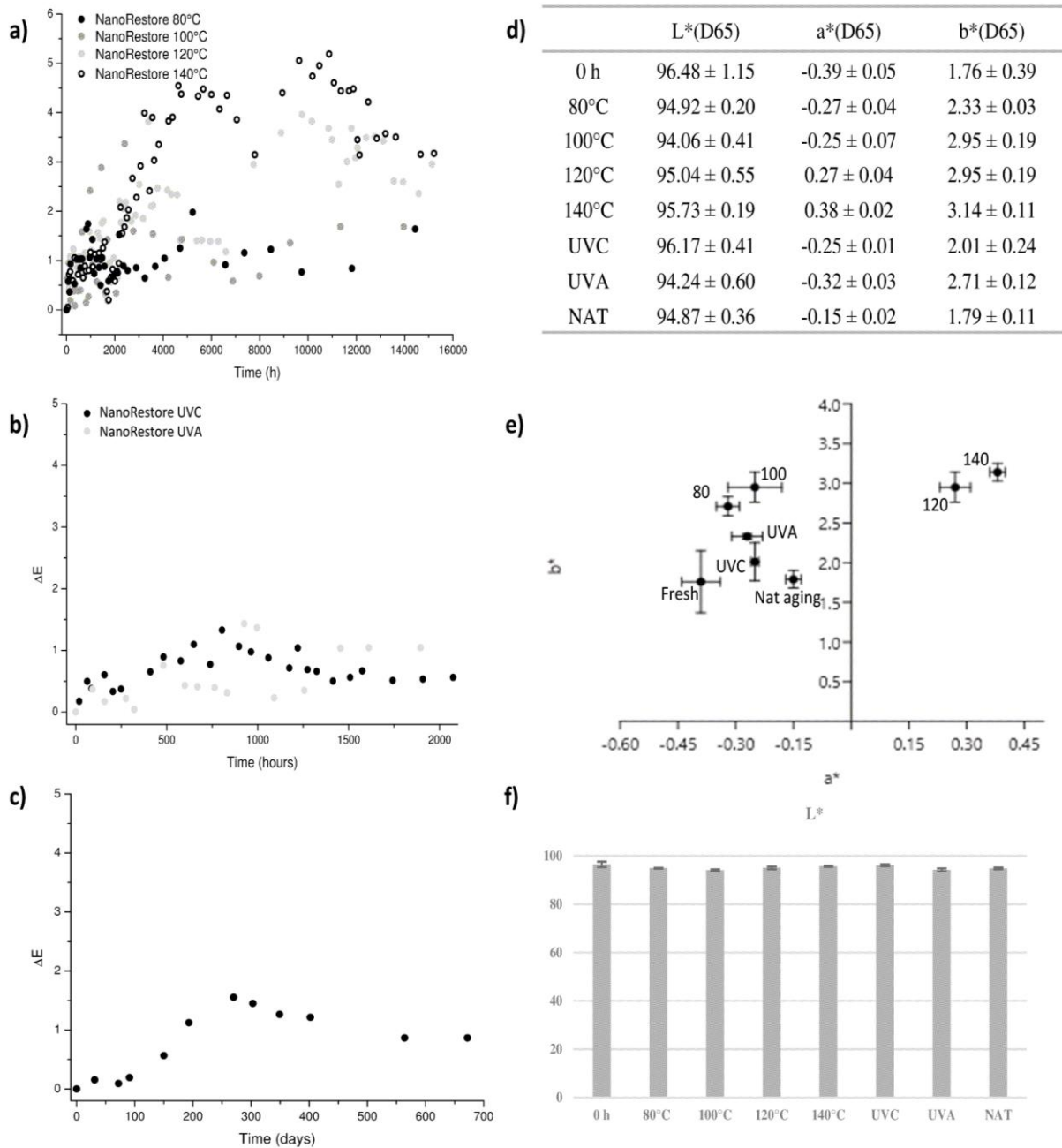
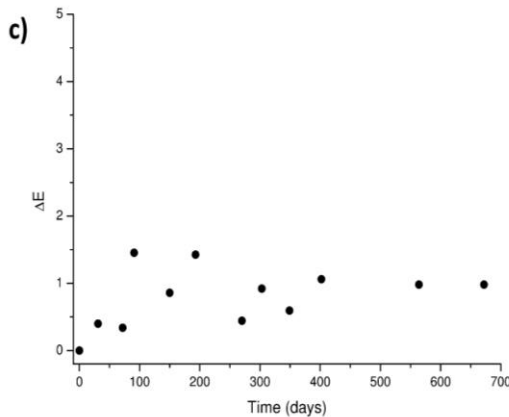
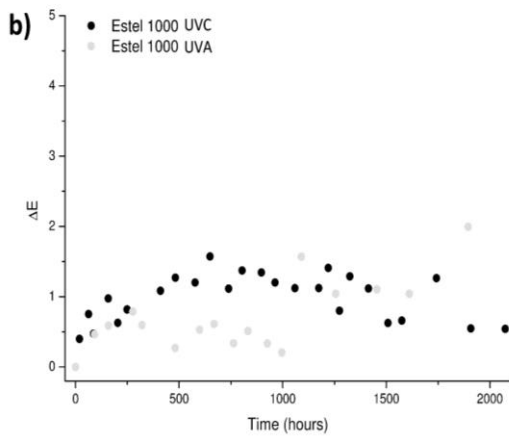
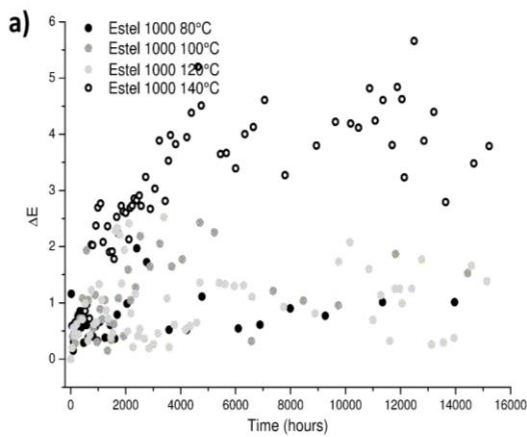


Figure 6. ΔE parameters determined for *NanoRestore* subjected to (a) thermal aging at 80, 100, 120 and 140°C, (b) photo-oxidative aging (UVC and UVA) and (c) natural aging; (d) colour parameters L^* , a^* and b^* of fresh and aged *NanoRestore* films; (e) plot of a^* vs b^* values (colour graph) of unaged and aged samples; (f) plot of L^* values of fresh and aged samples.

NanoRestore films, obtained from the colloidal dispersion of $\text{Ca}(\text{OH})_2$ NPs, showed a good resistance in terms of colour changes on considering all the aging tests conducted (Figures 6a, 6b and 6c). ΔE values determined are 1.55, 1.63, 2.98 and 3.17 for the samples subjected to thermal degradation at 80, 100, 120 and 140°C, 0.56 and 1.04 for the samples subjected to UVC and UVA aging conditions and 0.86 for the sample aged under natural conditions. The slightly colour changes are due to a shift towards yellow-orange shades (Figure 6e) and to darkening of the surface (low displacement of L^* values visible in Figure 6f). This colour changes, mainly observed for the samples aged at 120 and 140°C, are detectable since the first 4000 hours of aging time, after which the colour parameters vary only slightly.



	$L^*(D65)$	$a^*(D65)$	$b^*(D65)$
0 h	95.86 ± 0.78	-0.43 ± 0.04	1.90 ± 0.37
80°C	93.32 ± 1.72	-0.28 ± 0.04	2.88 ± 0.68
100°C	93.71 ± 0.49	-0.18 ± 0.05	3.06 ± 0.05
120°C	95.85 ± 0.83	0.31 ± 0.04	2.66 ± 0.32
140°C	95.91 ± 0.23	0.26 ± 0.03	3.08 ± 0.11
UVC	95.74 ± 0.82	-0.37 ± 0.02	2.11 ± 0.08
UVA	96.27 ± 0.51	-0.43 ± 0.01	2.45 ± 0.21
NAT	97.18 ± 0.33	-0.30 ± 0.00	1.61 ± 0.04

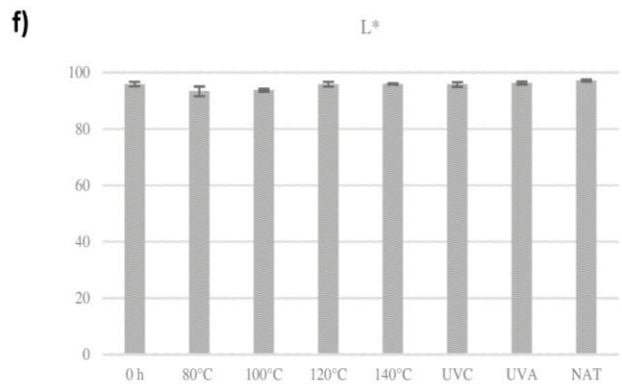
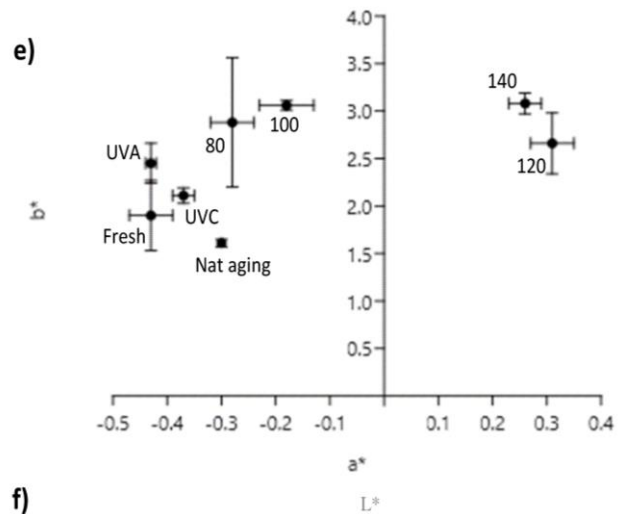


Figure 7. ΔE parameters determined for *Estel 1000* subjected to (a) thermal aging at 80, 100, 120 and 140°C, (b) photo-oxidative aging (UVC and UVA) and (c) natural aging; (d) colour parameters L^* , a^* and b^* of fresh and aged *Estel 1000* films; (e) plot of a^* vs b^* values (colour graph) of unaged and aged samples; (f) plot of L^* values of fresh and aged samples.

The high stability to colour changes observed in this study for *NanoRestore* is opposite to the data reported by Pondelak A. *et al.* [97], which determined ΔE value higher than 6 since the first month and higher than 11 after three months of natural aging of *NanoRestore* applied as wall painting consolidant. In its study, Pondelak A. attributed the colour changes recorded mainly to strong increase of lightness due to the formation of white haze on the surface of the material treated with *NanoRestore*. However, the results here reported leads to attribute these colour changes to a drawback of the specific environment of application rather than to a aging behaviour of the nanoparticulated product.

The inorganic *Estel 1000* consolidant based on *TEOS* showed a good resistance (Figures 7a, 7b and 7c), in terms of colour changes, towards all the aging tests conducted.

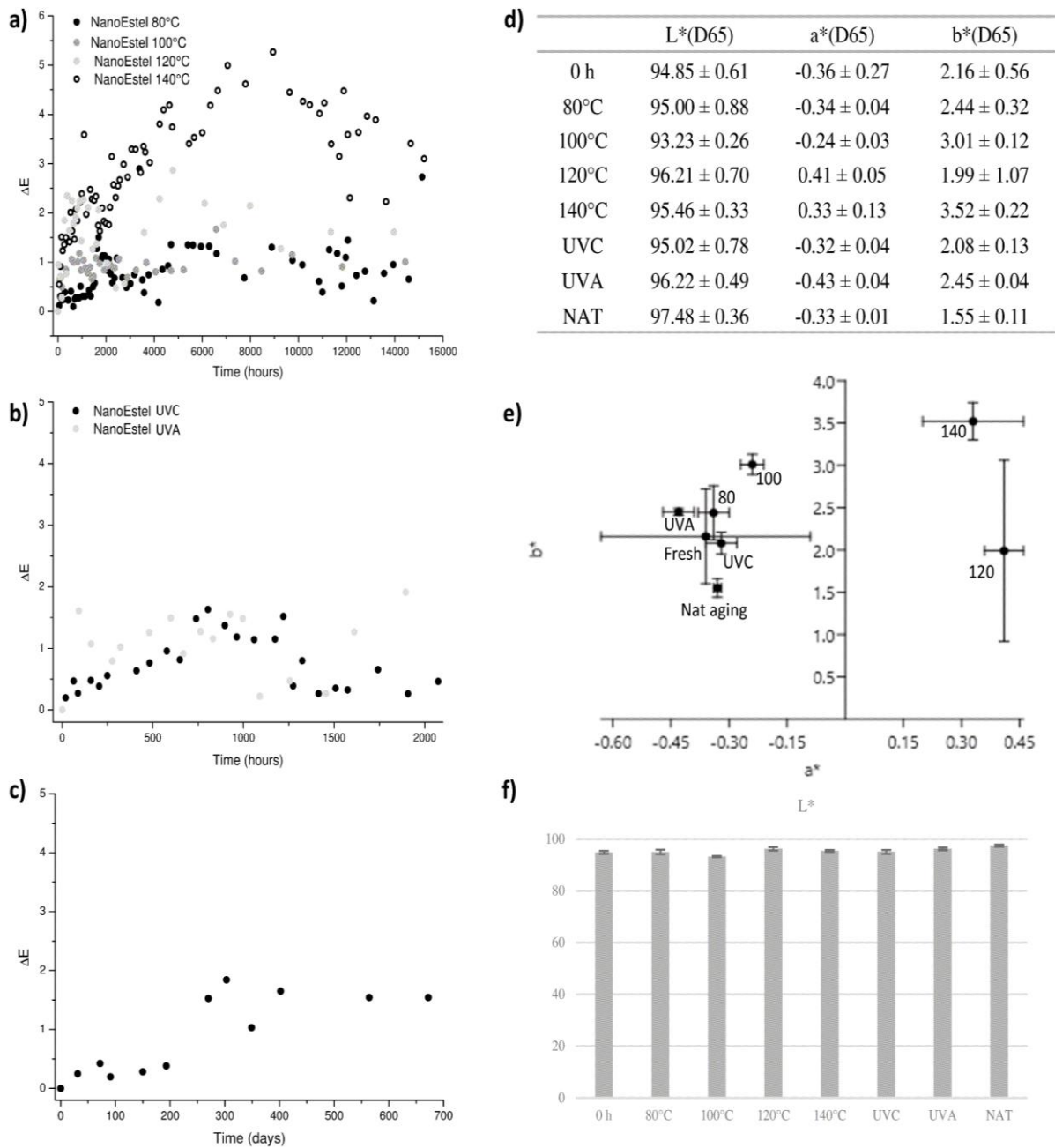


Figure 8. ΔE parameters determined for *NanoEstel* subjected to (a) thermal aging at 80, 100, 120 and 140°C, (b) photo-oxidative aging (UVC and UVA) and (c) natural aging; (d) colour parameters L^* , a^* and b^* of fresh and aged *NanoEstel* films; (e) plot of a^* vs b^* values (colour graph) of unaged and aged samples; (f) plot of L^* values of fresh and aged samples.

ΔE values of 1.01, 1.39, 1.52 and 1.78 have been determined for the samples subjected to thermal aging at 80, 100, 120 and 140°C, of 0.54 and 1.99 for the samples subjected to UVC and UVA photo-aging and of 0.74 for the sample aged under natural conditions. Colour changes are due to a slight shift towards yellow-orange shades (Figure 7e), but in films subjected to thermal aging a decrease of the L^* values was recorded, differently from the increment observed for the photo-aged samples (shift towards more clear tone, Figure 7f). The decrease of lightness can be attributed to the cracking of the brittle silica gel during the thermal aging [98], while the higher values determined for the L^* parameter after photo-aging can be explained on assuming forward cross-linking of the silica-based consolidant.

The total chromatic variations determined for *NanoEstel* are 1.05, 1.61, 2.10 and 2.73 for the samples subjected to thermal aging at 80, 100, 120 and 140°C (Figure 8a), 0.46 and 1.91 for the samples aged with UVC and UVA radiation (Figure 8b) and 1.54 for the sample aged under natural conditions (Figure 8c). *NanoEstel* exhibited colour changes strictly comparable (Figure 8e, shift towards yellow-orange shades) with those recorded for *Estel 1000*. However, for both the thermal- and photo-aging, as well as for the natural aging, no significant changes in the L^* parameter were revealed (Figure 8f). This can be explained taking into account that, as reported from Kim E.K. *et al.* [62d], films containing SiO_2 NPs do not crack during drying or aging, thus avoid variations of lightness of the treated surfaces.

8.2 Gloss measurements

Gloss is defined as the capability of a surface to reflect incident light, thus it is strictly related to the roughness of the surface and it is commonly used to assess the brilliance parameter of stone [99] and thermosetting films [100]. To the best of knowledge, only de la Rie E.R. *et al.* [44] have used gloss measurements to relate the roughness of the surface with the molecular weight and the refractive index of polymers used in conservation practice. They revealed that for an ideal specular surface the gloss is 100% and deviation from this value can be attributed to the refractive index and the molecular weight of the material as well as to light-scattering from the air-coating interface. In particular, they reported that the low molecular weight resins *Regalrez 1094*, *Laropal A81* and *AYAT* produced smoother coatings and higher gloss with respect to the high molecular weight resins *Paraloid B72* and *Paraloid B67*.

First of all, the gloss data collected for the fresh polymer samples surfaces allowed to confirm the observation of de la Rie E.R. *et al.*, since higher gloss values (137.1 GU) was determined for the polymer film based on the low molecular weight resin *Laropal A81*, with respect to the values obtained for the two acrylic-based polymers *Acril 33* and *Acril ME* (74.5 and 84.1 GU, respectively). On the other hand, high gloss value (131.7 GU) was measured also for the *Aquazol 500* sample. However, the high value recorded cannot be attributed to a different refractive index of the polymer *PEOX*, its value (1.520 [36]) being comparable with that of *Laropal A81* (1.5 [44a]) and with that of acrylic polymer films (1.48 [7]). The gloss of the films under investigation was assessed by measuring at the beginning and at the end of each aging test the specular reflection using 60° incident and reflected light [85]. Data reported are the average of three independent measures. The Δ_{gloss} parameter was determined as reported in Eq. (4) because of the degree of gloss can give useful information since it can describe the variation of a surface from glossy to opaque (Δ_{gloss} positive values) or vice versa (Δ_{gloss} negative values).

Table 8. Gloss variation (Δ_{gloss} %) determined for *Acril 33*, *Acril ME*, *Aquazol 500*, *Laropal A81*, *NanoRestore*, *Estel 1000* and *NanoEstel* at the end of thermal (T=80, 100, 120 and 140°C), photo-oxidative UVC ($\lambda=366$ nm) and UVA ($\lambda=254$ nm) and natural aging.

Sample	Thermo-oxidative aging				Photo-oxidative aging		Natural aging
	80°C	100°C	120°C	140°C	UVC ($\lambda=366$ nm)	UVA ($\lambda=254$ nm)	
<i>Acril 33</i>	18.5	36.5	69.5	99.5	-4.8	-7.3	-0.8
<i>Acril ME</i>	2.7	4.6	18.1	29.6	-1.5	-3.7	5.7
<i>Aquazol 500</i>	53.2	54.1	60.2	67.3	10.2	11.1	23.2
<i>Laropal A81</i>	15.5	22.6	24.8	28.4	1,1	1,8	15,8
<i>NanoRestore</i>	23.2	32.7	34.7	35.9	-5.2	-7.2	5.3
<i>Estel 1000</i>	-12.0	-17.9	-29.6	-49.1	-0.9	-6.6	-12.1
<i>NanoEstel</i>	9.0	13.1	14.2	29.6	-1.0	-2.8	7.0

Data in Table 8 revealed higher resistance of all the materials tested to the photo-oxidative aging conditions with respect to the thermal ones. The high resistance in terms of gloss retention is confirmed by Δ_{gloss} values lower than 12, which indicate negligible variation of gloss, thus of the roughness, of the surfaces.

High stability was shown also by all the materials tested during the two years of natural aging. The only significant gloss variation was recorded for the sample of *Aquazol 500*, for which Δ_{gloss} value of 23.2 was determined. Therefore, it is possible to identify in *Aquazol 500* the polymer with the lowest resistance in terms of gloss retention to the natural aging conditions.

As observable from the data reported in Table 8, for both the acrylic-based products a decrease of the gloss values during the thermal-aging tests was recorded. However, if these changes are acceptable for the *Acril ME* samples (Δ_{gloss} lower than 50), great variation of the brilliance (with surfaces varying from glossy to matt) was recorded for *Acril 33* after thermo-oxidative aging at 120 and 140°C. As reported above, both acrylic samples show great resistance, in terms of gloss retention, to the photo-oxidative UVC and UVA aging. However, it is important to note that, while the thermo-oxidation of the films implies a decrease of gloss values, the photo-oxidative aging leads to slightly increase of the brilliance of the polymer films. Anyway, also in terms of gloss retention, the acrylic product which exhibited the best performance with respect to the aging conditions studied is *Acril ME*.

Exactly as revealed from the colorimetric analyses, *Aquazol 500* showed low resistance with respect to the other polymers studied to thermal- and photo-oxidative aging as well as to natural aging. Δ_{gloss} values determined point out the clear shift from glossy to matt surface ($\Delta_{\text{gloss}} > 50$) and, with the exceptions of the sample of *Aquazol 500* aged at 120 and 140°C, are higher with respect to the other samples investigated under the same conditions.

The slight variations of gloss values (Δ_{gloss} lower than 30) determined for *Laropal A81* samples revealed high stability of this polymer to the aging conditions imposed, strictly comparable with *Acril ME*. However, for *Acril ME* significant variations were measured in the colour parameters, while *Laropal A81* guarantees high performance in terms of both colour and gloss retention.

NanoRestore samples subjected to thermal aging revealed a decrease of the gloss values (Δ_{gloss} positive), associated to opacification of the surface.

On the other hand, the aging of *Estel 1000* samples has involved an increase of the gloss values, probably due to an increase of the degree of the polymerization of the applied silica-based product.

Best performance in terms of gloss retention was however revealed by the nano-sized silica-based *NanoEstel*. On considering also the performances in terms of colour retention, *NanoEstel* appears the best inorganic product here considered in terms of retention of colorimetric and gloss parameters.

8.3 Thermogravimetric analyses

Thermogravimetric analyses (TGA) were performed to evaluate the decomposition pathway and the thermo-oxidative stability of the studied polymeric materials. The results are reported as the percentage mass as function of temperature (TGA curve) and its derivative curve (DTG). The activation energy (E) of the main stage, associated to the degradation of the polymeric fraction, was determined by means of Kissinger's method, which is based on the use of the temperature at the maximum rate of weight loss (T_m) at different heating rates.

Thermograms recorded for *Acril 33*, *Acril ME*, *Aquazol 500* and *Laropal A81* at heating rate of $25\text{ }^\circ\text{C min}^{-1}$ are shown in Figure 9.

The thermal decomposition of *Acril 33* shows that three reaction stages occur during degradation. The first degradation step appears around 247°C and it is composed of a main peak and a shoulder (Figure 9a). It corresponds to the massive thermal degradation associated to the decomposition of the polymeric fraction with a weight loss of 92.5%. The second and the third stage, with a weight loss of 5.3% and 2.2% respectively, are probably caused by impurities and additives present in the commercial sample. The decomposition of the sample ends at around 600°C with a weight loss of 100%.

The thermogram of *Acril ME* shows that two reaction stages occur during degradation. As for *Acril 33*, the first step is composed by a main peak and a shoulder (Figure 9b) and it is associated to the decomposition of the polymeric fraction. This stage starts from 276°C and implies a weight loss of 95.8%. The second stage appears around 472°C (4.2% weight loss) and is probably caused by the loss of the emulsion stabilizer. The decomposition of *Acril ME* ends around 600°C with a weight loss of 100%.

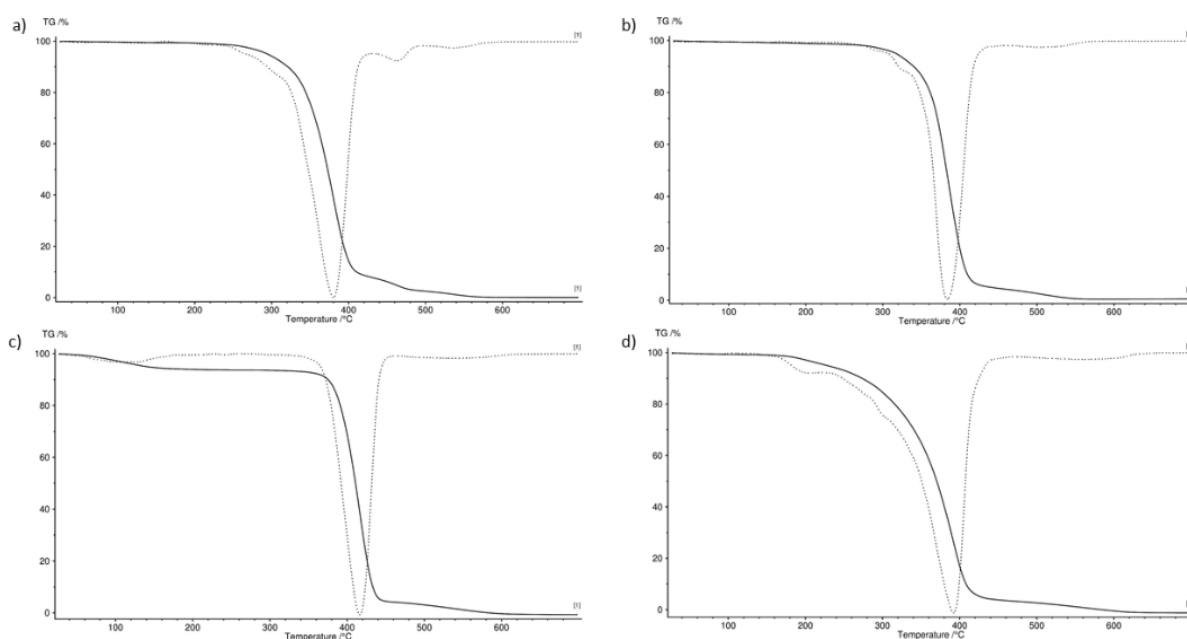


Figure 9. TGA (straight-line) and DTG (dots-line) curves recorded for (a) *Acril 33*, (b) *Acril ME*, (c) *Aquazol 500* and (d) *Laropal A81* at heating rate of $25^\circ\text{C min}^{-1}$ in the temperature range $25\text{--}700^\circ\text{C}$.

As shown in Figure 9c, the thermal decomposition of *Aquazol 500* in air is composed by three degradation steps. The first reaction stage is associated with the loss of the solvent retained by the dry polymer and resulted in a weight loss of 5.6%. The second stage appears around 344°C and it is caused by the massive degradation (89.9%) of the polymer. The third step starts from 485°C with a weight loss of 4.5%, most probably caused by additives or impurities present in the prepolymer. The decomposition of the sample ends around 600°C with a weight loss of 100%. This result does not agree with that reported by Orsini S.*et al.* [42], which have determined that the decomposition of *Aquazol* in nitrogen atmosphere happens in only one stage (degradation begins at 360°C), revealing the absence of compounds such as monomers, dimers, oligomers, co-polymers or additives.

The thermogram recorded at heating rate of 25°C min⁻¹ for *Laropal A81* shows that three reaction stages occur during degradation. The first step starts from 130°C and with a weight loss of 5.8%, is associated to the volatilization of the solvent (butylacetate) retained by the dry polymeric film. The second step appears around 239°C and it is composed by a broad peak with a series of shoulders (Figure 9d), suggesting that the polymer has a wide range of molecular weights. This stage leads to a weight loss of 90.2% and it is associated to the decomposition of the polymer. The third stage appears around 562°C and is probably caused by the degradation of some additives. The decomposition of *Laropal A81* ends around 670°C with a weight loss of 100%.

TGA measurements were carried out at several heating rates to determine the global kinetic constants of the main degradative step of the polymers. In Figures 10 are reported, as examples, the DTG curves recorded for the samples of *Acril ME* and *Aquazol 500* at different heating rates.

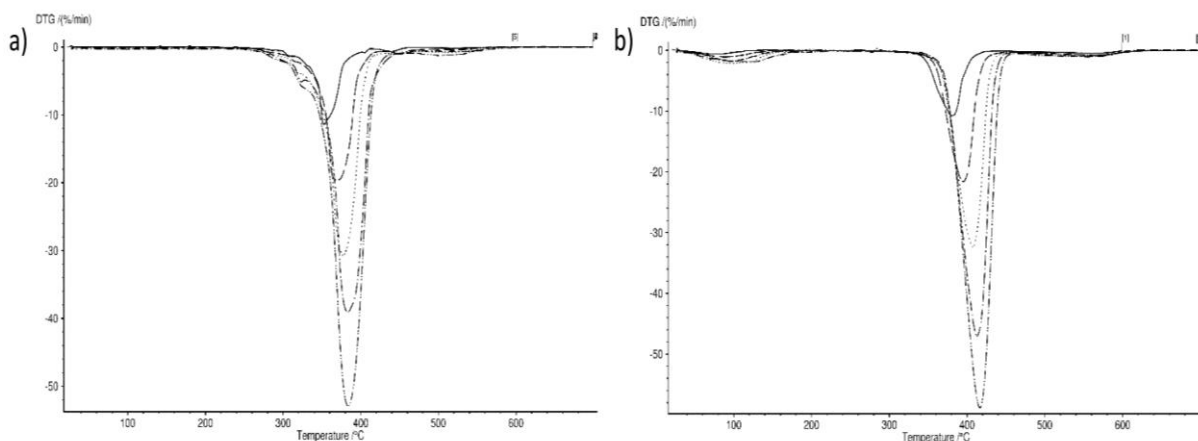


Figure 10. DTG curves recorded at 5 (straight line), 10 (discontinues line), 15 (dots), 20 (dots-line) and 25 (line-double dots) °C min⁻¹ for (a) *Acril ME* and (b) *Aquazol 500*.

The Kissinger's plots obtained for the samples *Acril 33*, *Acril ME*, *Aquazol 500* and *Laropal A81* are shown in Figure 11, while in Table 9 are reported the values of the extrapolated activation energies.

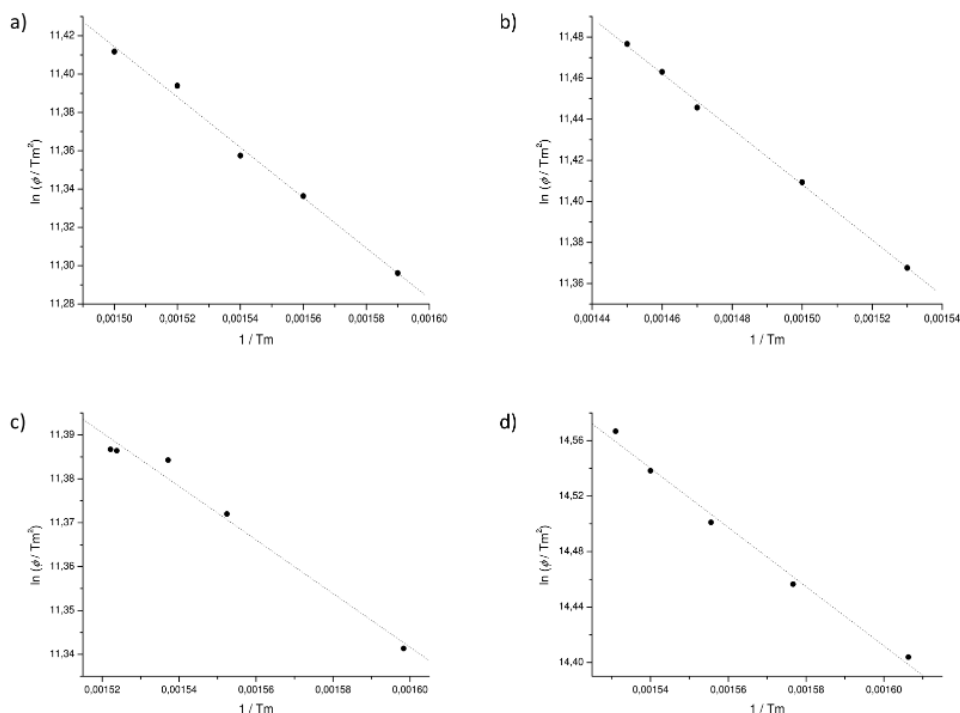


Figure 11. Kissinger's plot obtained for (a) *Acril 33*, (b) *Acril ME*, (c) *Aquazol 500* and (d) *Laropal A81*.

Table 9. Values of slope (B), R^2 and activation energy (E) determined from the linear interpolations of $\ln(\phi/T_m^2)$ versus $1/T_m$ at various heating rates for *Acril 33*, *Acril ME*, *Aquazol 500* and *Laropal A81*.

<i>Sample</i>	B	R^2	$E(\text{kJ/mol})$
<i>Acril 33</i>	-13120 ± 641	0.99643	109 ($\pm 5\%$)
<i>Acril ME</i>	-13498 ± 306	0.99922	112 ($\pm 2\%$)
<i>Aquazol 500</i>	-6103 ± 154	0.98967	51 ($\pm 2\%$)
<i>Laropal A81</i>	-21351 ± 171	0.9955	177 ($\pm 1\%$)

The two acrylic-based products show closely similar apparent activation energy, respectively of 109 ($\pm 5\%$) and 112 ($\pm 2\%$) kJ mol^{-1} for *Acril 33* and *Acril ME* (Table 9). The activation energies of the decomposition processes of several acrylic polymers and copolymers were extensively studied, although widely divergent data are reported [101]. As expected from these data, even if they are not directly comparable with ours because of the interaction between the two monomers which compose the commercial product [102], the unsaturation of the EA and MMA groups influences the thermal stability of *Acril 33*. In fact, the thermal degradation of *Acril 33* starts at lower temperature, 247°C, with respect to *Acril ME* (276°C), and its stability is slightly lower.

The apparent activation energies of the commercial products clearly follow the order *Laropal A81* \gg *Acril ME* $>$ *Acril 33* \gg *Aquazol 500* and for this reason we can identify in *Laropal A81* the more stable material here studied.

8.4 Dynamic Light Scattering (DLS) and Centrifugal Separation Analysis (CSA)

The colloidal stability and the hydrodynamic diameter of the two emulsions *Acril 33* and *Acril ME* and of the two nanoparticulated consolidants *NanoRestore* and *NanoEstel* were studied by means of CSA and DLS. Accordingly to the technical data sheets, the different materials were opportunely diluted before being analysed. Moreover, since in the technical data sheet of *NanoRestore* the product is recommended to be used within the year after the package opening, its colloidal stability was evaluated also after one-year of aging to reveal eventual modifications in the physical properties of the NPs dispersion.

The stability of dispersions was assessed by setting RPM from 1300 to 2800 (the linearity of the method was proved). The extrapolated sedimentation velocity values at gravity, obtained as the slope of the best fitting, was calculated and it is reported together with the correlation coefficient (R^2). The time analysis at each RPM tested was selected accordingly to the time needed to reach the complete sedimentation. The best conditions in terms of particles separation speed and time analysis were obtained at 2800 RPM. The colloidal stability of fresh and diluted (1:1, 1:2 and 1:100 or 1:10 in MilliQ water) *Acril 33* and *Acril ME* emulsions was investigated by means of CSA, and the transmission profiles recorded along the length of the cuvette are reported respectively in Figures 12 and 13.

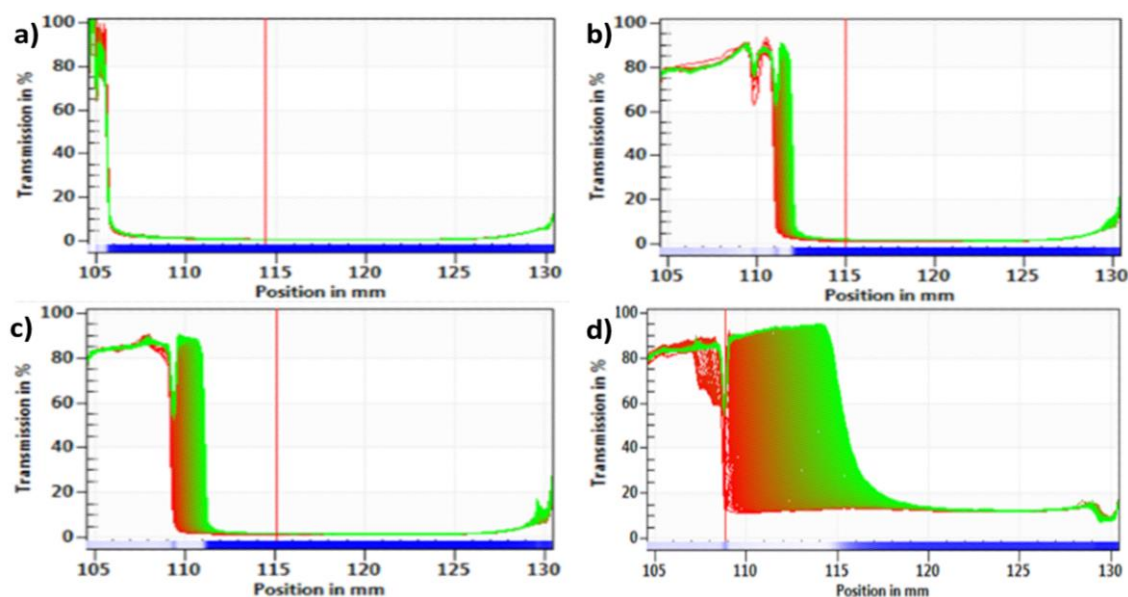


Figure 12. Transmission profiles of (a) fresh *Acril 33* and diluted (b) 1:1, (c) 1:2 and (d) 1:100 acrylic emulsion with MilliQ water.

The transmission profiles begins with very low transmission values (Figures 12a and 13a), between 0 and 15%, and in all the cases the settling of the particles is negligible at gravity. It was necessary to

dilute 1:100 for *Acril 33* and 1:10 for *Acril ME* to calculate the sedimentation velocity at gravity force by CSA, which resulted respectively $\leq 8 \times 10^{-4}$ ($R^2 > 0.994$) and $\leq 3 \times 10^{-4} \mu\text{m s}^{-1}$ ($R^2 > 0.999$).

DLS measurements on diluted (up to 1:100) *Acril 33* gave a distribution of 70 ± 15 nm, while for diluted 1:10 *Acril ME* a population of micelles with hydrodynamic diameter of 47 ± 7 nm was determined.

In general, high colloidal stability for both the two emulsions investigated was observed.

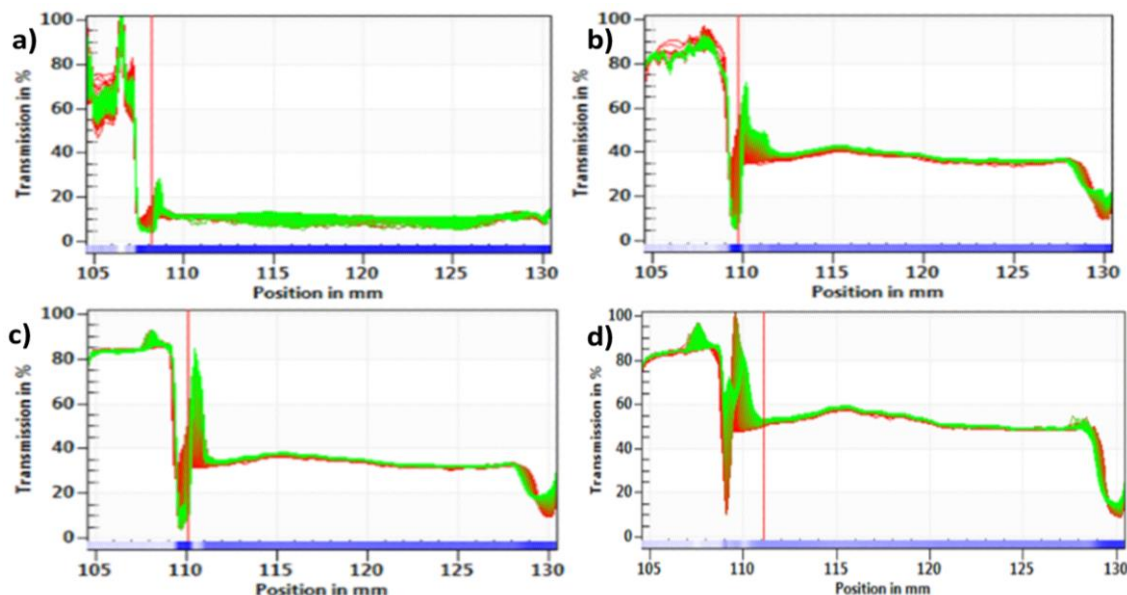


Figure 13. Transmission profiles of (a) fresh *Acril ME* and diluted (b) 1:1, (c) 1:2 and (d) 1:10 acrylic emulsion with MilliQ water.

The colloidal stability of fresh and diluted (1:2, 1:5 and 1:10 in 2-propanol) *NanoRestore* was investigated. As shown in Figure 14a, the transmittance profiles of the dispersion recorded along the length of the cuvette range from a minimum of transmittance (5%-35%) at the beginning of the analysis, when all the particles are dispersed, to 90% of the total transmittance, which represents the complete sedimentation of the particles. Moreover, the separations among the profiles in the fresh sample show different trends, suggesting the presence of at least two different populations of particles. As shown in Figures 14b, 14c and 14d, an increase of the dilution factor leads to a more homogeneous distribution of the transmittance profiles, phenomenon that can be tentatively attributed to a decrease of the interactions among particles. Finally, the sedimentation velocity of one-year aged *NanoRestore* revealed as the aging did not affect the main features of the starting dispersion in terms of sedimentation velocities distribution.

Particles size distribution of *NanoRestore* dispersion has been calculated through SEPView software and data are shown in Figure 15. As expected from the separations of the profiles depicted in Figure 14a, two different populations of particles can be detected in the fresh $\text{Ca}(\text{OH})_2$ NPs. The first population has an average diameter around 25 nm, while the second around 300 nm. As shown in Figures 15b, 15c and 15d the dilution of the dispersions with 2-propanol slightly decreases the width of particle size distributions, especially for 1:5 and 1:10 dilutions. As for unaged NPs $\text{Ca}(\text{OH})_2$ dispersion, the one-year

aged sample shows two populations of particles with a decrease of the biggest aggregates size towards 200 nm.

Accordingly to the results obtained by CSA, the transmission profiles of the fresh and one-year aged dispersions were analysed by considering two populations of particles through SEPView software. The profiles of the fresh sample were divided between 1 and 10 (first population) and between 11 and 131 (second population), while the profiles of the one-year aged dispersion were divided between 1 and 23 (first population) and between 24 and 131 (second population). This increased number of profiles of the first population moving from fresh to one-year aged dispersion, also associated to a reduced separation among them, indicates the presence of an increased number of large particles. However, as depicted in boxplots of Figure 15f, the one-year aged dispersion resulted to be more homogeneous.

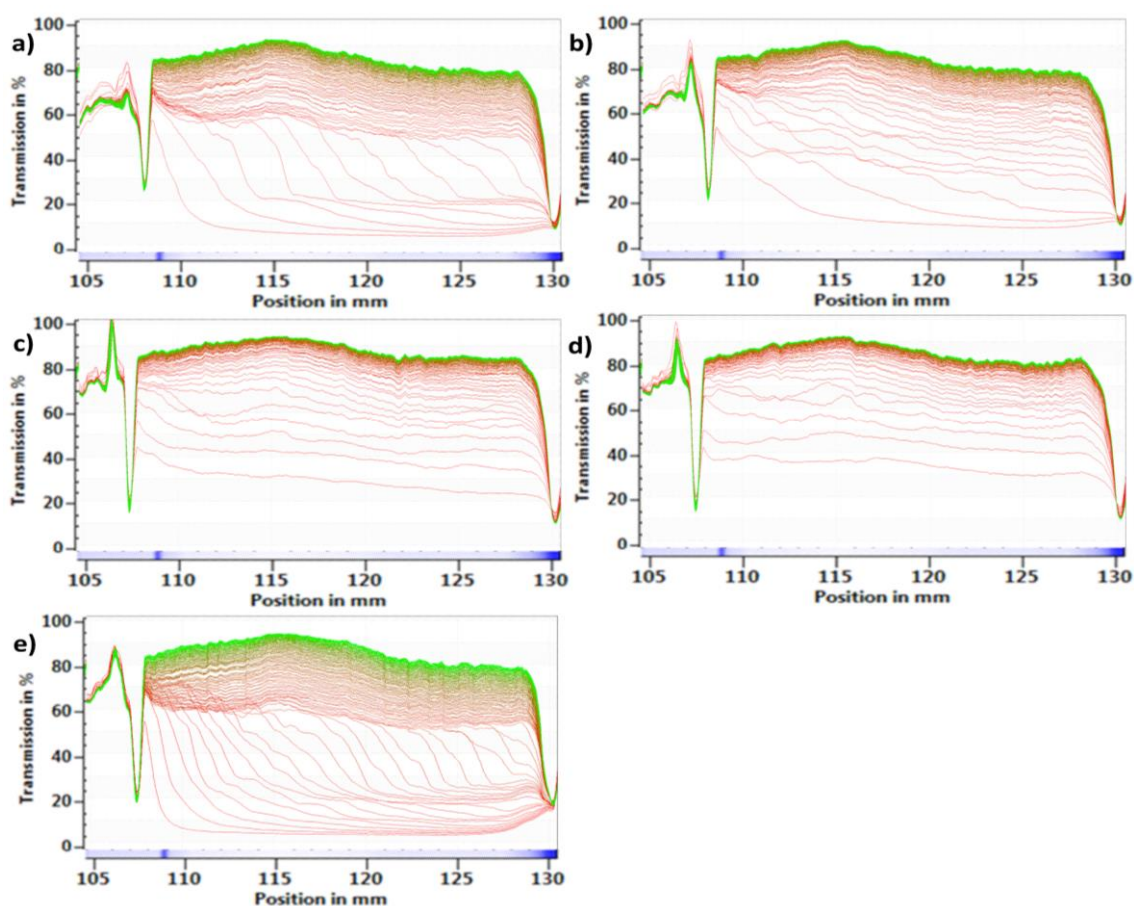


Figure 14. Typical transmission profiles of (a) fresh and diluted (b) 1:2, (c) 1:5 and (d) 1:10 Ca(OH)_2 NPs in 2-propanol.

The sedimentation velocity was calculated for the two populations of particles fitting experimental sedimentation data with linear regression ($R^2 > 0.992$) extrapolating sedimentation velocity values at gravity for each population. The results suggested a decrease of the settling values for the largest population of particles ($6.1 \cdot 10^{-2} \pm 6.6 \cdot 10^{-4}$ vs. $5.1 \cdot 10^{-2} \pm 6.9 \cdot 10^{-4} \mu\text{m s}^{-1}$), from the fresh to the one-year aged dispersion, while similar values ($5.8 \cdot 10^{-3} \pm 2.1 \cdot 10^{-4}$ vs. $5.5 \cdot 10^{-3} \pm 1.8 \cdot 10^{-4} \mu\text{m s}^{-1}$) have been obtained for the smallest population of particles.

Hydrodynamic particles size of the tested dispersions has been determined also by DLS. Differently from CSA results, a single population with an average hydrodynamic particles size of 336 ± 34 nm was detected for the fresh dispersion, accordingly to the data reported in the literature [56a, 103], and 665 ± 68 nm for one-year aged sample. On the other hand, agglomerates ($\phi > 1 \mu\text{m}$) were detected for 1:2, 1:5 and 1:10 diluted samples. The different results obtained from DLS and CSA can be ascribed to the physical principle of DLS, which is more sensitive to agglomerates rather than to primary NPs.

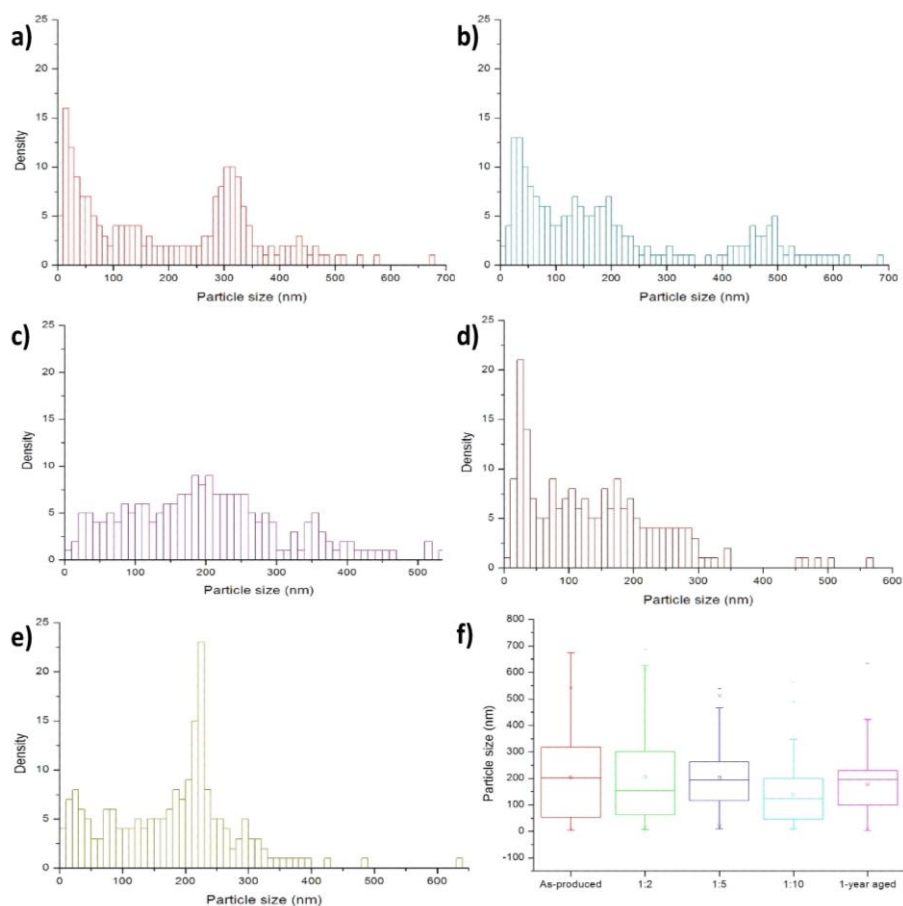


Figure 15. Particles size distributions obtained from CSA of (a) fresh and diluted (b) 1:2 (c) 1:5 and (d) 1:10 $\text{Ca}(\text{OH})_2$ NPs dispersion in 2-propanol, (e) particles size distribution of one-year aged NPs dispersion and (f) box plot of particles size values obtained for fresh, diluted and one-year aged samples.

The colloidal stability of fresh and diluted (1:1 and 1:2 with MilliQ water) *NanoEstel* dispersions was also investigated by CSA technique (Figure 16).

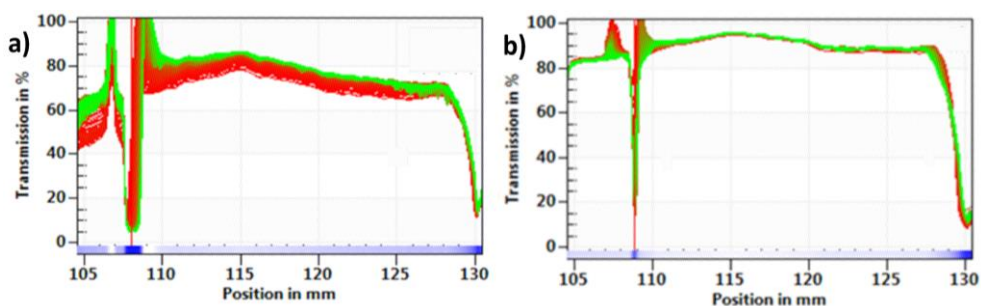


Figure 16. Typical transmission profiles of (a) fresh *NanoEstel* and (b) 1:2 diluted with MilliQ water.

Also for *NanoEstel* the settling of the NPs was very low at gravity (sedimentation velocities $\leq 0.01 \mu\text{m s}^{-1}$, $R^2 > 0.999$). However, the initial transmission profiles of both fresh and diluted dispersions begin with high transmission values, between 65 and 85%, indicating a certain instability of the dispersions. The hydrodynamic diameter of *NanoEstel* NPs was investigated by DLS, and the resulting average diameter is $19 \pm 3 \text{ nm}$.

8.5 Viscometric measurements

By dissolving a polymer in a suitable solvent, an increase of the solution viscosity is generally observed. Viscometry allows to determine the intrinsic viscosity of the polymer solution, which can be used to characterise the material under investigation, being dependent on the molecular weight. Moreover, the variation of the retention times of aged polymer with respect to the fresh ones allows to hypothesize the mechanism of degradation.

The flow times of *Acril 33* and *Acril ME* polymers solutions in the concentration range 0.25-1.25 g dL⁻¹ (acetone, 25°C) through a 100/200 Ostwald-glass capillary were evaluated. In Table 10 the retention times are reported as average of three independent measures, together with the calculated relative (η_{rel}), specific (η_{sp}) and reduced (η_{red}) viscosity.

Table 10. Flow times (s) of *Acril 33* and *Acril ME* solutions (concentration range 0.25-1.25 g dL⁻¹, acetone, 25°C, 100/200 Ostwald-glass capillary), relative viscosity (η_{rel}), specific viscosity (η_{sp}) and reduced viscosity (η_{red}).

[g dL ⁻¹]	<i>Flow time</i>	η_{rel}	η_{sp}	η_{red}	<i>Flow time</i>	η_{rel}	η_{sp}	η_{red}
<i>solv</i>	63.4 ± 0.4							
0.25	84.3 ± 0.6	1.330	0.330	1.320	66.6 ± 0.2	1.051	0.051	0.204
0.50	112.3 ± 0.1	1.772	0.772	1.544	70.8 ± 0.3	1.117	0.117	0.233
0.75	146 ± 1	2.299	1.299	1.732	74.9 ± 0.2	1.182	0.182	0.243
1.00	182 ± 2	2.882	1.882	1.882	81.2 ± 0.1	1.280	0.280	0.280
1.25	229 ± 1	3.624	2.624	2.099	87.3 ± 0.2	1.377	0.377	0.301

The plot of the reduced viscosity versus concentration gives an intrinsic viscosity of 1.15 ± 0.02 and 0.180 ± 0.007 dL g⁻¹ for, respectively, *Acril 33* and *Acril ME*. These data show as *Acril 33* exhibits an intrinsic viscosity of one order of magnitude higher than *Acril ME*, therefore lower molecular weight is expected for this last.

Solutions (0.1 g dL⁻¹) have been obtained from *Acril 33* and *Acril ME* samples aged under thermal (80°C) and photo-oxidative (UVA $\lambda=254$ nm) conditions. However, the samples subjected to thermo-oxidative aging did not completely dissolve and are therefore not suitable for viscometric analyses. Anyway, the loss of solubility indicates the formation of polymer fractions with higher molecular weight, thus probably the degradation mechanism involves at least cross-linking between polymer chains. On the other hand, solutions coming from the samples of *Acril 33* subjected to photo-oxidation showed a slight decrease of the retention times (Table 11). This result, together with the absence of formation of insoluble fractions, suggests that probably only fragmentation reactions occur during the degradation. Moreover, no significant variations in the retention times were recorded for *Acril ME* along 2000 hours of UVA aging, suggesting that no meaningful change occurs in the molecular weight of the polymer. Therefore, higher stability of *Acril ME* with respect to *Acril 33* to the photo-oxidative

conditions imposed was observed.

Table 11. Flow times (s) of aged *Acril 33* and *Acril ME* (concentration 0.1 g dL⁻¹, acetone, 25°C, 100/200 Ostwald type) under photo-oxidative (UVA $\lambda=254$ nm) conditions.

<i>Sample</i>	<i>0 h</i>	<i>1000 h</i>	<i>2000 h</i>
<i>Acril 33</i>	69.9 ± 0.8	64.4 ± 0.1	64.2 ± 0.1
<i>Acril ME</i>	64.8 ± 0.3	64.7 ± 0.5	64.9 ± 0.2

Flow times of *Aquazol 500* solutions in the concentration range 0.1-0.8 g dL⁻¹ in MilliQ water (25°C) through a 200/300 Ostwald type glass capillary were evaluated as average of three independent measurements. Data are reported in Table 12 together with the calculated relative, specific and reduced viscosity.

An intrinsic viscosity of 0.75 ± 0.03 dL g⁻¹ was evaluated from a plot of η_{rel} versus concentration. This value is in good agreement with the viscosity of 0.81 dL g⁻¹ reported for *PEOX* by Bernard A.M. [39a].

Table 12. Flow times (s) of *Aquazol 500* solutions (concentration range 0.1-0.8 g dL⁻¹, MilliQ water, 25°C, 200/300 Ostwald type), relative viscosity (η_{rel}), specific viscosity (η_{sp}) and reduced viscosity (η_{red}).

<i>[g dL⁻¹]</i>	<i>Flow time</i>	η_{rel}	η_{sp}	η_{red}
<i>solv</i>	197.6 ± 0.8			
<i>0.1</i>	213.1 ± 0.7	1.079	0.079	0.785
<i>0.3</i>	251.8 ± 0.4	1.274	0.274	0.914
<i>0.6</i>	326 ± 1	1.649	0.649	1.082
<i>0.8</i>	374 ± 1	1.893	0.893	1.116

Solutions (0.1 g dL⁻¹) have been obtained from *Aquazol 500* aged under thermal (80°C) and photo-oxidative (UVA $\lambda=254$ nm) conditions. The flow times of aged samples are reported in Table 13.

As for the acrylic polymers subjected to thermo-oxidative aging, the presence of insoluble fractions in the solutions indicates an increase in the molecular weight of the polymer, thus probably at least cross-linking reactions occur during the degradation of the polymer.

On the other hand, for *Aquazol 500* subjected to photo-oxidative degradation, a slight decrease of the retention times was recorded, suggesting that fragmentation reactions occur.

Table 13. Flow times (s) of aged *Aquazol 500* (concentration 0.1 g dL⁻¹, butylacetate, 25°C, 100/200 Ostwald type) under photo-oxidative (UVA, $\lambda=254$ nm) conditions.

<i>Aging</i>	<i>0 h</i>	<i>1000 h</i>	<i>2000 h</i>
<i>UVA</i>	210.8 ± 0.5	208.5 ± 0.8	206.5 ± 0.9

The flow times of *Laropal A81* solutions in the concentration range 1-10 g dL⁻¹ in butylacetate (25°C) through a 100/200 Ostwald type glass capillary were evaluated and are reported in Table 14 as average of three independent measurements, together with the calculated η_{rel} , η_{sp} and η_{red} .

An intrinsic viscosity of $0.042 \pm 0.001 \text{ dL g}^{-1}$ was evaluated for *Laropal A81*.

Table 14. Flow times (s) of *Laropal A81* solutions (concentration range 1-10 g dL⁻¹, butylacetate, 25°C, 100/200 Ostwald type), relative viscosity (η_{rel}), specific viscosity (η_{sp}) and reduced viscosity (η_{red}).

<i>[g dL⁻¹]</i>	<i>Flow time</i>	<i>η_{rel}</i>	<i>η_{sp}</i>	<i>η_{red}</i>
<i>solv</i>	115.9 ± 0.4			
<i>1.0</i>	121.5 ± 0.6	1.037	0.037	0.366
<i>5.0</i>	140.9 ± 0.1	1.048	0.048	0.048
<i>7.5</i>	174 ± 1	1.216	0.216	0.043
<i>10.0</i>	194 ± 1	1.505	0.505	0.067

Solutions (0.1 g dL⁻¹) have been obtained from aged *Laropal A81* samples under thermal (80°C) and photo-oxidative (UVA, $\lambda=254 \text{ nm}$) conditions. The flow times of aged samples are reported in Table 15.

Table 15. Flow times (s) of aged *Laropal A81* (concentration 0.1 g dL⁻¹, butylacetate, 25°C, 100/200 Ostwald type) under thermal (80°C) and photo-oxidative (UVA, $\lambda=254 \text{ nm}$) conditions.

<i>Unaged</i>	<i>Aging</i>	<i>813 h</i>	<i>2402 h</i>	<i>Aging</i>	<i>834 h</i>	<i>2000 h</i>
120.1 ± 0.8	80°C	117 ± 1	117 ± 1	UVA	118.0 ± 0.1	116.6 ± 0.4

For the samples subjected to both aging tests a slight decrease in the retention times was recorded. This, together with the absence of insoluble fractions, indicates that both thermal and photo-oxidative degradations of *Laropal A81* probably occur through fragmentation reactions rather than cross-linking mechanism.

8.6 Size Exclusion Chromatography (SEC) measurements

SEC analyses allowed to follow changes in the molecular weight distributions (MWD) and average molar masses (M_w , M_n and M_z) occurred over 2000 hours of thermo- and photo-oxidative (UVA $\lambda=254$ nm) aging. However, the samples aged at 100, 120 and 140°C remained insoluble in the solvent DMAc/LiCl 0.9%, thus only the samples aged at 80°C were analysed by means of SEC. Conclusions were drawn regarding the degradation kinetics and mechanisms of the polymers *Acril 33*, *Acril ME* and *Aquazol 500*.

SEC chromatograms of *Acril 33* after different thermo-oxidative (80°C) aging times are shown in Figure 17. As the aging time increases, the polymer increasingly degrades as shown by the shift of the MWD towards lower molar masses values.

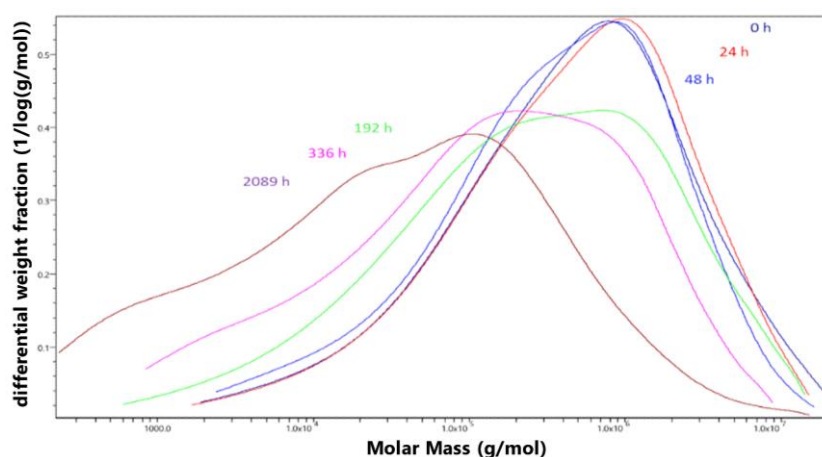


Figure 17. Molecular weight distributions (MWD) of *Acril 33* after increasing thermo-oxidative aging times.

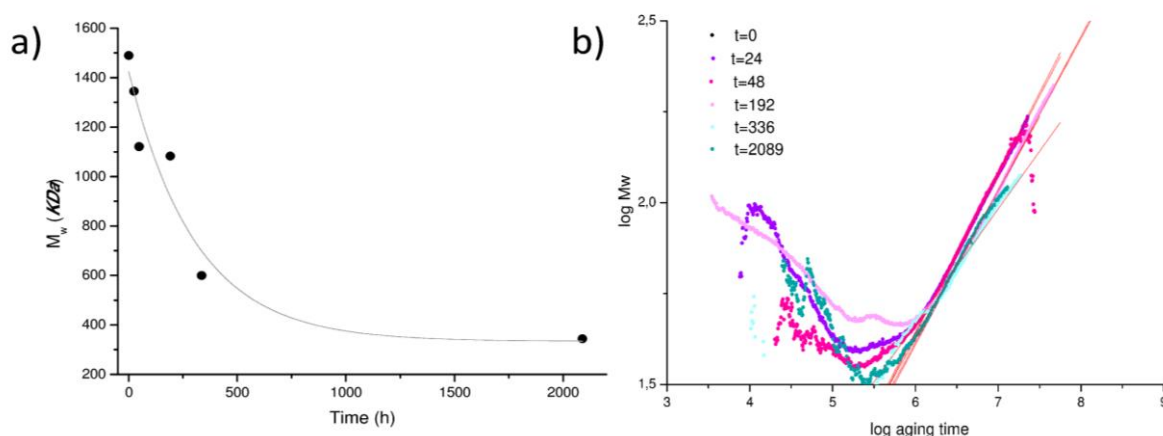


Figure 18. (a) Kinetics of the depolymerization process of the lower-MM, non-crosslinked soluble fractions; (b) Conformation plots of *Acril 33* along thermo-oxidative aging.

The cleavage of the polymer backbone with the formation of shorter-chain fragments seems the main degradation mechanism. However, the evaluation of the percent mass recovery (MS%) after SEC analysis (Table 16) reveals that upon thermo-oxidative aging, *Acril 33* most likely undergoes cross-

linking reactions rather than fragmentation. The evident decrease in RM% may, in fact, indicate that the portion of soluble polymer strongly decreases with aging. It is therefore reasonable to hypothesize that samples actually analysed were constituted by the lower-MM, non-crosslinked soluble fractions.

Table 16. Molar masses (M_n , M_w , M_z , kDa), dispersity (\mathcal{D} , M_w/M_n), radius of gyration (R_z , nm), percent recovery mass (RM %) and conformation plot slope (CPS) for increasing times of thermo-oxidative aging of *Acril 33*.

<i>Aging time</i>	M_n	M_w	M_z	\mathcal{D}	R_z	RM %	CPS
0	73	1490	6801	20.5	104.7	100	0.425
24	72	1345	5029	18.7	87.5	39	0.4325
48	63	1121	4835	17.8	83.8	43	0.4419
192	27	1082	5075	40.2	74.5	15	0.317
336	15	599	2932	39.6	63.7	11	0.406
2089	3	344	9245	101.5	38.3	28	0.468

The kinetic constant (k) of the degradation process was evaluated from the decay curve of the M_w values versus the aging time (Figure 18a) and is equal to $3.26 \times 10^{-3} \text{ (h}^{-1}\text{)}$. As shown in Figure 18b, the conformation plot slope parameter remains unchanged during the thermo-oxidative aging at 80°C , indicating that no significant variation in the shape of the polymer molecules occurs.

As showed in Figure 19, the exposure of *Acril 33* to UVA light ($\lambda=254 \text{ nm}$) causes a similar reduction of the molar masses of the polymer. However, as highlighted by the recovery mass values reported in Table 17, the polymer remains completely soluble in the solvent DMAc/LiCl 0.9% during the whole aging process. Therefore, it is reasonable to assume that a fragmentation mechanism is responsible for the polymer degradation.

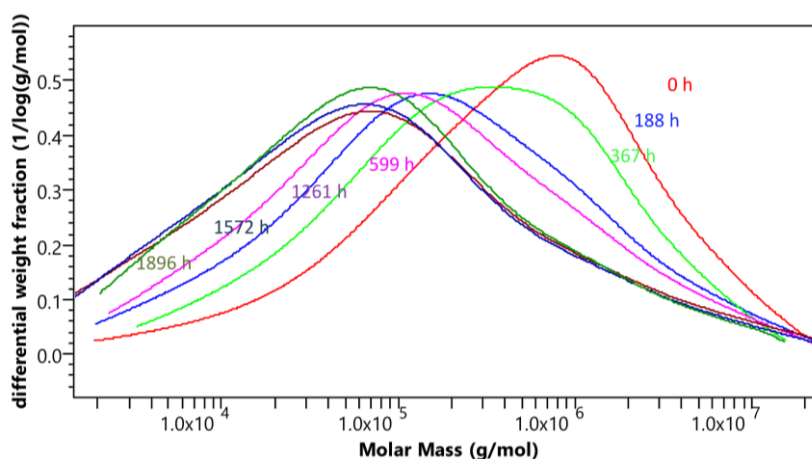


Figure 19. Molecular weight distributions (MWD) of *Acril 33* after increasing photo-oxidative aging times.

The kinetic constant of the depolymerization process (Figure 20a), calculated (as mentioned above) from the M_w -time decay curve, was found to be $2.93 \times 10^{-3} \text{ (h}^{-1}\text{)}$. In addition, changes in the slope of the conformation plots towards lower values (Table 17, Figure 20b) indicate that the shape of polymer molecules in solution modifies upon aging from random coil to sphere.

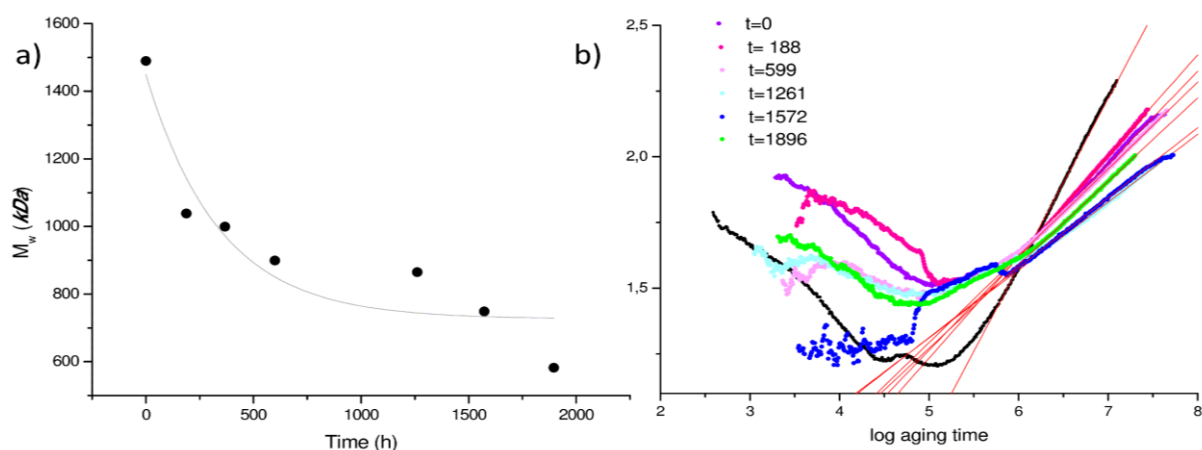


Figure 20. (a) Kinetics of the depolymerization process; (b) Conformation plots of *Acril 33* along UVA aging.

Table 17. Molar masses (M_n , M_w , M_z , kDa), dispersity (\mathcal{D} , M_w/M_n), radius of gyration (R_z , nm), percent recovery mass (RM %) and conformation plot slope (CPS) for increasing times of photo-oxidative aging of *Acril 33*.

<i>Aging time</i>	M_n	M_w	M_z	\mathcal{D}	R_z	RM %	CPS
0	73	1490	6801	20.5	104.7	100	0.425
188	35	1039	9041	29.8	86.2	100	0.354
367	62	999	5216	16.1	76.0	100	0.3846
599	32	899	8587	28.2	81.0	100	0.3302
1261	15	865	12029	59.0	66.7	100	0.2582
1572	16	749	10700	46.7	66.3	100	0.2660
1896	21	582	5938	28.2	65.3	100	0.1373

The *Acril ME* unaged sample showed a bimodal distribution of molar masses (Figure 21, red curve). As the thermo-oxidative aging proceeds, the MWD broadens and shifts to lower MM values, the distribution becoming monomodal (Figure 21).

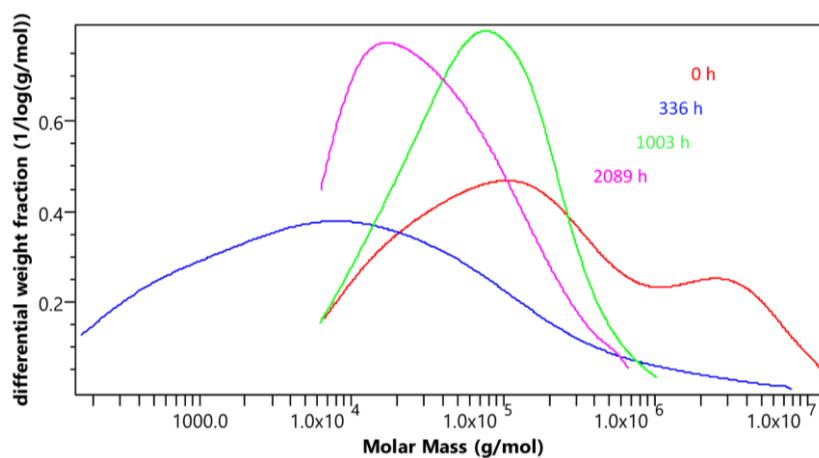


Figure 21. Molecular weight distributions (MWD) of *Acril ME* after increasing thermo-oxidative aging times.

Recovery mass % values significantly decrease during the first hours of aging (Table 18), indicating that the thermo-oxidative degradation of *Acril ME* may be primarily caused by cross-linking reactions. For

the lower-MM non-crosslinked soluble fractions the calculated kinetic constant (k) of the degradation process (Figure 22a) is $7.63 \times 10^{-3} \text{ (h}^{-1}\text{)}$. The conformation plots (Figure 22b) provide evidence that in solution *Acril ME* experiences a change in shape from sphere to random coil as a consequence of thermal aging.

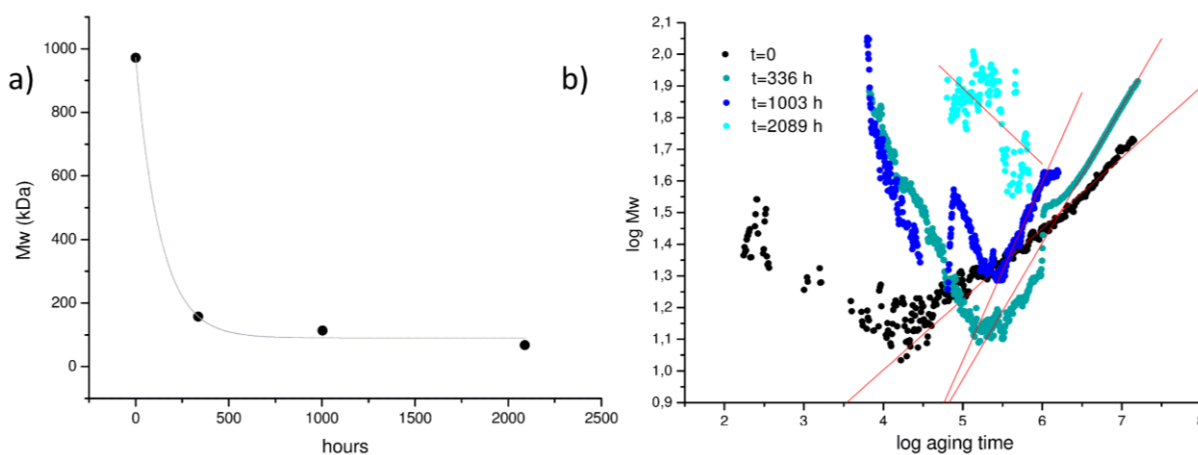


Figure 22. (a) Kinetics of the depolymerization process; (b) Conformation plots of *Acril ME* along thermo-oxidative aging.

Table 18. Molar masses (M_n , M_w , M_z , kDa), dispersity (\mathcal{D} , M_w/M_n), radius of gyration (R_z , nm), recovery mass % (RM %) and conformation plot slope (CPS) for increasing times of thermo-oxidative aging of *Acril ME*.

Aging time	M_n	M_w	M_z	\mathcal{D}	R_z	RM %	CPS
0	49	972	5203	19.8	50.9	100	0.223
336	2	157	3904	93.9	35.8	31	0.429
1003	37	114	295	3.1	26.3	38	0.564
2089	21	67	212	3.2	43	6	-0.24

Conversely, photo-oxidation of *Acril ME* does not induce significant variations in the MWD (Figure 23) in addition to the loss of the highest MM fractions already recorded after about 200 hours of aging. A slight decrease of the average molar masses was recorded and $3.10 \times 10^{-3} \text{ (h}^{-1}\text{)}$ was calculated as kinetic constant for the depolymerization process (Figure 24a).

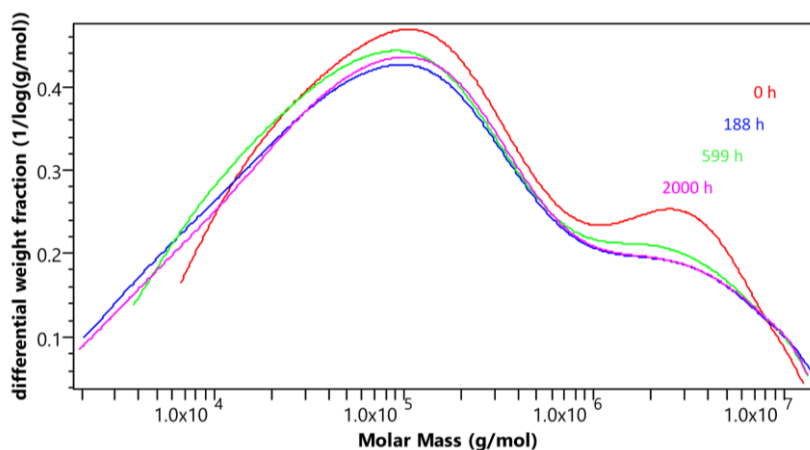


Figure 23. Molecular weight distributions (MWD) of *Acril ME* after increasing photo-oxidative aging times.

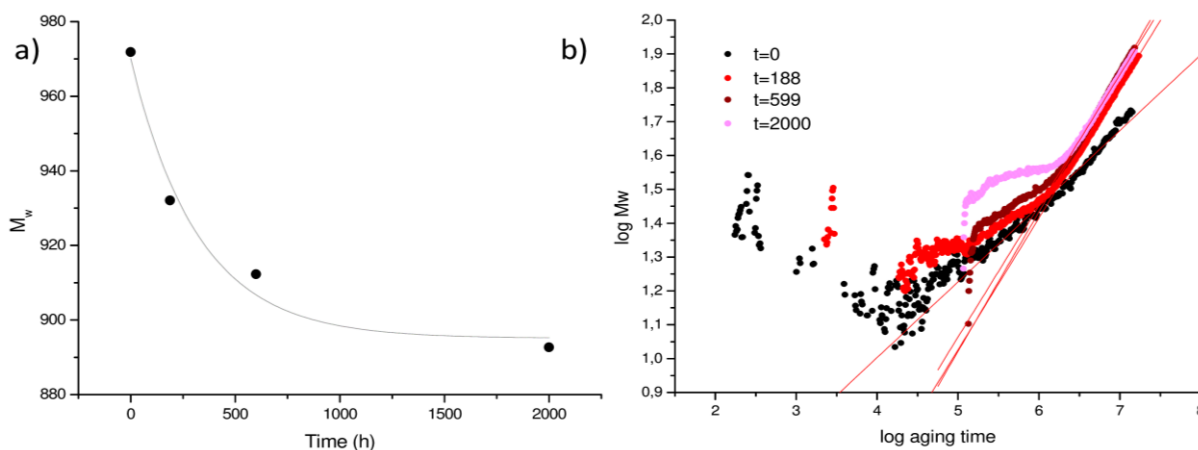


Figure 24. (a) Kinetics of the depolymerization process; (b) Conformation plots slope of *Acril ME* along UVA aging.

The maintenance of the percent recovery mass parameter around 100% indicates that under photo-oxidative condition the main degradative process is the chain fragmentation, while the increased conformation plot slope values (Table 19, Figure 24b) indicate that the shape of the polymer molecules in solution changes from sphere to random coil upon aging.

Table 19. Molar masses (M_n , M_w , M_z , kDa), dispersity (D , M_w/M_n), radius of gyration (R_z , nm), recovery mass % (RM %) and conformation plot slope (CPS) for increasing times of photo-oxidative aging of *Acril ME*.

<i>Aging time</i>	M_n	M_w	M_z	D	R_z	RM %	CPS
0	49	972	5203	19.8	50.9	100	0.223
188	23	932	6280	39.7	52.2	100	0.389
599	32	912	5685	28.2	54.7	90	0.411
2000	24	893	5760	36.5	55.1	100	0.387

Comparably to the other investigated polymers, upon thermal aging *Aquazol 500* suffers from degradation primarily associated to chain cleavage. As depicted in Figure 25, MWDs shift towards lower molar masses and the distribution changes from bimodal to broad and monomodal, thus indicating a primary fragmentation of the higher-MM portions and the consequent accumulation of shorter-length fractions. The kinetic constant (k) of the depolymerization process (Figure 26a) was calculated as $4.37 \times 10^{-3} \text{ (h}^{-1}\text{)}$.

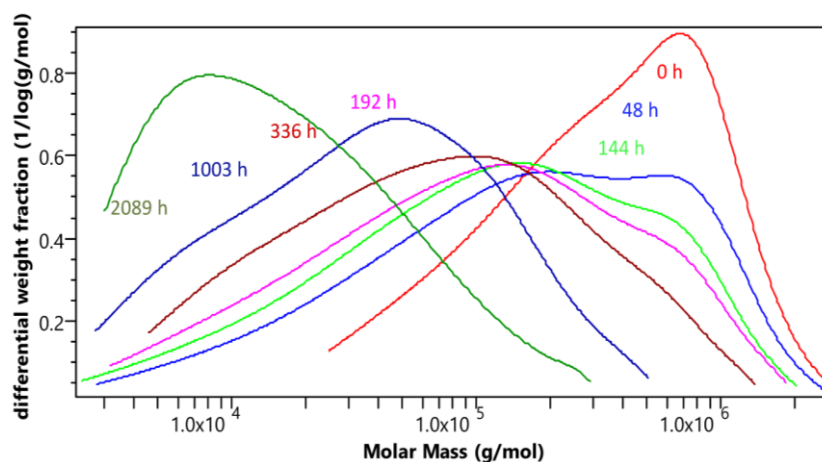


Figure 25. Molecular weight distributions (MWD) of *Aquazol 500* at increasing thermo-oxidative aging times.

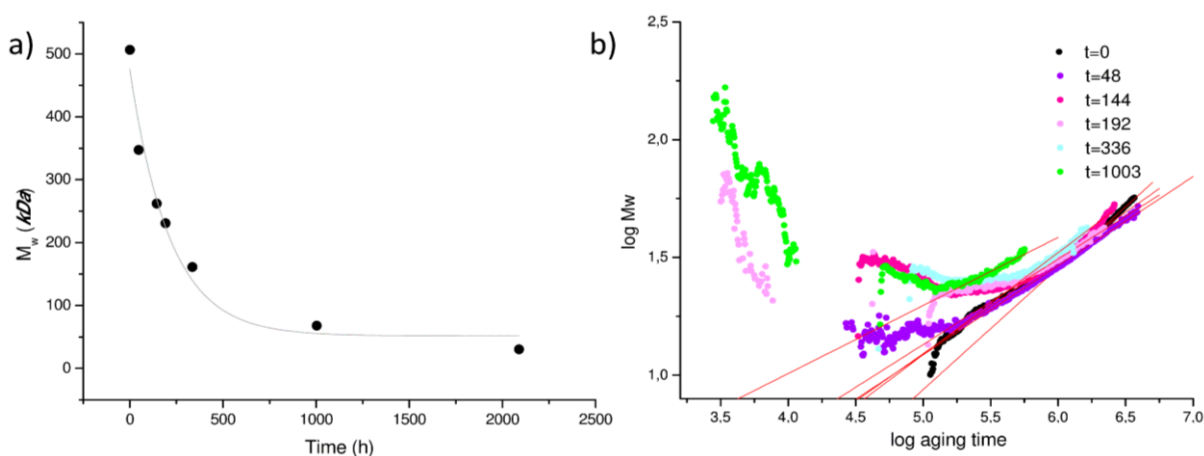


Figure 26. (a) Kinetics of the depolymerization process; (b) Conformation plots slope of *Aquazol 500* along thermo-oxidative aging.

Table 20. Molar masses (M_n , M_w , M_z , kDa), dispersity (\mathcal{D} , M_w/M_n), radius of gyration (R_z , nm), recovery mass % (RM %) and conformation plot slopes (CPS) for increasing times of thermo-oxidative aging of *Aquazol 500*.

Aging time	M_n	M_w	M_z	\mathcal{D}	R_z	RM %	CPS
0	174	506	953	2.9	28.9	100	0.517
48	46	347	912	7.5	27.5	91	0.378
144	36	262	729	7.4	28.7	73	0.401
192	33	231	678	7	27	75	0.363
336	30	161	489	5.4	26.8	86	0.43
1003	17	68	176	4	25.1	87	0.289
2089	10	30	93	3	25.4	7	---

When subjected to the UVA light ($\lambda=254$ nm), *Aquazol 500* exhibits a decrease in molar masses with M_w almost halved after 2000 hours (Figure 27). Since the recovery mass % (Table 21) remains sufficiently high and constant (i.e. the polymer remains completely soluble in the solvent DMAc/LiCl 0.9%), the degradation likely owes to fragmentation of the polymer backbone.

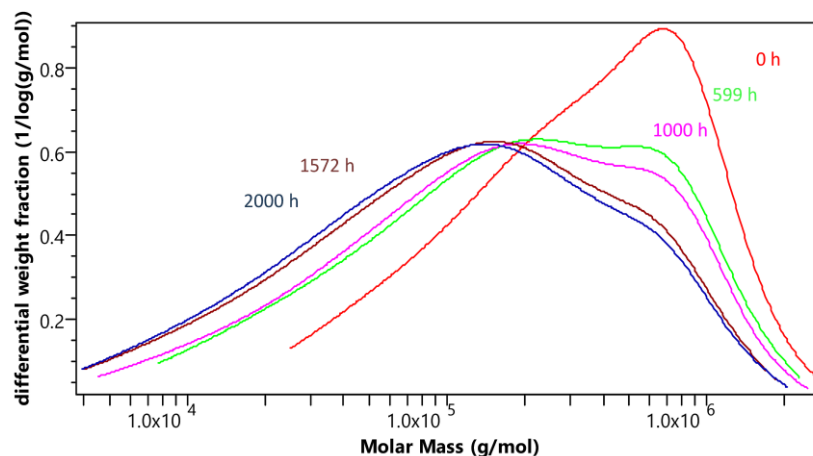


Figure 27. Molecular weight distributions (MWD) of *Aquazol 500* at increasing photo-oxidative aging times.

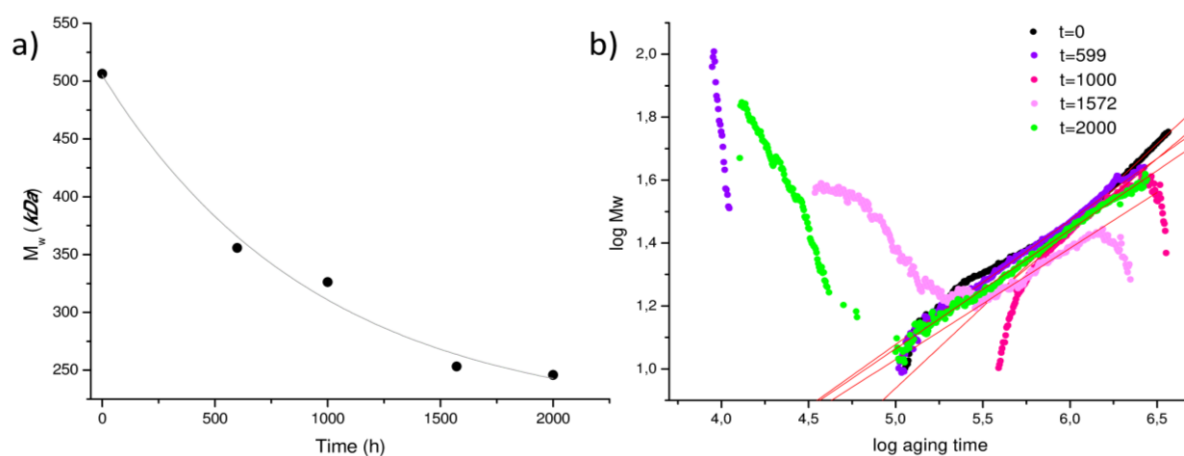


Figure 28. (a) Kinetics of the depolymerization process; (b) Conformation plots slope of *Aquazol 500* UVA aging.

The constant (k) of the depolymerization process (Figure 28a) was calculated as $1.05 \times 10^{-3} \text{ (h}^{-1}\text{)}$ while the conformation plots (Figure 28b) suggest that a random coil to sphere transition occurs to the polymer in solution during the photo-oxidative aging.

Table 21. Molar masses (M_n , M_w , M_z , kDa), dispersity (\mathcal{D} , M_w/M_n), radius of gyration (R_z , nm), recovery mass % (RM %) and conformation plot slope (CPS) for increasing times of photo-oxidative aging of *Aquazol 500*.

<i>Aging time</i>	M_n	M_w	M_z	\mathcal{D}	M_n	RM %	CPS
0	174	506	953	2.9	28.9	100	0.517
599	74	356	833	4.8	26.6	100	0.4
1000	58	326	824	5.6	19.5	100	0.466
1572	44	253	668	5.7	20.9	100	0.353
2000	42	246	697	5.8	24	100	0.377

Tables 22 and 23 show the average number of chain scissions (S) per macromolecule calculated, according to Eq. (12), respectively for the samples subjected to thermo- and photo-oxidative aging.

Table 22. Average number of chain scission (S) per macromolecule of polymer samples during thermo-oxidative aging (-- represents not available data).

<i>Aging time</i>	24	48	144	192	336	1003	2089
<i>Acril 33</i>	0	9	--	45	57	--	68
<i>Acril ME</i>	--	--	--	--	46	11	27
<i>Aquazol 500</i>	--	127	137	140	143	156	163

Table 23. Average number of chain scission (S) per macromolecule of polymer samples during photo-oxidative aging (-- represents not available data).

<i>Aging time</i>	188	367	599	1261	1572	2000
<i>Acril 33</i>	37	10	40	57	56	51
<i>Acril ME</i>	25	--	16	--	--	24
<i>Aquazol 500</i>	--	--	99	--	129	131

Data herein reported show as *Aquazol 500* exhibits the highest values of number of chain scissions in both the aging tests, suggesting its lower resistance to both thermal and photo-oxidative aging. On the other hand, *Acril ME* seems to be the polymer with the highest resistance to degradation under the same conditions.

8.7 FT-IR analyses

After proper characterization, the modifications of the characteristic absorption bands occurred due to thermo- and photo-oxidative aging as well as during natural aging were monitored by means of Fourier Transform Infrared Spectroscopy (FT-IR).

Acril 33 was characterized by means of FT-IR analysis after polymerization on KBr disk. The FT-IR spectrum collected is reported in Figure 29, while the characteristic peaks and their interpretation, according to Melo M.J. *et al.* [26b], Pintus V. *et al.* [92c] and Scaroni D. *et al.* [92h] are collected in Table 24.

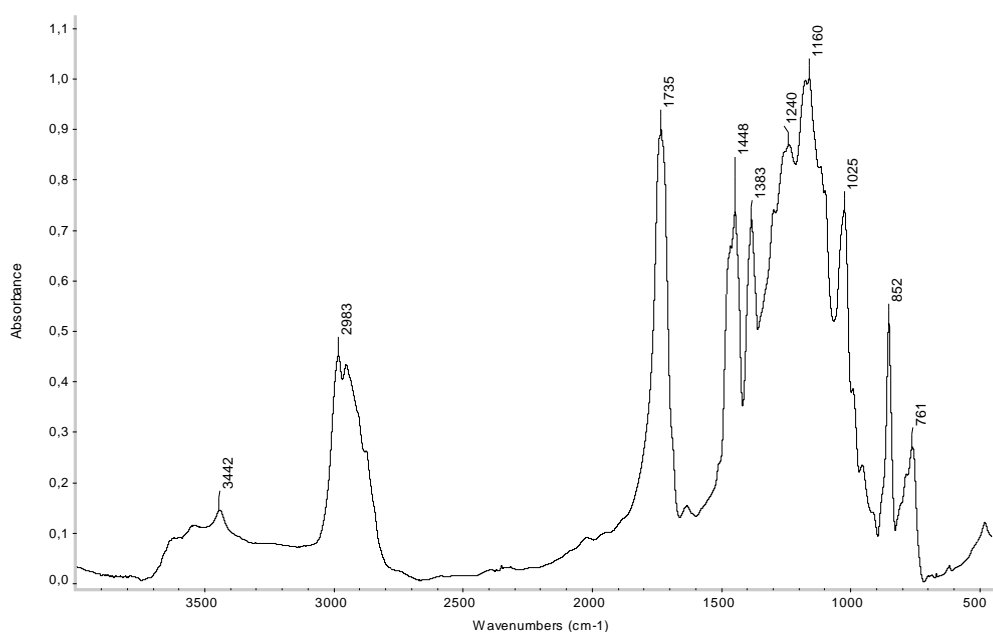


Figure 29. FT-IR spectrum of *Acril 33*.

Table 24. FT-IR absorptions peaks observed for *Acril 33*.

Wavenumber (cm^{-1})	Functional group	Assignments
3626, 3547, 3442	ν O-H	Hydroxyl groups
2983, 2952, 2905	ν C-H	Aliphatic bonds in EA MMA
1735	ν C=O	Carbonyl group
1448, 1383	δ CH ₃	CH ₃ in -COOCH ₃
1160, 1240	ν C-C(=O)-O	C-C(=O)-O MMA
1176	ν C(=O)-O-C	C(=O)-O-C MMA
1383, 1474	δ (CH ₂) CH ₃	α CH ₃
1025, 1160, 1240	δ C-O	O-C-C
997	ν C-C	Chain C-C
761, 852	ρ C-H	Aliphatic bonds in EA MMA

The FT-IR spectrum of *Acril 33* is characterized by the C=O stretching absorption at 1735 cm^{-1} , by the C–H stretching frequencies at 2983 cm^{-1} complemented by two smaller peaks at 2952 and 2905 cm^{-1} , and by a double peak of the C–H bending at 1474 and 1448 cm^{-1} and a less intense one at 1383 cm^{-1} . The O–C–C bending is detectable at 1025 cm^{-1} [26b], while the C–C vibration is detectable from the peak at 997 cm^{-1} . Additionally, the characteristic absorption bands of a polyethoxylated surfactant (*Triton X*), commonly used as emulsion stabilizer [104], were detected at 2875 , 1635 , 1466 , 1112 , 949 , 842 and 613 cm^{-1} .

Isothermal treatment at 80°C extended up to 10000 hours induced slight structural changes in the FT-IR spectrum of *Acril 33* (Figure 30), summarized as:

- broadening and increase followed by a decrease of the signal at 1735 cm^{-1} , associated to the stretching absorption of the carbonyl groups;
- appearance of a shoulder at 1782 cm^{-1} , attributable to the formation of lactone groups;
- decrease in intensity of all absorption bands in the finger print region;
- decrease of the intensity of the signal at 1448 cm^{-1} associated to the bending of the CH_3 in the lateral groups;
- decrease of the signal at 1025 cm^{-1} , associated to the bending of the O–C–C groups.

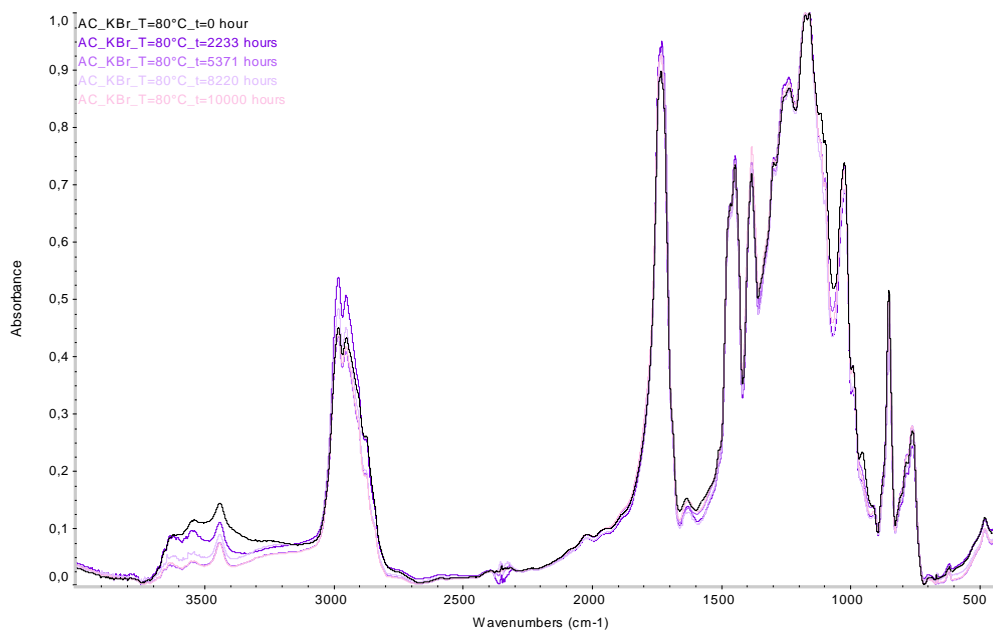


Figure 30. FT-IR spectra of *Acril 33* at increasing time of thermo-oxidative aging at 80°C .

On the other hand, the isothermal degradation of *Acril 33* at 100 , 120 and 140°C implies a massive modification of the FT-IR spectrum. In particular, as shown in Figures 31 and 32, the thermo-oxidative aging lead to a massive reduction of the intensity of all the characteristic pecks of the sample. Moreover, two new signals are detected as broad shoulders at 3234 and 2565 cm^{-1} . These signals appear since the first hours of aging and increase their intensity during thermo-oxidative aging. These bands, together

with the decrease and broadening of the C=O groups, can be attributed to the decomposition of the lateral groups, induced by the oxidation on the side chains [26d]. Furthermore, the signal at 1782 cm^{-1} , has been associated to the formation of lactone groups, while the appearance of the signal at 1620 cm^{-1} , characteristic of a C=C double bond, has been ascribed to the formation of terminal insaturations as a consequence of chain scission.

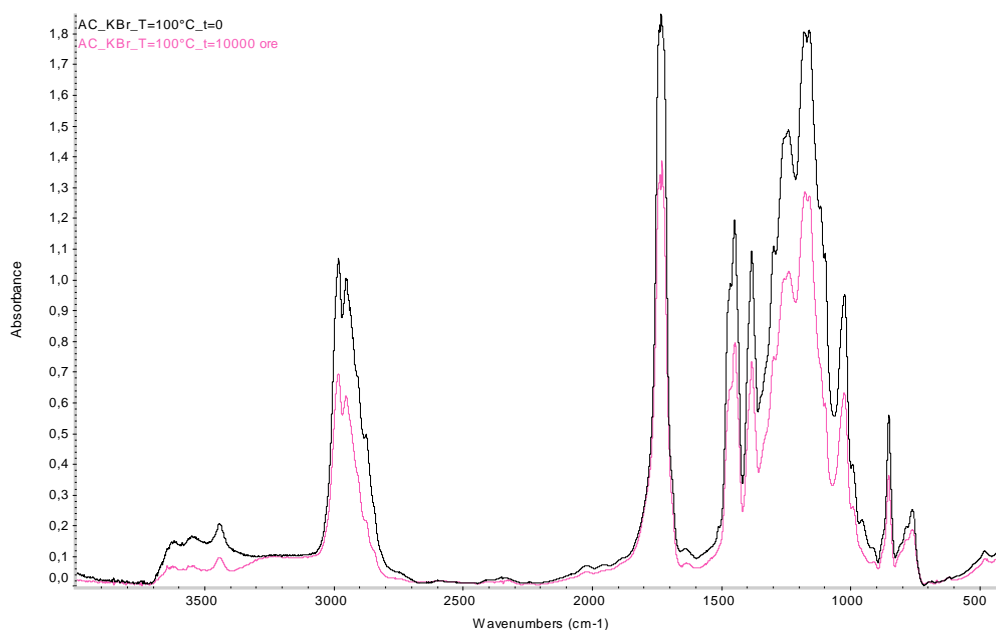


Figure 31. FT-IR spectra of *Acril 33* at the beginning and end of thermo-oxidative aging at 100°C .

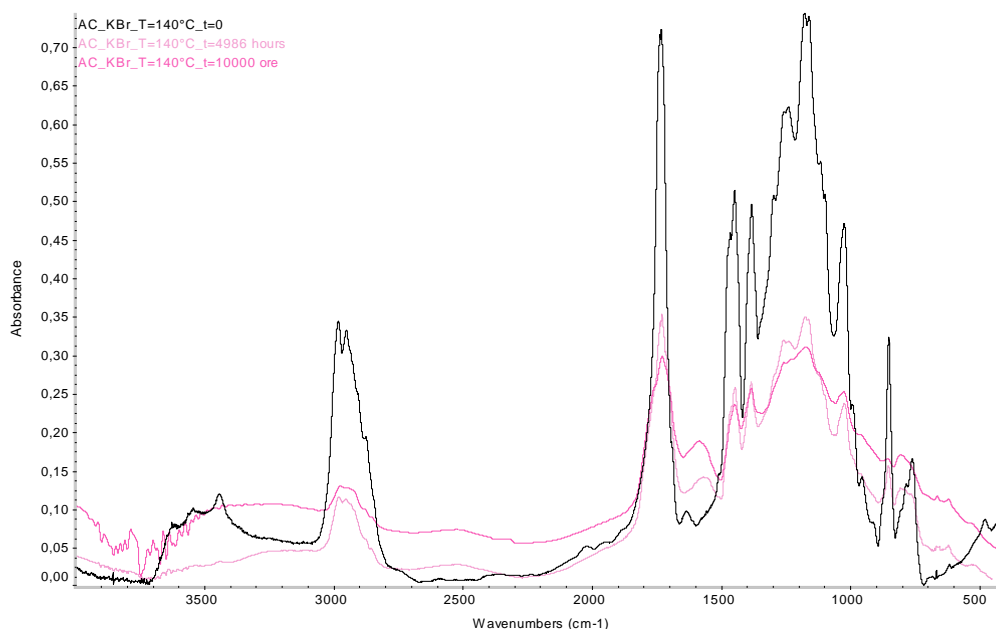
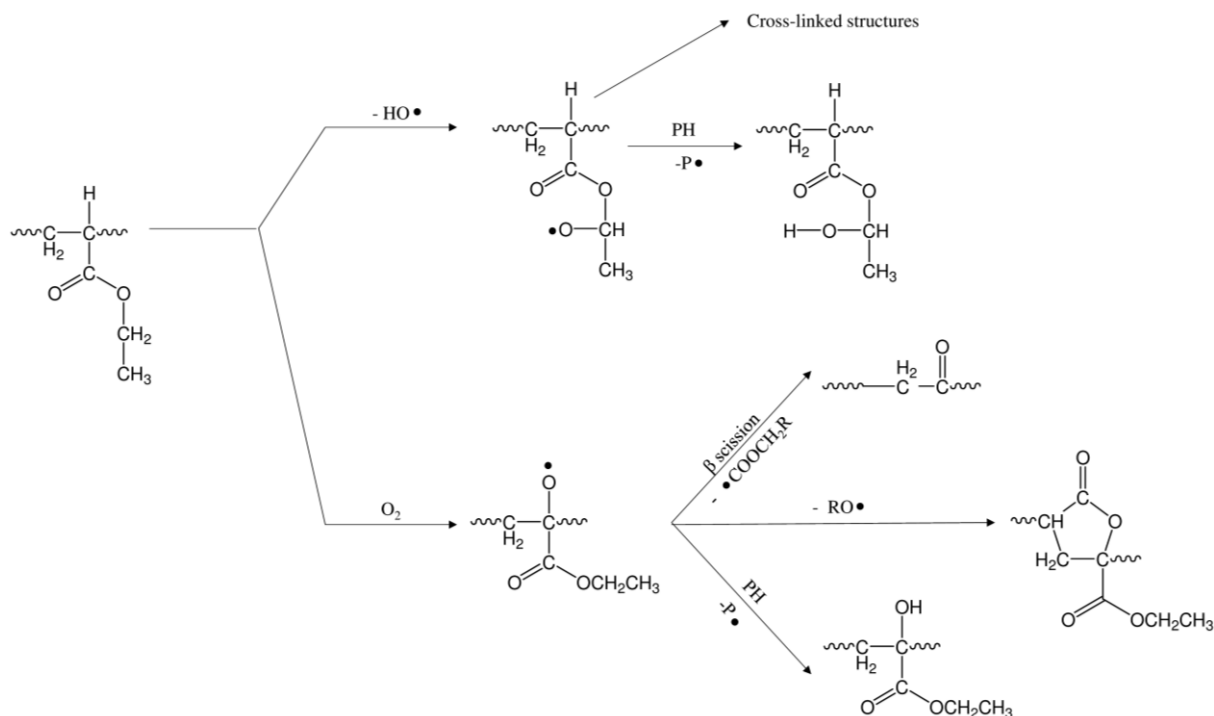


Figure 32. FT-IR spectra of *Acril 33* at increasing time of thermo-oxidative aging at 140°C .

Therefore, the results above reported, together with those of the SEC analyses, suggest that the mechanism of thermal degradation of *Acril 33* involved both cross-linking reactions of the polymer backbone and scission on the ester side group, resulting in the loss of volatile molecules and formation of lactone and hydroxyl groups. A possible scheme of reactions is shown in Scheme 11.



More specifically, the double mechanism is likely to initiate through the addition of oxygen molecules to the tertiary radical formed by abstraction of the labile hydrogen atom of the acrylic units, followed by hydrocarbon oxidation and progressive formation of OH groups [26c, 26d, 26e, 26g]. On the other hand, the tendency to form insoluble fractions observed during the SEC analyses is due to the accessible decomposition of the unstable secondary hydroperoxides [92n], which gives alkoxy radicals that decay via cross-linking.

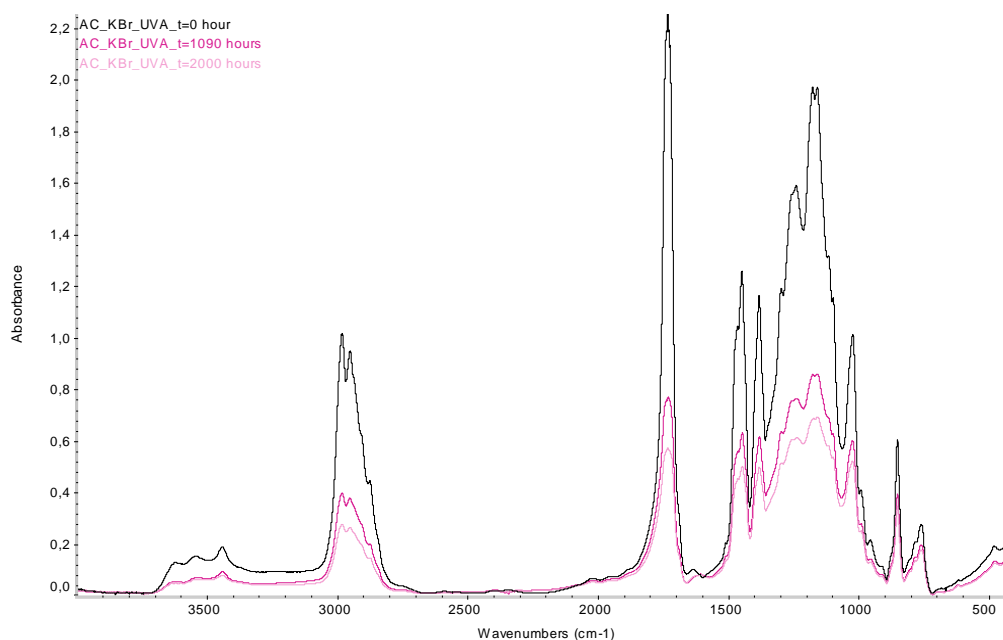


Figure 33. FT-IR spectra of Acril 33 at increasing time of UVA photo-oxidative aging.

Conversely, the photo-oxidation under UVA irradiation over 2000 hours of aging (Figure 33) or over two years of natural aging (Figure 34) implies a decrease and loss of resolutions of all the *Acril 33* characteristic signals, due to progressive loss of sample fractions, confirming that the photodegradation of *Acril 33* involved solely depolymerization mechanism, as reported above on the basis of SEC results.

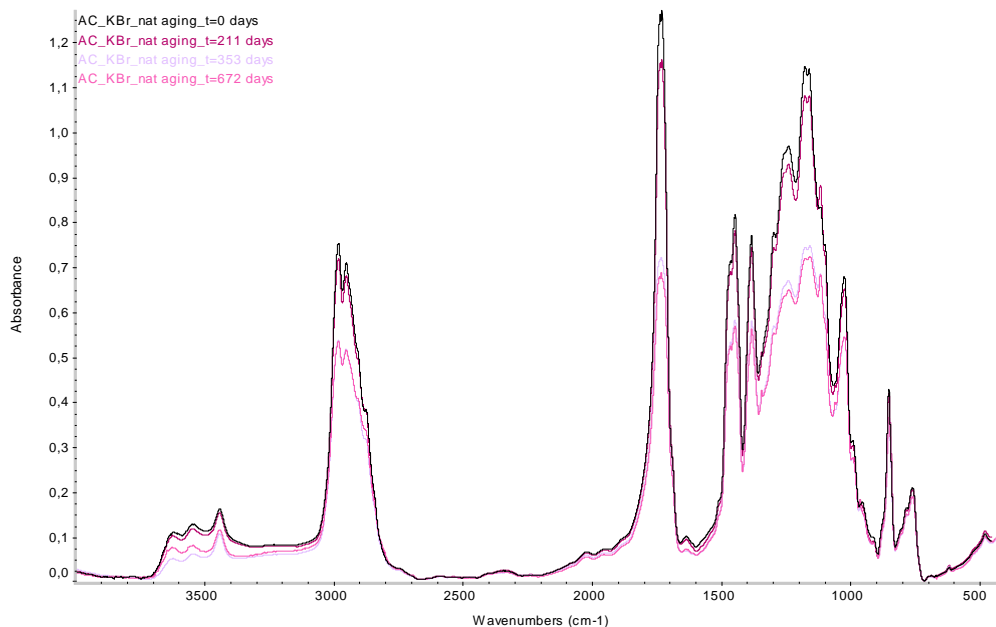


Figure 34. FT-IR spectra of *Acril 33* at increasing time of natural aging.

It is important to note that, if the mechanisms identified as responsible for thermal degradation of *Acril 33* are in good agreement with the results reported in the literature for similar acrylic resins [26d], the mechanism herein described for the photo-oxidation is in contrast with the data reported for the same commercial product in the literature [92i]. However, the different behaviour observed can be attributed to different aging conditions (irradiation wavelength, temperature, humidity) used in this work.

The *Acril ME* FT-IR spectrum is reported in Figure 35, while the characteristic peaks and their interpretation, according to Melo M.J. *et al.* [26b] and Favaro M. *et al.* [26i], are shown in Table 25. The FT-IR spectrum of *Acril ME* is characterized by the C=O stretching absorption at 1731 cm^{-1} , by the C–H stretching frequencies at 2957 and 2919 cm^{-1} , and by the bending of $\alpha\text{-CH}_3$ of the butyl groups at 1469 and 1365 cm^{-1} . The C-C(=O)-O bending (butyl groups) is detected at 1050 cm^{-1} [26b], while the C-C(=O)-C vibration is detectable from the peak at 1167 cm^{-1} . Moreover, also in the spectrum of *Acril ME* the characteristic absorption bands of the emulsion stabilizer *Triton X* were detected at 2875 , 1620 , 1466 , 1240 , 1147 , 1061 , and 843 cm^{-1} .

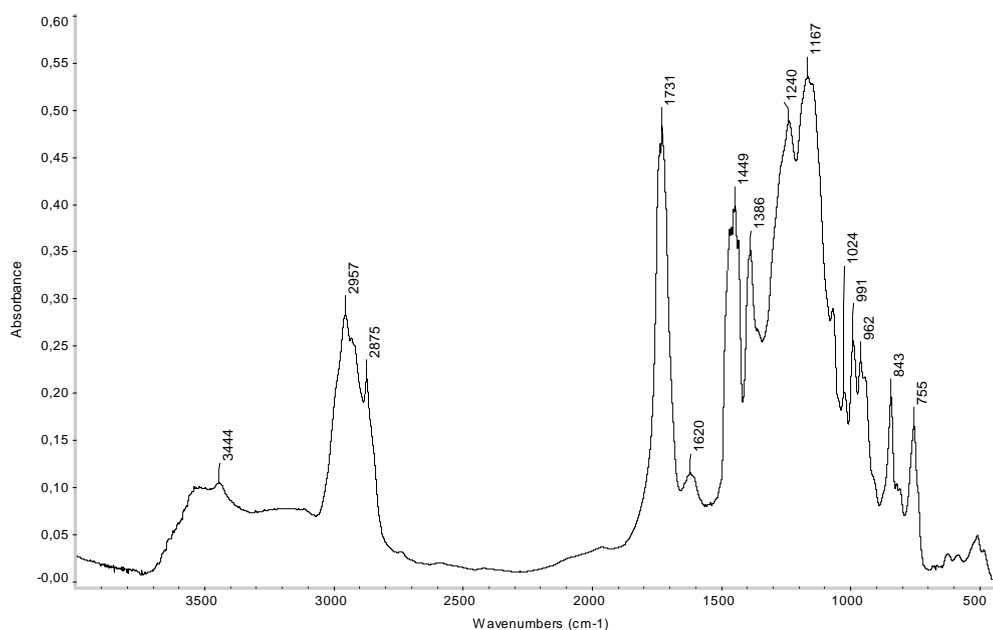


Figure 35. FT-IR spectrum of *Acril ME*.

Table 25. FT-IR absorptions peaks observed for *Acril ME*.

Wavenumber (cm ⁻¹)	Functional group	Assignments
3536, 3444	ν O-H	Hydroxyl groups
2957, 2919	ν C-H	Aliphatic bonds in EA MMA
1731	ν C=O	Carbonyl group
1449	δ CH ₃	CH ₃ in -COOCH ₃
1469, 1365	δ CH ₃	α - CH ₃
1240, 1268	ν C-O	C-O
1150	ν C-C(=O)-O	C-C(=O)-O in BMA
1167	ν C-C(=O)-C	C-C(=O)-C in BMA

The isothermal degradation at all the four temperatures (80, 100, 120 and 140°C) of *Acril ME* induce, as shown for example in Figures 36 and 37, significant variations in the FT-IR spectrum of the polymer. The variations in the spectra and then in the chemical structure of *Acril ME* can be summarized as:

- growth of the main carbonyl absorption at 1731 cm⁻¹ after the initial decrease, ascribable to the formation of ketone and aldehyde groups;
- decrease of the absorptions in the hydroxyl region, between 3220 and 3600 cm⁻¹, and of the stretching of the CH bonds in the region between 2750 and 3070 cm⁻¹;
- appearance of two broad peaks centred at 3155 and 2550 cm⁻¹, which appear since the first hours of aging and increase their intensity for further time of thermo-oxidative aging. These new signals, together with the decrease and broadening of the C=O groups, can be attributed to the decomposition of the butyl lateral groups, induced by the oxidation of the side chains [26d]. The

alkoxy radicals formed by the decomposition of the unstable secondary hydroperoxides may give β -scission followed by hydrogen abstraction or decay via cross-linking;

- appearance of a shoulder at 1782 cm^{-1} that may be assigned to stretching of C=O groups of γ -lactone, whose formation was demonstrated under the same aging conditions and it is due to the dehydration of two adjacent acid groups [28, 81c, 105] (Scheme 12).

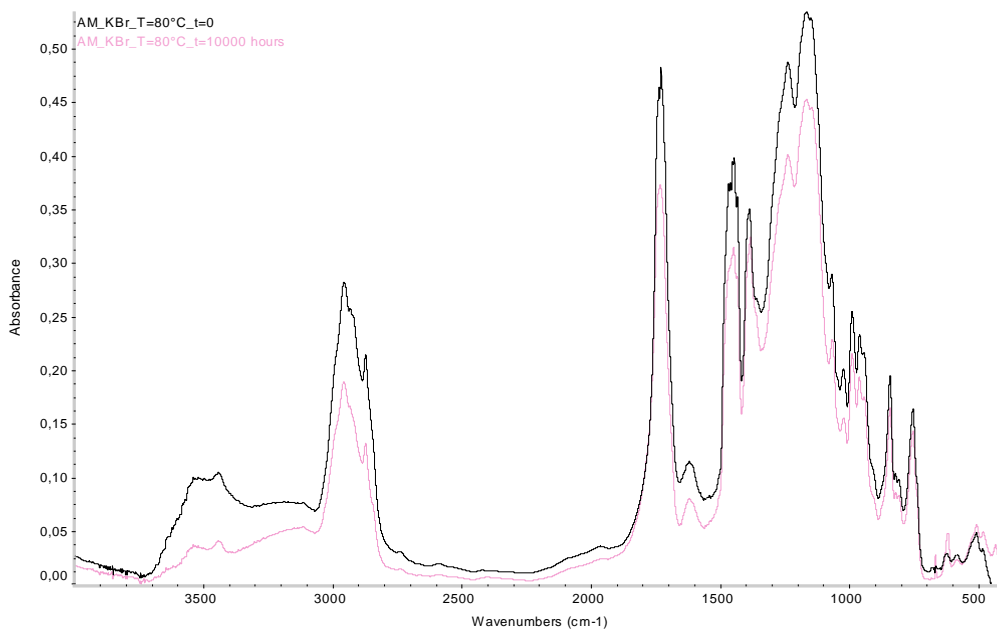


Figure 36. FT-IR spectra of *Acril ME* at the beginning and end of thermo-oxidative aging at 80°C.

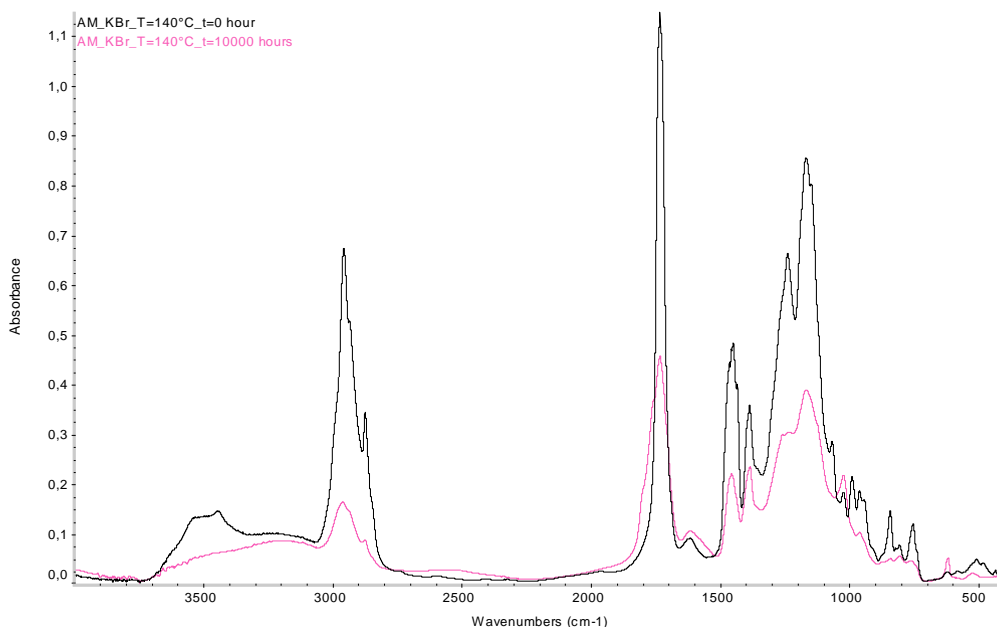
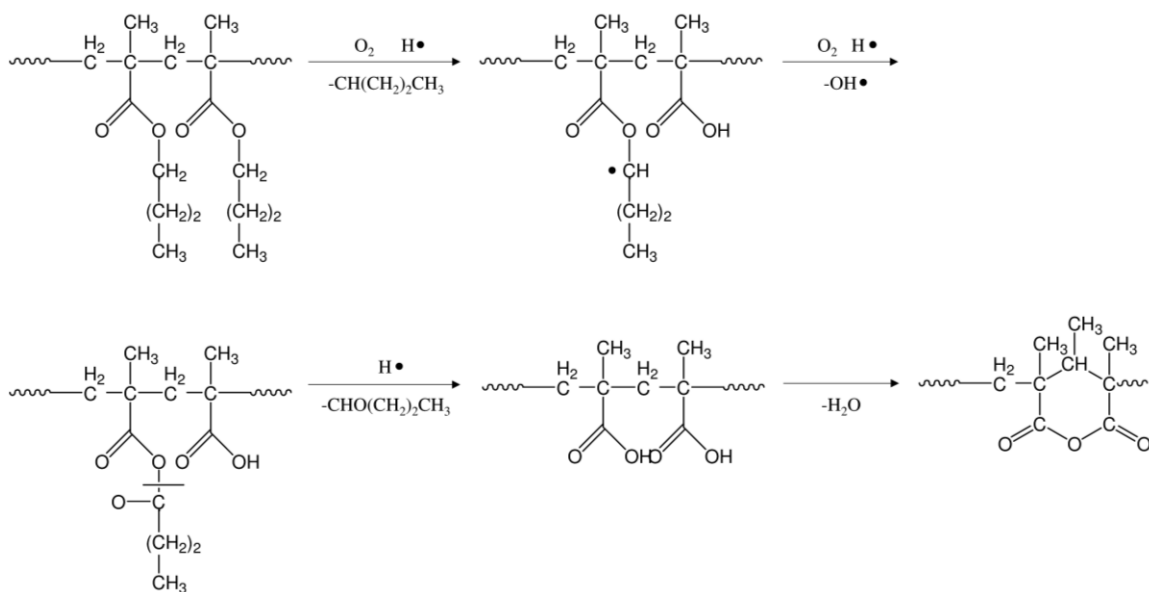
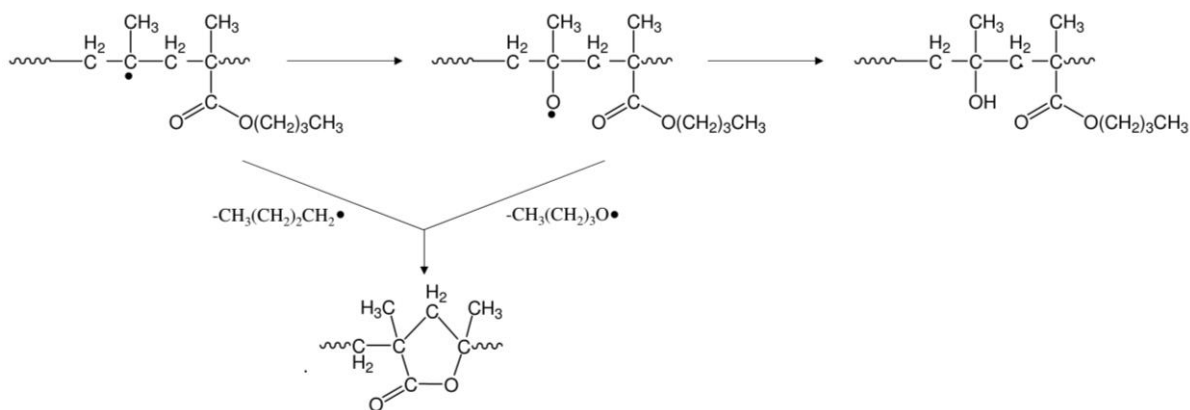


Figure 37. FT-IR spectra of *Acril ME* at the beginning and end of thermo-oxidative aging at 140°C.



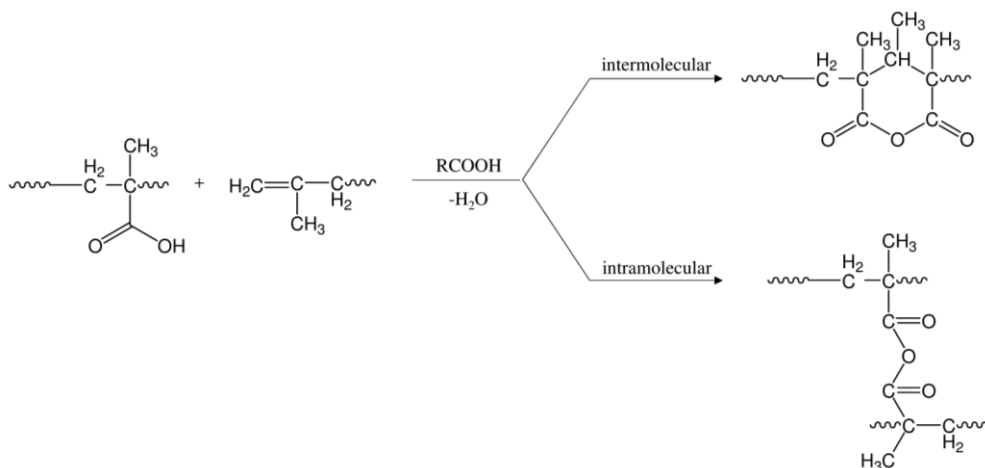
Scheme 12.

Another mechanism affording the formation of lactones is reported in Scheme 13.



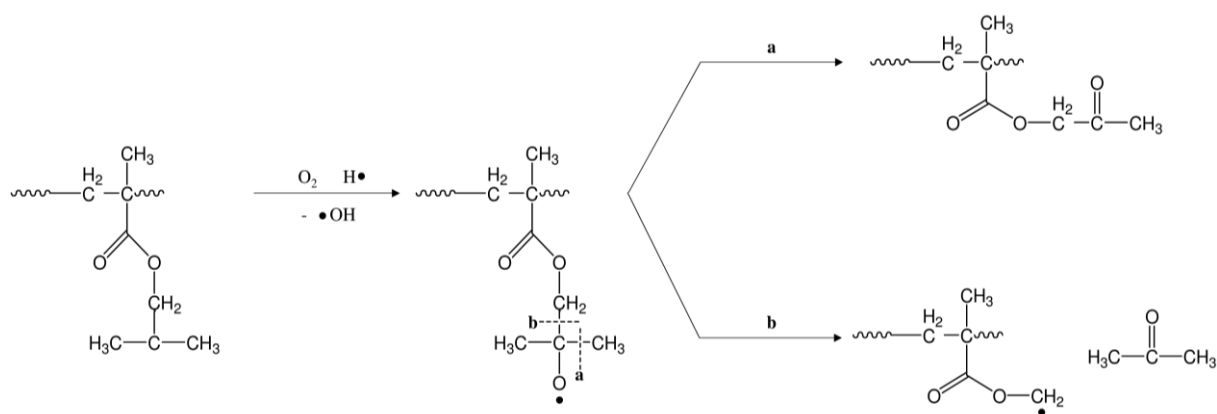
Scheme 13.

Moreover, through intramolecular reactions, hydroxyl groups can form cross-linked structures, as shown in Scheme 14.

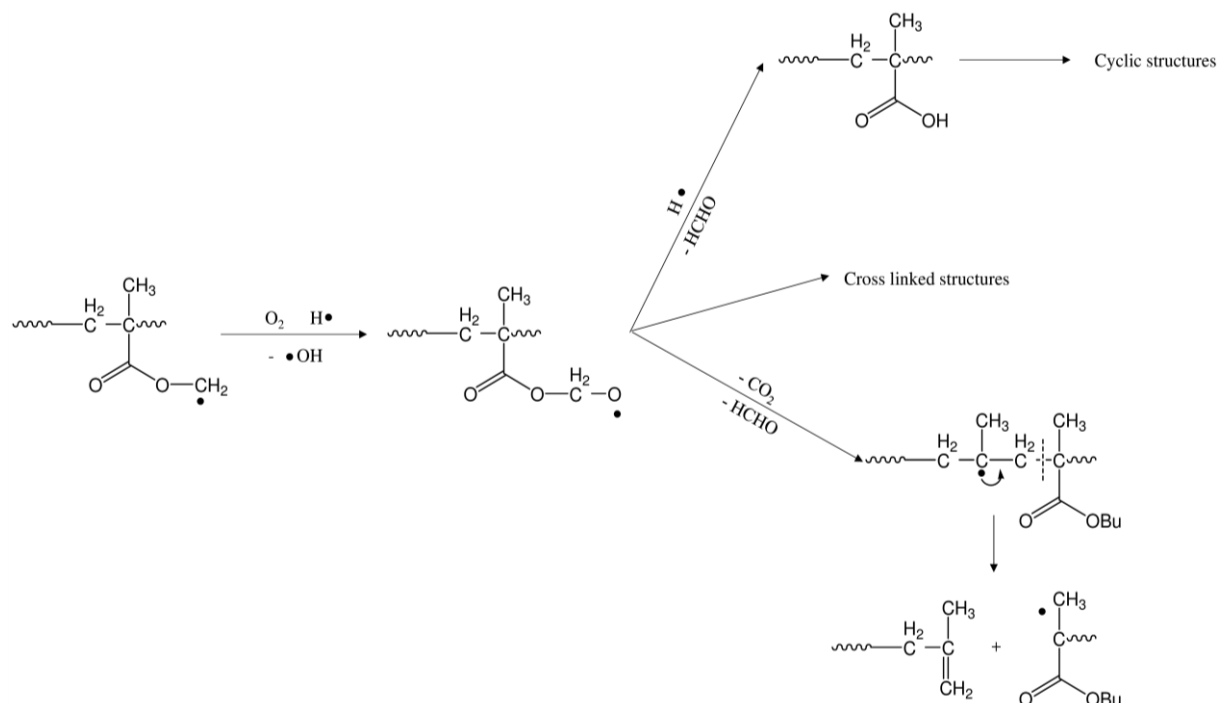


Scheme 14.

Possible mechanisms of degradation are shown in Schemes 15 and 16. The degradation is initiated by the addition of oxygen molecules to the tertiary radicals formed by abstraction of the labile hydrogen atom of the methacrylic moiety, and then the β -induced scission of alkoxy radicals can follow two distinct pathways [26d]. The first one leads to the formation of ketones (Scheme 15), while the second pathway induces the formation of alkoxy radicals which easily decompose to anhydrides and lead to the formation of γ -lactones following the dehydration of two adjacent acid groups (Scheme 16). Moreover, as shown in Scheme 16, cross-linked structures can be easily formed through bimolecular combination of radicals.



Scheme 15.



Scheme 16.

However, in the spectra reported above, the band at 1449 cm^{-1} decreases more than the one at 1050 cm^{-1} , indicating that the scission of ester groups prevails with respect to the elimination of the α -methyl groups in the lateral butyl units. Therefore, accordingly with the SEC results, it is possible to hypothesize

that the thermal degradation mechanism of *Acril ME* involves both oxidation of lateral butyl groups, leading to the formation of cyclic anhydrides, and cross-linking. Nevertheless, the growing insolubility of the polymer observed on increasing the time of thermo-oxidative aging suggests that prolonged aging favours reticulation instead of chain scission.

As reported for *Acril 33*, the photo-oxidation of *Acril ME* during 2000 hours of aging (Figure 38) implies only the decrease and loss of resolution of all the polymer characteristic signals, without the appearance of new peaks. Therefore, according to the results of the SEC analyses, the mechanism of photo-oxidative degradation is the reverse of the propagation step in an addition polymerization.

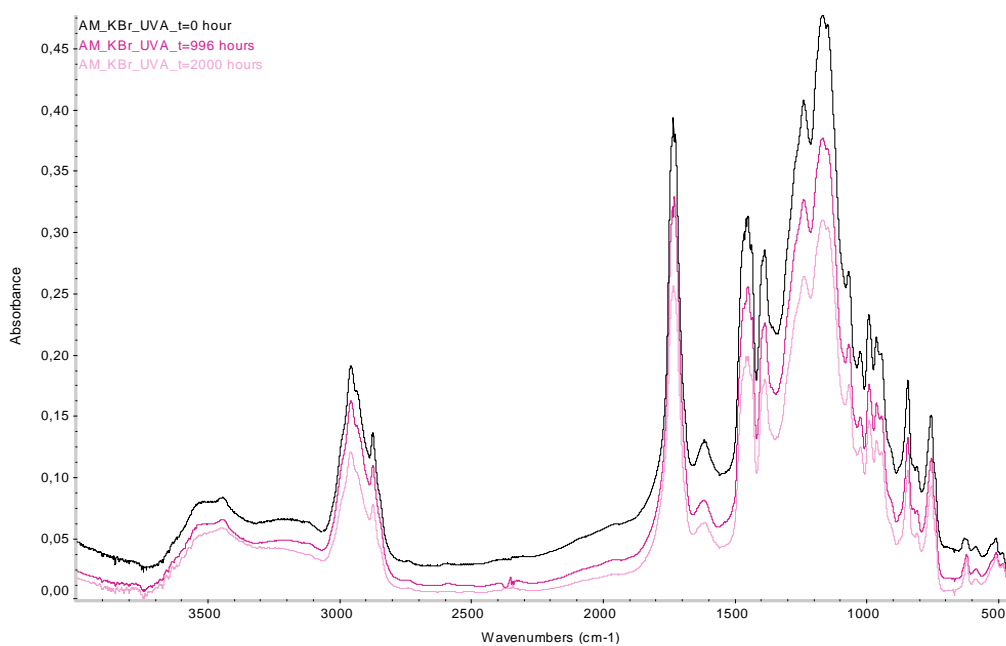


Figure 38. FT-IR spectra of *Acril ME* at increasing time of photo-oxidative UVA aging.

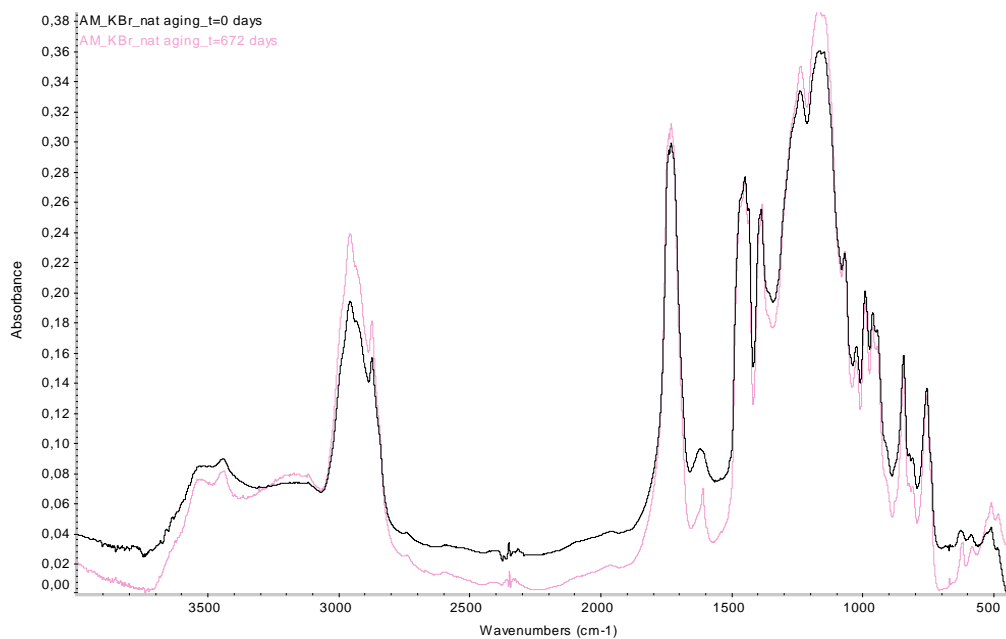


Figure 39. FT-IR spectra of *Acril ME* at the beginning and end of natural aging.

In particular, it is important to note that all the peaks intensities in the spectrum decrease to the same extent during the aging, allowing to suppose that the depolymerization is due to *chain-ends degradation* (a type of radicalic mechanism), i.e. it would occur through the successively release of the monomer units rather than only the lateral butyl groups.

Natural aging of Acril ME, on the contrary, induces spectral modifications strictly comparable with those observed during the thermal aging (Figure 39). Therefore, it is possible to identify the formation of γ -lactones and the cross-linking of radicals as the reactions responsible for polymer degradation.

As shown in Figure 40 and reported in Table 26, the spectrum of *Aquazol 500*, a tertiary amide, is characterized by a strong absorption peak at 1635 cm^{-1} attributed to the stretching of the amidic C=O bonds, by the stretching of the C-H bonds at 2980 , 2941 and 2878 cm^{-1} and by the peak at 1476 cm^{-1} , relative to the stretching of the C-N groups.

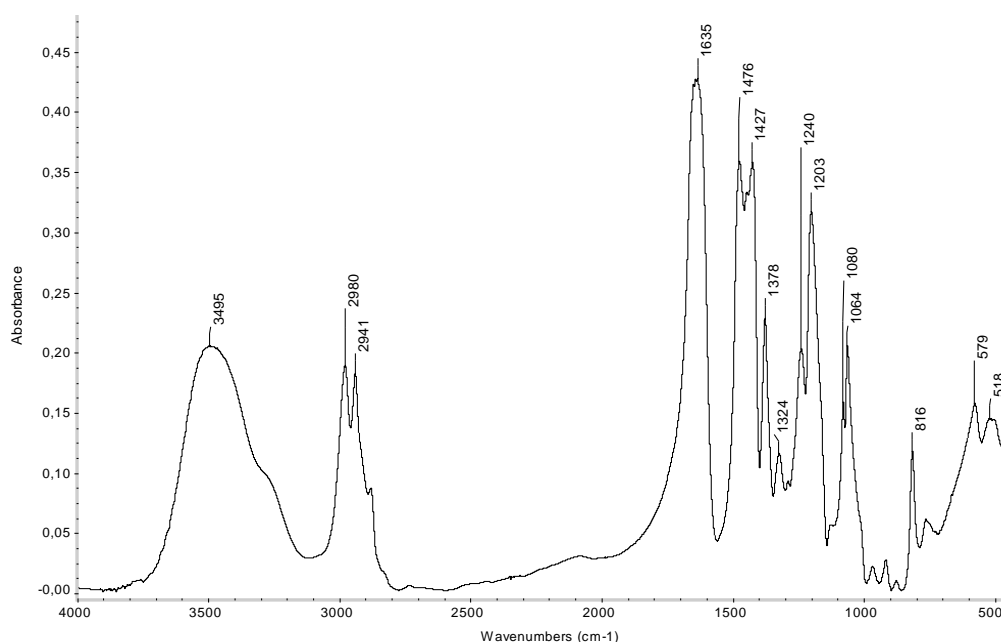


Figure 40. FT-IR spectrum of *Aquazol 500*.

Table 26. FT-IR absorptions peaks observed for *Aquazol 500*.

Wavenumber (cm^{-1})	Functional group	Assignments
3278	ν N-H	Amidic N-H
2980, 2941	ν C-H	Aliphatic bond
1635	ν C=O	Amidic C=O
1476	ν N-C	N-C(=O)-CH ₂ CH ₃

In addition, there are strong absorption peaks at 1427 , 1378 , 1203 , 1064 and 816 cm^{-1} attributed to methyl tosylate used as initiator in the polymerization process or to its hydrolysis product p-toluenesulfonic acid [37, 42, 106]. On the other hand, the broad signal at 3495 cm^{-1} is due to the solvent (water) retained in the dry film.

The isothermal degradation of *Aquazol 500* at 80°C (Figure 41) leads to the appearance of a shoulder at 1730 cm⁻¹, compatible with lactone groups (C=O stretching). Moreover, the new peak at 1540 cm⁻¹ (NH bending) together with the signals at 3078 and 3303 cm⁻¹ (NH stretching) can be attributed to a secondary amide. The lactone groups formed because of oxidation and the secondary amides deriving from depolymerization reactions have been identified as responsible for the reduction of solubility and molecular weight decrease observed by SEC analyses.

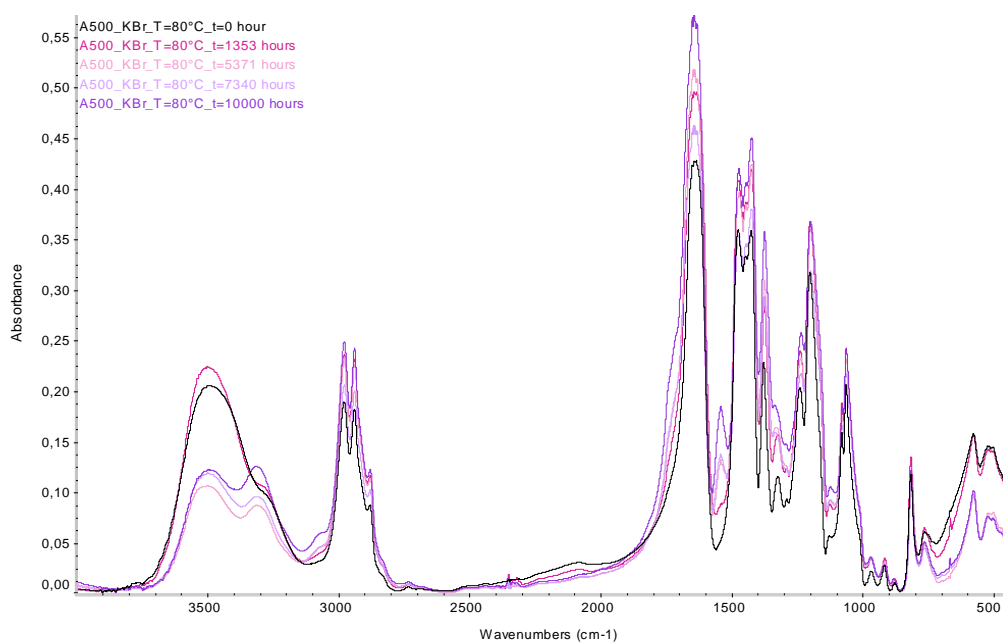


Figure 41. FT-IR spectra of *Aquazol 500* at increasing time of thermo-oxidative aging at 80°C.

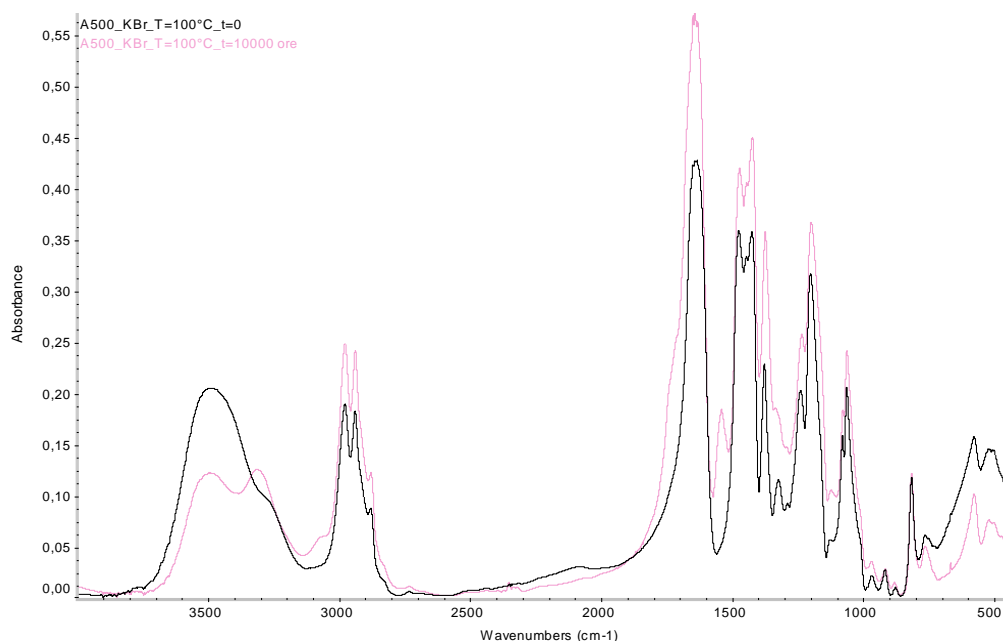


Figure 42. FT-IR spectra of *Aquazol 500* at the beginning and end of thermo-oxidative aging at 100°C.

Also the thermal degradations at 100, 120 and 140°C induced the same variations in the spectrum of Aquazol 500. However, as shown for example in Figure 42, a contemporary relevant decrease of the signal intensity of the more important peaks of the amides is also observed, suggesting that prolonged aging or aging at high temperatures favour cross-linking reaction rather than chain scission, in agreement with SEC results.

The photo-oxidative aging of *Aquazol 500* (Figure 43) induces a decrease and loss of resolution of all the polymer characteristic signals, and new peaks were not observed. Accordingly to the results of the SEC analyses, only depolymerization reactions are involved in the mechanism of photo-oxidative degradation.

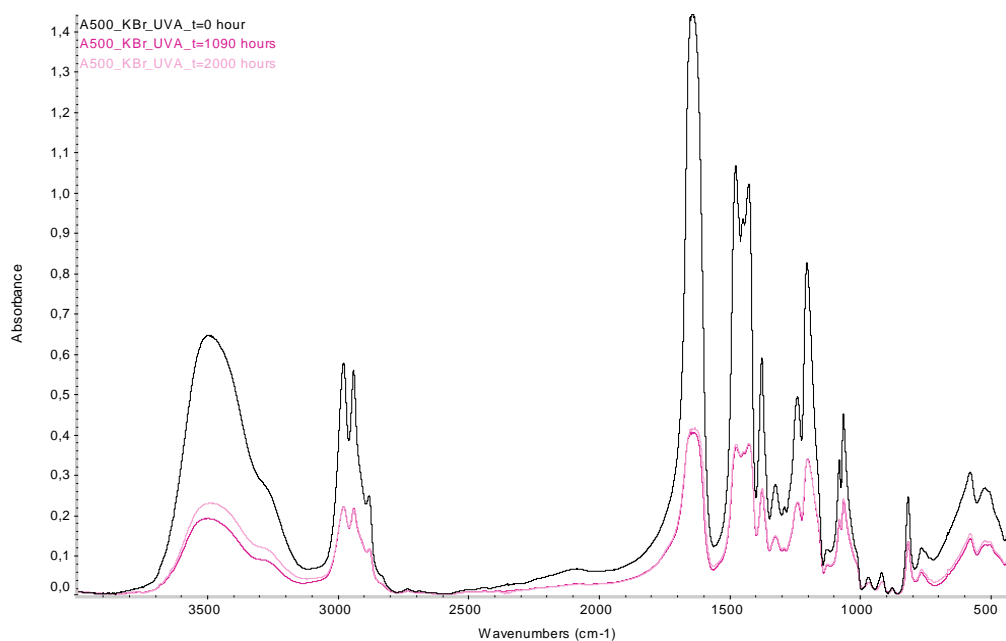


Figure 43. FT-IR spectra of *Aquazol 500* at increasing time of UVA photo-oxidative aging.

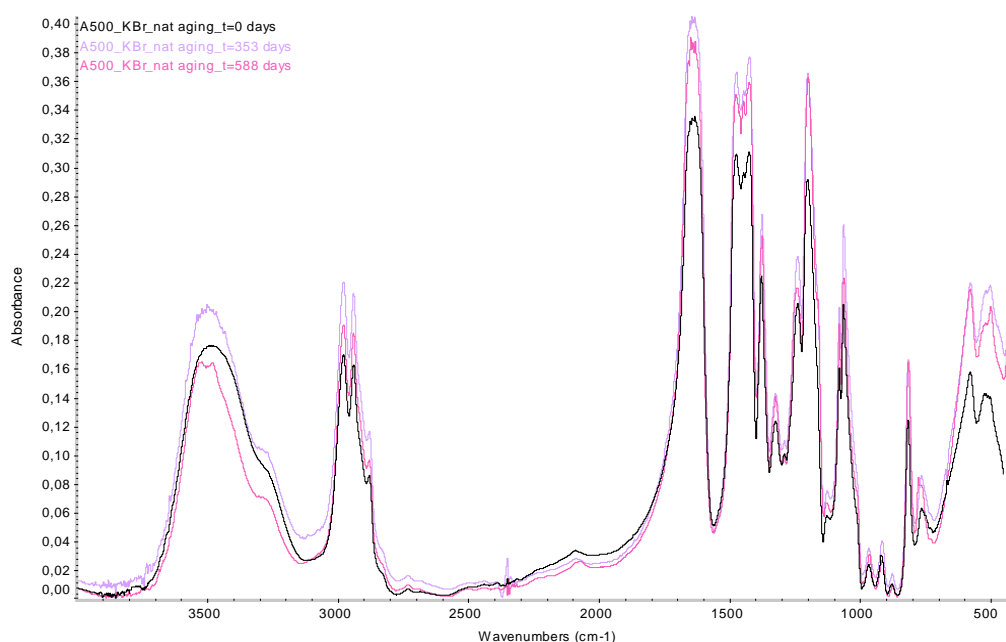


Figure 44. FT-IR spectra of *Aquazol 500* at increasing time of natural aging.

As reported for *Acril ME*, the natural aging of *Aquazol 500* (Figure 44) induces spectrum variations similar to those reported for the thermal-oxidative aging. Therefore, most probably the depolymerization mechanism forecast the loss of low molecular weight fractions, with the consequent formation of lactones groups and the conversion from tertiary to secondary amides.

The FT-IR spectrum of the sample of *Laropal A81* is reported in Figure 45, while the characteristic peaks and their interpretation, accordingly to Zhang Y. *et al.* [51a] are summarized in Table 27.

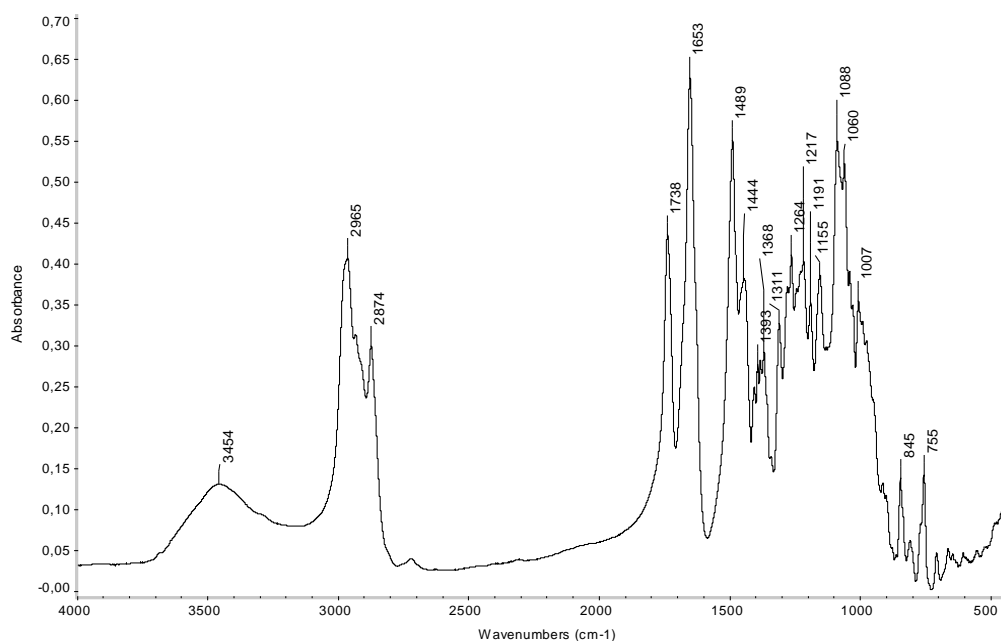


Figure 45. FT-IR spectrum of *Laropal A81*.

Table 27. FT-IR absorptions peaks observed for *Laropal A81*.

Wavenumber (cm^{-1})	Functional group	Assignments
3287	ν N-H	Amidic group
2965, 2936	ν C-H	Amidic group
2874	ν C-H	Aldehydic group
1738	ν C=O	Aldehydic group
1653	ν C=O	Amidic group
1393	δ -CH(CH ₃) ₂	
1368	δ -C(CH ₃) ₂	
1311	ν N-C	N-C(=O)-C-
1217, 1191	δ -C(CH ₃) ₂	carbon framework

The FT-IR spectrum of *Laropal A81* is dominated by the stretching vibration of C=O bonds (1653 cm^{-1}). This signal, together with the C-N stretching at 1311 cm^{-1} , is associated to the amide groups deriving from the α -ureidoalkylation reactions between urea and isobutyraldehyde. The absorption peak

at 1738 cm^{-1} and the relatively weak peak at 2874 cm^{-1} are instead assigned respectively to the stretching vibration modes of the C=O and C–H bonds in the aldehyde groups. The peaks at 1393 and 1368 cm^{-1} are assigned to the symmetric bending of C–H bonds in the $-\text{CH}(\text{CH}_3)_2$ and $-\text{C}(\text{CH}_3)_2$ groups, respectively. Moreover, the two peaks at 1217 and 1191 cm^{-1} are attributed to the bending of the $-\text{C}(\text{CH}_3)_2-$ groups in the framework and confirm the presence of gem-dimethyl structures. On the other hand, the broad band centred at 3454 cm^{-1} is ascribed to the stretching vibrations of the O–H groups involved in hydrogen-bonding interaction [107] while the weak peak at 3287 cm^{-1} is attributed to the stretching of N–H groups, due to the presence in the prepolymer of 1,3-bis-hydroxyisobutyl-urea, derived from side reaction between urea and isobutyraldehyde [108].

The isothermal degradation of *Laropal A81* at the two lowest temperatures (80 and 100°C) does not induce significant variations in the structure of the polymer, as shown for example in Figure 46. Only a slight reduction of the intensity of the peaks in the hydroxyl and aliphatic regions was observed.

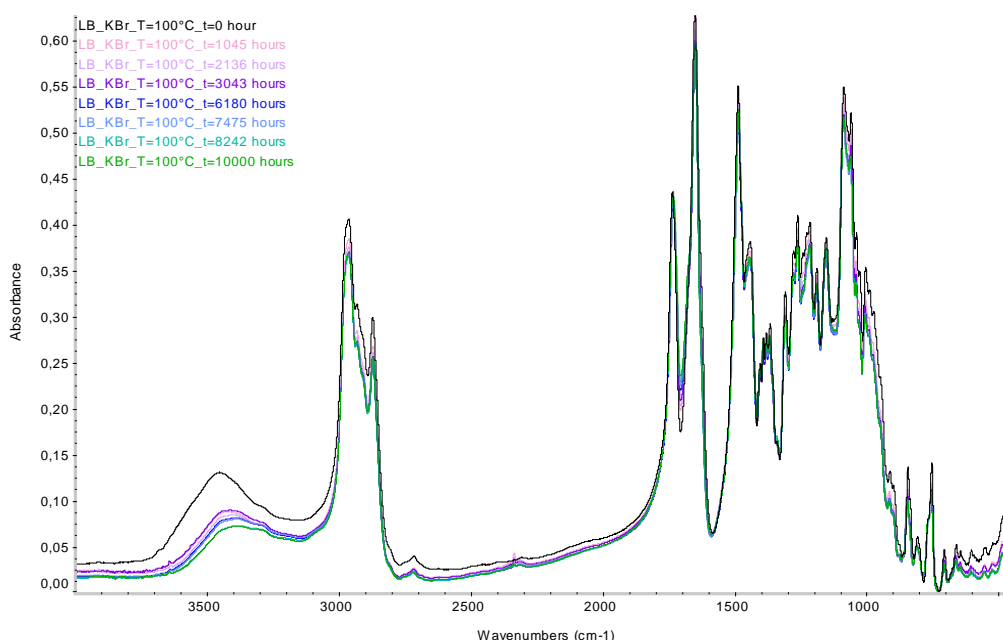


Figure 46. FT-IR spectra of *Laropal A81* at increasing time of thermo-oxidative aging at 100°C .

On the other hand, the prolonged aging at 120°C and the thermo-oxidative aging at 140°C lead to massive variations in the spectrum of *Laropal A81*. As shown for example in Figure 47 (purple curve), thermal degradation induced (since the first until 6000 hours of aging) spectral modification summarized as:

- disappearance of the peaks at 1653 and 1311 cm^{-1} , attributable to an overall change of the polymeric structure due to the loss of the amidic groups;
- disappearance of the peaks at 1393 and 1368 cm^{-1} , assigned to the symmetric bending of C–H bonds in the $-\text{CH}(\text{CH}_3)_2$ and $-\text{C}(\text{CH}_3)_2$ groups;
- appearance of new peaks at 1610 and 3137 cm^{-1} , attributed respectively to stretching vibrations of C=O and linked H-bonded OH groups.

Instead, for prolonged exposure to high temperature (pink curve in Figure 47), *Laropal A81* exhibited a completely loss of spectral resolution together with the disappearance of all the characteristic peaks of the polymer. Moreover, the appearance of new signals at 2969, 2930, 2860, 1732, 1687, and 1383 cm^{-1} was recorded, attributable to non-aromatic hydrocarbons compounds.

Therefore, the mechanism identified as responsible for thermal degradation of *Laropal A81* is depolymerization due to the progressive loss of low molecular weight fractions.

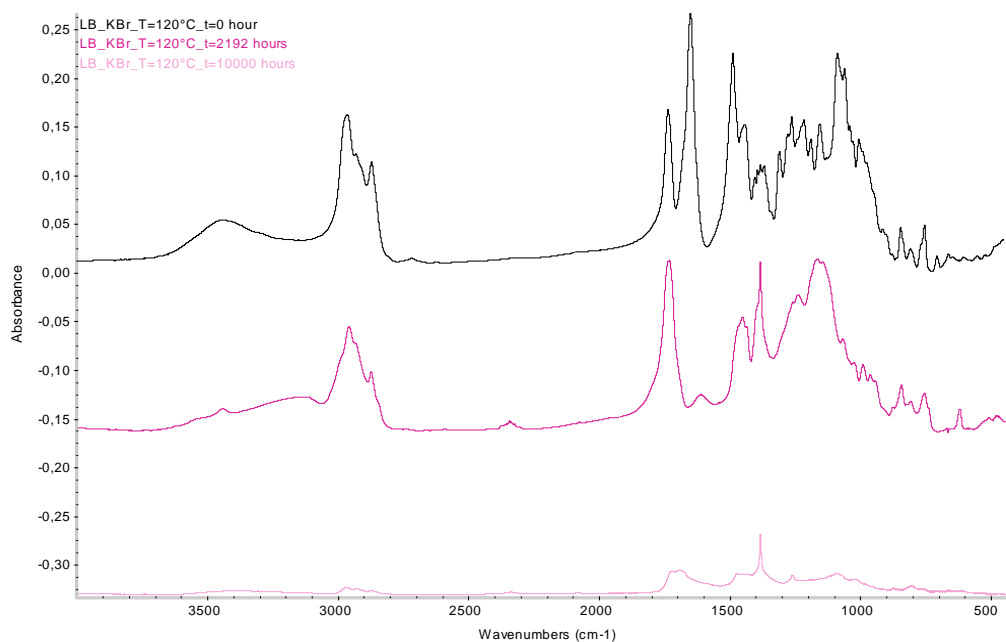


Figure 47. FT-IR spectra of *Laropal A81* at increasing time of thermo-oxidative aging at 120°C.

Conversely, the photo-oxidation under UVA radiation of *Laropal A81* revealed a high stability of the polymer with negligible variations in the intensity of the characteristic signals (Figure 48).

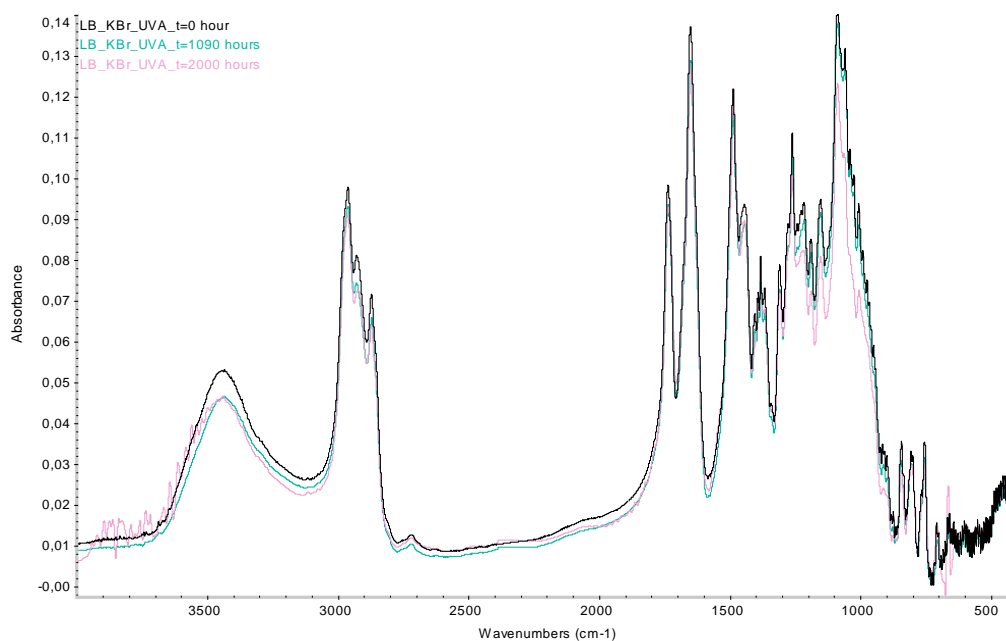


Figure 48. FT-IR spectra of *Laropal A81* at increasing time of UVA photo-oxidative aging.

Moreover, no changes were recorded also after two years of natural aging (Figure 49).

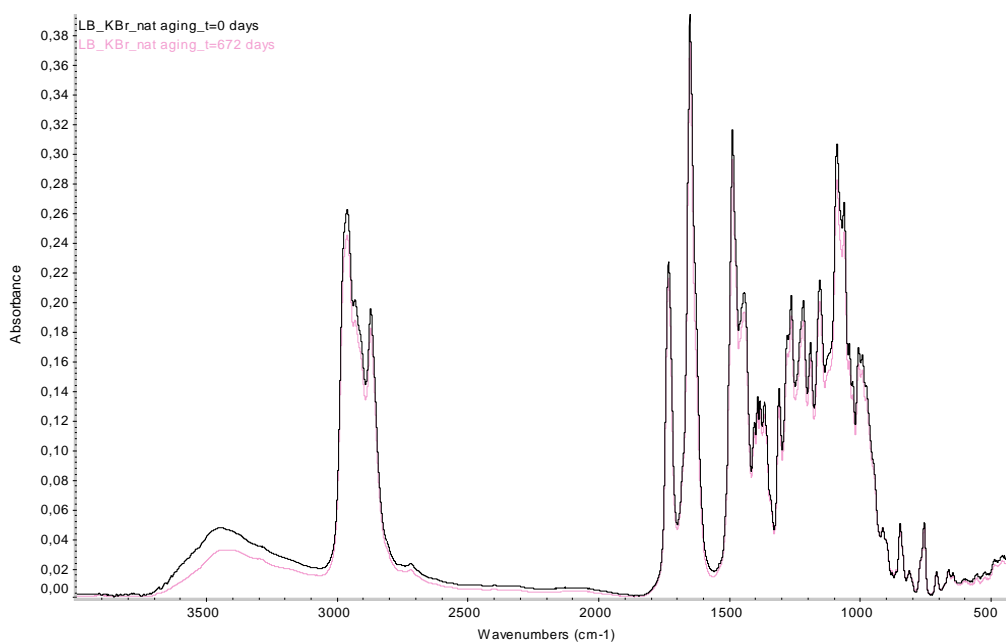


Figure 49. FT-IR spectra of *Laropal A81* at the beginning and end of natural aging.

The FT-IR spectrum of *Estel 1000* is shown in Figure 50, while the characteristic peaks and their interpretation are collected in Table 28. The spectrum of the sample is dominated by the peak at 1081 cm⁻¹ which, together with the signals at 1442, 1483, 2878 and 2930, cm⁻¹, has indicates the formation of a silica gel following the polymerization of the *TEOS*-based commercial product.

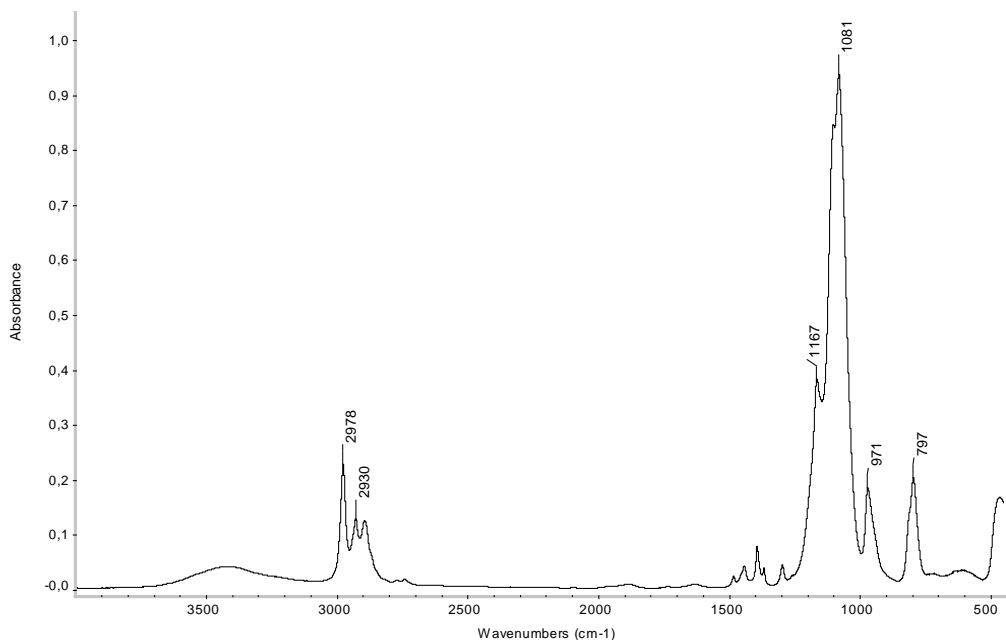


Figure 50. FT-IR spectra of *Estel 1000*.

Table 28. FT-IR absorptions peaks observed for *Estel 1000*.

Wavenumber (cm ⁻¹)	Functional group	Assignments
3414	ν O-H	Hydroxyl groups
2978, 2930, 2895	ν C-H	Aliphatic bond
1628	δ O-H	Hydroxyl groups
1483, 1442	δ C-H	Aliphatic bonds
1394	δ _s C-H	methyl group
1167	ρ C-H	methyl group
1099	ν Si-O-Si	Siloxane chain in linear structure
1081	ν Si-O-Si	Siloxane chain in cyclic structure

As shown for example in Figure 51 (purple curve), the isothermal and photo-UVA aging of *Estel 1000* induced firstly the loss of the ethylic fractions from the silica-gel network, observable mainly on the basis of the disappearance of the signals at 1394 and 1167 cm⁻¹, attributed respectively to the bending and the rocking of the C-H bonds in the lateral methyl groups.

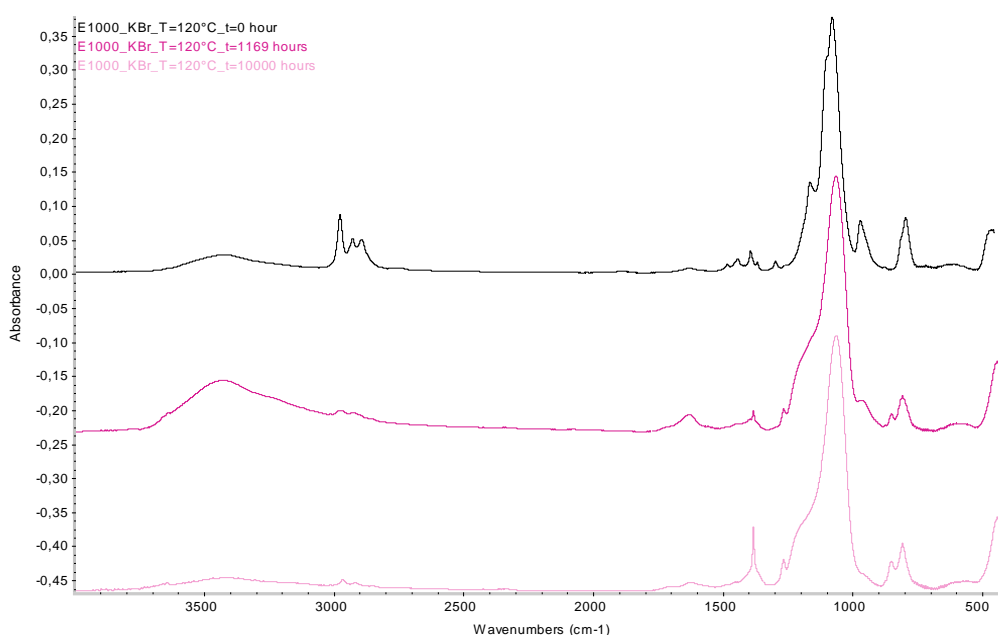


Figure 51. FT-IR spectra of *Estel 1000* at increasing thermo-aging at 120°C.

Nevertheless, for extended aging times a shift of the peak at 1081 towards 1062 cm⁻¹ was observed (pink curve in Figure 51). This spectral modification, together with the appearance of the peaks at 852 and 800 cm⁻¹, as well as the weak signal at 1260 cm⁻¹, suggest that the mechanism of thermal- and photo-degradation involved the formation of amorphous silica and silicone.

The same aging behaviour was observed also for the sample subjected to natural aging (Figure 52), allowing to suppose low stability of the inorganic *TEOS* consolidant.

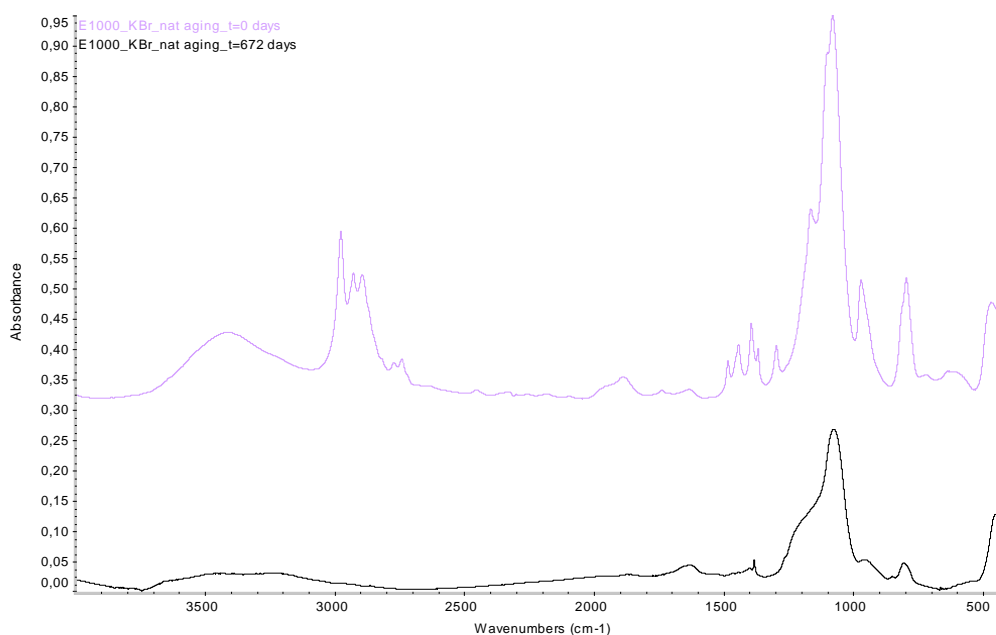


Figure 52. FT-IR spectra of *Estel 1000* at the beginning and end of natural aging.

On the other hand, the film obtained from the silica NPs *NanoEstel* exhibited high stability respect both thermal- and photo-aging as well as natural aging, showing no changes in the spectra of aged samples with respect to the fresh one. As shown in Figure 53, also for prolonged aging the spectrum of *NanoEstel* is dominated by the peaks at 1108 and 800 cm^{-1} , associated to amorphous silica. The only detected variation in the spectrum is the disappearance of the broad band centred at 3435 cm^{-1} , due to the retention of solvent (water) in the fresh dry film.

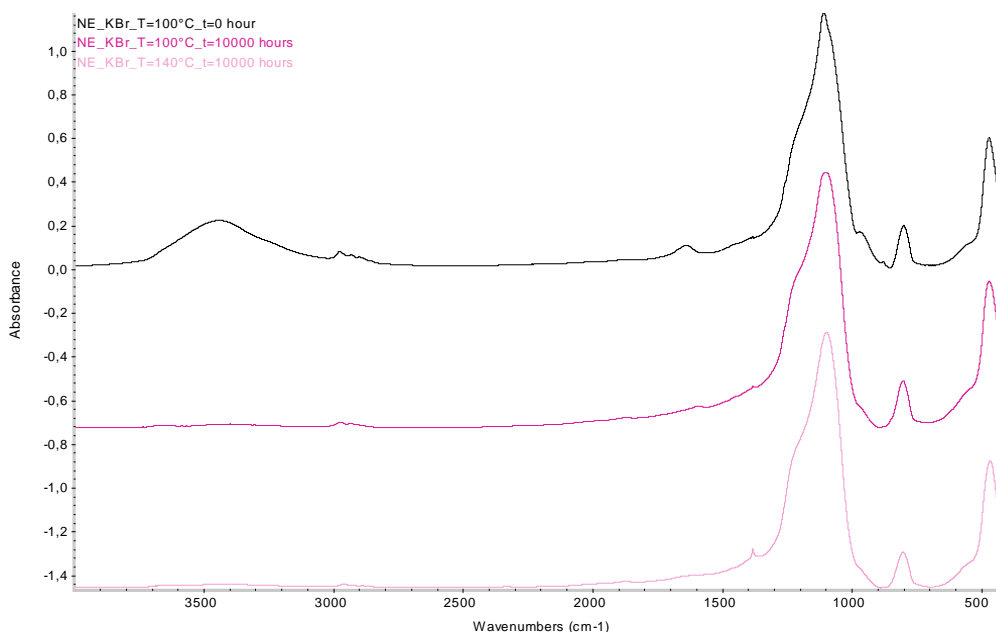


Figure 53. FT-IR spectra of *NanoEstel* at increasing time of thermo-oxidative aging at 100°C.

The spectrum of *NanoRestore* (black curve in Figure 54) is characterized by all the peaks of a basic carbonate, the most important being the stretching of the C=O bonds at 1625 cm^{-1} and the spike signal

at 3643 cm^{-1} , this last associated to the stretching vibration of the basic O-H bonds.

NanoRestore exhibited high stability towards both thermal- and photo-aging, as well as towards natural aging. No changes were in fact recorded in the FT-IR spectra of the samples after all the aging experiments. Therefore was observed that *NanoRestore* preserves its basic character also after prolonged aging at high temperature (curve purple in Figure 54), corroborating its use as alkaline reservoir for deacidification of wood [57b, 57c], paper and canvas [56a].

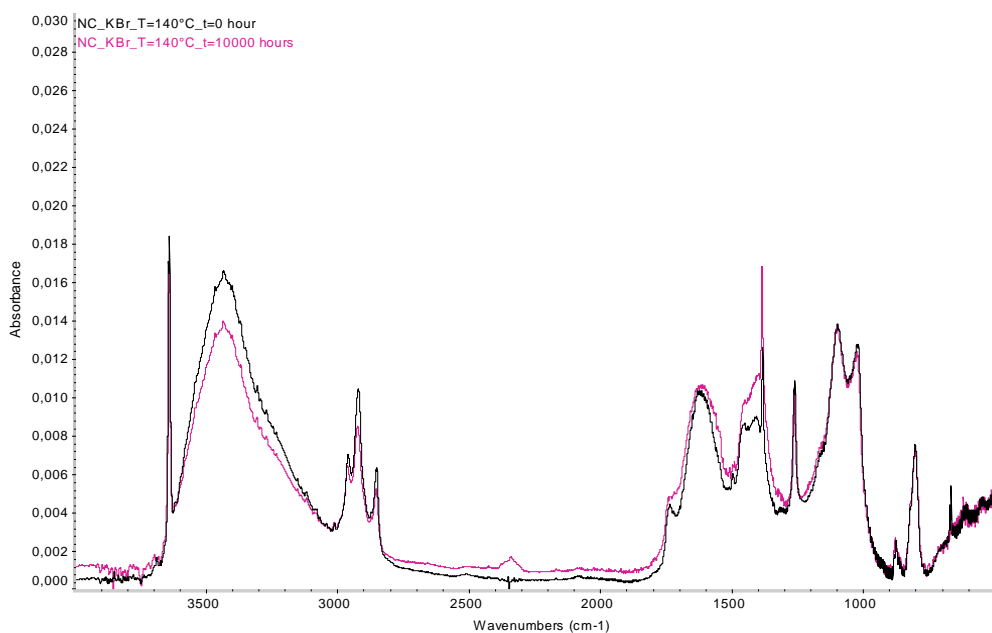


Figure 54. FT-IR spectra of *NanoRestore* at the beginning and end of thermo-oxidative aging at 140°C.

8.8 Photoluminescence measurements

The phenomenon of luminescence in lanthanide complexes is due to intra-energy conversion from the ligand singlet to the triplet, and then to the excited state of the central lanthanide ion followed by narrowband $f-f^*$ electronic transitions. The influence of the ligands and of the matrices in the luminescence behaviour of lanthanide-based materials was extensively studied [690, 109]. However, for the best of knowledge, the photoluminescence behaviours of the complexes $\text{Ln}(\text{NO}_3)_3(\text{phen})_2$ ($\text{Ln}=\text{Eu}$; Tb) dispersed in matrices useful for conservation practice, have not yet been investigated.

Analyses have been carried out on pure complexes and doped matrices as well as on selected aged (UVA $\lambda=254$ nm, $T=28 \pm 2^\circ\text{C}$, $\text{UR}=45\%$, up to 1200 hours) samples.

The photoluminescence emission ($\lambda_{\text{ex}}=292$ nm) and excitation spectra ($\lambda_{\text{em}}=615$ nm) of the pure $\text{Eu}(\text{NO}_3)_3(\text{phen})_2$ complex were collected at room temperature and are reported in Figure 55. PL, PLE, lifetime (τ) and quantum yield (Q_i) data are reported in Table 29, where the intensity ratio of the individual $^5\text{D}_0-^7\text{F}_j$ transition in the PL spectra is also provided.

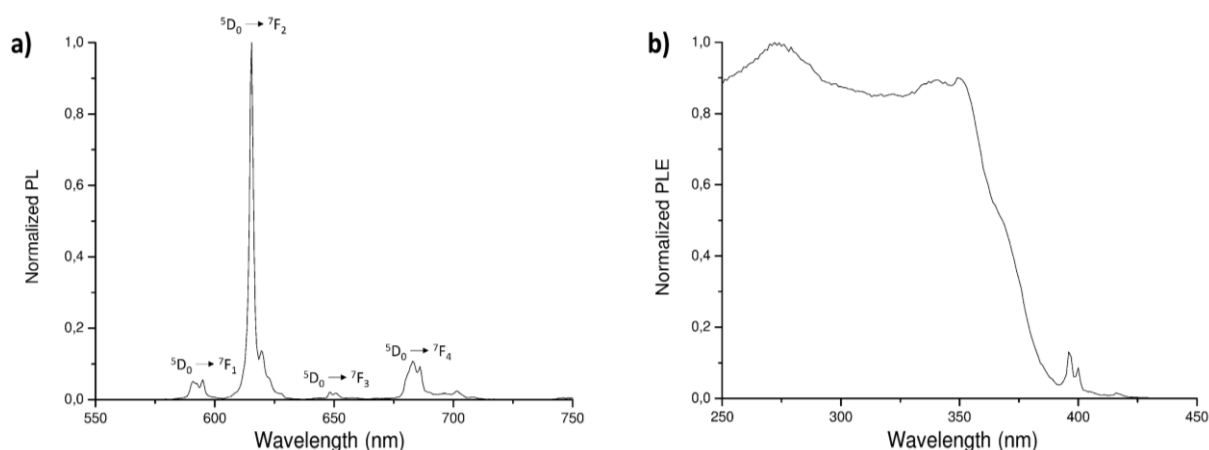


Figure 55. Normalized (a) PL ($\lambda_{\text{ex}}=292$ nm) and (b) PLE ($\lambda_{\text{em}}=615$ nm) spectra of $\text{Eu}(\text{NO}_3)_3(\text{phen})_2$ complex.

Table 29. PL ($\lambda_{\text{ex}}=292$ nm, 298 K, nm), PLE ($\lambda_{\text{em}}=615$ nm, 298 K, nm), luminescent lifetime ($\lambda_{\text{ex}}=292$ nm, $\lambda_{\text{em}}=615$ nm, 298 K, nm) and Q_i data of pure $\text{Eu}(\text{NO}_3)_3(\text{phen})_2$ complex.

	PL data ($\lambda_{\text{ex}}=292$ nm, 298 K, nm): 591, 595 ($^5\text{D}_0-^7\text{F}_1$, 8%); 615, 620, 623, 628 ($^5\text{D}_0-^7\text{F}_2$, 67%); 648, 650 ($^5\text{D}_0-^7\text{F}_3$, 3%); 683, 686, 690, 702 ($^5\text{D}_0-^7\text{F}_4$, 22%).
<i>Eu(NO₃)₃(phen)₂</i>	PLE data ($\lambda_{\text{em}}=615$ nm, 298 K, nm): $\lambda < 385$ (max at 274); 396, 400 (Eu^{3+} excitation).
	Luminescent lifetime ($\lambda_{\text{ex}}=292$ nm, $\lambda_{\text{em}}=615$ nm, 298 K): $\tau = 1.24$ ms.
	$Q_i = 77\%$.
	Chromaticity coordinates: $x=0.664$; $y=0.336$.

The emission spectrum of pure $\text{Eu}(\text{NO}_3)_3(\text{phen})_2$ complex is dominated by the $^5\text{D}_0-^7\text{F}_2$ transition centred at 615 nm. Excitation at 350 nm instead of 292 nm did not cause any meaningful variation.

The excitation spectrum (PLE) of pure $\text{Eu}(\text{NO}_3)_3(\text{phen})_2$ complex was collected using $\lambda_{\text{em}}=615$ nm. A broad band in the near UV region ($\lambda < 385$ nm) with maximum at 274 nm was recorded, associated to the

excitation of the ligand. In the PLE spectrum can be also detected peaks at 396 and 400 nm associated to the direct excitation of the Eu(III) trivalent ion.

The luminescence lifetime (τ) of pure $\text{Eu}(\text{NO}_3)_3(\text{phen})_2$ is 1.24 ms (Figure 56a), and an intrinsic quantum yield (Q_i) around 77% was calculated.

The chromaticity coordinates x and y were estimated from the PL spectrum of the pure $\text{Eu}(\text{NO}_3)_3(\text{phen})_2$ complex and are, respectively, 0.664 and 0.336. As observable from the chromaticity diagram in Figure 56b, these coordinates correspond to a red-orange dye with colour purity close to 1.00.

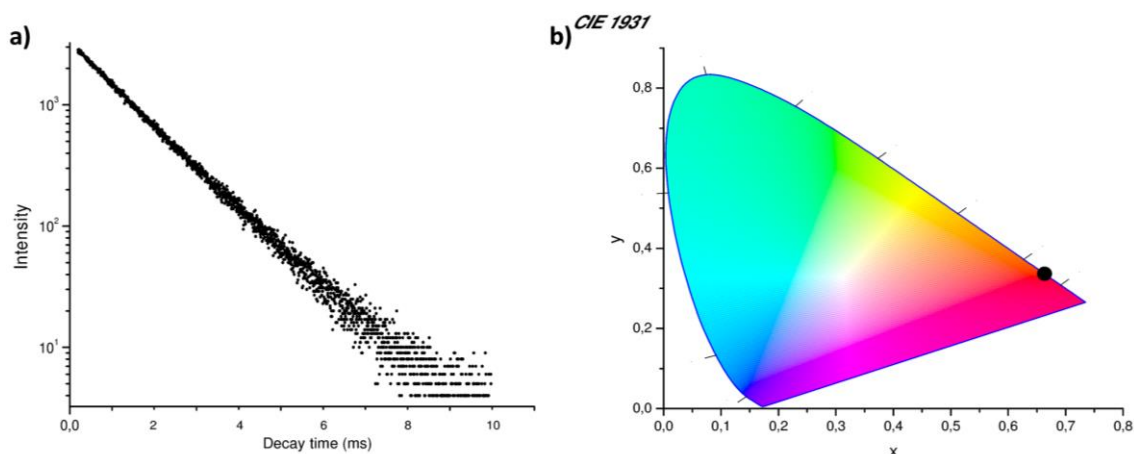


Figure 56. (a) Luminescence decay curve ($\lambda_{\text{ex}}=292$ nm, $\lambda_{\text{em}}=615$ nm) of pure $\text{Eu}(\text{NO}_3)_3(\text{phen})_2$ complex; (b) Chromaticity diagram of pure $\text{Eu}(\text{NO}_3)_3(\text{phen})_2$ complex.

The IR solid-state spectrum of pure $\text{Eu}(\text{NO}_3)_3(\text{phen})_2$ complex is reported in Figure 57. According to the literature [76], the FT-IR spectrum shows the C=N stretching at 1627 cm^{-1} , and two intense absorptions associated to the N=O and O-N-O asymmetric stretching of $\kappa^2\text{-NO}_3$ at 1498 and 1314 cm^{-1} respectively.

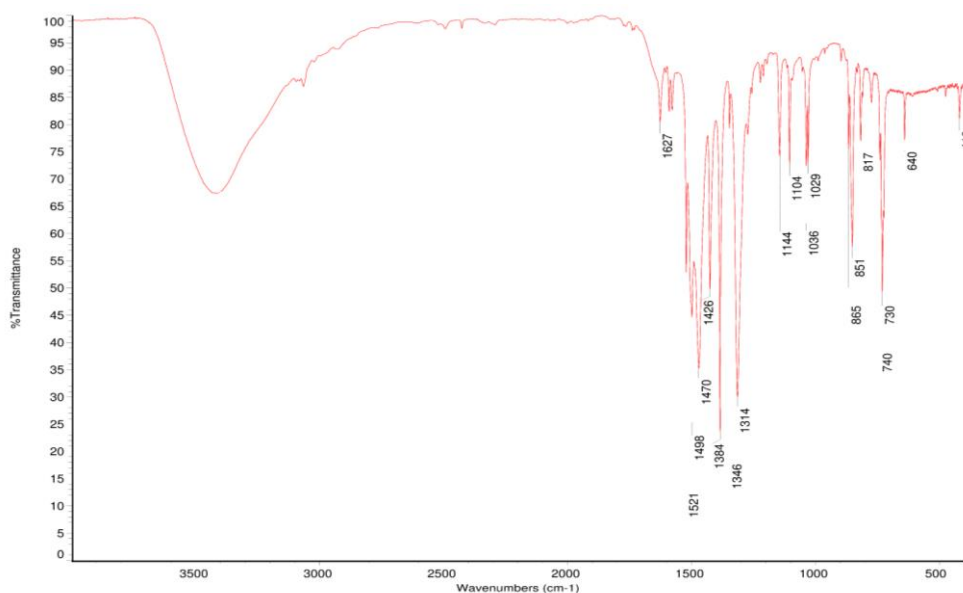
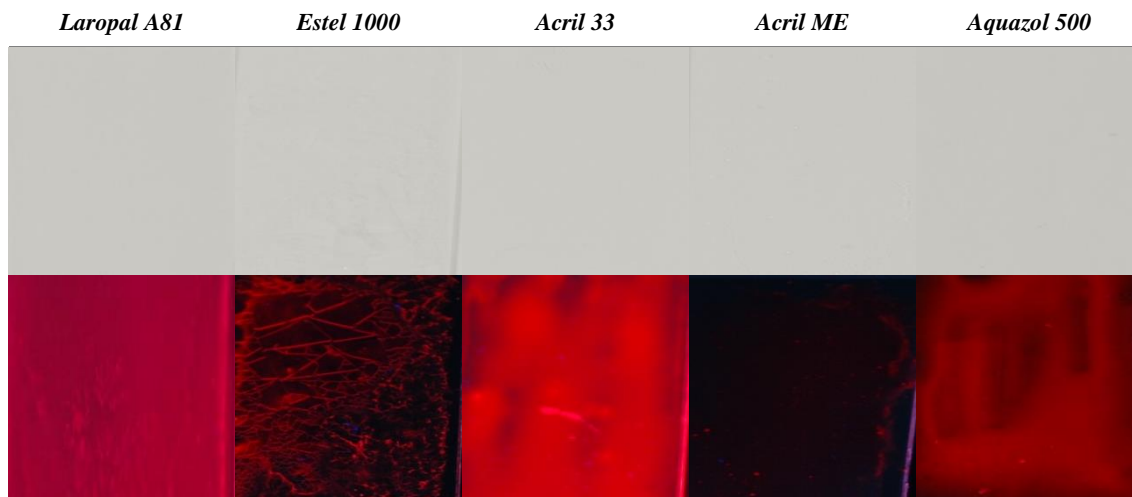


Figure 57. FT-IR solid-state spectrum of pure $\text{Eu}(\text{NO}_3)_3(\text{phen})_2$ complex.

The luminescence properties of trivalent europium complexes dispersed in polymer and inorganic matrices were intensively investigated [110]. However, a direct comparison of the luminescence yields can be done only among systems showing the same PL and PLE spectra of the pure complex.

Samples containing $\text{Eu}(\text{NO}_3)_3(\text{phen})_2$ have been prepared by adding weighted amounts (from 0 to 10% w/w) of the complex to the consolidants or binder materials *Acril 33* (AC), *Acril Me* (ME), *Aquazol 500* (A500), *Laropal A81* (LB), *Estel 1000* (E1000) and *NanoEstel* (NE). These matrices have been chosen to investigate the effects of different chemical structures on the photoluminescence behaviour of the pure complex. High luminescence was observed, in most of the cases, for concentration of the dopant of the 0.25% w/w. Therefore, for comparative purpose, was decided to evaluate the luminescence characteristics of coatings obtained adding 0.25% w/w of europium complex to each matrix. Table 30 reports the pictures of the samples of $\text{Eu}(\text{NO}_3)_3(\text{phen})_2$ -doped films (0.25% w/w) under visible and UV ($\lambda_{\text{ex}}=254$ nm) light.

Table 30. Samples of $\text{Eu}(\text{NO}_3)_3(\text{phen})_2$ -doped films (0.25% w/w) under visible (above) and UV (below, $\lambda_{\text{ex}}=254$ nm) light.



The photoluminescence emission and excitation spectra of doped films have been recorded and are collected in Figures 58 and 59, respectively.

In the samples where *Laropal A81* and *Estel 1000* have been used as matrices the PL spectra are strictly comparable to those reported above for the pure compound, as also observable from the data collected in Table 31. The luminescence of Eu(III) is in all the cases dominated by the $^5\text{D}_0\text{-}^7\text{F}_2$ transition centred at 615 nm. This indicates that no meaningful interaction between $\text{Eu}(\text{NO}_3)_3(\text{phen})_2$ and the matrices occurs or that the site symmetry of the lanthanide centre is maintained with respect to the pure compound [111].

The radiative lifetimes (τ) collected for *Laropal A81* and *Estel 1000* matrices (see Figure 60 for the decay curves) are strictly comparable with that of the pure complex $\text{Eu}(\text{NO}_3)_3(\text{phen})_2$, with variations below 10%. These results agree with the negligible changes in the PL spectra described above. The lower values obtained for the intrinsic quantum yields of these doped matrices with respect to the pure dopant can be attributed to the different refractive index of the two binders/consolidants.

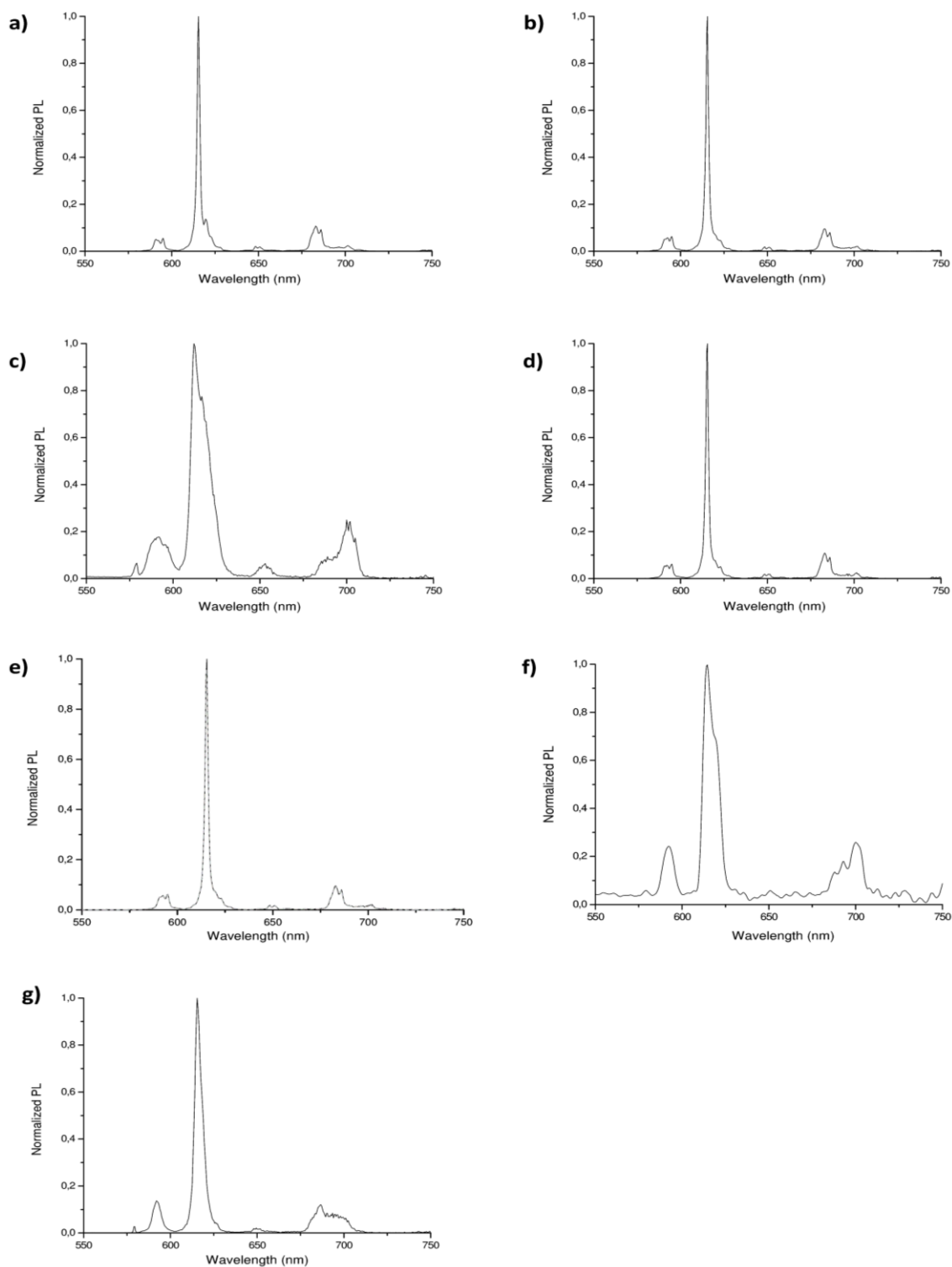


Figure 58. Normalized PL spectra (298 K, $\lambda_{ex}=292$ nm) of europium-based (0.25% w/w) samples. (a) $\text{Eu}(\text{NO}_3)_3(\text{phen})_2$; (b) $\text{LB_Eu}(\text{NO}_3)_3(\text{phen})_2$; (c) $\text{NE_Eu}(\text{NO}_3)_3(\text{phen})_2$; (d) $\text{E1000_Eu}(\text{NO}_3)_3(\text{phen})_2$; (e) $\text{AC_Eu}(\text{NO}_3)_3(\text{phen})_2$; (f) $\text{AM_Eu}(\text{NO}_3)_3(\text{phen})_2$; (g) $\text{A500_Eu}(\text{NO}_3)_3(\text{phen})_2$.

On the other hand, the use of *Acril 33*, *Acril Me*, *Aquazol 500* and *NanoEstel* matrices caused relevant changes in the emission and excitation spectra. One of the main changes detected is, in the PL spectrum of the nanosilica doped matrix ($\text{NE_Eu}(\text{NO}_3)_3(\text{phen})_2$), the drop of the relative intensity of the hypersensitive ${}^5\text{D}_0$ - ${}^7\text{F}_2$ transition between 615 to 612 nm. This suggests an increase of symmetry of the inner coordination sphere of the Eu(III) centre [111].

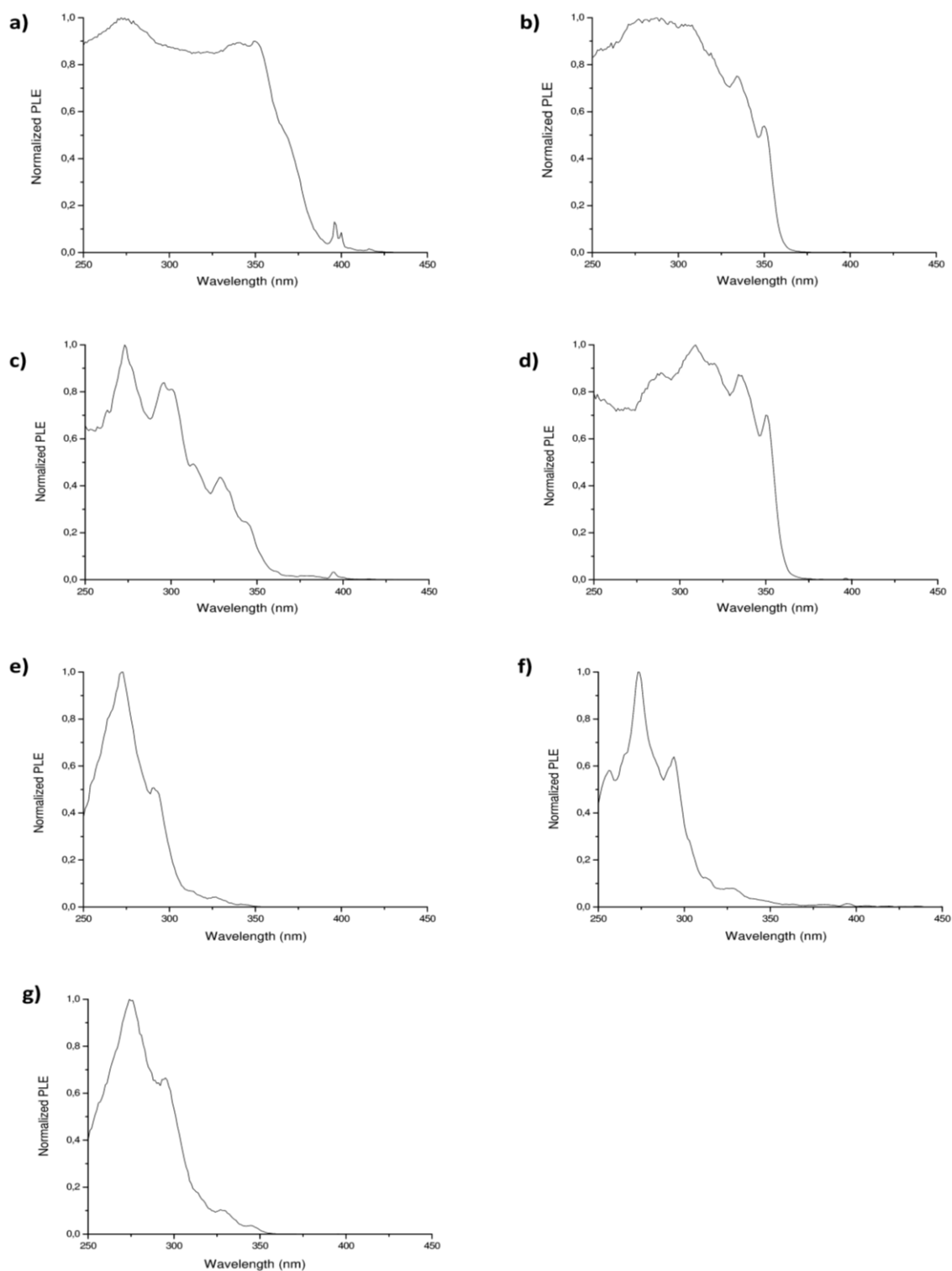


Figure 59. Normalized PLE spectra (298 K, $\lambda_{em}=615$ nm) of europium-based (0.25% w/w) samples. (a) $\text{Eu}(\text{NO}_3)_3(\text{phen})_2$; (b) $\text{LB_Eu}(\text{NO}_3)_3(\text{phen})_2$; (c) $\text{NE_Eu}(\text{NO}_3)_3(\text{phen})_2$; (d) $\text{E1000_Eu}(\text{NO}_3)_3(\text{phen})_2$; (e) $\text{AC_Eu}(\text{NO}_3)_3(\text{phen})_2$; (f) $\text{AM_Eu}(\text{NO}_3)_3(\text{phen})_2$; (g) $\text{A500_Eu}(\text{NO}_3)_3(\text{phen})_2$.

Chromaticity changes of pure $\text{Eu}(\text{NO}_3)_3(\text{phen})_2$ once dispersed in different matrices were evaluated. The chromaticity coordinates x and y reported in Table 31 highlight scarce variations in the colorimetric parameters, despite the changes in PL spectra above observable for most of the matrices.

Table 31. PL ($\lambda_{\text{ex}}=292$ nm, 298 K, nm), PLE ($\lambda_{\text{em}}=615$ nm, 298 K, nm), luminescent lifetime ($\lambda_{\text{ex}}=292$ nm, $\lambda_{\text{em}}=615$ nm, 298 K, nm) and Q_i data of europium-based (0.25% w/w) films.

<i>Eu(NO₃)₃(phen)₂</i>	<p>PL data ($\lambda_{\text{ex}}=292$ nm, 298 K, nm): 591, 595 (⁵D₀₋₇F₁, 8%); 615, 620, 623, 628 (⁵D₀₋₇F₂, 67%); 648, 650 (⁵D₀₋₇F₃, 3%); 683, 686, 690, 702 (⁵D₀₋₇F₄, 22%).</p> <p>PLE data ($\lambda_{\text{em}}=615$ nm, 298 K, nm): $\lambda < 385$ (max at 274); 396, 400 (Eu³⁺ excitation).</p> <p>Luminescent lifetime ($\lambda_{\text{ex}}=292$ nm, $\lambda_{\text{em}}=615$ nm, 298 K): $\tau = 1.24$ ms.</p> <p>$Q_i=77\%$.</p> <p>Chromaticity coordinates: $x=0.664$; $y=0.336$.</p>
<i>LB_Eu(NO₃)₃(phen)₂</i>	<p>PL data ($\lambda_{\text{ex}}=292$ nm, 298 K, nm): 590, 592, 595 (⁵D₀₋₇F₁, 10%); 615, 620, 623, 628 (⁵D₀₋₇F₂, 66%); 648, 651 (⁵D₀₋₇F₃, 3%); 683, 686, 702 (⁵D₀₋₇F₄, 21%).</p> <p>PLE data ($\lambda_{\text{em}}=615$ nm, 298 K, nm): $\lambda < 308$; 319, 335, 350, 396 (Eu³⁺ excitation).</p> <p>Luminescent lifetime ($\lambda_{\text{ex}}=292$ nm, $\lambda_{\text{em}}=615$ nm, 298 K): $\tau = 1.14$ ms.</p> <p>$Q_i=60\%$.</p> <p>Chromaticity coordinates: $x=0.660$; $y=0.340$.</p>
<i>NE_Eu(NO₃)₃(phen)₂</i>	<p>PL data ($\lambda_{\text{ex}}=292$ nm, 298 K, nm): 579 (⁵D₀₋₇F₀, 2%); 587, 589, 591, 595, 597 (⁵D₀₋₇F₁, 13%); 612, 616, 619, 623 (⁵D₀₋₇F₂, 64%); 650, 653, 654, 656 (⁵D₀₋₇F₃, 4%); 687, 700, 702, 705 (⁵D₀₋₇F₄, 17%).</p> <p>PLE data ($\lambda_{\text{em}}=615$ nm, 298 K, nm): 273, 295, 301, 313, 328, 344, 395 (Eu³⁺ excitation).</p> <p>Luminescent lifetime ($\lambda_{\text{ex}}=292$ nm, $\lambda_{\text{em}}=615$ nm, 298 K): $\tau = 0.60$ ms.</p> <p>$Q_i=22\%$.</p> <p>Chromaticity coordinates: $x=0.651$; $y=0.349$.</p>
<i>E1000_Eu(NO₃)₃(phen)₂</i>	<p>PL data ($\lambda_{\text{ex}}=292$ nm, 298 K, nm): 591, 593, 595 (⁵D₀₋₇F₁, 8%); 615, 620, 623, 628 (⁵D₀₋₇F₂, 67%); 648, 650, 652 (⁵D₀₋₇F₃, 3%); 683, 686, 690, 701, 702 (⁵D₀₋₇F₄, 22%).</p> <p>PLE data ($\lambda_{\text{em}}=615$ nm, 298 K, nm): $\lambda < 321$ (max at 308); 334, 336, 350, 396 (Eu³⁺ excitation).</p> <p>Luminescent lifetime ($\lambda_{\text{ex}}=292$ nm, $\lambda_{\text{em}}=615$ nm, 298 K): $\tau = 1.18$ ms.</p> <p>$Q_i=65\%$.</p> <p>Chromaticity coordinates: $x=0.661$; $y=0.339$.</p>
<i>AC_Eu(NO₃)₃(phen)₂</i>	<p>PL data ($\lambda_{\text{ex}}=292$ nm, 298 K, nm): 580 (⁵D₀₋₇F₀, 1%); 590, 591, 593 (⁵D₀₋₇F₁, 11%); 615, 620 (⁵D₀₋₇F₂, 65%); 650 (⁵D₀₋₇F₃, 2%); 687, 695, 700 (⁵D₀₋₇F₄, 21%).</p> <p>PLE data ($\lambda_{\text{em}}=615$ nm, 298 K, nm): 272, 290, 293, 313, 326, 342 (Eu³⁺ excitation).</p> <p>Luminescent lifetime ($\lambda_{\text{ex}}=292$ nm, $\lambda_{\text{em}}=615$ nm, 298 K): $\tau = 1.20$ ms.</p> <p>$Q_i=56\%$.</p> <p>Chromaticity coordinates: $x=0.646$; $y=0.345$.</p>
<i>AM_Eu(NO₃)₃(phen)₂</i>	<p>PL data ($\lambda_{\text{ex}}=292$ nm, 298 K, nm): 580 (⁵D₀₋₇F₀, 7%); 592 (⁵D₀₋₇F₁, 12%); 615, 618, 620, 631, 635 (⁵D₀₋₇F₂, 51%); 646, 650, 654 (⁵D₀₋₇F₃, 5%); 686, 693, 700, 701, 703 (⁵D₀₋₇F₄, 25%).</p> <p>PLE data ($\lambda_{\text{em}}=615$ nm, 298 K, nm): 256, 265, 273, 294, 313, 328, 346, 396 (Eu³⁺ excitation).</p> <p>Luminescent lifetime ($\lambda_{\text{ex}}=292$ nm, $\lambda_{\text{em}}=615$ nm, 298 K): $\tau = 1.25$ ms.</p> <p>$Q_i=49\%$.</p> <p>Chromaticity coordinates: $x=0.632$; $y=0.368$.</p>
<i>A500_Eu(NO₃)₃(phen)₂</i>	<p>PL data ($\lambda_{\text{ex}}=292$ nm, 298 K, nm): 579 (⁵D₀₋₇F₀, 1%); 590, 592 (⁵D₀₋₇F₁, 10%); 615, 620, 627 (⁵D₀₋₇F₂, 65%); 648, 649, 652 (⁵D₀₋₇F₃, 3%); 687, 690, 693, 698 (⁵D₀₋₇F₄, 21%).</p> <p>PLE data ($\lambda_{\text{em}}=615$ nm, 298 K, nm): 275, 295, 313, 328, 345 (Eu³⁺ excitation).</p> <p>Luminescent lifetime ($\lambda_{\text{ex}}=292$ nm, $\lambda_{\text{em}}=615$ nm, 298 K): $\tau = 0.76$ ms.</p> <p>$Q_i=38\%$.</p> <p>Chromaticity coordinates: $x=0.660$; $y=0.340$.</p>

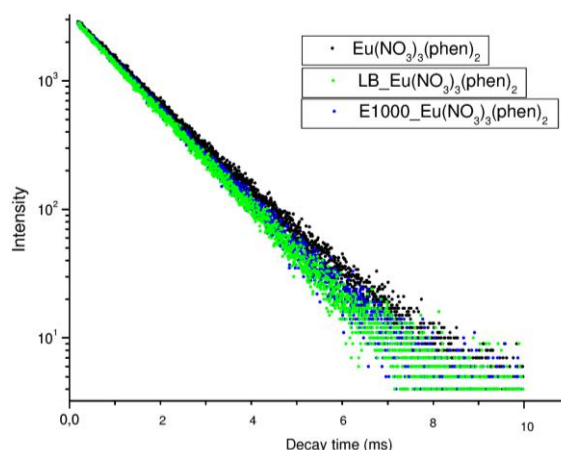


Figure 60. Comparison between the luminescence decay curves ($\lambda_{\text{ex}}=292$ nm, $\lambda_{\text{em}}=615$ nm) of pure $\text{Eu}(\text{NO}_3)_3(\text{phen})_2$ complex (black), $\text{LB_Eu}(\text{NO}_3)_3(\text{phen})_2$ (green) and $\text{E1000_Eu}(\text{NO}_3)_3(\text{phen})_2$ (blue).

Although the PL spectra of Tb(III) are less informative about changes of the coordination sphere around this metal ion with respect to Eu(III), the closely similar chemistry of the two trivalent lanthanide ions allows to suppose comparable behaviour of the corresponding complexes. Also in this case, for comparative purpose, was decided to evaluate the luminescence behaviour of the coatings obtained adding 0.25% w/w of terbium complex to each matrix.

The photoluminescence emission ($\lambda_{\text{ex}}=292$ nm, 298 K) and excitation ($\lambda_{\text{em}}=544$ nm) spectra of the pure $\text{Tb}(\text{NO}_3)_3(\text{phen})_2$ complex were collected and are reported in Figure 61. PL, PLE, τ and Q_i data are collected in Table 32.

The emission spectrum (Figure 61a) of the pure $\text{Tb}(\text{NO}_3)_3(\text{phen})_2$ complex is dominated by the $^5\text{D}_4 \rightarrow ^7\text{F}_5$ transition centred at 544 nm. The PL spectrum was collected also in this case using $\lambda_{\text{ex}}=350$ nm, showing no meaningful changes. The excitation spectrum of pure $\text{Tb}(\text{NO}_3)_3(\text{phen})_2$ complex was collected at λ_{em} of 544 nm (298 K). As observable in Figure 62b, the excitation range of the ligands useful for Tb(III) emission is the UV region ($\lambda < 380$ nm) with maximum at 270 nm.

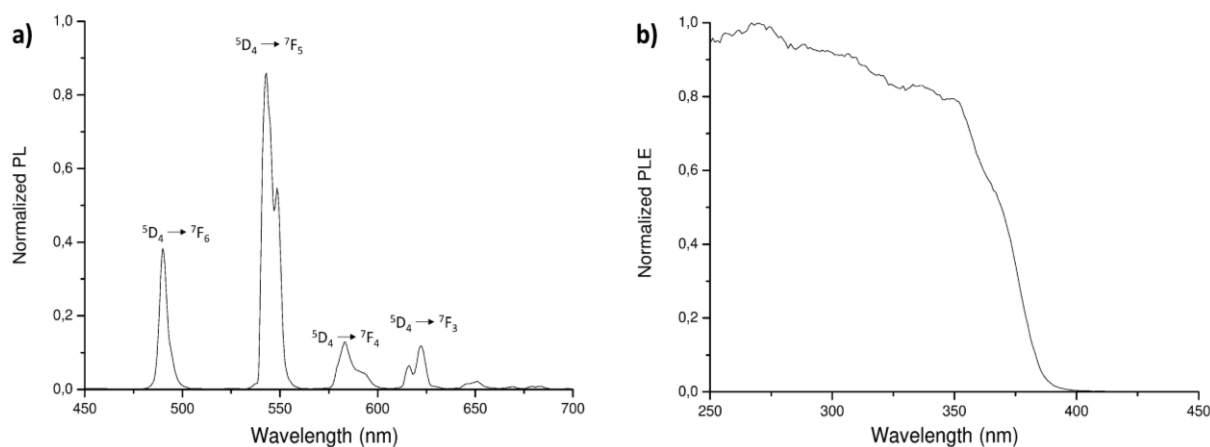


Figure 61. Normalized (a) PL ($\lambda_{\text{ex}}=292$ nm) and (b) PLE ($\lambda_{\text{em}}=544$ nm) spectra of $\text{Tb}(\text{NO}_3)_3(\text{phen})_2$ complex.

The luminescent lifetime (τ) is 0.14 ms at room temperature, about one order of magnitude lower than the typical values for strongly emitting terbium complexes and corresponds to an intrinsic quantum yield

(Q_i) of 3% on the basis of the equation $Q_i = \tau/4.75$ [95]. This result was expected because it is known that the sensitization of Tb(III) by 1,10-phenanthroline is lower with respect to Eu(III) because of the closeness of the 5D_4 resonance level and phenanthroline triplet state.

The chromaticity coordinates x and y were estimated from the PL spectrum of pure $Tb(NO_3)_3(phen)_2$ and are, respectively, 0.336 and 0.593. As can be seen in the chromaticity diagram in Figure 62, these colorimetric coordinates correspond to a bright green dye.

Despite the quite poor luminescent features of $Tb(NO_3)_3(phen)_2$, appreciable photoluminescence was observed for the complex dispersed in different matrices. In Table 33 are shown the pictures of the $Tb(NO_3)_3(phen)_2$ -doped films (0.25% w/w) under visible and UV ($\lambda_{ex}=254$ nm) light.

Table 32. PL ($\lambda_{ex}=292$ nm, 298 K), PLE ($\lambda_{em}=544$ nm, 298 K, nm), luminescent lifetime ($\lambda_{ex}=292$ nm, $\lambda_{em}=544$ nm, 298 K, nm) and Q_i values of $Tb(NO_3)_3(phen)_2$.

<i>Tb(NO₃)₃(phen)₂</i>	PL data ($\lambda_{ex}=292$ nm, 298 K, nm): 490 ($^5D_4-^7F_6$, 19%); 544, 548 ($^5D_4-^7F_5$, 61%); 583, 593 ($^5D_4-^7F_4$, 11%); 616, 621 ($^5D_4-^7F_3$, 9%).
	PLE data ($\lambda_{em}=544$ nm, 298 K, nm): $\lambda < 380$ (max at 270).
	Luminescent lifetime ($\lambda_{ex}=292$ nm, $\lambda_{em}=544$ nm, 298 K): $\tau = 0.14$ ms.
	$Q_i = 3\%$.
	Chromaticity coordinates: $x = 0.336$; $y = 0.593$.

CIE 1931

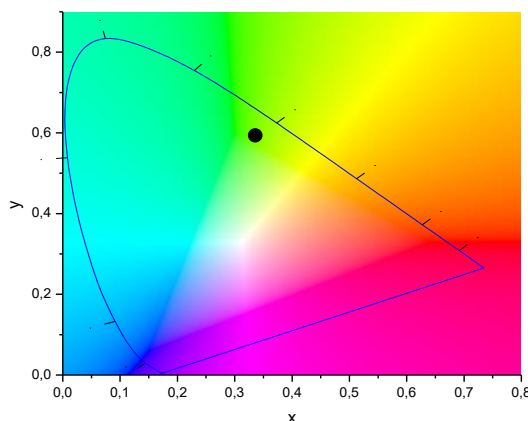
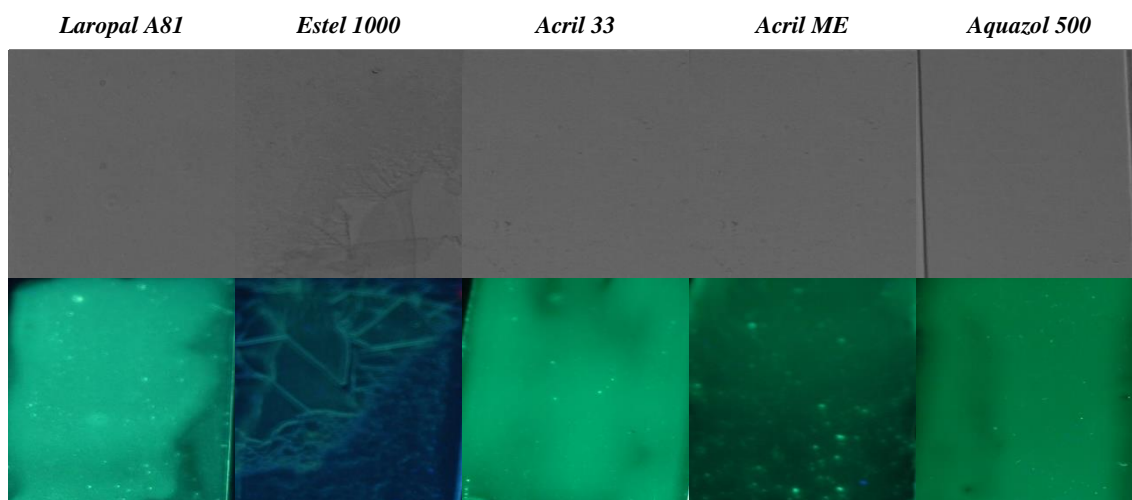


Figure 62. Chromaticity diagram (x, y) of pure $Tb(NO_3)_3(phen)_2$ complex.

Table 33. Samples of $Tb(NO_3)_3(phen)_2$ -doped (0.25% w/w) films under visible (above) and UV (below, $\lambda_{ex}=254$ nm) light.



The PL and PLE spectra of the terbium-based (0.25% w/w) samples were collected and are reported, respectively, in Figures 63 and 64. PL, PLE, τ , Q_i and the chromaticity coordinates x and y are collected in Table 34.

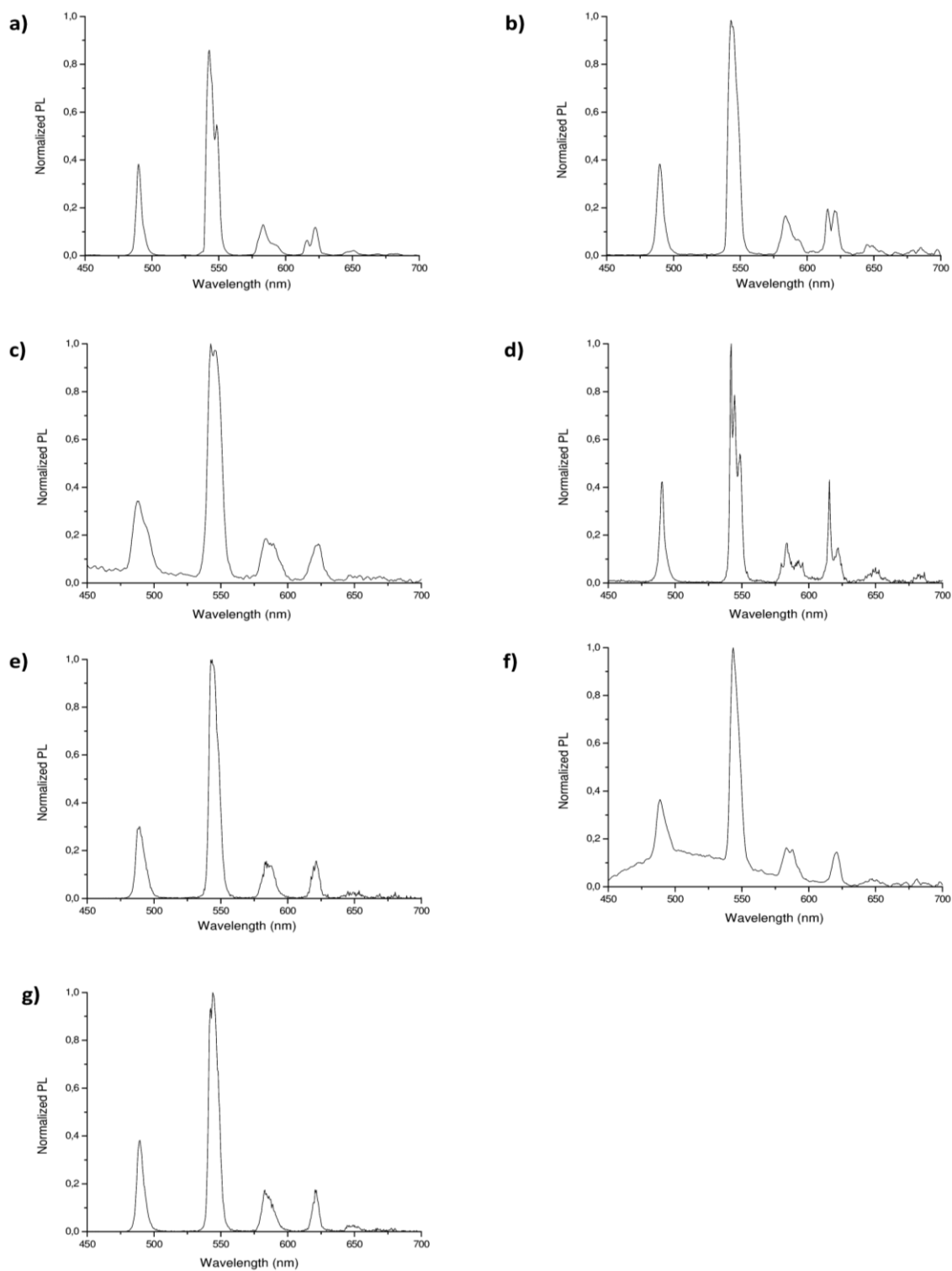


Figure 63. Normalized PL spectra (298K, $\lambda_{ex}=292$ nm) of terbium-based (0.25% w/w) samples. (a) Tb(NO₃)₃(phen)₂; (b) LB_Tb(NO₃)₃(phen)₂; (c) NE_Tb(NO₃)₃(phen)₂; (d) E1000_Tb(NO₃)₃(phen)₂; (e) AC_Tb(NO₃)₃(phen)₂; (f) AM_Tb(NO₃)₃(phen)₂; (g) A500_Tb(NO₃)₃(phen)₂.

As highlighted in Figure 63, the emission spectrum of pure $\text{Tb}(\text{NO}_3)_3(\text{phen})_2$ appears comparable only with the samples where the matrix is *Laropal A81*. Besides changes in the shapes of the bands, in the cases of $\text{NE_Tb}(\text{NO}_3)_3(\text{phen})_2$ and $\text{AM_Tb}(\text{NO}_3)_3(\text{phen})_2$ the superposition of fluorescence bands is clearly observable.

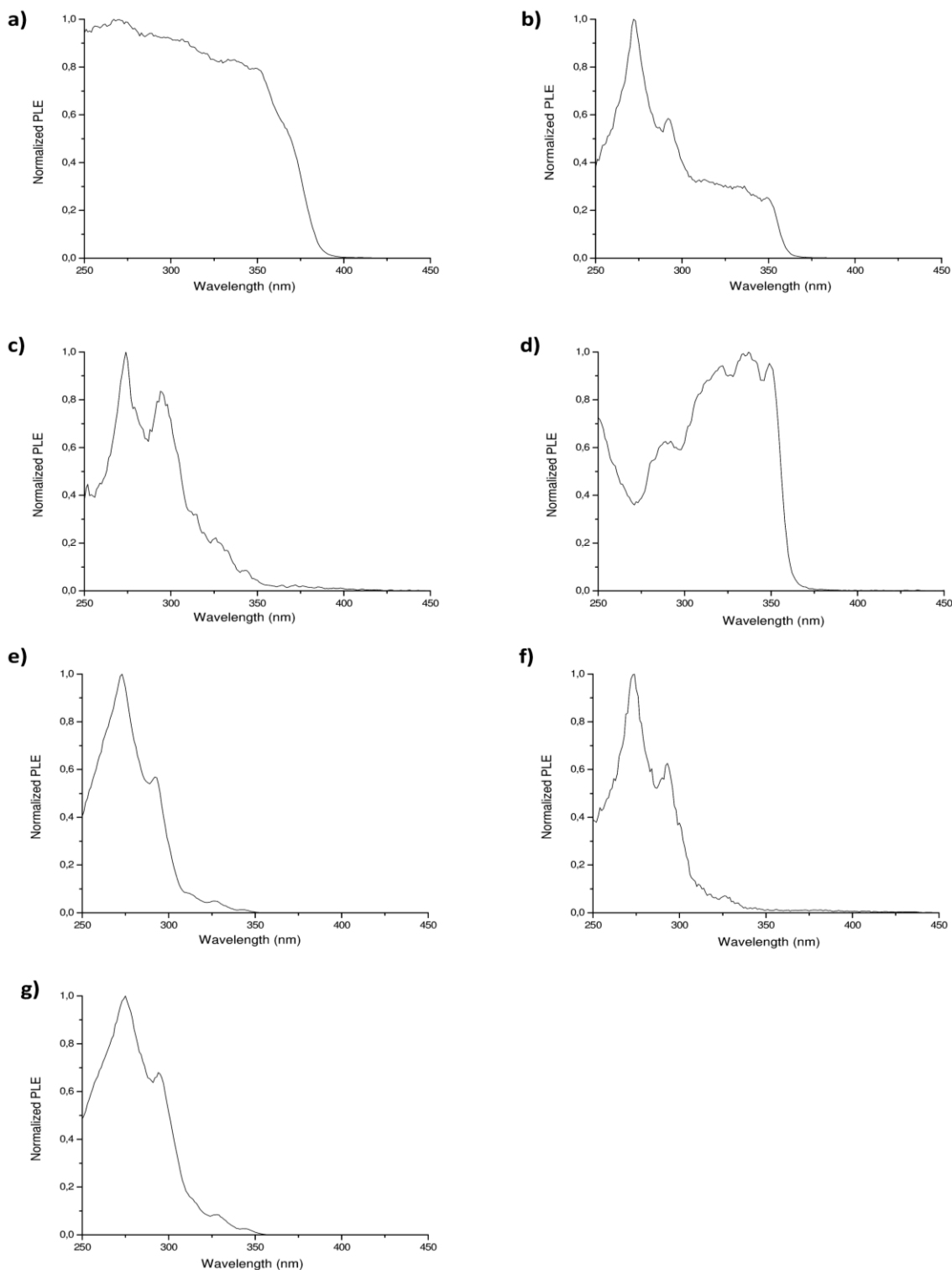


Figure 64. Normalized PLE spectra (298K, $\lambda_{em}=544$ nm) of terbium-based (0.25% w/w) samples. (a) $\text{Tb}(\text{NO}_3)_3(\text{phen})_2$; (b) $\text{LB_Tb}(\text{NO}_3)_3(\text{phen})_2$; (c) $\text{NE_Tb}(\text{NO}_3)_3(\text{phen})_2$; (d) $\text{E1000_Tb}(\text{NO}_3)_3(\text{phen})_2$; (e) $\text{AC_Tb}(\text{NO}_3)_3(\text{phen})_2$; (f) $\text{AM_Tb}(\text{NO}_3)_3(\text{phen})_2$; (g) $\text{A500_Tb}(\text{NO}_3)_3(\text{phen})_2$.

Table 34. PL ($\lambda_{ex}=292$ nm, 298 K, nm), PLE ($\lambda_{em}=544$ nm, 298 K, nm), luminescent lifetime ($\lambda_{ex}=292$ nm, $\lambda_{em}=544$ nm, 298 K, nm) of terbium-based (0.25% w/w) films.

<i>Tb(NO₃)₃(phen)₂</i>	<p>PL data ($\lambda_{ex}=292$ nm, 298 K, nm): 490 ($^5D_4-^7F_6$, 19%); 544, 548 ($^5D_4-^7F_5$, 61%); 583, 593 ($^5D_4-^7F_4$, 11%); 616, 621 ($^5D_4-^7F_3$, 9%).</p> <p>PLE data ($\lambda_{em}=544$ nm, 298 K, nm): $\lambda < 380$ (max at 270).</p> <p>Luminescent lifetime ($\lambda_{ex}=292$ nm, $\lambda_{em}=544$ nm, 298 K): $\tau = 0.14$ ms.</p> <p>$Q_f = 3\%$.</p> <p>Chromaticity coordinates: $x = 0.336$; $y = 0.593$.</p>
<i>LB_Tb(NO₃)₃(phen)₂</i>	<p>PL data ($\lambda_{ex}=292$ nm, 298 K, nm): 490 ($^5D_4-^7F_6$, 17%); 544 ($^5D_4-^7F_5$, 56%); 584, 594 ($^5D_4-^7F_4$, 13%); 615, 621 ($^5D_4-^7F_3$, 13%).</p> <p>PLE data ($\lambda_{em}=544$ nm, 298 K, nm): 272, 292, 335, 349.</p> <p>Luminescent lifetime ($\lambda_{ex}=292$ nm, $\lambda_{em}=544$ nm, 298 K): $\tau_1 = 0.09$ ms (68%); $\tau_2 = 1.19$ ms (32%).</p> <p>Chromaticity coordinates: $x = 0.337$; $y = 0.568$.</p>
<i>NE_Tb(NO₃)₃(phen)₂</i>	<p>PL data ($\lambda_{ex}=292$ nm, 298 K, nm): 489 ($^5D_4-^7F_6$, 22%); 542, 546 ($^5D_4-^7F_5$, 52%); 584, 599 ($^5D_4-^7F_4$, 12%); 623 ($^5D_4-^7F_3$, 4%).</p> <p>PLE data ($\lambda_{em}=544$ nm, 298 K, nm): 274, 279, 295, 315, 326, 333, 344.</p> <p>Luminescent lifetime ($\lambda_{ex}=292$ nm, $\lambda_{em}=544$ nm, 298 K): $\tau = 0.12$ ms.</p> <p>$Q_f = 2\%$.</p> <p>Chromaticity coordinates: $x = 0.320$; $y = 0.535$.</p>
<i>E1000_Tb(NO₃)₃(phen)₂</i>	<p>PL data ($\lambda_{ex}=292$ nm, 298 K, nm): 490 ($^5D_4-^7F_6$, 17%); 542, 544, 548 ($^5D_4-^7F_5$, 51%); 580, 583, 592, 595 ($^5D_4-^7F_4$, 14%); 618, 622 ($^5D_4-^7F_3$, 18%).</p> <p>PLE data ($\lambda_{em}=544$ nm, 298 K, nm): 280, 288, 292, 322, 333, 337, 349.</p> <p>Luminescent lifetime ($\lambda_{ex}=292$ nm, $\lambda_{em}=544$ nm, 298 K): $\tau_1 = 0.16$ ms (72%); $\tau_2 = 0.06$ ms (18%).</p> <p>Chromaticity coordinates: $x = 0.384$; $y = 0.538$.</p>
<i>AC_Tb(NO₃)₃(phen)₂</i>	<p>PL data ($\lambda_{ex}=292$ nm, 298 K, nm): 489 ($^5D_4-^7F_6$, 19%); 544 ($^5D_4-^7F_5$, 62%); 583, 587 ($^5D_4-^7F_4$, 12%); 618, 619, 621 ($^5D_4-^7F_3$, 7%).</p> <p>PLE data ($\lambda_{em}=544$ nm, 298 K, nm): 273, 292, 313, 327, 344.</p> <p>Luminescent lifetime ($\lambda_{ex}=292$ nm, $\lambda_{em}=544$ nm, 298 K): $\tau = 1.29$ ms.</p> <p>$Q_f = 27\%$.</p> <p>Chromaticity coordinates: $x = 0.337$; $y = 0.567$.</p>
<i>AM_Tb(NO₃)₃(phen)₂</i>	<p>PL data ($\lambda_{ex}=292$ nm, 298 K, nm): 490 ($^5D_4-^7F_6$, 28%); 544 ($^5D_4-^7F_5$, 47%); 583, 588 ($^5D_4-^7F_4$, 11%); 621 ($^5D_4-^7F_3$, 14%).</p> <p>PLE data ($\lambda_{em}=544$ nm, 298 K, nm): 254, 262, 274, 290, 293, 300, 326.</p> <p>Luminescent lifetime ($\lambda_{ex}=292$ nm, $\lambda_{em}=544$ nm, 298 K): $\tau = 1.53$ ms.</p> <p>$Q_f = 32\%$.</p> <p>Chromaticity coordinates: $x = 0.321$; $y = 0.536$.</p>
<i>A500_Tb(NO₃)₃(phen)₂</i>	<p>PL data ($\lambda_{ex}=292$ nm, 298 K, nm): 490 ($^5D_4-^7F_6$, 19%); 544 ($^5D_4-^7F_5$, 60%); 583, 586, 587, 588 ($^5D_4-^7F_4$, 13%); 620, 621 ($^5D_4-^7F_3$, 8%).</p> <p>PLE data ($\lambda_{em}=544$ nm, 298 K, nm): 275, 294, 315, 327, 345.</p> <p>Luminescent lifetime ($\lambda_{ex}=292$ nm, $\lambda_{em}=544$ nm, 298 K): $\tau = 1.01$ ms.</p> <p>$Q_f = 21\%$.</p> <p>Chromaticity coordinates: $x = 0.338$; $y = 0.592$.</p>

Variations in the coordination sphere are suggested also by lifetime measurements. For instance, in the case of LB_Tb(NO₃)₃(phen)₂ two decay processes were determined. The first, fast, has a lifetime of 0.09 ms, while for the second, slow, the τ value is about 1.19 ms. For the samples AC_Tb(NO₃)₃(phen)₂, AM_Tb(NO₃)₃(phen)₂ and A500_Tb(NO₃)₃(phen)₂ an enhancement of the luminescence was recorded with τ values of, respectively, 1.29, 1.53 and 1.09 ms.

Moreover, also the comparison of the PL spectra of the doped matrices with that of the pure compound indicates alteration of the terbium compound. The broad band collected for the pure compound is replaced by a series of peaks whose wavelengths depend upon the choice of the matrices.

The chromaticity of the terbium-doped films was evaluated. Higher variability in the colorimetric coordinates were revealed with respect to the europium-based films, with variations in terms of colour. In the samples LB_Tb(NO₃)₃(phen)₂, E1000_Tb(NO₃)₃(phen)₂ and AC_Tb(NO₃)₃(phen)₂ a shift to green-yellow dye was determined, while for the samples NE_Tb(NO₃)₃(phen)₂ and AM_Tb(NO₃)₃(phen)₂ a shift to green-cyano dye was observed.

Finally, the photoluminescence emission and excitation spectra of doped films were evaluated after 2000 hours of UVA ($\lambda=254$ nm) aging. Luminescent lifetimes (τ) and quantum yields (Q_i) determined for the europium- and terbium-doped (0.25% w/w) matrices are collected in Table 35.

Happily, in most of the cases the photoluminescence of the samples is sufficient to be easily detectable by human eye also after ageing (Tables 36 and 37) and this is particularly true for the films based on the red emitter Eu(NO₃)₃(phen)₂.

Table 35. Radiative lifetimes (τ) and intrinsic quantum yields (Q_i) of europium- ($\lambda_{em}=615$ nm) and terbium-based ($\lambda_{em}=544$ nm) (0.25% w/w) samples before and after 2000 hours of photo-oxidative UVA ($\lambda=254$ nm) aging.

Sample	unaged		aged		Sample	unaged		aged	
	τ (ms)	Q_i %	τ (ms)	Q_i %		τ (ms)	Q_i %	τ (ms)	Q_i %
LB_Eu(NO ₃) ₃ (phen) ₂	1.14	60	1.15	59	LB_Tb(NO ₃) ₃ (phen) ₂	$\tau_1=0.09$ $\tau_2=1.19$	-	$\tau_1=0.03$ $\tau_2=1.26$	-
NE_Eu(NO ₃) ₃ (phen) ₂	0.60	22	0.67	26	NE_Tb(NO ₃) ₃ (phen) ₂	0.12	2	0.14	3
E1000_Eu(NO ₃) ₃ (phen) ₂	1.18	65	1.17	64	E1000_Tb(NO ₃) ₃ (phen) ₂	$\tau_1=0.16$ $\tau_2=0.06$	-	0.03	0.6
AC_Eu(NO ₃) ₃ (phen) ₂	1.20	56	1.13	53	AC_Tb(NO ₃) ₃ (phen) ₂	1.29	27	1.21	25
AM_Eu(NO ₃) ₃ (phen) ₂	1.25	49	1.39	34	AM_Tb(NO ₃) ₃ (phen) ₂	1.53	32	1.12	23
A500_Eu(NO ₃) ₃ (phen) ₂	0.76	38	0.75	37	A500_Tb(NO ₃) ₃ (phen) ₂	1.01	21	1.02	21

Table 36. Samples of $\text{Eu}(\text{NO}_3)_3(\text{phen})_2$ -doped (0.25% w/w) films before (above) and after (below) 2000 hours of photo-oxidative UVA ($\lambda=254$ nm) aging under UV ($\lambda_{\text{ex}}=254$ nm) light.

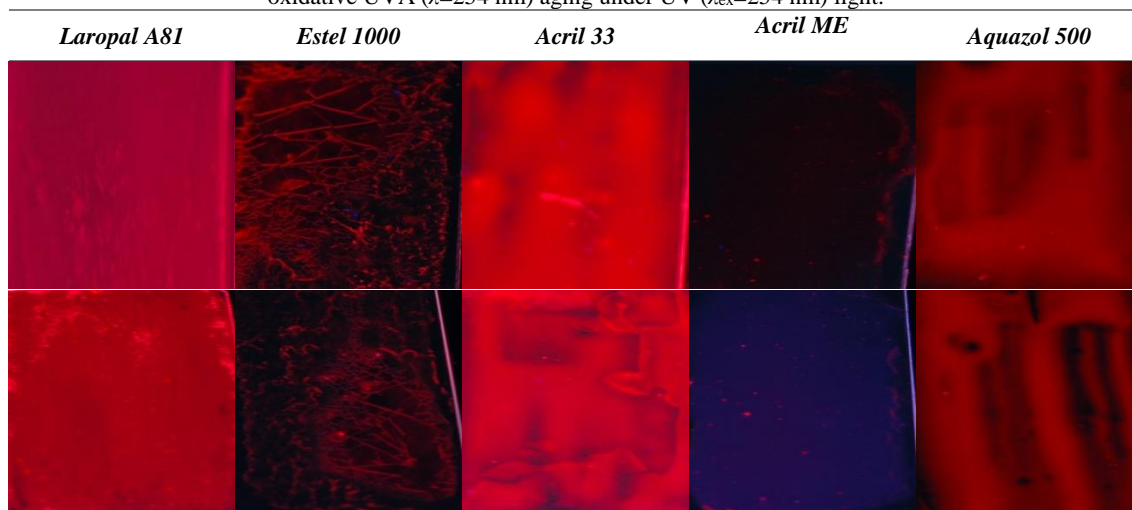
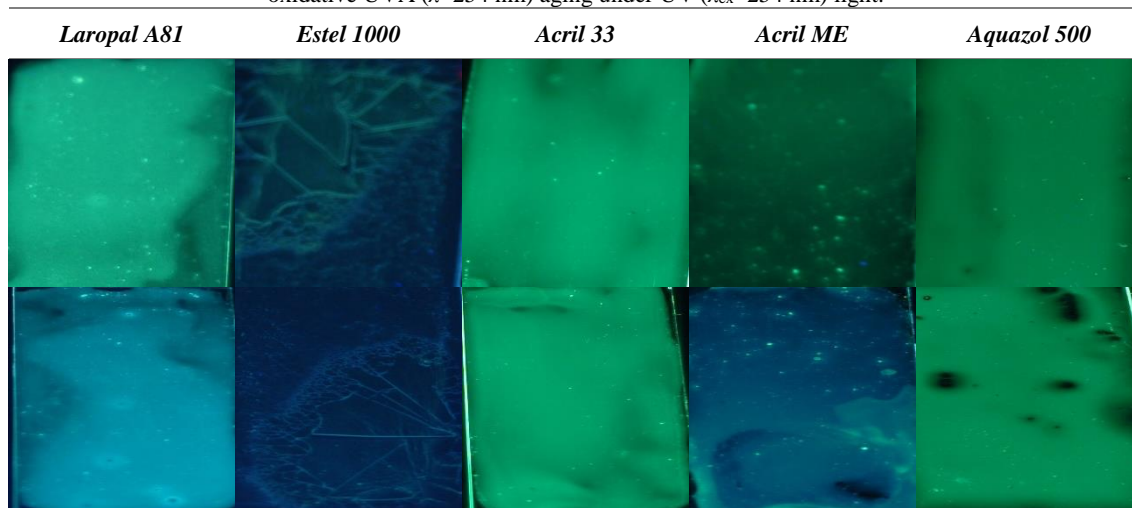


Table 37. Samples of $\text{Tb}(\text{NO}_3)_3(\text{phen})_2$ -doped (0.25% w/w) films before (above) and after (below) 2000 hours of photo-oxidative UVA ($\lambda=254$ nm) aging under UV ($\lambda_{\text{ex}}=254$ nm) light.



As shown in Figure 65, the PL spectra of the aged europium-based films showed no meaningful variations of the emission spectra with respect to the fresh samples, except for the *Acril ME*- and *Aquazol 500*-based films. The variations in the PL spectra of these samples are due, in the case of *Acril ME*, to fluorescence from the binder (raising of the baseline) and to the decrease of the intensity of the ${}^5\text{D}_0 \rightarrow {}^7\text{F}_4$ transition (Figure 65e), while in the case of *Aquazol 500* to an enhancement of the relative intensity of the ${}^5\text{D}_0 \rightarrow {}^7\text{F}_1$ and ${}^5\text{D}_0 \rightarrow {}^7\text{F}_4$ transitions and to a contemporary broadening of the ${}^5\text{D}_0 \rightarrow {}^7\text{F}_4$ transition (Figure 65f).

Similar effects of photo-oxidative ageing can be supposed also for the corresponding terbium-based samples. However, if this is true for the AM_ $\text{Tb}(\text{NO}_3)_3(\text{phen})_2$ sample (Figure 66e), the PL spectrum of the A500_ $\text{Tb}(\text{NO}_3)_3(\text{phen})_2$ (Figure 66f) sample remains unchanged after the aging. On the other hand, an enhancement of the relative intensity of the ${}^5\text{D}_0 \rightarrow {}^7\text{F}_3$ and ${}^5\text{D}_0 \rightarrow {}^7\text{F}_4$ transitions with respect to the ${}^5\text{D}_0 \rightarrow {}^7\text{F}_1$ one was observed for the sample E1000_ $\text{Tb}(\text{NO}_3)_3(\text{phen})_2$ (Figure 66c).

Moreover, the comparison between the excitation spectra (PLE) suggested that negligible changes occur

in the ligands field around both europium and terbium ions after ageing (for example see Figure 67).

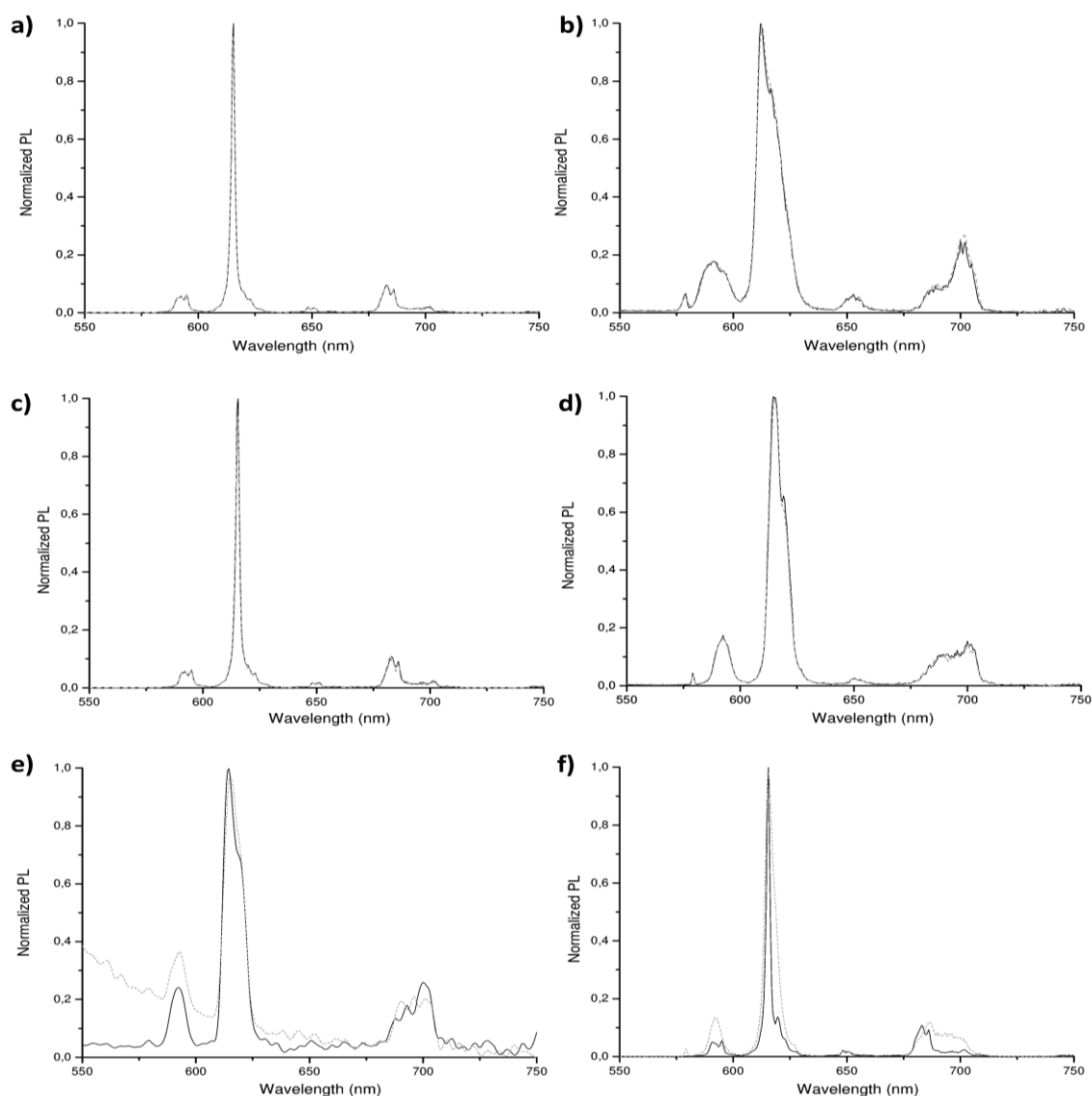


Figure 65. Comparison between normalized PL spectra (298 K, $\lambda_{ex}=292$ nm) of europium-based freshly (straight line) and aged (dot-line) (0.25% w/w) samples. a) LB_Eu(NO₃)₃(phen)₂; b) NE_Eu(NO₃)₃(phen)₂; c) E1000_Eu(NO₃)₃(phen)₂; d) AC_Eu(NO₃)₃(phen)₂; e) AM_Eu(NO₃)₃(phen)₂; f) A500_Eu(NO₃)₃(phen)₂.

Further information about the photo-stability of the doped films was obtained considering the radiative lifetimes (τ) reported in Table 35. Photo-oxidative ageing caused really small variations of τ values (below 1%) with respect to the freshly prepared samples, a result in agreement with the negligible variations of the PL spectra above described. At the same time, the intrinsic quantum yields are quite similar between unaged and aged samples.

Only for the samples NE_Eu(NO₃)₃(phen)₂ and NE_Tb(NO₃)₃(phen)₂ an increase of the radiative lifetime was detected after the photo-oxidative aging. As revealed from the FT-IR analyses, aging involves the removal of the water (solvent) retained from the silica films. This aging feature has a positive effect on the luminescence properties of the doped films because it leads to the decrease of the non-radiative decay by reducing the vibrational interactions between the lanthanide complexes and the O-H oscillators.

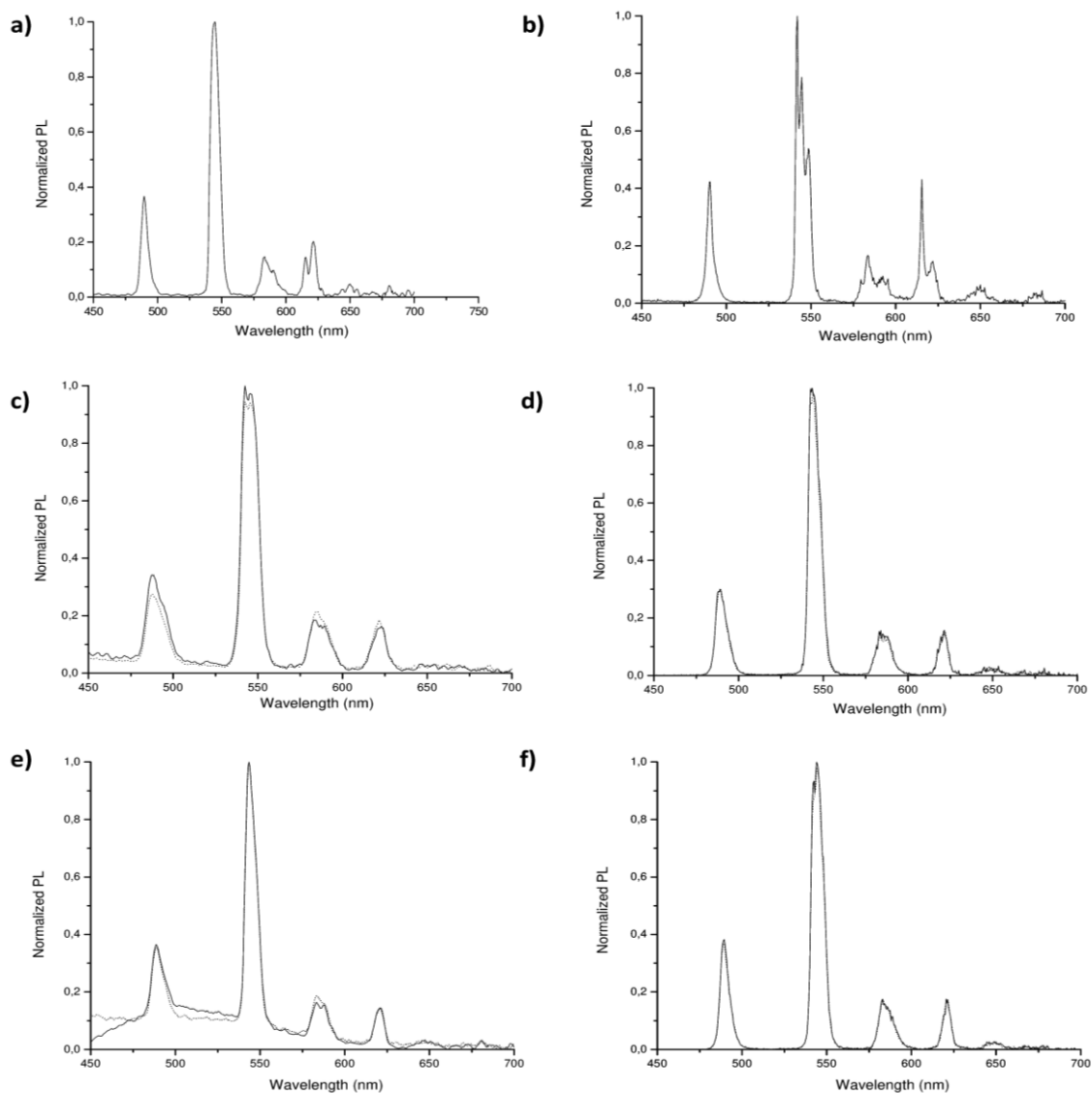


Figure 68. Comparison between normalized PL spectra (298 K, $\lambda_{ex}=292$ nm) of terbium-based unaged (straight line) and aged (dot-line) (0.25% w/w) samples. a) LB_Tb(NO₃)₃(phen)₂; b) NE_Tb(NO₃)₃(phen)₂; c) E1000_Tb(NO₃)₃(phen)₂; d) AC_Tb(NO₃)₃(phen)₂; e) AM_Tb(NO₃)₃(phen)₂; f) A500_Tb(NO₃)₃(phen)₂.

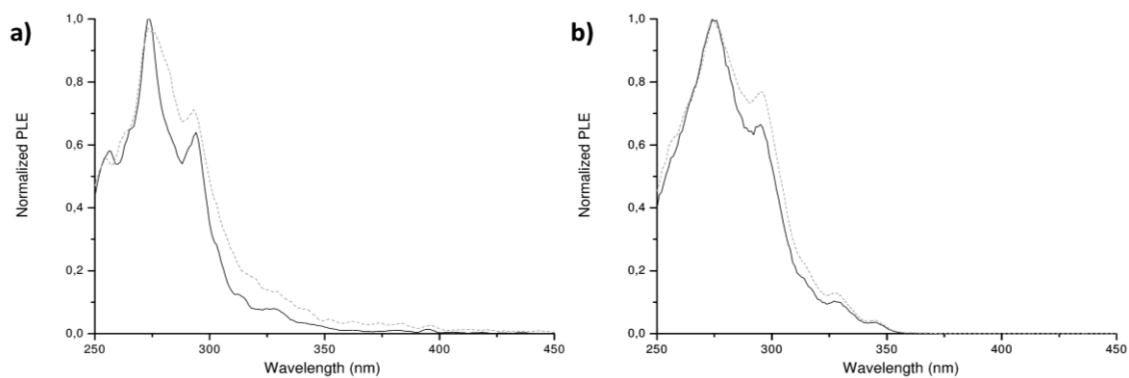


Figure 67. Normalized PLE spectrum (298 K, $\lambda_{em}=615$ nm) of freshly (straight line) and aged (dots-line) (0.25% w/w) a) AM_Tb(NO₃)₃(phen)₂ and b) A500_Tb(NO₃)₃(phen)₂ samples.

9. Concluding Remarks

The first aim of the study was to characterize and ascertain the degrading mechanisms occurring in different polymeric and nanostructured commercial products. In order to achieve this result, several samples were previously analyzed mainly by Thermogravimetric Analysis (TGA), Dynamic Light Scattering (DLS), Centrifugal Separation Analysis (CSA), Viscometry, Size Exclusion Chromatography (SEC) and Fourier Transform Infrared Spectroscopy (FT-IR). Afterwards, long-lasting experiments carried out, never attempted before, allowed to evaluate the degradation mechanisms and kinetics by means of SEC, FT-IR, colorimetric and gloss measurements. Therefore, different aging behaviours and mechanisms have been identified as responsible of thermo- and photo-oxidative aging as well as natural aging.

Thermogravimetric analyses (TGA) revealed that *Acril 33* and *Acril ME* have similar activation energy, respectively of 109 ($\pm 5\%$) and 112 ($\pm 2\%$) kJ mol⁻¹. However, the lower stability of *Acril 33* was revealed by the fact that thermal degradation begins at lower temperature with respect to *Acril ME*, 247 instead 276°C. On the other hand, *Laropal A81* and *Aquazol 500* showed, respectively, the highest and lowest resistance to the thermal-degradation with activation energy of 213 ($\pm 1\%$) and 61 ($\pm 2\%$) kJ mol⁻¹, respectively. The activation energy calculated by thermogravimetric analyses follows the order *Laropal A81* >> *Acril ME* > *Acril 33* >> *Aquazol 500*, identifying in *Laropal A81* the polymer more stable towards thermal decomposition.

High colloidal stability was revealed for both *Acril 33* and *Acril ME*, for which were calculated sedimentation velocities at gravity force of, respectively, $\leq 8 \times 10^{-4}$ and $\leq 3 \times 10^{-4}$ $\mu\text{m s}^{-1}$. Moreover, DLS measurements allowed to determine particle size distributions centered at, respectively, 70 ± 15 and 47 ± 7 nm.

SEC and FT-IR analyses showed that the mechanism of thermal degradation of *Acril 33* involves both cross-linking reactions of the polymer backbone and scission on the ester side groups, resulting in the loss of volatile molecules and formation of lactone and hydroxyl groups. Moreover, the tendency to form insoluble fractions observed during SEC and viscometric analyses was attributed to decomposition of the unstable secondary hydroperoxides, which gives alkoxy radicals that decay via cross-linking. The kinetic constant (k) of the degradation process was calculated and it is equal to 3.26×10^{-3} (h⁻¹). The high values of ΔE determined at the end of the thermo-oxidative aging tests, which correspond to a shift towards yellow-orange shades, were attributed to the formation of lactone groups, that act as chromophores. Moreover, high instability of the polymer was recorded also in terms of gloss retention, with surfaces varying from glossy to matt.

On the other hand, photodegradation of *Acril 33* involves solely depolymerization mechanism, and the M_w -time decay curve allowed to calculate a kinetic constant of depolymerization of 2.93×10^{-3} (h⁻¹).

The higher stability to photo-oxidative aging with respect to thermal-aging was highlighted not only by the lower kinetic constant of the depolymerization process, but also from the negligible variations recorded in the colour and gloss parameters after 2000 hours of UVA aging.

Thermal decomposition of *Acril ME* involves both fragmentation and cross-linking reactions with the last prevailing for prolonged aging. SEC analyses allowed to calculate the kinetic constant of the depolymerization process ($7.63 \times 10^{-3} \text{ h}^{-1}$) while FT-IR analyses revealed that thermal degradation leads to the formation of ketones and alkoxy radicals, followed by further decomposition to anhydrides and formation of γ -lactones by dehydration of two adjacent acid groups. The variations in the colour parameters, particularly high for the sample aged at 140°C , are attributed to the formation of lactone groups. On the other hand, *Acril ME* exhibited high resistance in terms of gloss retention also for prolonged aging at high temperature.

Conversely, photo-oxidation of *Acril ME* occurred only by chain-ends degradation, although no significant variation in the MWD was recorded after 2000 hours of aging. SEC analysis gave a kinetic constant of the fragmentation process of $3.10 \times 10^{-3} \text{ h}^{-1}$, while FT-IR showed that this process is the reverse of the polymerization, since the degradation occurred through the elimination of the entire monomeric *BMA* units rather than only the lateral butyl groups. Moreover, the high stability of *Acril ME* to photo-oxidation was also revealed by the negligible variations in the colour and gloss parameters after 2000 hours of aging.

In general, higher stability of *Acril ME* with respect to *Acril 33* was observed.

The isothermal degradation of *Aquazol 500* occurred through a double mechanism of degradation. On one hand, chain scissions of the polymer backbone followed by loss of side chains lead to the formation of lactone groups and secondary amides (kinetic constant of the process $4.37 \times 10^{-3} \text{ h}^{-1}$). On the other hand, it was showed as prolonged aging or aging at higher temperatures favour cross-linking reactions rather than chain scission. As reported above, the great variation in the colour parameters can be attributed to the formation of chromophores groups (lactones), while the variation in the chemical structure is responsible of the massive decrease of the gloss parameter, with surfaces varying from gloss to matt during the aging.

It was shown as depolymerization reactions (kinetic constant equal to $1.05 \times 10^{-3} \text{ h}^{-1}$) are exclusively involved in the mechanism of photo-oxidative degradation of *Aquazol 500*. Although good stability in terms of colour and gloss retention was observed, the variations in the gloss parameter of the samples of *Aquazol 500* exposed to both UVC and UVA radiations are the highest registered among all the materials tested. This suggests that *Aquazol 500* has the lowest stability to photo-oxidation among the samples herein studied.

As expected from the TGA results, *Laropal A81* exhibited the higher resistance to thermo-oxidative aging. Only the aging at high temperatures (120 and 140°C) induced variations in the FT-IR spectrum

attributable to the progressive loss of low molecular weight fractions and to the formation of non-aromatic hydrocarbons compounds. The high stability was confirmed also by the slight variation of colour parameters (ΔE lower than 5 also after 15000 hours of thermo-oxidative aging at 140°C) as well as by the negligible variation in the retention times of aged solutions determined by viscometric analyses. On the other hand, structural changes are recognized as responsible of the slightly variations of gloss.

Moreover, *Laropal A81* revealed high stability also with respect to photo-oxidation with negligible variations in both chemical and physical properties.

Overall, the results obtained indicate that both thermal and photo-oxidative degradations of *Laropal A81* probably occur through fragmentation rather than cross-linking reactions.

CSA and DLS measurements gave interesting information about the alcoholic dispersion of CaOH₂ NPs. The transmittance profiles of *NanoRestore* allowed to individuate two populations of particles in both fresh and one-year aged dispersions. Average diameters of 25 and 300 nm were determined by CSA for the two populations in fresh dispersion. However, a decrease of the biggest aggregates size towards 200 nm was revealed after one-year of aging. Good colloidal stability was revealed, since only slight decrease of the settling values was measured for the largest population of particles after one-year aging (from $6.1 \cdot 10^{-2} \pm 6.6 \cdot 10^{-4}$ to $5.1 \cdot 10^{-2} \pm 6.9 \cdot 10^{-4}$ $\mu\text{m s}^{-1}$). Moreover, similar values have been obtained for the smallest population of particles before and after aging ($5.5 \cdot 10^{-3} \pm 1.8 \cdot 10^{-4}$ and $5.8 \cdot 10^{-3} \pm 2.1 \cdot 10^{-4}$ $\mu\text{m s}^{-1}$).

NanoRestore exhibited high stability towards both thermal- and photo-aging. FT-IR analyses showed that the CaOH₂ NPs preserved their basic character also for prolonged aging at high temperature, corroborating their use as alkaline reservoir for deacidification of wood, paper and canvas. No significant variation was recorded in the colour parameters, except the decrease of the L* parameter, attributable to partial loss of the sample from the treated surface. Moreover, *NanoRestore* exhibited, together with *Acril ME*, the best performance in terms of gloss retention.

FT-IR analyses have revealed as thermal- and photo-aging of *Estel 1000* involves the formation of amorphous silica and silicone. However, good resistance was revealed in terms of colour changes towards all the aging tests conducted. On the other hand, gloss measurements showed that silica films become bright after aging.

Good performance was observed in terms of colloidal stability for the NPs *NanoEstel* dispersion. The sedimentation velocity of the silica NPs was found to be very low at gravity (≤ 0.01 $\mu\text{m s}^{-1}$) and a sharp distribution of the hydrodynamic diameter of the particles, centred at 19 ± 3 nm, was revealed by DLS measurements.

Silica NPs *NanoEstel* exhibited high stability with respect to both thermal- and photo-aging, showing no changes in the spectra of aged samples with respect to the fresh one and negligible variations in both

colour and gloss parameters. Therefore, given the results here reported, the use of silica NPs is preferable to the *TEOS* solvent-based product not only for the non-toxicity of the first, but also for its better performance over time.

The second objective of this work consisted in the synthesis and characterization of visible-emitting lanthanide complexes with well-designed antenna-ligands, to be used as dopants for the commercial products here studied in order to obtain luminescent materials allowing easy discrimination between original and retouched or consolidated areas. To this scope, the complexes $\text{Eu}(\text{NO}_3)_3(\text{phen})_2$ and $\text{Tb}(\text{NO}_3)_3(\text{phen})_2$ have been synthesized, characterized pure and embedded in *Acril 33*, *Acril Me*, *Aquazol 500*, *Laropal A81*, *Estel 1000* and *NanoEstel*. First of all, it is important to note that very low concentration of complex $\text{Ln}(\text{NO}_3)_3(\text{phen})_2$ (0.25% w/w) was, in most of the cases, sufficient to guarantee a high luminescence of the doped film.

The pure $\text{Eu}(\text{NO}_3)_3(\text{phen})_2$ exhibited luminescence lifetime of 1.24 ms and an intrinsic quantum yield of 77%. No meaningful interaction between $\text{Eu}(\text{NO}_3)_3(\text{phen})_2$ and the matrix occurred only using *Laropal A81* and *Estel 1000*, with radiative lifetimes strictly comparable with that of the pure complex. On the other hand, the use of *Acril 33*, *Acril Me*, *Aquazol 500* and *NanoEstel* matrices caused a variation of the inner coordination sphere of the Eu(III) centre.

The luminescent lifetime of $\text{Tb}(\text{NO}_3)_3(\text{phen})_2$ complex is 0.14 ms, corresponding to an intrinsic quantum yield of 3%. Despite the quite poor luminescent features of pure $\text{Tb}(\text{NO}_3)_3(\text{phen})_2$, appreciable photoluminescence was observed for the complex once dispersed in the different matrices, although variations in the coordination sphere were revealed. In particular, a positive effect was determined for the samples AC_ $\text{Tb}(\text{NO}_3)_3(\text{phen})_2$, AM_ $\text{Tb}(\text{NO}_3)_3(\text{phen})_2$ and A500_ $\text{Tb}(\text{NO}_3)_3(\text{phen})_2$, for which an enhancement of the luminescence was recorded with τ values of, respectively, 1.29, 1.53 and 1.09 ms. Finally, the photoluminescence features of the doped films were evaluated after 2000 hours of UVA ($\lambda=254$ nm) aging. High stability to photo-oxidative aging was revealed by all the samples tested with luminescence easily detectable by human eye also after aging.

Appendix A

Journal of Cultural Heritage xxx (2017) xxx–xxx



Available online at
ScienceDirect
www.sciencedirect.com

Elsevier Masson France
EM|consulte
www.em-consulte.com/en



Original article

Consolidation of Vicenza, Arenaria and Istria stones: A comparison between nano-based products and acrylate derivatives

Giulia Gheno^a, Elena Badetti^{b,*}, Andrea Brunelli^b, Renzo Ganzerla^a, Antonio Marcomini^{b,*}

^a DSMN, Department of Molecular Sciences and Nanosystems, Ca' Foscari University of Venice, Scientific Campus, Via Torino 155, 30172 Mestre, VE, Italy

^b DAIS, Department of Environmental Sciences, Informatics and Statistics, Ca' Foscari University of Venice, Scientific Campus, Via Torino 155, 30172 Mestre, VE, Italy

ARTICLE INFO

Article history:

Received 7 November 2017

Accepted 19 February 2018

Available online xxx

Keywords:

Stone consolidation
Nano-based products
Acrylate derivatives
Natural and simulated UVB aging
Color and gloss variations

ABSTRACT

Nano-based formulations are emerging as successful materials besides the use of conventional products for the consolidation of carbonate works of art e.g. stone, mortars or mural paintings. In this work, the physico-chemical characteristics, performances and consolidation efficacy in terms of external appearance of commercial NanoRestore Ca(OH)₂ and NanoEstel SiO₂ dispersions were investigated and compared with two commercial acrylates derivatives, Acril 33 and Acril ME. The colloidal stability of the different consolidants was investigated by dynamic light scattering (DLS) and centrifugal separation analysis (CSA) techniques. As expected, acrylate emulsions showed a higher colloidal stability than the inorganic nanoparticle dispersions, with sedimentation velocity from 10⁻⁴ to 10⁻² μm/s. The examined consolidants were applied on three different stones, widely used in historical buildings in Venice: Vicenza, Arenaria and Istria stones, representing macro-, meso- and microporous materials, respectively. The absorption capacity, color and gloss variation of the different stone materials were comparatively evaluated after the consolidants application. An accordance among porous structure of the substrates, hydrodynamic particle size and amount of consolidants absorbed was observed for nano-based formulations. The weathering resistance under natural and UVB aging conditions were also investigated for the consolidated stone samples, and recorded as changes of color, gloss and surface morphology. NanoRestore and NanoEstel showed the best performances under the natural aging while the UVB irradiation seemed to not induce significant modification in the surface morphology of the treated stone samples.

© 2018 Elsevier Masson SAS. All rights reserved.

1. Introduction

The persistent exposure to the combined action of natural weathering and anthropogenic pollution over time can cause several damages to lime- and silica-based porous materials used in both artworks and architectural manufacturing. Air pollution, the presence of soluble salts and biodeteriogens [1–5] can induce flaking of the surface layers, powdering, formation of small blisters and loss of large area of the artefact [6,7]. In this context, one of the main challenges in conservation and restoration field is the use of compatible consolidants, which can avoid deterioration without altering the main characteristics of the stone materials restored. Furthermore, the durability of the treatment and the long-term stability of the consolidated substrates should be ensured [8–15].

In the field of stone conservation, calcium hydroxide is one of the most promising products suitable for consolidating calcareous materials (e.g. stone sculptures, monuments or wall paintings)

because it is converted into calcium carbonate as a result of carbonation, when exposed to atmospheric CO₂ under moist conditions. Ca(OH)₂ is generally applied as a saturated aqueous solution, however, due to its low solubility, large amount of solution is needed. Consequently, the treatment of stone materials with large amounts of water could be detrimental to porous matrices, favoring the pore collapse through freeze–thaw cycles and the transport of soluble salts [16]. Additional drawbacks are the incomplete conversion of calcium hydroxide into calcium carbonate, as well as the post treatment chromatic alteration and the low penetration depth [17]. Moreover, the stability of aqueous Ca(OH)₂-based dispersion is not always ensured, although few exceptions are reported in literature [18]. Fast clustering and sedimentation of the hydroxide particles can in fact occur, with scarce penetration and veiling of the treated surface [19].

To enhance the consolidant performances of Ca(OH)₂, engineered nanomaterials (ENM) based formulations have been developed [20]. In detail, dispersions of Ca(OH)₂ nanoparticles (NPs) in water or short-chain alcohols have been largely studied to establish their potential use for consolidation of limestone and carbonatic painted surfaces [16,21–23], wood [24], paper and

* Corresponding authors.

E-mail address: elena.badetti@unive.it (E. Badetti).

<https://doi.org/10.1016/j.culher.2018.02.013>

1296-2074/© 2018 Elsevier Masson SAS. All rights reserved.

Please cite this article in press as: G. Gheno, et al., Consolidation of Vicenza, Arenaria and Istria stones: A comparison between nano-based products and acrylate derivatives, Journal of Cultural Heritage (2017), <https://doi.org/10.1016/j.culher.2018.02.013>

canvas deacidification [25], as well as for archaeological bones treatment [26]. The nano-size of the particles eases the penetration of the product through porous substrates and increases the particle reactivity with respect to CO₂ by turning into calcium carbonate. Several methodologies of Ca(OH)₂ NPs synthesis have been reported [27–32], and the related formulations showed different features like degree of dispersibility, particle size distribution and particle structure, which are expected to affect the consolidation process. Literature studies showed that Ca(OH)₂ NPs dispersed in short-chain alcohols exhibited a higher colloidal stability than using water as dispersant, significantly improving the degree of consolidation by decreasing agglomeration rate of particles [21,33,34].

As far as silica-based stones consolidation, commercial products containing alkoxy-silanes, such as tetraethoxysilane (TEOS), are commonly used [35]. These products, polymerizing *in situ* via a sol-gel process within the porous structure of the stone to be consolidated, increase the mechanical properties of the materials. However, they can form a dense microporous network of gel that tend to become brittle and susceptible to cracking. Moreover, this network can obstruct the porous of the materials promoting a significant reduction of water permeability [36]. To improve consolidation performances, nanosilica-based products were synthesized by a template synthesis in which a surfactant was used as structure-directing agent during the polymerization process. Following this procedure, silica nanoparticles with uniform size and ordered mesopores were obtained. The presence of surfactants avoids the cracking of the gel during the drying phase because of a coarsening of the gel network that reduces the capillary pressure [37,38]. Furthermore, the advantage of using nanosilica-based product with respect to the traditional solvent-based TEOS is the non-hazardous solvents employed and the reduced time necessary to obtain the gel network. In this case in fact, the hydrolysis step is skipped and the film is formed by condensation of the silica NPs. On the other hand, the capability of silica nanoparticles to penetrate porous materials with respect to the solvent-based silica product have not been yet deeply investigated [39].

Acrylic resins have also been largely used in conservation practice. They are thermoplastics copolymers based on monomers derived from acrylic and methacrylic acid. Depending on the ratio of the monomers, it is possible to structure a resin with specific molecular weight and physico-chemical characteristics [40]. During the early 1930s, acrylic polymers started to be used as picture varnishes because of their initial resistance to yellowing, their solubility in hydrocarbons solvents, their ability to form flexible and transparent films and their glass transition temperature, preventing the dirty pick-up. Unfortunately, these resins resulted unsuitable for long-term uses, due to the unexpected cross-linking, cracking and yellowing exhibited when the polymers were exposed to natural light [41]. At the end of the 1940s, a more stable acrylic resin system was introduced with the commercial name of Paraloid. This acrylic polymer applied in solution was recommended for a wide range of applications, such as textile, wood and pigments consolidants, as adhesives for paper and, due to its hydrophobicity, as consolidant and water repellent for stones [42]. In particular, Paraloid B72, a copolymers of methyl methacrylate and ethyl acrylate [P(MMA/EA)] soluble in organic solvents, showed an improved stability at different aging conditions [43,44]. After their application, transparent films are formed by coalescence of the particles in the dispersion. In the last years, the growing attention towards human health and environment has led to water-based emulsions safer than the original formulations.

In this context, four different stone consolidants NanoRestore, NanoEstel, acrylic-based emulsion Acril 33 and micro emulsion Acril ME were investigated. The physico-chemical characterization of the commercial suspensions was performed by means of

dynamic light scattering (DLS) and centrifugal separation analysis (CSA). The consolidants were then applied on three different stones, i.e. Vicenza, Arenaria and Istria stone that are representative of macro-, meso- and microporous materials. These stones have been selected for their abundance in architectural decorative apparatus of numerous venetian palaces and churches such as the Basilica of San Marco and Palazzo Ducale [45]. To the best of our knowledge, the application of consolidants on these stones is still scarcely investigated, as well as their use on historic surfaces which is still limited and mainly confined to scientific research [46,47]. Before the application step, Brunauer-Emmet-Teller (BET) analysis was carried out to evaluate the specific surface area and the total pore volumes of the three different stone materials. Afterwards, the consolidated stones samples were investigated under natural aging and laboratory test conditions, i.e. UVB aging. In fact, it is recommended to run both accelerated and natural aging tests in parallel to accurately evaluate materials durability [21]. Stereomicroscopic measurements were carried out to observe the variations in the physical and morphological characteristics of the treated surfaces, while colorimetric and gloss [48] measurements were performed to evaluate the chromatic variations which can occur on the surfaces after the consolidation treatments due to natural and artificial aging. Beside the consolidation effectiveness, the knowledge of the aesthetic variations occurring on historic surfaces treated with different consolidants after aging is of interest for a large community of end-users (e.g. architects, curators, conservators). Moreover, only few studies have been focused on the effect of venetian environment on weathering of the stone investigated [49,50]; with still a lack of knowledge on their consolidation and aesthetic surface variations before and after aging testing.

2. Experimental

2.1. Materials

All the commercial products tested were provided by CTS (Altavilla Vicentina, Italy). NanoRestore is a 2-propanol dispersion of Ca(OH)₂ NPs (5 g/L solid concentration). NanoEstel is an aqueous colloidal dispersion of nano-sized silica (solid content 30%) stabilized with sodium hydroxide (NaOH < 0.5%). Acril 33 is an aqueous emulsion (solid content 46%) of ethylacrylate and methylmethacrylate copolymer while Acril ME is a water based micro emulsion (solid content 41%) of the polymer poly(butyl methacrylate).

Vicenza, Arenaria and Istria stones 5 × 5 × 2 cm³ were provided by Laboratorio Morselletto (Vicenza, Italy), with a porosity of approx. 27, 5 and 0.7%, respectively, which confirmed data already reported in literature [51–53]. Vicenza stone is a light ivory calcareous rock, principally composed by calcite and dolomite, extracted from the Oligocene horizons in Colli Berici (Vicenza, Italy). It is the result of the sedimentation of innumerable minute fossils, which create its texture. Arenaria is a clastic sedimentary rock composed mainly by sand-sized minerals or rock grains with a dark grey color. Istria stone is instead a sedimentary compact rock with a micritic structure and a whitish color, formed during the lower Cretaceous. According to their features, the stones types described above have been extensively used as building materials in venetian architectures.

2.2. Nano-based and acrylates consolidants characterization

The dispersion stability of each consolidant was carried out by dynamic light scattering (DLS) and centrifugal separation analysis (CSA). Hydrodynamic particle diameter was measured by DLS by means of a multi-angle Nicomp ZLS Z3000 (Particle Sizing System, Port Richey, FL, USA) with an optical fiber set at 90° scattering angle

($W = 25$ mW, $\lambda = 639$ nm, at 25°C). Particle sedimentation velocity was calculated by CSA, employing the Multiwavelength Dispersion Analyzer LUMiSizer 651 at $\lambda = 470$ nm. Briefly, the samples were analyzed in polycarbonate cuvette with 10 mm optical path every 50 seconds at 25°C and 2800 rotation per minute (RPM). The transmission profiles, which are the raw data generated by CSA, moved from the lowest values of transmittance (indicating the highest amount of particles in the suspension) to the maximum transmittance, corresponding to the total sedimentation of particles in the cuvette (i.e. plateau). The variation of the transmission profiles over time and space allowed to calculate particle sedimentation velocity [54]. The overall results from DLS and CSA were reported as an average of three independent measurements.

After the physico-chemical characterization of the commercial dispersions, the consolidation test was carried out by applying Nanorestore, NanoEstel, Acril 33 and Acril ME on Vicenza, Arenaria and Istria stones. Before the consolidation treatment, the stone blocks were carefully washed and brushed in distilled water for 3 times in order to remove all the soluble salts and then dried in a static oven at 60°C . The consolidants were applied by brush until refusal and the samples were maintained in controlled conditions ($T = 25^\circ\text{C}$ and $UR = 30\%$) until reaching a constant weight. The amount of absorbed product was estimate as the difference in weight between the consolidated and the untreated stone samples for three independent measurements (10 weight measurements for each consolidated stone). Three samples for each substrate were prepared.

2.3. Stones characterization

Stereomicroscopic measurements were carried out with a Nikon SMZ1270 with magnifications of 10 or $20\times$ on the treated surfaces. The films morphology was recorded by a Nikon DS-Fi2 camera with Nikon Digital Sight DS-L3 software.

Brunauer-Emmet-Teller (BET) analysis was carried out using a ASAP 2010 of MicroMetrics to evaluate the specific surface area ($\text{m}^2 \text{g}^{-1}$) and the total pore volumes of the different stones using nitrogen multilayer adsorption measured as a function of relative pressure. Before BET analysis the samples were degassed at 10^{-3} Torr at 130°C for 12 hours. BET analysis was conducted at -196°C , temperature of condensation of the N_2 . The total pores volume was determined at P/P_0 of 0.98.

The stones consolidated with the tested formulations were investigated as fresh and under natural and UVB aging conditions. Natural aging of the samples was carried out exposing the samples to Venice-Mestre (Italy) outdoor conditions in a rigid plastic support with an inclination of 60° over 2 years. UV accelerated aging tests were carried out in a UVB chamber, under a monochromatic UVB radiation ($\lambda = 254$ nm) at $28 \pm 2^\circ\text{C}$ and relative humidity of 45% up to 1200 hours. The variation of treated samples color was monitored at incremental time intervals, monthly for natural aging and

100 hours for the UVB aging. The color measurements were carried out by a Konica Minolta spectrophotometer according to CIE Lab color space method [55,56]. The parameters L^* , a^* , b^* were simultaneously collected. L^* stands for the lightness ($L^* = 0$ corresponds to black, $L^* = 100$ corresponds to white), while a^* and b^* are the color-opponent dimensions: a^* is the red/green balance ($-a^*$ corresponds to green and $+a^*$ corresponds to red) and b^* is the yellow/blue balance ($-b^*$ corresponds to blue and $+b^*$ corresponds to yellow). The total variation of color (ΔE^*) was calculated by the equation $[(\Delta L^*)^2 + (\Delta a^*)^2 + (\Delta b^*)^2]^{1/2}$. The parameters ΔL^* , Δa^* and Δb^* refer to the difference between the aged samples and the untreated ones ($\Delta L^* = L^*_{t=x} - L^*_{t=0}$; $\Delta a^* = a^*_{t=x} - a^*_{t=0}$; $\Delta b^* = b^*_{t=x} - b^*_{t=0}$).

The specular gloss of the untreated, treated and aged stone samples, i.e. the ratio of the luminous flux reflected from the samples in the specular direction for a specified source and receptor angle, was determined with a Picogloss 503 (Ericksen) at the incident angle of 20° , according to ASTM D523-08, 2004 [28]. The gloss retention ($\Delta\text{gloss} \%$) was calculated between the untreated and the consolidated surface as $[(\text{gloss}_{(\text{untreated})} - \text{gloss}_{(\text{treated})})/\text{gloss}_{(\text{untreated})} \times 100]$ and between the unaged and aged samples as $[(\text{gloss}_{(t=0)} - \text{gloss}_{(t=x)})/\text{gloss}_{(t=0)} \times 100]$.

3. Results and discussion

3.1. Colloidal characterization of consolidants

The colloidal stability of Nanorestore $\text{Ca}(\text{OH})_2$ and NanoEstel SiO_2 NPs dispersions was investigated by CSA and DLS techniques. In detail, as far as particle sedimentation velocity, a method already developed [57] was applied to Nanorestore and Nanoestel and the transmittance profiles of the two nano-based dispersions are displayed in Fig. 1. As it can be clearly observed by transmittance profiles, the settling of Nanoestel NPs is very low if compared to Nanorestore results, showing sedimentation velocities $\leq 0.01 \mu\text{m/s}$ at gravity vs $0.04 \mu\text{m/s}$ calculated for Nanorestore. This indicates the higher stability of Nanoestel with respect to Nanorestore in alcoholic dispersion.

Furthermore, hydrodynamic particle size of the tested dispersions was determined by DLS. A population with an average hydrodynamic particle size of 336 ± 34 nm was detected for Nanorestore dispersion while 165 ± 28 nm was obtained for Nanoestel.

As far as the acrylic derivatives, the emulsions were opportunely diluted for CSA and DLS measurements (see Fig. S1 in the Supporting Information). Sedimentation velocity values and average size distribution were $\leq 3 \times 10^{-4} \mu\text{m/s}$ and 70 ± 15 nm for Acril 33 and $\leq 8 \times 10^{-4} \mu\text{m/s}$ and 47 ± 7 nm for Acril ME. In conclusion, the highest colloidal stability of both acrylic emulsions with respect to the nano-based dispersions investigated was proved.

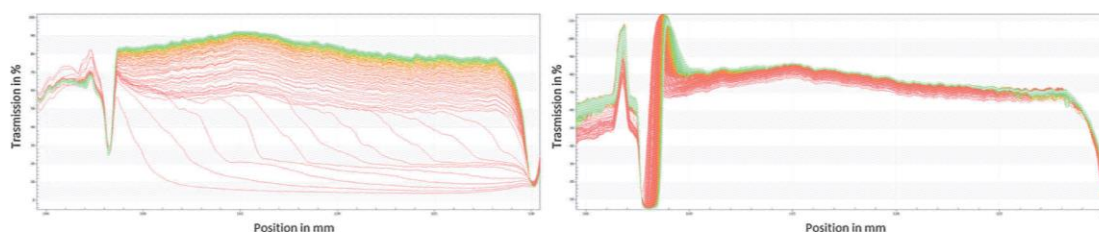


Fig. 1. Typical transmission profiles at 2800 RPM of Nanorestore dispersion (left) and Nanoestel dispersion (right).

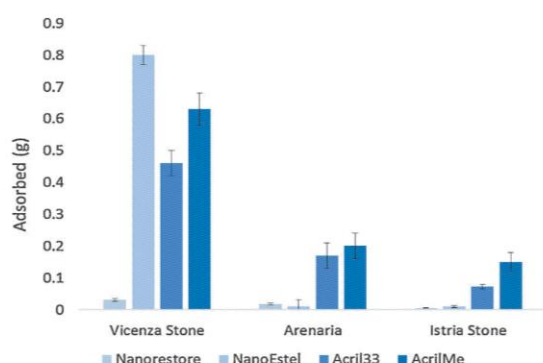


Fig. 2. Comparison among NanoRestore, NanoEstel, Acril 33 and Acril ME adsorption from Vicenza, Arenaria and Istria stones.

The amount of NanoRestore, NanoEstel, Acril 33 and Acril ME adsorbed on the three different stone substrates was measured as weight difference and the overall data are reported in SI (Table S2). Adsorption results (Fig. 2), according to BET measurements, showed as Vicenza stone is the material with the highest capacity to adsorb the consolidants investigated because of its biggest pores size. On the other hand, Istria stone showed the lowest adsorption of consolidants, as expected for a microporous material. Comparing the recorded amounts of the different consolidants adsorbed, NanoRestore and NanoEstel showed the lowest values of adsorption (<0.04 g) for each stone investigated, except for NanoEstel which was strongly adsorbed on Vicenza stone (0.80 g). NanoEstel probably better penetrate in Vicenza stone pores because of its smaller particles size with respect to NanoRestore. Acril 33 and Acril ME were instead absorbed in relevant amounts with respect to inorganic nano-based materials by all the stones investigated. This finding can be ascribed to the different way in which inorganic NPs and acrylates interact with the substrates, acrylates in fact usually form a film on the surface of the stones.

To better understand this behavior, the surface morphology of Vicenza, Arenaria and Istria stones was further investigated by stereo microscope analysis (Fig. 3), before and after each consolidation treatment. The results highlighted that the stone samples treated with NanoRestore underwent a slightly whitened of the surface. As far as the surface treated with NanoEstel, a thin homogeneous transparent and bright film without cracks was observed, while Acril 33 and Acril ME completely changed the original aspects of the stone supports creating a transparent, bright and thick film

3.2. Stone surface characterization

3.2.1. Consolidated stones

The surface area and the total pore volumes of the different stones were investigated by BET method before the consolidants applications and confirmed the micro- meso- and macro-porosity of Istria, Arenaria and Vicenza stone respectively (Table S1 in SI).

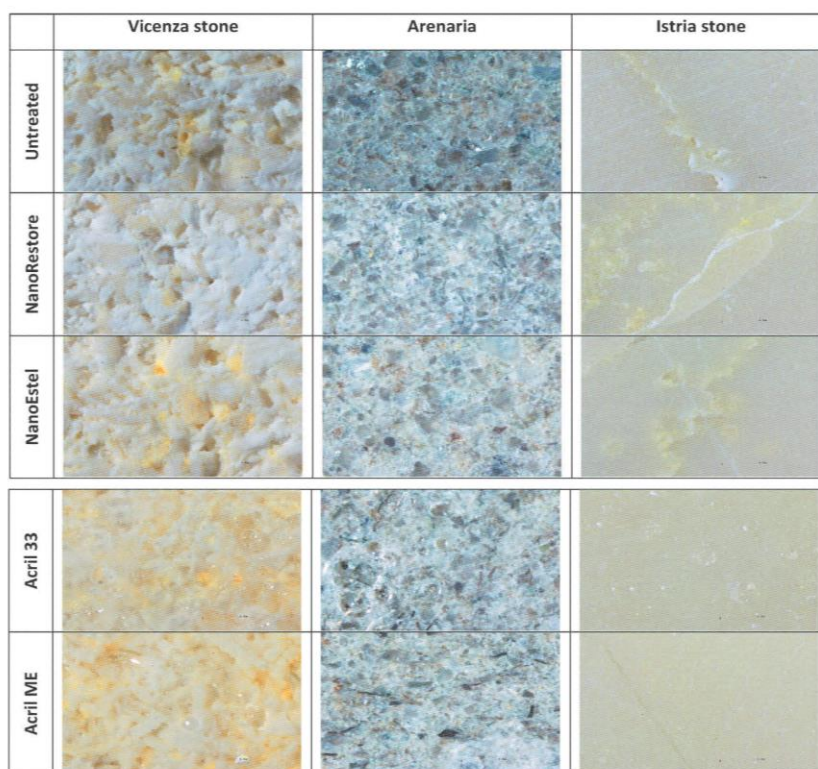


Fig. 3. Micrographs (20 ×) of the surface morphology of the stone samples before (untreated) and after the consolidation treatment with NanoRestore, NanoEstel, Acril 33 and Acril ME.

Please cite this article in press as: G. Gheno, et al., Consolidation of Vicenza, Arenaria and Istria stones: A comparison between nano-based products and acrylate derivatives, Journal of Cultural Heritage (2017), <https://doi.org/10.1016/j.culher.2018.02.013>

Table 1
Color parameters Δa^* , Δb^* , ΔL^* and ΔE and gloss variation ($\Delta gloss\%$) values determined for Vicenza, Arenaria and Istria stone after the consolidation treatments with NanoRestore, NanoEstel, Acril 33 and Acril ME.

Stone sample	Consolidant	Δa^*	Δb^*	ΔL^*	ΔE	$\Delta gloss\%$
Vicenza	NanoRestore	-1.59	5.89	5.11	7.96 (0.76)	-13 (0.1)
	NanoEstel	-0.97	8.17	3.08	8.78 (1.15)	33 (0.1)
	Acril 33	-0.62	11.25	1.90	11.42 (2.37)	-173 (0.2)
Arenaria	Acril ME	0.30	13.58	-1.94	13.72 (0.72)	-39 (0.1)
	NanoRestore	-1.10	5.46	5.43	7.78 (0.65)	-22 (0.2)
	NanoEstel	-0.83	7.11	0.29	7.16 (0.77)	-54 (0.2)
Istria	Acril 33	-0.82	6.56	0.88	6.67 (0.69)	-1109 (0.1)
	Acril ME	-0.70	6.59	0.11	6.63 (0.33)	-1256 (0.2)
	NanoRestore	-0.74	6.64	3.55	7.57 (1.37)	-18 (0.2)
Istria	NanoEstel	-0.58	9.15	2.25	9.44 (1.86)	-51 (0.2)
	Acril 33	-0.85	8.56	2.24	8.89 (2.54)	-666 (0.3)
	Acril ME	-1.16	8.39	0.85	8.51 (1.51)	-527 (0.2)

Data are average of three measurements (standard deviation in brackets).

with a large number of air bubbles. In result, the polymeric layer covering the surface appeared to change the natural morphology of the stone and to occlude the pores.

Furthermore, colorimetric and gloss analysis allowed to observe variations in terms of ΔE and $\Delta gloss\%$ with respect to the untreated stones (Table 1). A general tendency of the treated stone samples to yellowing was observed and, as it can be seen in the color graph of Fig. 4, this chromatic variation induced the simultaneous decrease of a^* values (shift to green shades) and the increase of b^* values (shift to yellowing shades). On the other hand, the lightness variations (i.e. increment in the L^* values), as shown in Table 1 indicated

a slightly shift towards clearer shades (whitening effect of the consolidants). This behavior was shown mostly for the stone samples consolidates with $Ca(OH)_2$ NPs.

In general, the overall results in Table 1 for Vicenza stone highlighted the best performances of NanoRestore in terms of color and gloss retention among the consolidants tested, showing the lowest ΔE (7.96) and $\Delta gloss\%$ (-13) values. Small color and gloss variations ($\Delta E=8.78$ and $\Delta gloss\%=-33$) were also recorded after NanoEstel treatment. Thus, both the inorganic NPs exhibited good consolidant performances by maintaining the original characteristics of the untreated surface. However, they presented opposite trends in term of gloss variation. NanoRestore in fact, induced a slightly decrease in the gloss of the treated surface (negative values of $\Delta gloss\%$, indicating an increase of the surface brilliance), while NanoEstel showed positive values of $\Delta gloss\%$ (indicating more opacity than the untreated material). On the other hand, significant variations of color and gloss retention were recorded for Vicenza stone treated with the two acrylic-based consolidants. In particular, the highest values of $\Delta gloss\%$ (-173) recorded for Vicenza stone treated with Acril 33, highlighted a surface modification after the treatment.

As far as Arenaria, even if Acril 33 and Acril ME seemed the most compatible consolidants with ΔE values of 6.67 and 6.63 respectively, they formed a glossy layer on the surface of the stones that changes significantly the gloss values of the original materials with extremely high $\Delta gloss\%$ variations in both cases.

Finally, taking into account Istria stone, the most compatible consolidant was also in this case NanoRestore (Table 1), which induced a slightly whitening of the surface but not a significant

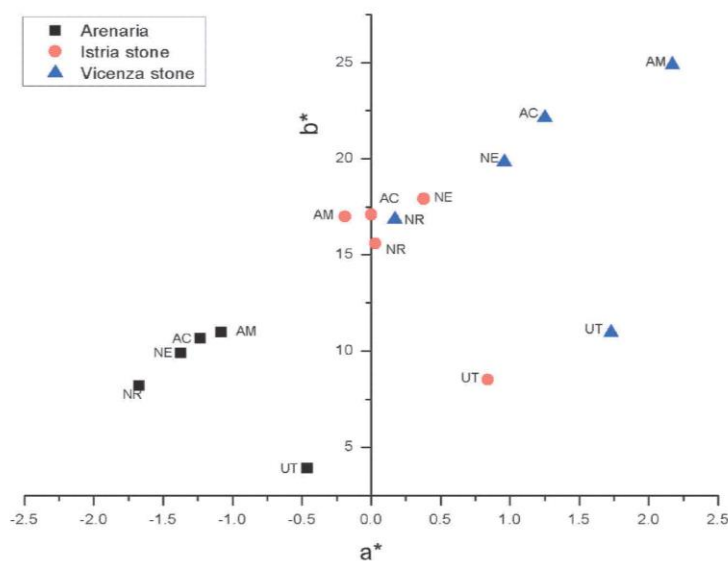


Fig. 4. Plot of a^* vs b^* values (color graph) determined for untreated (UT) Vicenza stone (Δ), Arenaria (■) and Istria stone (O) and treated samples with NanoRestore (NR), NanoEstel (NE), Acril 33 (AC) and Acril ME (AM).

Please cite this article in press as: G. Gheno, et al., Consolidation of Vicenza, Arenaria and Istria stones: A comparison between nano-based products and acrylate derivatives, Journal of Cultural Heritage (2017), <https://doi.org/10.1016/j.culher.2018.02.013>

variation in the color parameters ($\Delta E = 7.57$) and in the gloss values ($\Delta \text{gloss \%} = -18$). The nanosilica-based consolidant induces similar variation in the color parameters ($\Delta E = 9.44$) but higher gloss variations ($\Delta \text{gloss \%} = -51$) with respect to NanoRestore. Acrylates present high gloss variations of the treated surfaces towards highly negative values, indicating an increase of the surface brilliance after the stone treatment. In conclusion, the overall results in Table 1 suggested that the inorganic NPs consolidants showed the lowest color and gloss surface variation for all the treated stones (Fig. 4).

3.2.2. Natural and UVB aging of treated stones

Stone samples treated with NanoRestore, NanoEstel, Acril 33 and Acril ME were exposed to different aging environments, a natural outdoor aging over 2 years (in Venice-Mestre, Italy) and an artificial (UVB) aging for 1200 hours. Total color (ΔE) and gloss ($\Delta \text{gloss \%}$) variations values obtained after both aging experiments are reported in Table 2.

As far as natural aging, Vicenza stone treated samples showed the highest ΔE variations regardless the consolidant applied, with values ranging from 21.6 to 25.6, while for Arenaria and Istria stones, the lowest ΔE values were observed for samples treated with nano-based consolidants (values ten times lower than those obtained for the treatment with acrylate derivatives). Furthermore, ΔE variations over time were also investigated along the two years of aging experiments performed and the overall results obtained for each consolidant are reported in Fig. 5. From these data, it can be clearly observed the highest and fast increment of ΔE for all the stones samples treated with Acril 33 and Acril Me emulsions.

In detail, as displayed by the color graph reported in Fig. S2 (SI), the total chromatic variations observed for the different stones are principally linked to a shift in the coordination color towards a

Table 2

ΔE and $\Delta \text{gloss \%}$ values determined for Vicenza, Arenaria and Istria stone after natural outdoor and UVB aging.

Stone sample	Consolidant	Natural aging		UVB aging	
		ΔE	$\Delta \text{gloss \%}$	ΔE	$\Delta \text{gloss \%}$
Vicenza	NanoRestore	24.21 (2.64)	61 (0.1)	3.94 (1.65)	-8 (0.1)
	NanoEstel	21.63 (10.62)	50 (0.1)	2.98 (2.01)	-25 (0.1)
	Acril 33	25.61 (2.56)	59 (0.2)	4.88 (0.77)	-37 (0.6)
	Acril ME	24.18 (3.34)	75 (0.1)	4.18 (0.96)	-75 (0.1)
Arenaria	NanoRestore	9.90 (3.63)	33 (0.1)	1.51 (0.64)	-16 (0.2)
	NanoEstel	8.88 (2.44)	25 (0.1)	1.84 (1.47)	-37 (0.1)
	Acril 33	17.59 (4.55)	97 (0.3)	3.15 (0.78)	-17 (0.1)
	Acril ME	24.85 (1.83)	97 (1.2)	2.79 (0.36)	-24 (0.1)
Istria	NanoRestore	9.78 (1.33)	44 (0.1)	3.73 (1.25)	-22 (0.2)
	NanoEstel	11.43 (1.59)	40 (0.1)	2.67 (1.52)	-7 (0.1)
	Acril 33	22.43 (2.92)	91 (1.4)	2.85 (1.37)	-34 (0.3)
	Acril ME	18.39 (3.41)	87 (1.6)	3.85 (0.55)	-57 (0.2)

Data are average of three measurements (standard deviation in brackets).

red-brown dye. Moreover, as reported in Fig. S3 and Fig. S4 (SI), a decrease of L^* values was recorded for Vicenza and Arenaria stones treated with the different consolidants, except for Arenaria with NanoEstel. In this last case, a whitening of the surface occurred, probably due to the formation of a thick silica-based layer derived from the crosslinking of the consolidants precursor. On the other hand, as showed in Fig. S5 (SI), no significant variation in terms of lightness was determined for Istria stone exposed to natural aging, except for the samples treated with the two acrylic-based products, highlighting a massive darkening of the surface.

The colorimetric changes observed were mainly ascribed to deposition and entrapment of dust and atmospheric particles into the stone pores, as shown in Fig. S6 (SI). In the specific case of

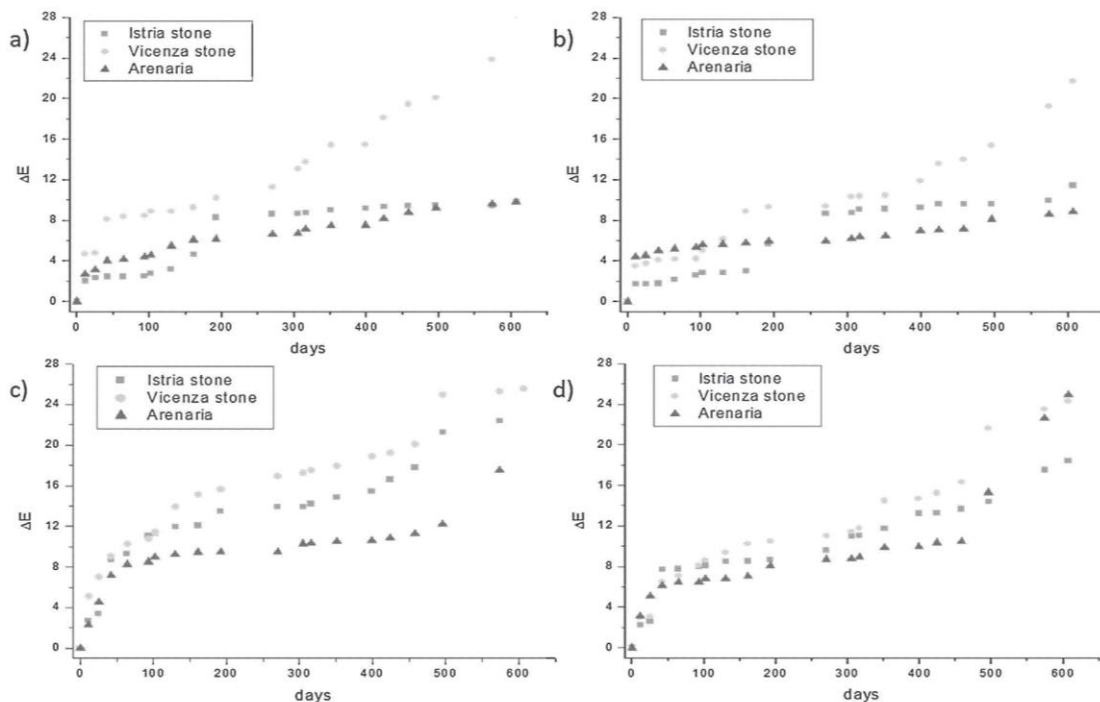


Fig. 5. ΔE parameter determined for the samples of Vicenza, Arenaria and Istria stone treated with (a) NanoRestore, (b) NanoEstel, (c) Acril 33 and (d) Acril ME and exposed at incremental time of natural outdoor aging conditions.

Please cite this article in press as: G. Gheno, et al., Consolidation of Vicenza, Arenaria and Istria stones: A comparison between nano-based products and acrylate derivatives, Journal of Cultural Heritage (2017), <https://doi.org/10.1016/j.culher.2018.02.013>

aged Vicenza stone samples, the shift towards the dark red color observed (Fig. S2 in SI) was finally attributed to the presence and diffuse growth of freshwater *Chlorophyta* microalgae, from the family of *Haematococcaceae*. Optical microscope analysis (Fig. 6) highlighted the presence of this unicellular microalgae (size ranging from 40 to 120 μm), which contains blood-red carotenoid pigment astaxanthin (3,3'-dihydroxy- β,β -carotene-4,4'-dione) in the cytoplasmic lipid globules of their cells. These pigments are produced and rapidly accumulated when the environmental conditions become unfavorable for normal cell growth [58,59], explaining the dark red color observed in treated Vicenza stones after the natural aging process.

Concerning $\Delta\text{gloss}\%$ (Table 2), the natural aging induced a reduction in the gloss values for all the stone samples investigated ($\Delta\text{gloss}\% > 0$). This indicates an opacification of the surface layers treated with the different consolidants. In detail, the inorganic NPs products, NanoRestore and NanoEstel, showed low gloss variations always $< 50\%$ for all the treated materials except for Vicenza stone

treated with NanoRestore (61%). The best performances for these consolidants were obtained in the treatment of Arenaria. On the other hand, Acril 33 and Acril ME consolidants induced a highest opacification of the treated surfaces with $\Delta\text{gloss}\%$ ranging from 59 to 97%.

As far as UVB aging (Table 2), the laboratory conditions employed for the test seemed to not induce any significant color variation of the treated stone surfaces, showing ΔE always < 5 . Also in this case, ΔE variations over time were investigated (Fig. 7), confirming the low color alteration induced by UVB aging conditions over 1200 hours of analysis.

Moreover, according to the stereo microscope images (Fig. S7 in SI), the surface appeared to be similar to the one of the original untreated stones, and the formation of craquelure or microfractures was not observed after 1200 hours of UVB aging.

As far as $\Delta\text{gloss}\%$ (Table 2), conversely to what observed during natural aging, UVB aging induced an increase in the gloss values of the surface. The increment of the brightness of the surface can be

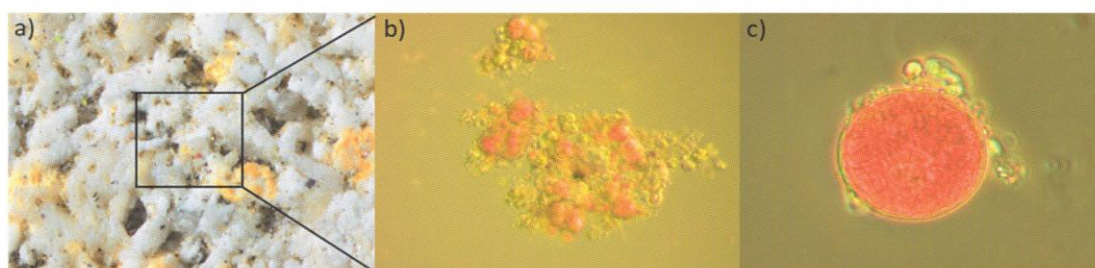


Fig. 6. Micrographs of Vicenza stone treated with NanoRestore and exposed over two years to outdoor conditions. a: stone surface at 20 \times ; b: Chlorophyta microalgae observed on the surface at 200 \times ; c: Chlorophyta microalgae at 400 \times .

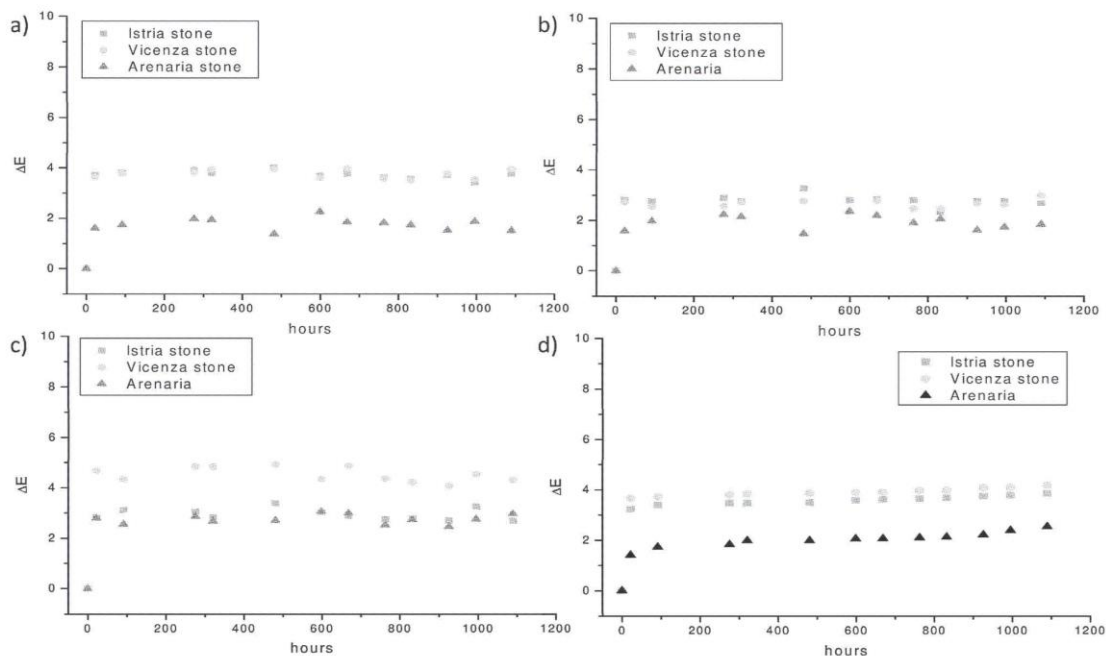


Fig. 7. ΔE parameter determined for the samples of Vicenza, Arenaria and Istria stone treated with (a) NanoRestore, (b) NanoEstel, (c) Acril 33 and (d) Acril ME and exposed at incremental time of UVB aging conditions.

Please cite this article in press as: G. Gheno, et al., Consolidation of Vicenza, Arenaria and Istria stones: A comparison between nano-based products and acrylate derivatives, Journal of Cultural Heritage (2017), <https://doi.org/10.1016/j.culher.2018.02.013>

explained, in the cases of polymeric consolidants film of NanoEstel, Acril 33 and Acril Me, with an increase of the degree of polymerization of the commercial products exposed to UVB irradiation [60]. Furthermore, in the case of the NanoRestore, the increment of gloss can be ascribed to a further conversion of $\text{Ca}(\text{OH})_2$ NPs to CaCO_3 [18]. In general, a good resistance to photo-degradation was observed for all the stone surfaces treated with both the inorganic consolidants and Acril 33, with $\Delta\text{gloss} \%$ values ranging from -37 to -7 , while high variations were observed for AcrilMe (up to -75) (Fig. 7).

4. Conclusions

In this study, commercial Nanorestore, Nanoestel, Acril 33 and Acril ME were applied on Vicenza, Arenaria and Istria stones, for investigating their surface appearance after the consolidation treatment. The overall results obtained by the followed approach, in which colorimetric and gloss measurements were combined with stereo microscope analysis and adsorption measurements, provided useful insights on the most suitable product in the stones consolidation with respect to Venice environment. In detail, the worst performances in terms of highest color and gloss alterations of the stones surface were observed under natural aging conditions with respect to UVB. Among the three stones investigated, Vicenza stone resulted the most sensitive material towards aging degradation after the treatment with all the consolidants, while among all the consolidants applied, nano-based materials showed the best performances, highlighting the importance of nanotechnology in stone conservation field.

Acknowledgements

The authors are grateful to University Ca' Foscari of Venice for the financial support and to C.T.S. S.p.A. (Altavilla Vicentina, Vicenza, Italy) for the consolidants products investigated.

Appendix A. Supplementary data

Supplementary data associated with this article can be found, in the online version, at <http://www.sciencedirect.com> and <https://doi.org/10.1016/j.culher.2018.02.013>.

References

- [1] F. Corvo, J. Reyes, C. Valdes, F. Villaseñor, O. Cuesta, D. Aguilar, P. Quintana, Influence of air pollution and humidity on limestone materials degradation in historical buildings located in cities under tropical coastal climates, *Water, Air, Soil Pollut.* 205 (2009) 359, <http://dx.doi.org/10.1007/s11270-009-0081-1>.
- [2] A.H. Webb, R.J. Bawden, A.K. Busby, J.N. Hopkins, Studies on the effects of air pollution on limestone degradation in Great Britain, *Atmos. Environ. Part B: Urban Atmos.* 26 (1992) 165–181, [http://dx.doi.org/10.1016/0957-1272\(92\)90020-5](http://dx.doi.org/10.1016/0957-1272(92)90020-5).
- [3] M. Maguregui, A. Sarmiento, I. Martínez-Arkarazo, M. Angulo, K. Castro, G. Arana, N. Etxebarria, J.M. Madariaga, Analytical diagnosis methodology to evaluate nitrate impact on historical building materials, *Anal. Bioanal. Chem.* 391 (2008) 1361–1370, <http://dx.doi.org/10.1007/s00216-008-1844-z>.
- [4] M.F. Orihuela, J. Abad, J.F. González Martínez, F.J. Fernández, J. Colchero, Nanoscale characterisation of limestone degradation using scanning force microscopy and its correlation to optical appearance, *Eng. Geol.* 179 (2014) 158–166, <http://dx.doi.org/10.1016/j.enggeo.2014.06.022>.
- [5] G. Caneva, M.P. Nugari, O. Salvadori, *La biologia vegetale per i beni culturali*, I, 2nd ed., 2007.
- [6] L. Toniolo, M. Boriani, G. Guidi, *Built heritage: monitoring conservation management*, Springer International Publishing, Switzerland, 2015.
- [7] S.Y. Xie, J.F. Shao, W.Y. Xu, Influences of chemical degradation on mechanical behaviour of a limestone, *Int. J. Rock Mech. Min. Sci.* 48 (2011) 741–747, <http://dx.doi.org/10.1016/j.ijrmms.2011.04.015>.
- [8] M. Matteini, Inorganic treatments for the consolidation and protection of stone artefacts, *Conserv. Sci. Cult. Herit.* 8 (2008).
- [9] C. Conti, C. Colombo, D. Dellasega, M. Matteini, M. Realini, G. Zerbi, Ammonium oxalate treatment: evaluation by μ -Raman mapping of the penetration depth in different plasters, *J. Cult. Herit.* 12 (2011) 372–379, <http://dx.doi.org/10.1016/j.culher.2011.03.004>.
- [10] B. Doherty, M. Pamplona, R. Selvaggi, C. Miliani, M. Matteini, A. Sgamellotti, B. Brunetti, Efficiency and resistance of the artificial oxalate protection treatment on marble against chemical weathering, *Appl. Surf. Sci.* 253 (2007) 4477–4484, <http://dx.doi.org/10.1016/j.apsusc.2006.09.056>.
- [11] C. Conti, I. Aliatis, M. Casati, C. Colombo, M. Matteini, R. Negrotti, M. Realini, G. Zerbi, Diethyl oxalate as a new potential conservation product for decayed carbonatic substrates, *J. Cult. Herit.* 15 (2014) 336–338, <http://dx.doi.org/10.1016/j.culher.2013.08.002>.
- [12] D. Chelazzi, G. Poggi, Y. Jaidar, N. Toccafondi, R. Giorgi, P. Baglioni, Hydroxide nanoparticles for cultural heritage: consolidation and protection of wall paintings and carbonate materials, *J. Colloid Interface Sci.* 392 (2013) 42–49, <http://dx.doi.org/10.1016/j.jcis.2012.09.069>.
- [13] R. Giorgi, M. Ambrosi, N. Toccafondi, P. Baglioni, Nanoparticles for cultural heritage conservation: calcium and barium hydroxide nanoparticles for wall painting consolidation, *Chem. A Eur. J.* 16 (2010) 9374–9382, <http://dx.doi.org/10.1002/chem.201001443>.
- [14] R. Giorgi, L. Dei, P. Baglioni, A New method for consolidating wall paintings based on dispersions of lime in alcohol, *Stud. Conserv.* 45 (2000) 154–161, <http://dx.doi.org/10.1179/sic.2000.45.3.154>.
- [15] A. Pondelek, S. Kramar, M.L. Kikelj, A. Sever Škapin, In-situ study of the consolidation of wall paintings using commercial and newly developed consolidants, *J. Cult. Herit.* 28 (2017) 1–8, <http://dx.doi.org/10.1016/j.culher.2017.05.014>.
- [16] P. Baglioni, D. Chelazzi, R. Giorgi, G. Poggi, Colloid and materials science for the conservation of cultural heritage: cleaning, consolidation, and deacidification, *Langmuir*, 29 (2013) 5110–5122, <http://dx.doi.org/10.1021/la3045456n>.
- [17] V. Daniele, G. Taglieri, R. Quaresima, The nanolimes in cultural heritage conservation: characterisation and analysis of the carbonation process, *J. Cult. Herit.* 9 (2008) 294–301, <http://dx.doi.org/10.1016/j.culher.2007.10.007>.
- [18] C. Rodriguez-Navarro, E. Ruiz-Agudo, M. Ortega-Huertas, E. Hansen, Nanostructure and irreversible colloidal behavior of $\text{Ca}(\text{OH})_2$: implications in cultural heritage conservation, *Langmuir*, 21 (2005) 10948–10957, <http://dx.doi.org/10.1021/la051338f>.
- [19] P. Baglioni, D. Chelazzi, R. Giorgi, E. Carretti, N. Toccafondi, Y. Jaidar, Commercial $\text{Ca}(\text{OH})_2$ nanoparticles for the consolidation of immovable works of art, *Appl. Phys. A*, 114 (2014) 723–732, <http://dx.doi.org/10.1007/s00339-013-7942-6>.
- [20] P. Baglioni, D. Chelazzi, Nanoscience for the conservation of works of art, *The Royal Society of Chemistry*, 2013, <http://dx.doi.org/10.1039/9781849737630>.
- [21] M. Ambrosi, L. Dei, R. Giorgi, C. Neto, P. Baglioni, Colloidal particles of $\text{Ca}(\text{OH})_2$: properties and applications to restoration of frescoes, *Langmuir*, 17 (2001) 4251–4255, <http://dx.doi.org/10.1021/la010269b>.
- [22] L. Dei, B. Salvadori, Nanotechnology in cultural heritage conservation: nanometric slaked lime saves architectonic and artistic surfaces from decay, *J. Cult. Herit.* 7 (2006) 110–115, <http://dx.doi.org/10.1016/j.culher.2006.02.001>.
- [23] I. Natali, M.L. Saladino, F. Andriulo, D. Chillura Martino, E. Caponetti, E. Carretti, L. Dei, Consolidation and protection by nanolime: recent advances for the conservation of the graffiti, Carceri dello Steri Palermo and of the 18th century lunettes, SS. Giuda e Simone Cloister, Corniola (Empoli), *J. Cult. Herit.* 15 (2014) 151–158, <http://dx.doi.org/10.1016/j.culher.2013.03.002>.
- [24] R. Giorgi, D. Chelazzi, P. Baglioni, Nanoparticles of calcium hydroxide for wood conservation. The deacidification of the Vasa Warship, *Langmuir*, 21 (2005) 10743–10748, <http://dx.doi.org/10.1021/la0506731>.
- [25] R. Giorgi, L. Dei, M. Ceccato, C. Schettino, P. Baglioni, Nanotechnologies for conservation of cultural heritage: paper and canvas deacidification, *Langmuir*, 18 (2002) 8198–8203, <http://dx.doi.org/10.1021/la025964d>.
- [26] I. Natali, P. Tempesti, E. Carretti, M. Potenza, S. Sansoni, P. Baglioni, L. Dei, Aragonite crystals grown on bones by reaction of CO_2 with nanostructured $\text{Ca}(\text{OH})_2$ in the presence of collagen. Implications in archaeology and paleontology, *Langmuir*, 30 (2014) 660–668, <http://dx.doi.org/10.1021/la404085v>.
- [27] B. Salvadori, L. Dei, Synthesis of $\text{Ca}(\text{OH})_2$ nanoparticles from diols, *Langmuir*, 17 (2001) 2371–2374, <http://dx.doi.org/10.1021/la0015967>.
- [28] A. Nanni, L. Dei, $\text{Ca}(\text{OH})_2$ nanoparticles from W/O microemulsions, *Langmuir*, 19 (2003) 933–938, <http://dx.doi.org/10.1021/la026428o>.
- [29] T. Liu, Y. Zhu, X. Zhang, T. Zhang, T. Zhang, X. Li, Synthesis and characterization of calcium hydroxide nanoparticles by hydrogen plasma-metal reaction method, *Mater. Lett.* 64 (2010) 2575–2577, <http://dx.doi.org/10.1016/j.matlet.2010.08.050>.
- [30] V. Daniele, G. Taglieri, Nanolime suspensions applied on natural lithotypes: the influence of concentration and residual water content on carbonation process and on treatment effectiveness, *J. Cult. Herit.* 11 (2010) 102–106, <http://dx.doi.org/10.1016/j.culher.2009.04.001>.
- [31] V. Daniele, G. Taglieri, Synthesis of $\text{Ca}(\text{OH})_2$ nanoparticles with the addition of Triton X-100. Protective treatments on natural stones: preliminary results, *J. Cult. Herit.* 13 (2012) 40–46, <http://dx.doi.org/10.1016/j.culher.2011.05.007>.
- [32] E. Fratini, M.G. Page, R. Giorgi, H. Cölfen, P. Baglioni, B. Demé, T. Zemb, Competitive surface adsorption of solvent molecules and compactness of agglomeration in calcium hydroxide nanoparticles, *Langmuir*, 23 (2007) 2330–2338, <http://dx.doi.org/10.1021/la062023i>.
- [33] E. Hansen, E. Doehne, J. Fidler, J. Larson, B. Martin, M. Matteini, C. Rodriguez-Navarro, E. Pardo, C. Price, A. de Tagle, J. Teutonico, N. Wiess, A review of selected inorganic consolidants and protective treatments for porous calcareous materials, *Rev. Conserv.* 4 (2003) 13–25.
- [34] C. Rodriguez-Navarro, A. Suzuki, E. Ruiz-Agudo, Alcohol dispersions of calcium hydroxide nanoparticles for stone conservation, *Langmuir*, 29 (2013) 11457–11470, <http://dx.doi.org/10.1021/la4017728>.

Please cite this article in press as: G. Gheno, et al., Consolidation of Vicenza, Arenaria and Istria stones: A comparison between nano-based products and acrylate derivatives, *Journal of Cultural Heritage* (2017), <https://doi.org/10.1016/j.culher.2018.02.013>

- [35] G. Wheeler, Alkoxysilanes and the consolidation of stone, Getty Conservation Institute, Los Angeles, 2005.
- [36] M.J. Mosquera, D.M. de los Santos, A. Montes, L. Valdez-Castro, New nanomaterials for consolidating stone, *Langmuir*. 24 (2008) 2772–2778, <http://dx.doi.org/10.1021/la703652y>.
- [37] G.W. Scherer, S.A. Pardenek, R.M. Swiatek, Viscoelasticity in silica gel, *J. Non. Cryst. Solids*. 107 (1988) 14–22, [http://dx.doi.org/10.1016/0022-3093\(88\)90086-5](http://dx.doi.org/10.1016/0022-3093(88)90086-5).
- [38] G.W. Scherer, Theory of drying, *J. Am. Ceram. Soc.* 73 (1990) 3–14, <http://dx.doi.org/10.1111/j.1151-2916.1990.tb05082.x>.
- [39] A. Zornoza-Indart, P. Lopez-Arce, Silica nanoparticles (SiO₂): influence of relative humidity in stone consolidation, *J. Cult. Herit.* 18 (2016) 258–270, <http://dx.doi.org/10.1016/j.culher.2015.06.002>.
- [40] C. Horie, *Materials for conservation: organic consolidants, adhesives and coatings*, Butterworths, London; Boston, 1987.
- [41] R. Feller, On picture varnishes and their solvents, *Rev. and e*, 1985.
- [42] G. Amoroso, *Trattato di scienza della conservazione dei monumenti*, Alinea Editrice Firenze, Italy, 2002.
- [43] O. Chiantore, M. Lazzari, Photo-oxidative stability of paraloid acrylic protective polymers, *Polymer (Guildf)*. 42 (2001) 17–27, [http://dx.doi.org/10.1016/S0032-3861\(00\)00327-X](http://dx.doi.org/10.1016/S0032-3861(00)00327-X).
- [44] E. Jablonski, T. Learner, J. Hayes, M. Golden, Conservation concerns for acrylic emulsion paints, *Stud. Conserv.* 48 (2003) 3–12, <http://dx.doi.org/10.1179/sic.2003.48.Supplement-1.3>.
- [45] L. Lazzarini, *Pietre e marmi antichi. Natura, caratterizzazione, origine, storia d'uso, diffusione, collezionismo*, CEDAM, Padova, 2004.
- [46] P.M. Carmona-Quiroga, S. Martínez-Ramírez, H.A. Viles, Efficiency and durability of a self-cleaning coating on concrete and stones under both natural and artificial ageing trials, *Appl. Surf. Sci.* 433 (2018) 312–320, <http://dx.doi.org/10.1016/j.apsusc.2017.10.052>.
- [47] P. Munafo, G.B. Goffredo, E. Quagliarini, TiO₂-based nanocoatings for preserving architectural stone surfaces: an overview, *Constr. Build. Mater.* 84 (2015) 201–218, <http://dx.doi.org/10.1016/j.conbuildmat.2015.02.083>.
- [48] N. Careddu, G. Marras, The effects of solar UV radiation on the gloss values of polished stone surfaces, *Constr. Build. Mater.* 49 (2013) 828–834, <http://dx.doi.org/10.1016/j.conbuildmat.2013.09.010>.
- [49] P. Maravelaki-Kalaitzaki, G. Biscontin, Origin, characteristics and morphology of weathering crusts on Istria stone in Venice, *Atmos. Environ.* 33 (1999) 1699–1709, [http://dx.doi.org/10.1016/S1352-2310\(98\)00263-5](http://dx.doi.org/10.1016/S1352-2310(98)00263-5).
- [50] A. Paleni, S. Curri, *Biological aggression of works of art in Venice Biodeterior. Mater*, 1st ed., 2, Applied Science Publishers, London, 1972, pp. 392–400.
- [51] C. Manganelli Del Fa, La porosita nei materiali lapidei naturali e artificiali: problematiche di determinazione della porosita: correlazione tra caratteristiche fisiche dei materiali, porosita, dinamica dei fluidi, degrado e trattamenti conservativi, *Supplement*, Modena, 2002.
- [52] P. Maravelaki-Kalaitzaki, R. Bertoncello, G. Biscontin, Evaluation of the initial weathering rate of Istria stone exposed to rain action, in Venice, with X-ray photoelectron spectroscopy, *J. Cult. Herit.* 3 (2002) 273–282, [http://dx.doi.org/10.1016/S1296-2074\(02\)01236-0](http://dx.doi.org/10.1016/S1296-2074(02)01236-0).
- [53] E. Molina, G. Cultrone, E. Sebastián, F.J. Alonso, L. Carrizo, J. Gisbert, O. Buj, The pore system of sedimentary rocks as a key factor in the durability of building materials, *Eng. Geol.* 118 (2011) 110–121, <http://dx.doi.org/10.1016/j.enggeo.2011.01.008>.
- [54] D. Lerche, Dispersion stability and particle characterization by sedimentation kinetics in a centrifugal field, *J. Dispers. Sci. Technol.* 23 (2002) 699–709, <http://dx.doi.org/10.1081/DIS-120015373>.
- [55] International ASTM, ASTM D2244-16 – standard practice for calculation of color tolerances and color differences from instrumentally measured color coordinates, 2016.
- [56] G. Wyszecki, W. Stiles, *Color science: concepts and methods, quantitative data and formulae*, 2nd Edition, 2000, pp. 2000.
- [57] A. Brunelli, A. Zabeo, E. Semenzin, D. Hristozov, A. Marcomini, Extrapolated long-term stability of titanium dioxide nanoparticles and multi-walled carbon nanotubes in artificial freshwater, *J. Nanoparticle Res.* 18 (2016) 113, <http://dx.doi.org/10.1007/s11051-016-3412-3>.
- [58] M. Elliot, Morphology and life history of *Haematococcus pluvialis*, *Arch. Protistenk.* 82 (1934) 250–272.
- [59] S. Boussiba, Carotenogenesis in the green alga *Haematococcus pluvialis*: cellular physiology and stress response, *Physiol. Plant.* 108 (2000) 111–117, <http://dx.doi.org/10.1034/j.1399-3054.2000.108002111.x>.
- [60] G. Wypych, *Handbook of material weathering*, 5th Edition, Elsevier, 2013.

Appendix B

Temperature ($^{\circ}\text{C}$, Figure B1), relative humidity (% , Figure B2), rainfall (mm/month, Figure B3) and total solar irradiation (MJ/m^2 , Figure B4) parameters (ARPAV data, Favaro Veneto station) at which the consolidated stones samples were exposed during the two years of outdoor natural aging.

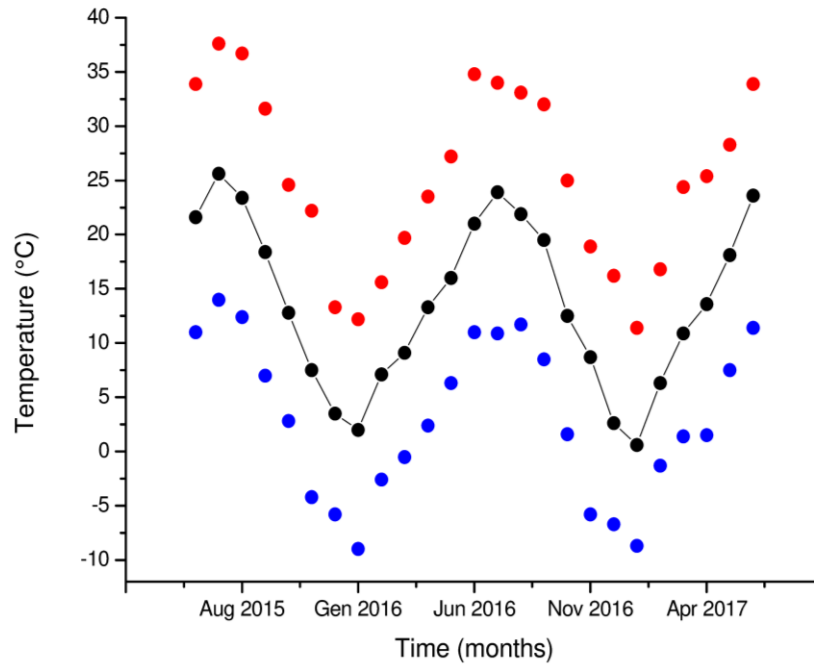


Figure B1. Monthly average (black dots) and maximum (red dots) and minimum (blue dots) values recorded from June 2015 and 2017 for the parameter temperature ($^{\circ}\text{C}$).

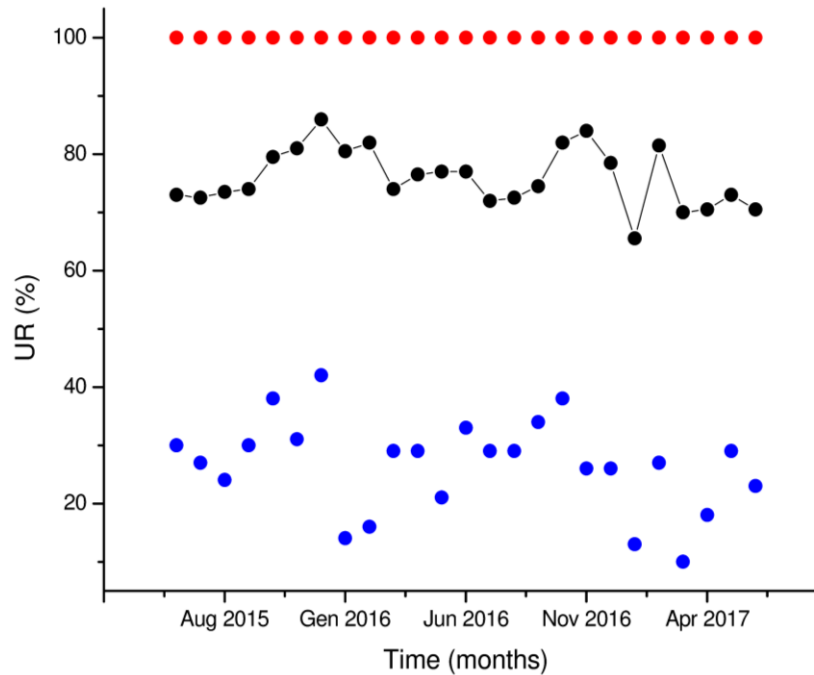


Figure B2. Monthly average (black dots) and maximum (red dots) and minimum (blue dots) values recorded from June 2015 and 2017 for the parameter relative humidity (%).

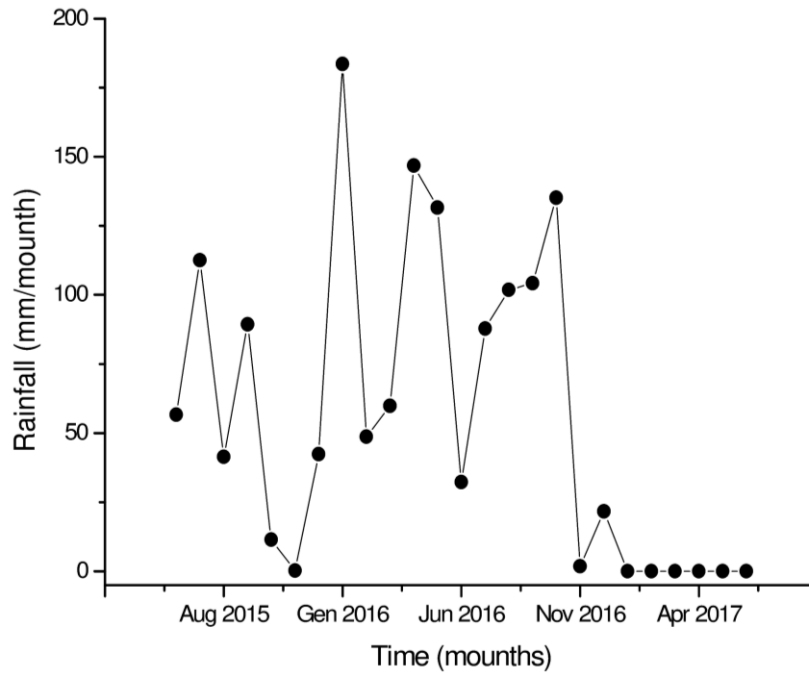


Figure B3. Monthly average (black dots) values recorded from June 2015 and 2017 for the parameter rainfall (mm/month).

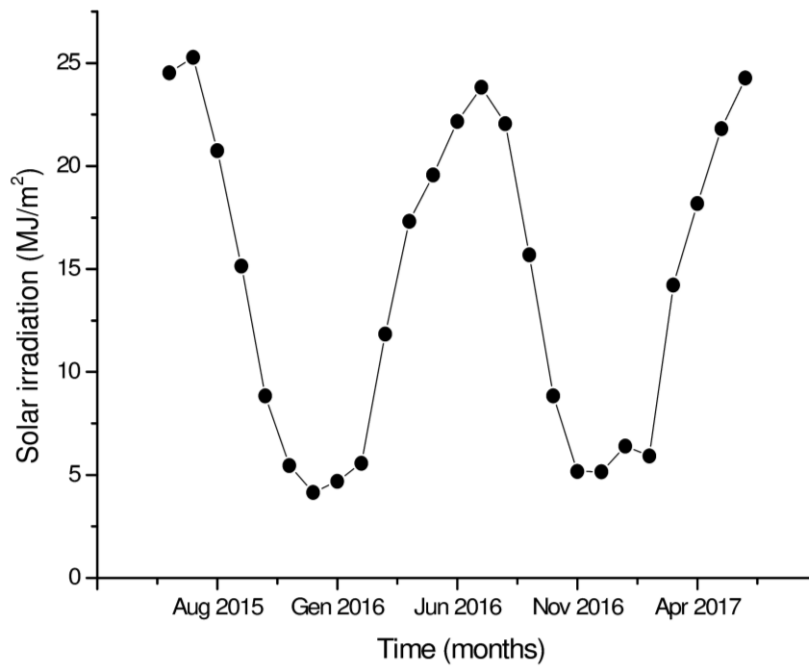


Figure B4. Monthly average (black dots) values recorded from June 2015 and 2017 for the parameter solar irradiation (MJ/m²).

Appendix C

Progress in Organic Coatings 101 (2016) 90–99



Contents lists available at ScienceDirect

Progress in Organic Coatings

journal homepage: www.elsevier.com/locate/porgcoat



Accelerated weathering degradation behaviour of polyester thermosetting powder coatings



Giulia Gheno^{a,*}, Renzo Ganzerla^a, Marco Bortoluzzi^a, Roberto Paganica^b

^a Dipartimento di Scienze Molecolari e Nanosistemi, Università Ca' Foscari di Venezia, Via Torino 155, 30170 Venezia Mestre, Italy

^b AkzoNobel Powder, Center of Expertise Manager for Industrial & Consumer in Coatings, Via Silvio Pellico 10, 22100 Como, Italy

ARTICLE INFO

Article history:

Received 29 January 2016

Received in revised form 6 July 2016

Accepted 9 July 2016

Keywords:

Accelerated weathering degradation

Thermosetting powder coatings

SUNTEST

UVA

UVB

Aging

ABSTRACT

The development of new products and their introduction in the market need rapid and reliable accelerated durability tests have the capacity to predict the service lifetimes of the materials. In this paper we report time-consuming standardised procedures in order to study the durability and the stability of typical polyester powder coatings, used as surface and structure white decorative finish in external architecture. SUNTEST, UVA and UVB accelerated aging tests were done in order to compare the resistance to weathering degradation of different kinds of coatings, four of standard durable and seven of superdurable type. The stability of the single formulation was determined through the evaluation of some chemicals and physical changes on aged samples respect the unaffected one. ATR measurements showed as the degradation differ mainly on the specific type of reactive binder system meanwhile the DSC measurements showed if the accelerate aging processes involved hydrolysis or an increase of the degree of polymerization. A good resistance, in term of gloss and colour retention, were also determined.

© 2016 Elsevier B.V. All rights reserved.

1. Introduction

The durability of an organic coating can be defined as its resistance to undesirable changes caused by the natural environment to which it is exposed during its service life. Thermosetting powder coatings have a very important role in the varnish industry because they guaranteed, after curing, a cross-linked structure that provides a high-quality, durable finish. Thermosetting powder coatings are made by a mix of pigments, additives and fillers in a particular binder (reactive system) suitable to create a coating film. The success of powder coatings in the last decades was originated from the attractive combination of features that they offer: ecological safety, cost effectiveness, energy saving and excellent product performance [1–3].

The choice of the resins is of paramount importance, because most of the properties of the final coating are determined by the binder system, where the resin is the mayor component [4–7]. Polyester-based powder coatings, the most used binder system in Europe, can be divided into standard and superdurable on the basis of its UV resistance. The standard durable coatings are based on resins manufactured mainly using the terephthalic diacid (TPA),

meanwhile superdurable polyester powder coatings mainly contain isophthalic acid (IPA) as diacid. The replacement of TPA with IPA provides, however, lower flexibility to the final system [8,9]. The better mechanical properties of the resins based on TPA seems due to a combined effect of several properties, i.e., cross linking density, thermal expansion coefficient and glass transition temperature [10]. All this features guaranteed, for the superdurable resins, a higher activation energies necessary to give the degradation process and, consequently, a high resistance. In our previous study, in fact, we had determinate an activation energies respectively of 214 and 251 kJ mol⁻¹ for a standard and a superdurable resins [11].

The mainly factors who affect the stability of materials are temperature, oxygen, water, pollutants, sunlight and, in particular, the UV radiation. During a natural exposure, instead, all the factors listed above will be presented and in some cases will be combined to each other or with other environmental variables, such as wind. In addition, the rate at which the binder system degradation occurs in natural conditions will be very widely, depending on the specific site temperature, time of year, substrate, polymer material, etc. For these reasons, the effect of the natural weathering degradation is difficult to estimate or predict correctly if we don't consider a wide range of artificial aging test [12]. The degradation of thermosetting powder coatings involved, in most of the cases, loss of gloss, discoloration, chalking, embrittlement, etc. Whereas a finish coating has aesthetics, further than protective function, the weath-

* Corresponding author.

E-mail address: giulia.gheno@unive.it (G. Gheno).

Table 1
Titanium dioxide characteristic.

TiO ₂	Description	TiO ₂ content%	Post-treatments	
			Al ₂ O ₃	SiO ₂
Kronos 2360	Titanium Dioxide manufactured by the chloride process with outstanding weather resistance	92	x	x
Ti-Pure R960	Titanium Dioxide manufactured by the chloride process with outstanding weather resistance	89	x	x

ering stability is an important paramount. The ideal evaluation of stability would be to expose the materials in its intended service environment but, for the industry, this is a nonviable and unacceptably very expensive and consuming time practice. Therefore, it is necessary to reduce the time needed to predict coating life. Standard test procedures are essential features of any technical process. The increase in global trade has encouraged co-operation between countries to produce international standard. For example, the International Organisation for Standardisation (ISO) brings together the standard support of twenty countries. One of the most common methods to assessing outdoor coating durability is to monitor the gloss loss and the colour retention during natural exposure in sites of extreme climates, typically Miami in Florida, Wittmann in Arizona and Hook in Holland [13]. To obtain satisfactory results in this way, however, five or more years of exposition are necessary. Florida exposure, in particular, are industrially accepted and provide an acceleration of approximately five years for every years of test. The most stringent weatherability limits for powder coatings are currently set by UNI AN ISO 2810 (or AAMA 2604-98), which specifies a minimum gloss retention of 50% after five years of exposure [13]. The weathering of materials can also accelerate with the use of an Equatorial Mounts with Mirror Acceleration (EMMA) or an Equatorial Mounts with Mirror Acceleration equipped with a water spray cycle (EMMAQUA) machines [14]. With these systems we accelerate the aging nine times faster than in a natural exposure thanks to movable aluminium mirrors that focused the rays of sun upon the samples. However, exactly as in the case of Florida exposure, the method results very expensive due to the necessity to send the samples in the specific climate region. Moreover the correlation between the natural exposure and laboratory tests its often poorly.

In a classical accelerate aging chamber, on the other hand, we imposed only one extreme weathering degradation parameter at every test and we recorded the response to this stress. The most common way to accelerate the degradation of materials consist in the use of higher intensity and/or shorter wavelength radiation. The photo-oxidation of powder coatings its mailing caused by the resin absorbing UV radiation: it is in fact the wavelength between 290–370 nm that causes most damages. The radiation source specified in European standard for artificial weathering devices are xenon, carbon and mercury arc beyond the fluorescence tube. The main advantages of this methods is the narrow control of the weathering conditions and the fast time of the acceptably response [9,15].

In this paper we report time-consuming standardised procedures in order to study the durability and the stability of typical polyester coatings used as surface and structure decorative finish in external architecture. Although the goal of this investigation is to estimate the service lifetime of common thermosetting powder coatings, accelerated weathering test has been performed according to UNI EN ISO 11341 [16] and UNI EN ISO 11507 [17]. In particular, we compared the resistance to artificial weathering degradation of different kinds of coatings, four of standard durable and seven of superdurable types. The stability of the single formu-

lation was determined through the evaluation of some chemical and physical changes on aged samples.

2. Experimental section

2.1. Materials

The polyester thermosetting coatings used in this study are available on market and were supplied by the manufacturer Akzo Nobel Coatings S.p.A. as typical white finish for external architecture surface. The polyester resins used for manufacturing these thermosetting powder coatings are of saturated type with carboxyl functionality. Small amount (2%) of many glycols, neopentylglycol (NPG) in particular, and polyacids were added. We compared the weathering stability of two different standard durable resins, where the main diacid is terephthalic acid (TPA), with four different types of superdurable binder systems, where the main diacid is the isophthalic one (IPA). The reactive system is based, in all the cases, on polyester resins and β -hydroxyalkylamides (CAS n. 6334-25-4) combined in a proportion of 96/4 or 95/5. In the formulations were also added two different types of titanium dioxide (Rutile) as white pigment who differ only for the purity of the mineral rutile as reported in Table 1. A filler (barium sulphate) and standard additives (flow agents, waxes, degassing agents and thermal stabilizers) are also present. In the samples indicated below as **A4**, **D5** and **D7** are also added two ultraviolet absorbers. The first is available in the market with the name Tinuvin 405, is based on tetramethyl piperidine (CAS n. 137658-79-8) and improve the stability of the film converting the UV radiation into heat. The second UV stabilizer, Tinuvin 622, is a hindered amine light stabiliser (HALS), a free radical scavengers. The details of the samples are reported in Table 2.

2.2. Methods

The artificially simulated sunlight test has been performed with a SUNTEST CPS+ made by ATLAS Heraeus Industrietechnik. The chamber was equipped with a Xenon NXe 1500B lamp and provided cycle of 102 min of immersion of the samples in distilled water interchanged with 18 min of radiation ($300 \leq \lambda \leq 800$ nm) at the maximum temperature of $60 \pm 2^\circ\text{C}$ [16]. The emissions of the lamp in the infrared and UV region were cut off with specific filters make the effect registered with this accelerate aging test strictly compared with those of natural exposure [2]. The differences in the physical and chemicals properties of the samples were monitored around every 250 h for a maximum time of exposure of 1000 h [16].

The UV aging tests has been performed with Accelerated Weathering Tester Model QUV-se made by QUV. In the UVB chamber the exposure of the panels provided cycles of 4 h of irradiation, with a peak intensity at 313 nm and maximum temperature of $50 \pm 2^\circ\text{C}$, interchanged with 4 h in condensing humidity at $40 \pm 2^\circ\text{C}$ [17]. The differences in the physio-chemical properties of the samples were monitored around every 50 h, for a maximum time of exposure of 1000 h [17]. UVA aging provided cycles of 4 h of irradiation, with peak intensity at 340 nm at the maximum temperature of $60 \pm 2^\circ\text{C}$,

Table 2
Powder coatings formulations.

Sample	Resin ^{a,b}	Resin number	TPA/PGG IPA/NPG ratio	Resin Acid Number (mgKOH/g)	Resin/Hardener ratio ^c	Pigment ^d	UV absorbers ^e
A	Standard Durable carboxylated polyester resin based on NPG and TPA	2618	98/2	30–36	95/5	Kronos 2360	
A1	Standard Durable carboxylated polyester resin based on NPG and TPA	4125	98/2	24–26	96/4	Kronos 2360	
A2	Standard Durable carboxylated polyester resin based on NPG and TPA	4125	98/2	24–26	96/4	Ti-Pure R960	
A4	Standard Durable carboxylated polyester resin based on NPG and TPA	2618	98/2	30–36	95/5	Kronos 2360	HALS + UV absorbers
D	Super Durable carboxylated polyester resin based on NPG and IPA	885	98/2	33–37	95/5	Kronos 2360	
D1	Super Durable carboxylated polyester resin based on NPG and IPA	4080	98/2	35–37	95/5	Kronos 2360	
D2	Super Durable carboxylated polyester resin based on NPG and IPA	9959	98/2	30–36	95/5	Kronos 2360	
D3	Super Durable carboxylated polyester resin based on NPG and IPA	4130	98/2	22–28	96/4	Kronos 2360	
D5	Super Durable carboxylated polyester resin based on NPG and IPA	4130	98/2	22–28	96/4	Kronos 2360	HALS + UV absorbers
D6	Super Durable carboxylated polyester resin based on NPG and IPA	4130	98/2	22–28	96/4	Ti-Pure R960	
D7	Super Durable carboxylated polyester resin based on NPG and IPA	4130	98/2	22–28	96/4	Ti-Pure R960	HALS + UV absorbers

^a Hydroxyl number of hardener 620–700 mg/KOH.

^b NPG = Neopentyl glycol.

^c Resin + Hardener = 64%.

^d pigment percentage of 30%.

^e UV absorbers percentage of 3%. All the samples contain also filler (3%), waxes, degassing and flow agent.

interchanged with 4 h in condensing humidity at $40 \pm 2^\circ\text{C}$ [17]. The differences in the physical and chemical properties of the samples were monitored around every 250 h for a maximum time of 5000 h of exposure [17].

The changes in chemical properties were determined using a Perkin Elmer System 2000 FT-IR couple with a Perkin Elmer AutoIMAGE FT-IR Microscope. ATR spectra were collected in the region from 4000 to 400 cm^{-1} and were recorded after different periods of aging, always in the same area of the expose surface. A total of 64 scans were collected at resolution of 4 cm^{-1} .

Differential Scanning Calorimetry measurements were made, in order to evaluate an eventually decrease or increase in the degree of polymerization, with a DSC Q100 of TA Instrument. The measurements provided a first cycle of heating, from 25 to 120°C with a heating rate of $10^\circ\text{C min}^{-1}$, followed by a cooling of the sample at 25°C and a second cycle of analysis, made with the same conditions of the first cycle.

Colour measurements were carried out using a SPECTRAFLASH SF600X spectrophotometer with a resolution of 2 nm , as indicated in the CIE Lab colour space method and recommended for the characterization of surfaces in industry [18]. The values of ΔE^* parameters, i.e. the colorimetric parameter that indicates the total variation of colour, was calculated on the basis of the equation $\sqrt{(\Delta L^*)^2 + (\Delta a^*)^2 + (\Delta b^*)^2}$ [19].

The specular gloss of the coatings, i.e. the ratio of the luminous flux reflected from the samples in the specular direction for a specified source and receptor angle, was determined with a Picogloss 503 made by Erichsen at the incident angle of 60° with a resolution of 1 GU , according to UNI EN ISO 2813 [20]. The retention of gloss was calculated on the basis of equations $\Delta\delta/\delta$ where the parameter $\Delta\delta$ is refer to the differences between the gloss parameter of the aged samples and the unaffected ones ($\Delta\delta = \delta_{(t=x)} - \delta_{(t=0)}$) while the parameter δ is refer to the specular gloss of the unaged ($\delta_{(t=0)}$) coatings.

3. Results and discussion

3.1. FTIR-ATR analysis

As weathering is a surface phenomenon, FTIR-ATR analyses are a good method to follow qualitatively the chemical changes which occur during degradation [8,10,21–24]. FTIR-ATR analyses were performed first at all on the standard and super durable unaffected samples. Table 3 summaries the main IR absorption bands of analytical interest identified in the studied powder coating. Meanwhile the standard durable resins are clearly noticeable from the super durable ones (Fig. 1), the single isophthalic or terephthalic resins studied are practically indistinguishable one to each other. Moreover, FTIR-ATR spectra do not permit to discern between the two different types of Titanium dioxide added as white pigment or on the presence of the UV absorbers.

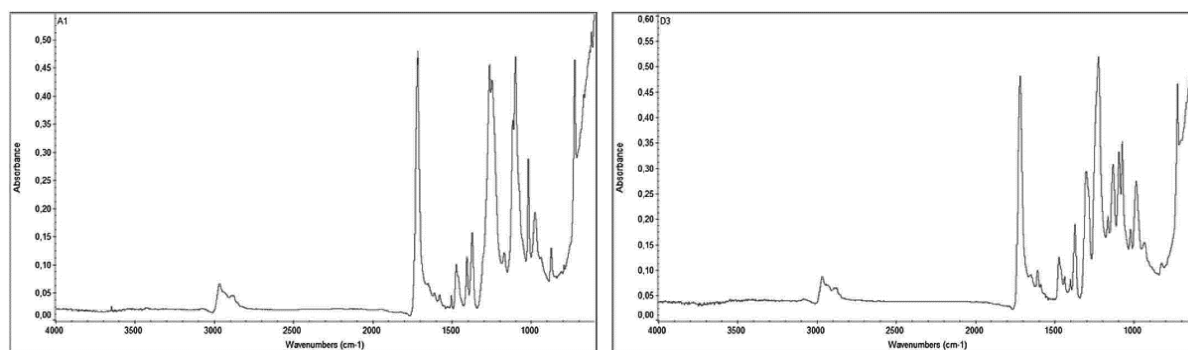
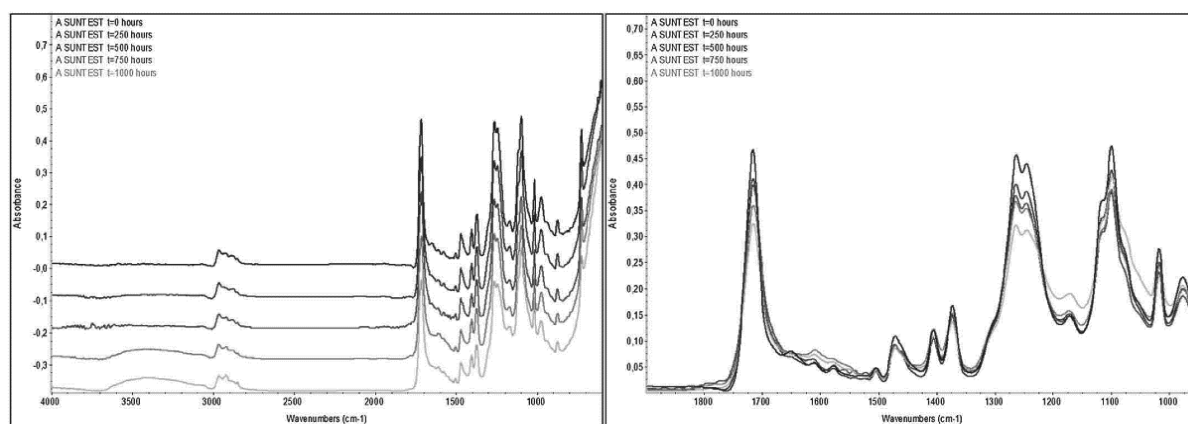
To follow the chemical and structural changes of the reactive binder, FTIR-ATR spectra were recorded after different periods of exposure for every accelerated aging test. In general were observed as the replacement of the pigment Kronos 2368 with the Ti-Pure R-960, do not involved any particular variation in the morphology of the FTIR-ATR spectra during the accelerated aging tests. In fact no particular chemical changes were observed, also if the titanium dioxide is a strong absorber of UV radiation and a photoactive specie that, especially in presence of humidity, promote the formation of hydroxyl radicals which initiate breakdown of the binder. Moreover we observed as the addition of the UV absorbers implied an incubation time. The lag in the time at which the morphology of the FTIR-ATR spectra started to change, can be assigned to the time necessary to have the consumption of the antioxidant additives mixed in the polyester resins.

The FTIR-ATR spectra recorded every 250 h of SUNTEST accelerated aging test for the sample **A** are reported in Fig. 2. The aging involved a progressive decrease of intensity and broadening of every IR band absorption associated to the resin system. This was observed especially for the signals at 1652 cm^{-1} , associated to the

Table 3

Main IR absorption bands of analytical interest identified for the standard and the superdurable powder coating.

IR absorption band (cm ⁻¹)	Functional group assignment	Compounds assignments
500	Ti—O	TiO ₂ (pigment)
939, 1264, 1431, 1611	bending C—O	Standard durable resin
976, 1072, 1578	bending —CH— aromatic	Standard and super durable resin
989, 1071, 1475	bending C=O	Super durable resin
1018	stretching C—O—C aromatic	Standard and super durable resin
609, 639, 983	SO ₄ =	Barium sulphate (filler)
1102, 1171	C—O—C aliphatic ester	Standard durable resin
1240, 1305	C—O	Super durable resin
1375	bending —CH ₃	Standard and super durable resin
1388, 1474	bending —CH ₂ — aliphatic	Standard and super durable resin
1504, 1578, 1611	Stretching —CH ₂ — terephthalic	Standard durable resin
1587, 1608	Stretching —CH ₂ — isophthalic	Super durable resin
1652	stretching C=O	Curing agent
1723	stretching C=O	Standard durable resin
1726	stretching C=O	Super durable resin
2852, 2927	stretching —CH ₂ —	Waxes (additives)
2890	stretching —CH—	Standard durable resin
2893	stretching —CH—	Super durable resin
2964	stretching —CH ₂ —	Standard durable resin
2968	stretching —CH ₂ —	Super durable resin
3079	stretching —CH— aromatic	Standard and super durable resin

**Fig. 1.** Comparison between the FTIR-ATR spectra of the standard A1 (left) and the superdurable D3 (right) powder coatings.**Fig. 2.** FTIR-ATR spectra recorded during the SUNTEST aging test for the sample A.

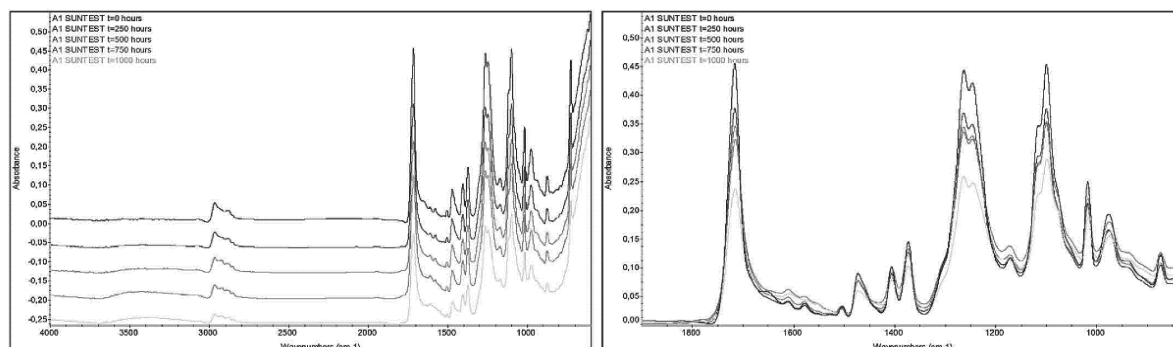


Fig. 3. FTIR-ATR spectra recorded during the SUNTEST aging test for the sample A1.

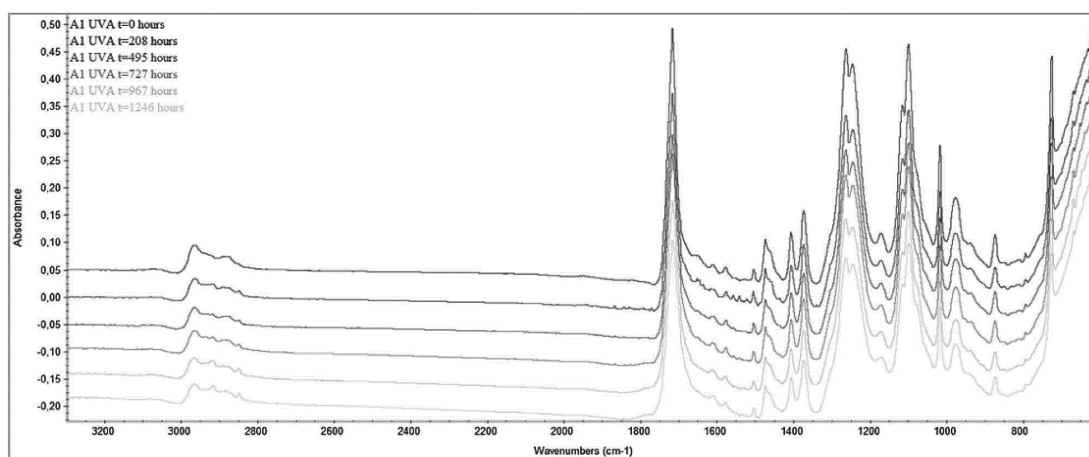


Fig. 4. FTIR-ATR spectra recorded, within the first 1000 h of aging, every 250 h of UVA exposure for the sample A1.

reticulate polymers. A loss of CH and CH₂ groups is recorded as expressed by decrease of absorption between 3000 and 2800 cm⁻¹ and around 1474 cm⁻¹. Starting from 500 h of aging, we observed the formation of a new peak at 3378 cm⁻¹ associated to the –OH stretching vibration of hydroxyl groups, which may originate from the hydrolysis of the ester groups. Simultaneously was recorded the appearance of carbonyl groups absorbing at higher frequencies than CO in ester groups, 1778 instead of 1723 cm⁻¹, that are assigned to anhydride carbonyl groups. A photo-induced oxidation mechanism generated by photo-inductor **R** can explain our data. *Maetens* [8], in fact, worked under several weathering condition and observed that in presence of oxygen the inductor **R** photolyse and produced a strong oxidizing radical **ROO•** that attacks preferably CH₂ in β-position to the CO ester group. The anhydride groups formed could be extracted by water, present in the aging chamber, causing cleavage of polymeric chains. For this reasons we hypothesized that the degradation process involved a hydrolytic mechanism. All the changes in the FTIR-ATR spectra just described were observed also for the formulation **A2**, **D1**, **D5**, **D7** and **D8**.

On the other hand, for the sample **A1**, **D**, **D2**, **D3** and **D6** we had identify in the variation of the degree of polymerization the mechanism of degradation. In fact, as shown for the sample **A1** in Fig. 3, also after 1000 h of aging test, was still present the peak at 1652 cm⁻¹ associated to a reticulate systems. The only difference

in the IR spectra recorded for increasing time of aging were a progressive decrease of intensity and a simultaneous broadening of the peak associated to the reactive system.

The variation of the degree of polymerization were recorded also for both the standard durable and for the four super durable resins subject at the UVA photo-oxidation. An example is reported in Fig. 4 for the standard durable powder coating **A1**. For the samples **A**, **A1**, **A2** and **A4** the decrease of intensity of the IR band absorption were recorded immediately, just after 250 h of aging. Meanwhile, in the cases of the super durable powder coatings, the decrease of intensity of the peak started only after 1000 h of exposure. Also in this case, these phenomenon was observed especially for the signals at 1652 cm⁻¹, associated to the reticulate polymers. Those signals disappear completely after 3000 h of aging in the standard durable sample, meanwhile were still present in the super durable powder coatings after 5000 h of aging. Moreover starting from 750 h of aging we had observed, only for the standard durable systems, the formation of a shoulder at 1778 cm⁻¹, associated to a formation of anhydride carbonyl groups.

The FTIR-ATR spectra recorded at increasing time of UVB aging for the sample **A1** is reported, as example, in Fig. 5. In all the samples where the binders were the standard durable resins, just from the first 72 h of UVB aging, we observed the formation of a shoulder at 1778 cm⁻¹, due to a formation of anhydride carbonyl degradation

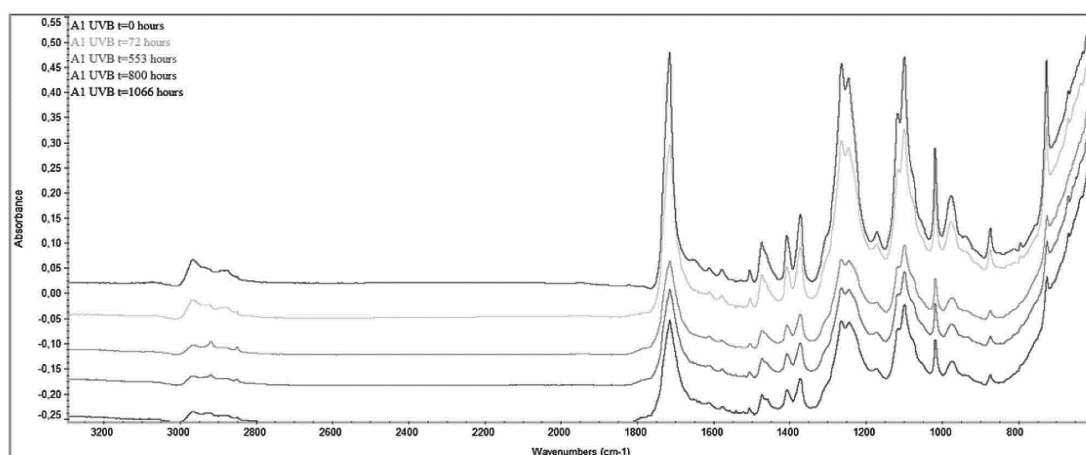


Fig. 5. FTIR-ATR spectra recorded during 1000 h of UVB exposure for the sample A1.

product. Moreover, we observed, at the same time, the disappear of the signal of the reticulate powder coatings at 1652 cm^{-1} . This behaviour was the same operated from the UVA radiation but, the higher energy of the UVB wavelength, make more fast and strength the change in the chemical structure of the polymer. Also for the super durable resins we had observed, but only after 200 h of aging, the progressive decrease of the intensity of each IR absorption, the simultaneously disappear of the peak at 1652 cm^{-1} and the formation of a shoulders at 1778 cm^{-1} . The more long time necessary to have a variation in the morphology of the FTIR-ATR spectra indicated a higher resistance of the super durable resins respect the UV photo-oxidation.

3.2. DSC analysis

In order to verify if the mechanism of degradation undergoes through a decrease or an increase of the degree of polymerization, we compared the values of the glass transition temperature (T_g) of the unaffected thermosetting powder coatings with the aged ones. In fact, it is well know that thermal analysis can allows the explanation of powder coating systems and show easily the mechanism of degradation [1,25]. An increase of the glass transition temperature is due to an increase of the degree of polymerization of the materials subjected to degradation process. Meanwhile a decrease of T_g values is associated to hydrolysis or to a decrease of the degree of polymerization of the thermosetting powder coatings [2]. In particular, the DSC measurements were performed before and after 1000 h of SUNTEST and UVB aging. The results are reported in Table 4.

For the samples **A**, **A2**, **D1**, **D5**, and **D7** subjected to SUNTEST aging, we had determinate negative values of ΔT_g meanwhile for the samples **A1**, **D**, **D2**, **D3** and **D6** the same parameter was positive. For this reasons, we confirmed that for the samples **A**, **A2**, **D1**, **D5**, and **D7** the aging process involved hydrolysis of the binder system meanwhile for the samples **A1**, **D**, **D2**, **D3** and **D6** the mechanism of weathering is the increase of the degree of polymerization. The sample **D1** showed the biggest value of ΔT_g parameter that pointed out the biggest change in chemical structure. On the other hand, the sample **D2**, characterized by the presence of the resin number 4130, showed the highest stability at the SUNTEST aging conditions.

For the samples undergoes to UVB accelerated aging test, the samples **A1**, **A4**, **D**, **D3**, **D5** and **D7** showed high T_g values in the

Table 4

Values of glass transition temperature (T_g) of the samples unaffected and subject to 1000 h of exposure in SUNTEST and UVB chamber.

Sample	$T_{gr=i}$ ($^{\circ}\text{C}$) ^a	$T_{gr=f}$ ($^{\circ}\text{C}$) ^b	ΔT_g	$T_{gr=f}$ ($^{\circ}\text{C}$) ^c	ΔT_g
A	65,34	64,67	-0,67	64,87	-0,47
A1	63,8	64,77	0,97	64,80	1,00
A2	66,27	63,61	-2,66	63,82	-2,45
A4	60,81	61,15	0,34	61,03	0,22
D	59,35	71,05	11,7	59,67	0,32
D1	77	59,49	-17,51	69,56	-7,44
D2	62,77	63,07	0,30	61,48	-1,29
D3	63,81	65,22	1,41	63,92	0,11
D5	61,91	60,88	-1,03	62,28	0,37
D6	64,03	65,73	1,7	63,04	1,01
D7	65	62,07	-2,93	61,71	-3,29

a = T_g values of unaffected sample; b = T_g values of the samples after 1000 h of SUNTEST aging; c = T_g values after 1000 h of UVB aging.

aged samples respect in the unaffected ones and this stand for an increase of the degree of polymerization. For the samples **A**, **A2**, **D1**, **D2** and **D7** we observed a lower T_g values for the aged sample and for this reason we can hypothesize that the degradation process involve a decrease of degree of polymerization. Also in this case, the sample **D1** showed the biggest value of ΔT_g parameter, or the worst stability. The resin that showed the highest stability at the UVB aging conditions was instead the number 4130.

It is important to note that, in general, the replacement of the pigment Kronos 2368 with the Ti-Pure R-960 involved, in both the aging processes, higher variation in the ΔT_g values. For this reason we individuated in the pigment Ti-Pure R-960 a less stable white pigment. From Table 4 is also visible as the UV absorbers increase the chemical resistance of the samples **A4** and **D5**. A negative effect was recorded only for the sample **D7**.

3.3. Loss of gloss

The parameter loss of gloss was used to follow the physical changes in the samples. In fact when a pigmented film degrades, the surface gradually roughens due to the body of the binder being lost, which is seen as a loss of gloss. The particle of the pigments remain upon the surface in the form of non-bound powdery: this process termed chalking. Gloss is assessed by monitoring the reflection from the surface of a visible beam of light in relation to a standard black glass surface. For the main common coating spec-

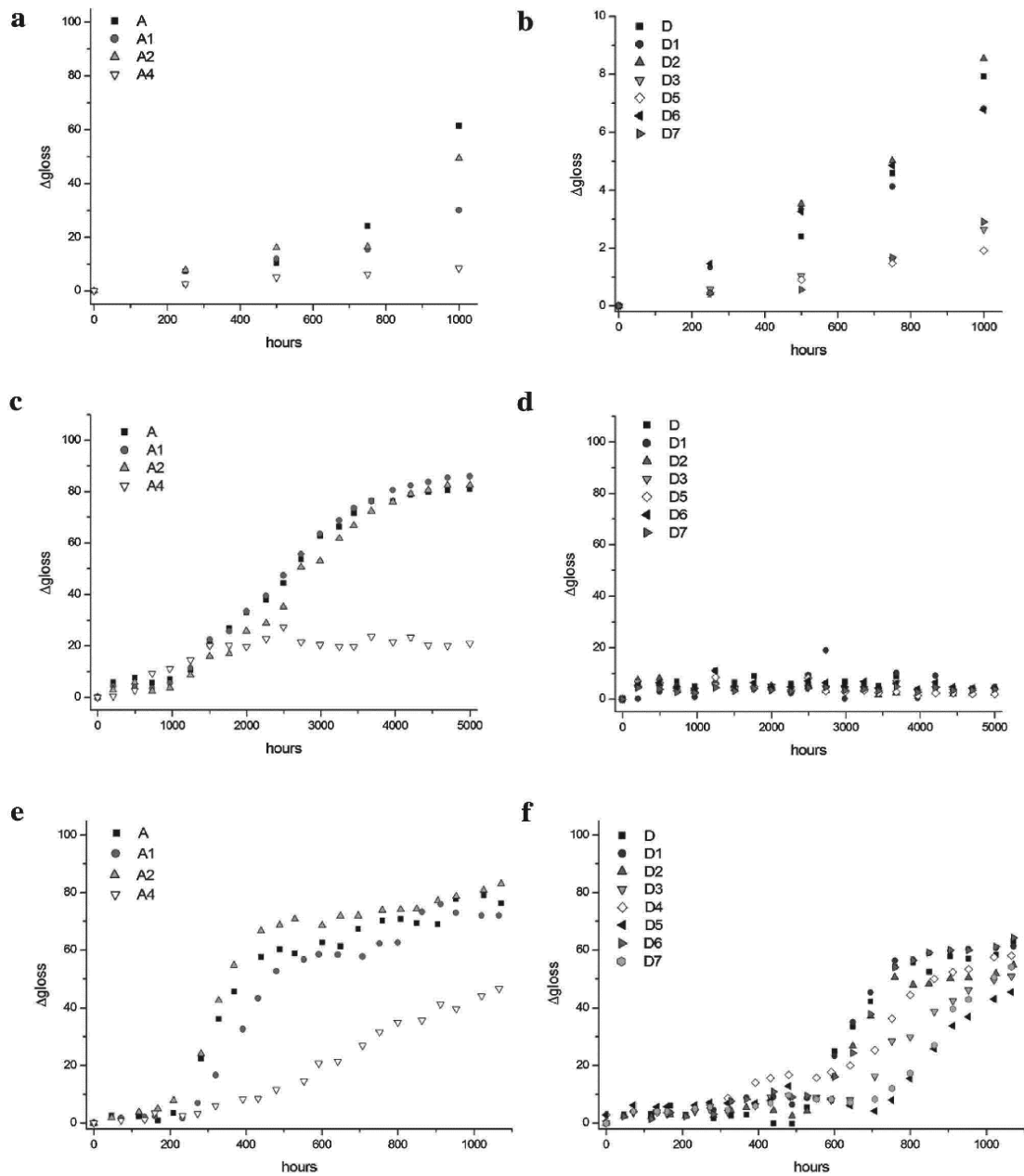


Fig. 6. Plot of loss of gloss versus time of aging determined for: (a) standard durable samples over the SUNTEST aging; (b) superdurable samples over the SUNTEST aging; (a) standard durable samples over the UVA aging; (b) superdurable samples over the UVA aging; (a) standard durable samples over the UVB aging; (b) superdurable samples over the UVB aging.

ification it is usually to indicate the maximum time to which the coating will maintain a gloss level greater than 50% of its original value [16,17,20]. In Fig. 6 are reported the plot of loss of gloss (Δ gloss%) versus time of aging determined for all the samples over the SUNTEST, UVA and UVB exposure.

In general we had determined a good resistance in terms of loss of gloss at every accelerated aging condition and the slope of the curves showing that photo-oxidation proceeds at a rate which is largely lower in an IPA-based than TPA-based powder coating. From the data was evident that the super durable resins number

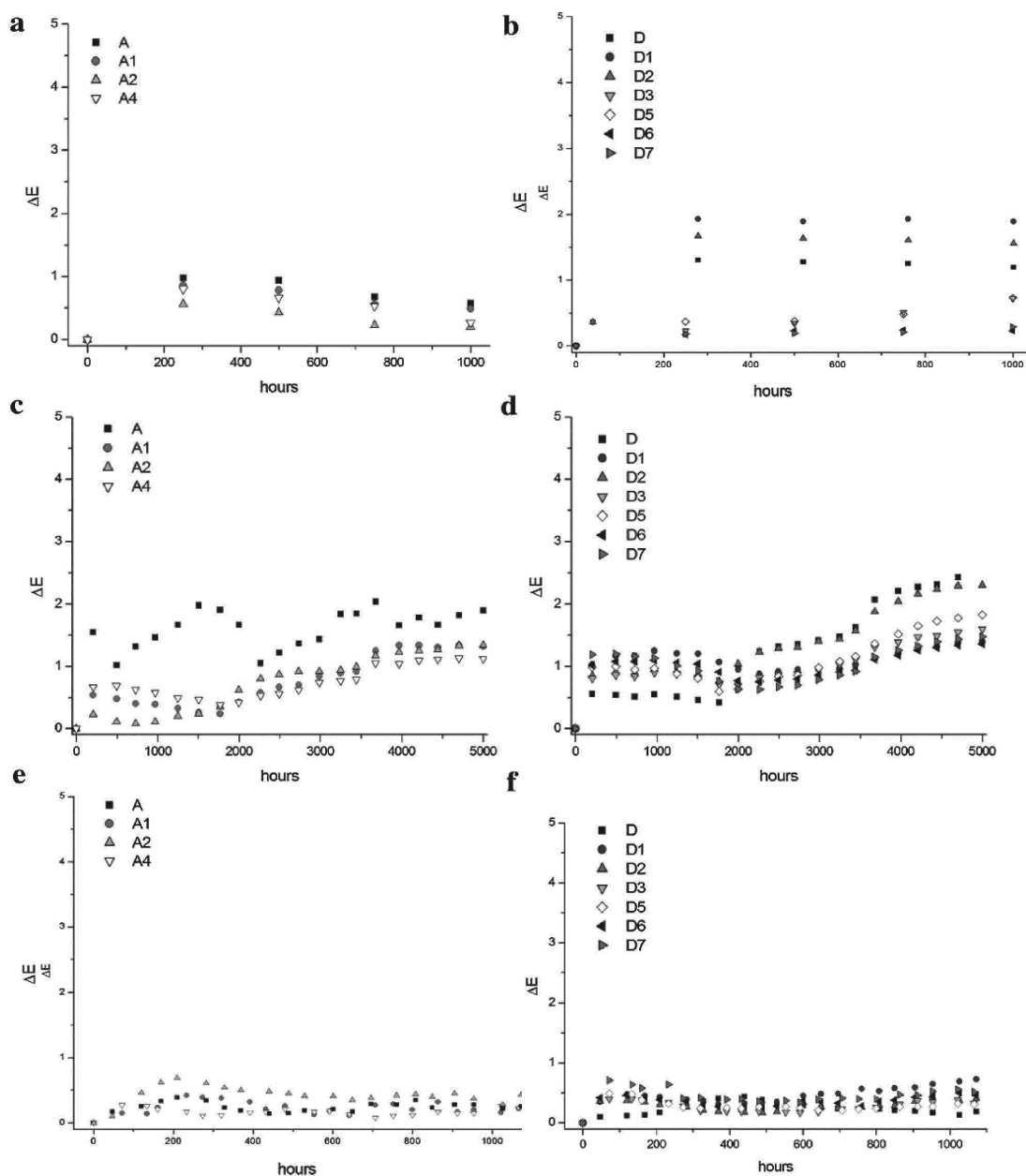


Fig. 7. Plot of ΔE parameter versus time of aging determined for: (a) standard durable samples over the SUNTEST aging; (b) superdurable samples over the SUNTEST aging; (c) standard durable samples over the UVA aging; (d) superdurable samples over the UVA aging; (e) standard durable samples over the UVB aging; (f) superdurable samples over the UVB aging.

4130 guaranteed the better weathering resistance and how the super durable systems supply high performance then the standard durable binder.

For the SUNTEST aging we can also observed as:

- after 1000 h of exposure, the loss of gloss were lower than 50 and 10% respectively for the standard and the superdurable resins;
- the sample **A1** showed a better resistance than the sample **A**, as demonstrated from the loss of gloss of 30 and 60%, respectively, at the end of the aging test;

- the addition of the UV absorbers improve enormously the retention of gloss of a standard durable powder coating with a loss of gloss lower than 10% at the end of the aging test;
- the weathering behavior of the superdurable resin number 4130 were not significantly influenced by addition of the UV absorbers.

The loss of gloss determined during the UVA exposure showed as:

- at the end of the accelerated aging test, the standard durable samples were seriously compromised. However, as indicate from the standard UNI AN ISO 2813, the loss of gloss were lower than 50% after 2500 h of aging and this stand for a good resistance at the UVA photo-oxidation;
- for the standard durable resins the process involved two consecutive steps (Fig. 6c). The first step, fast, ended after 1000 h of aging and implicated a loss of gloss lower than 10%. The second process, slow, ended around 5000 h of aging and involved a progressive and massive loss of gloss (higher of 80%);
- for the super durable formulations, the maximum loss of gloss determined were lower than 10% after 5000 h of exposure.

The plot of loss of gloss for the UVB aging showed as:

- for the standard durable resins, the process involved two consecutive steps. The first step, slow, ended until 275 h of exposure and involved a loss of gloss around 5%. In the following 100 h of aging, any variation in the gloss values was determined. From 400 h of exposure, started a rapid variation of the parameter with a loss of gloss of the 75% after 1000 h of exposure;
- the plot of loss of gloss versus time of aging for the superdurable samples showed two consecutive steps. The first step ended after 600 for the sample **D**, **D1** and **D2**, and after 750 h of exposure for the sample **D3** and involved, in all the cases, a loss of gloss lower than 10%. The second step, quick, implied a loss of gloss of 50–61% at the end of the aging test;
- the two standard durable resins showed an opposite trend respect the SUNTEST and the UV photo-oxidation. In fact, the best performance was guaranteed from the resin number 4125 when the photo-oxidation are strictly comparable at the solar ones meanwhile the high resistance at the UV photo-degradation was guaranteed from the resin number 2618.

3.4. Colorimetric measurements

The changes in physical properties were followed also through the evaluation of the change of colorimetric parameters. The values of the parameters a^* , b^* and L^* were recorded every 250 (for the SUNTEST and UVA) and 50 (for the UVB) hours of exposure.

The plot of ΔE parameter versus time of SUNTEST, UVA and UVB aging is reported in Fig. 7. The values of the ΔE parameter were ever lower than 5 and this stands for a good resistance in term of discoloration. Finally, we observed for all the aging tests, that the adding of UV absorbers or the replacement of the white pigments with one another not influenced the resistance to the photo-oxidation.

4. Conclusion

The more common techniques, which can be used to evaluate the rate and the extent of thermosetting powder coatings degradation occurs as a result of weathering degradation have been performed. FTIR-ATR measurements shown that, although

the samples degraded during both SUNTEST and UV exposure, the chemistry of degradation was different and depends mainly on the specific type of reactive system in the samples. The results highlight a faster rate of degradation occurred under UVB exposure. For all the accelerated aging tests, the addition of the UV absorbers implied an incubation time, or a lag in the time at which the morphology of the FTIR-ATR spectra started to change. Differential Scanning Calorimetry measurements shown whether accelerated aging processes involved hydrolysis or an increase of the degree of polymerization of the binder system. ΔT_g parameter permitted to individuate in the pigment Ti-Pure R-960 the less stable white pigment. Moreover, the DSC runs shown as the addition of UV absorbers increase the chemical resistance of the thermosetting powder coatings. Finally we had determined a good resistance in term of gloss and colour retention for all the samples testing. The more long time necessary to have a variation in the morphology of the FTIR-ATR spectra and the lower values of the Δ gloss and ΔE parameters determined for the super durable resins, confirmed their higher resistance to photo-oxidation.

Acknowledgments

The authors gratefully acknowledge the Cà Foscari University of Venice for the financial support (Ateneo Found 2013) and the Akzo Nobel Coatings (Como, Italy) for providing the samples.

References

- [1] J.M. Moranchó, J.M. Salla, X. Ramis, A. Cadenato, *Thermochim. Acta* 419 (2004) 181.
- [2] T.A. Misesv (Ed.), *Powder Coatings Chemistry and Technology*, Wiley, New York, 1991.
- [3] P.G. De Lange, *Powder Coatings—Chemistry and Technology*, Vicentz Network, Hannover, 2004.
- [4] S.S. Lee, H.K. Z.Y. Han, J.G. Hilborn, J.A. Manson, *Prog. Org. Coat.* 36 (1999) 79.
- [5] G. Bocchi, *Adv. Mater. Process.* 4 (1999) 23.
- [6] M. Korhoner, P. Starck, B. Lofgren, P. Mikkila, O. Horimi, *J. Coat. Technol.* 75 (2003) 67.
- [7] D.M. Howell, *Powder Coatings—The Technology Formulation and Application of Powder Coatings*, Wiley, London, 2000.
- [8] D. Maetens, *Prog. Org. Coat.* 58 (2007) 172.
- [9] B.W. Johnson, R. McIntyre, *Prog. Org. Coat.* 27 (1996) 95.
- [10] R. van der Linde, Eim G. Belder, Dan Y. Perera, *Prog. Org. Coat.* 40 (2000) 215.
- [11] G. Gheno, R. Ganzerla, M. Bortoluzzi, R. Paganica, *Prog. Org. Coat.* 78 (2015) 239.
- [12] (a) F. Deflorian, et al., *Prog. Org. Coat.* 59 (2007) 244;
- (b) F. Deflorian, et al., *Corros. Sci.* 50 (2008) 2360;
- (c) Y. Zhang, et al., *Polym. Degrad. Stabil.* 98 (2013) 527;
- (d) D.R. Bauer, *Polym. Degrad. Stabil.* 69 (2000) 307;
- (e) L.F.E. Jacques, *Prog. Polym. Sci.* 25 (2000) 1337;
- (f) S. Brunnee, et al., *O. Polym. Test.* 24 (2005) 25;
- (g) E. Scrinzi, S. Rossi, F. Deflorian, *Corros. Rev.* 29 (2011) 275.
- [13] (a) UNI EN ISO 2810, published 01-06-2005; Paints and varnishes – Natural weathering of coatings – exposure and assessment;
- (b) Accelerated and natural testing of materials, *Alpas Technology Oxford*;
- (c) E. Oakley, *J. Paint Technol.* 43 (1971) 555;
- (d) J.L. Scott, T.E. Anderson, *J. Oil Colour Chem. Assoc.* 59 (1976) 404;
- (e) H. Hoffman, K. Vogel, *Polym. Paint Colour J.* 175 (1985) 849;
- (f) A.B. Wooton, *Polym. Paint Colour J.* 183 (1993) 346.
- [14] UNI EN. ISO 877-3, published 2009; Plastics – Methods of exposure to solar radiation – Part 3: Intensified weathering using concentrated solar radiation. (c) ASTM D4364-13; Standard practice for performing outdoor accelerated weathering tests of plastic using concentrated sunlight.
- [15] (a) J.K. Fink, *Reactive Polymers Fundamentals and Application*, William Andrew Elsevier, 2013;
- (b) C. Decker, et al., *Polym. Degrad. Stabil.* 83 (2004) 309;
- (c) S. Rossi, et al., *J. Coat. Technol. Res.* 13 (2016) 427.
- [16] UNI EN. ISO 11341, published 01-09-2004; Paints and varnishes – Artificial weathering and exposure to artificial radiation – Exposure to filtered xenon-arc radiation.
- [17] UNI EN. ISO 11507, published 18-10-2007; Paints and varnishes – Exposure of coatings to artificial weathering – Exposure to fluorescent UV lamps and water.

- [18] ASTM D2244-11, Standard Practice for Calculation of Color Tolerances and Color Differences from Instrumentally Measured Color Coordinates.
- [19] G. Wyszecki, *Color Science; Concept and Methods Quantitative Data and Formulae*, Wiley, New York, 2000.
- [20] UNI AN ISO 2813:1999; *Paints and varnishes—Determination of specular gloss of non-metallic paint film at 20°, 60° and 85°*.
- [21] S.G. Croll, A.D. Skaja, *J. Coat. Technol.* 75 (2003) 85.
- [22] D.R. Bauer, J.L. Gerlock, R.A. Dickie, *Prog. Org. Coat.* 15 (1987) 209.
- [23] A. Rivaton, F. Serre, J.L. Gardette, *Polym. Degrad. Stab.* 62 (1998) 127.
- [24] G. Botelho, A. Queirós, S. Liberal, P. Gijssman, *Polym. Degrad. Stab.* 74 (2001) 39.
- [25] (a) B. Singh, N. Sharma, *Prog. Org. Coat.* 93 (2008) 561;
(b) R. Mafi, S.M. Mirabedini, M.M. Attar, S. Moradian, *Prog. Org. Coat.* 54 (2005) 164;
(c) D.F. Parra, et al., *Thermochim. Acta* 386 (2002) 143;
(d) S. Montserrat, Y. Calventus, J.H. Hutchinson, *Prog. Org. Coat.* 55 (2006) 35;
(e) R. van der Linde, E.G. Belder, D.Y. Perera, *Prog. Org. Coat.* 40 (2000) 215.

Appendix D. Scientific publications and conferences papers

- Gheno G, Ganzerla R, Bortoluzzi M, Enrichi F, Sintesi e proprietà luminescenti di scorpionato-complessi impiegati come marcatori in interventi di restauro, Atti del XV Congresso della Società Chimica Italiana divisione Chimica dell'Ambiente e dei Beni Culturali, Bergamo, June 2015.
- Gheno G, Ganzerla R, Bortoluzzi M, Paganica R, Accelerated weathering degradation behaviour of polyester thermosetting powder coatings, in *Progress in Organic Coatings* 101 (2016) pp 90–99.
- Uzumyemezoglu VS, Orsega EF, Gheno G, Le ceramiche di Iznik (XVI-XVII sec.): caratterizzazione storico-stilistica e indagini chimico-fisiche di campioni rappresentativi, Atti del Congresso "I Giovani e il Restauro", Roma, Gennuary 2016.
- Gheno G, Brunelli A, Badetti E, Marcomini A, Ganzerla R, On the stability of colloidal calcium hydroxide nanoparticles dispersion for stone conservation, Atti del XVI Congresso della Società Chimica Italiana divisione Chimica dell'Ambiente e dei Beni Culturali, Lecce, June 2016.
- Cavarro F, Ganzerla R, Gheno G, Manente S, Redolfi Bristol S, Zucchetta M, Franzoi P, Malavasi S, The price of beauty: habitat constraints on carotenoid-based colouration in a small euryhaline teleost, I Congresso Nazionale Congiunto SITE - UZI - SIB, Milano, August 2016.
- Gheno G, Badetti E, Brunelli A, Ganzerla R, Marcomini A, Consolidation of Vicenza, Arenaria and Istria stones: a comparison between nano-based products and acrylate derivatives, in *journal of cultural heritage* (2017).
- Cavarro F, Gheno G, Ganzerla R, Zucchetta M, Franzoi P, Malavasi S, Habitat constraints on carotenoid-based coloration in a small euryhaline teleost, *Ecology and Evolution* 00 (2018) 1-9.

References

- [1] Chiantore O, Rava A, *Conservare l'arte contemporanea, Problemi, Metodi, Materiali, Ricerche*, Mondadori Electa, Milano, 2005.
- [2] (a) Tessera E, Antonelli F, Sperti L, Ganzerla R, Maravelaki N, *Polym. Degrad. Stabil.* 110 (2014) 232; (b) Ferreira Pinto AP, Delgado RJ, *J. Cult. Herit.* 9 (2008) 38; (c) Ginell WS, Coffman R, *Stud. Conserv.* 43 (1998) 242; (d) Cavaletti R, Lazzarini L, Marchesini L, Marinelli G, A new type of epoxy resin for the structural consolidation of badly decayed stones, *Vth International congress on deterioration and conservation of stone, Lausanne, 2 (1985) 769*.
- [3] Bovey FA, Winslow FH, *Macromolecules, an introduction to polymer science*, Academic Press Inc Ltd., London, 1979.
- [4] Seymour Raymond B, *Additives for polymers, Introduction to polymer chemistry*, McGraw-Hill Book Company, New York. 1971.
- [5] Feller Robert L, *Accelerated Aging, Photochemical and Thermal Aspects*, The J. Paul Getty Trust, USA, 1994.
- [6] Feller Robert L, *Bulletin de l'Institute royale du Patrimoine artistique* 15 (1975) 135.
- [7] Horie V, *Materials for conservation, Organic consolidants, adhesives and coatings*, Taylor and Francis Group, New York, 2010.
- [8] For some examples see: (a) ASTM D2244:2016, Standard Practice for Calculation of Colour Tolerances and Colour Differences from Instrumentally Measured Colour Coordinates; (b) UNI EN ISO 11507:2007, Paints and varnishes - Exposure of coatings to artificial weathering - Exposure to fluorescent UV lamps and water; (c) UNI EN ISO 2810:2005, Paints and varnishes - Natural weathering of coatings - exposure and assessment; (d) UNI EN ISO 11341:2004, Paints and varnishes - Artificial weathering and exposure to artificial radiation - Exposure to filtered xenon-arc radiation; (e) UNI AN ISO 2813:1999; Paints and varnishes – Determination of specular gloss of non-metallic paint film at 20°, 60° and 85°; (f) ISO 105-A05:1996, Textiles - Tests for colour fastness - Part A05: Instrumental assessment of change in colour for determination of grey scale rating; (g) ISO 105-J03:1995, Textiles - Tests for colour fastness - Part J03: Calculation of colour differences; (h) ISO 10977:1993, Photography – Processed photographic colour films and paper paints – Methods for measuring image stability; (i) ISO 787-15:1986, General methods of test for pigments and extenders, Part 15: Comparison of resistance to light of coloured pigments of similar types; (j) ISO 473:1982, Lithopone pigments for paints - Specifications and methods of test.
- [9] Laidler Keith J, *Chemical kinetics*, Tata McGraw-Hill Publishing Company Ltd., New Delhi, 1978.

- [10] Wypych G, Handbook of Material Weathering (V Edition), ChemTech Publishing, Canada, 1995.
- [11] Grassie N, Scott G, Polymer degradation and stabilization, Cambridge University Press, New York, 1985.
- [12] Singh B, Sharma N, Polym. Degrad. Stabil. 93 (2008) 561.
- [13] Ghosh P, Polymer science and technology of plastics and rubbers, Tata McGraw-Hill Publishing Company Ltd., New Delhi, 1990.
- [14] Halim Hamid S, Handbook of polymer degradation (II Edition), CRC Press, New York, 2000.
- [15] Tayler DR, J. Macromol. Sci. Part C Polym. Rev. 44 (2004) 351.
- [16] Harvey JA, Chemical and Physical Aging of Plastics in Handbook of Environmental Degradation of Materials (II editions), Elsevier, 2012.
- [17] Ebnesajjad S, Surface and Material characterization techniques in Handbook of Adhesives and surface preparation, William Andrew Applied Science Publishers, 2011.
- [18] Dobkowski Z, Polym. Degrad. Stabil. 91 (2006) 488.
- [19] (a) Blaine RL, Kissinger HE, Thermochim. Acta 540 (2012) 1; (b) Wuzella G, Kandelbauer A, Mahendran AR, Teischinger A, Prog. Org. Coat. 70 (2011) 186; (c) Silva AML, Li RWC, Matos JR, Gruber J, J. Therm. Anal. Calorim. 59 (2006) 675; (d) Parra DF, Mercuri LP, Matos JR, Brito HF, Romano RR, Thermochim. Acta 386 (2002) 143; (e) Cho YS, Shim M, Kim S, Mater. Chem. Phys. 52 (1998) 94; (f) Starink MJ, Thermochim. Acta 288 (1996) 97; (g) Flynn JH, J. Therm. Anal. Calorim. 44 (1995) 499; (h) Ozawa T, Thermochim. Acta 203 (1992) 159; (i) Ozawa T, J. Therm. Anal. 2 (1970) 301; (l) Friedman HL, J. Polim. Sci., Part C 6 (1963) 183; (m) Kissinger HE, Anal. Chem. 29 (1957) 1702; (n) Šesták J, J. Therm. Anal. Calorim. 117 (2014) 3.
- [20] Svoboda R, Málek J, J. Therm. Anal. Calorim. 115 (2014) 1961.
- [21] Feldman D, J. Polym. Environ. 10 (2002) 163.
- [22] Bonaduce I, Carlyle L, Colombini MP, Duce C, Ferrari C, Ribechini E, Selleri P, Tiné MR, PLOS One 7 (2012) e49333.
- [23] Feller Robert L, Preservation of paper and textiles of historic and artistic value, Stage in deterioration of organic materials, J. C. Williams Ed, USA, 1997.
- [24] Feller Robert L, On Picture varnishes and their solvents, E.H. Jones (Eds.), Case Western Reserve University, 1971.

- [25] Jablonsky E, Learner T, Hayes J, Golden M, *Rev. Conserv.* 4 (2003) 3.
- [26] (a) Kashiwagi T, Hirata T, Brown JE, *Macromolecules* 18 (1985) 131; (b) Melo MJ, Bracci S, Camaiti M, Chiantore O, Piacenti F, *Polym. Degrad. Stabil.* 66 (1999) 23; (c) Chiantore O, Trossarelli L, Lazzari M, *Polym.* 41 (2000) 1657; (d) Lazzari M, Chiantore O, *Polym.* 41 (2000) 6447; (e) Kaczmarek H, Kaminâska A, van Herk A, *Eur. Polym. J.* 36 (2000) 767; (f) Chiantore O, Lazzari M, *Polym.* 41 (2001) 17; (g) Chiantore O, Lazzari M, *Polym.* 42 (2001) 17; (h) Bracci S, Melo MJ, *Polym. Degrad. Stabil.* 80 (2003) 533; (i) Favaro M, Mendichi R, Ossola F, Russo U, Simon S, Tomasin P, Vigato PA, *Polym. Degrad. Stabil.* 91 (2006) 3083; (l) Lazzari M, Scalarone G, Malucelli G, Chiantore O, *Prog. Org. Coat.* 70 (2011) 116.
- [27] Allen NS, *Degradation and stabilization of polyolefins*, Applied Science Publishers, London, 1983.
- [28] Lazzari M, Kitayama T, Hatada K, Chiantore O, *Macromolecules* 31 (1998) 8075.
- [29] Crook J, Learner T, *The Impact of Modern Paints*, Watson-Guption Publishers, New York, 2000.
- [30] Learner T, *Stud. Conserv.* 46 (2001) 225.
- [31] (a) Erlebacher JD, Mecklenburg MF, Tumosa CS, *Polym. Prepr.* 33 (1992) 646; (b) Whitmore PM, Colaluca VG, *Stud. Conserv.* 40 (1995) 51; (c) Whitmore PM, Colaluca VG, Farrell E, *Stud. Conserv.* 41 (1996) 250; (d) Jones FN, Mao W, Ziemer PD, Xiao F, Hayes J, Golden M, *Prog. Org. Coat.* 52 (2005) 9; (e) Camaiti M, Borgioli L, Rosi L, *Science and technology*, (2011) 100; (f) Milani C, Ombelli M, Morresi A, Romani A, *Surf. Coat. Technol.* 151 (2002) 273; (g) Allen NS, Parker MJ, Regan CJ, *Polym. Degrad. Stabil.* 47 (1995) 117; (h) Scalarone D, Lazzari M, Castelvetro V, Chiantore O, *Chem. Mater.* 19 (2007) 6107.
- [32] Chiu T, Thill B, Fairchok W, *Poly(2-ethyl-2-oxazoline): A New Water- and Organic-Soluble Adhesive in Water-Soluble Polymers: Beauty with Performance*, J. Glass ed., Washington, 1986.
- [33] (a) Lee SC, Chang Y, Yoon YS, Kim C, Kwon IC, Kim YH, Jeong SJ, *Macromolecules* 32 (1999) 1847; (b) Chamberlin TA, Madison NL, US Patent 4.001.160 (1997).
- [34] (a) Cataldi A, Deflorian F, Pegoretti A, *Int. J. Adhes. Adhes.* 62 (2015) 92; (b) Muros V, WAAC Newsletter 1 (2012) 9; (c) Ebert B, Singer B, Grimaldi N, *J. Am. Inst. Conserv.* 35 (2012) 62; (d) Patricia Smithen E, Turnbull R, *Stud. Conserv.* 55 (2010) 313; (e) Milton O'Connell C, *A Simple Solution to a Complex Problem: The Consolidation of Joan Miros Portrait of a Young Girl in Modern Paints Uncovered*, Getty Publications, Los Angeles, California, 2007; (f) Borgioli L, Cremonesi P, *Le resine sintetiche usate nel trattamento di opere policrome*, Ed Il Prato, Padova, 2005; (g) Arslanoglu J, WAAC Newsletter Volume 26 (2004) 14; (h) Shelton C, *The Use of Aquazol-Based Gilding Preparations*, American Institute for Conservation of Historic and Artistic Works paintings Specialty Group

Postprints, Norfolk, Virginia, 1996.

[35] Calore R, Frizza L, Jaxa-Chamiec M, Rizzonelli L, Stevanato N, Tisato F, Aquazol 500, Una possibile alternativa ecocompatibile alla colla animale nella preparazione degli stucchi per il restauro dei dipinti. Test preliminari per la stabilità, lavorabilità e comportamenti in Le fasi finali nel restauro delle opere policrome mobili, atti del Quinto congresso internazionale COLORE E CONSERVAZIONE, Trento, 2010.

[36] *Aquazol* Product Information Sheet, Polymer Chemistry Innovations, Inc..

[37] Wolbers RC, McGinn M, Duerbeck D, "Poly-(2-Ethyl-2-Oxazoline): A New Conservation Consolidant", in *Painted Wood: History and Conservation*, The Getty Conservation Institute, V. Dorge and F. Carey Howlett ed., Williamsburg, Virginia, 1994.

[38] Fardi T, Stefanis E, Panayiotou C, Abbott S, van Loon S, *J. Cult. Herit.* 15 (2014) 583.

[39] (a) Bernard AM, Molecular modelling of poly(2-ethyl-2-oxazoline), PhD thesis of the Georgia Institute of Technology, 2008; (b) Bosetti E, A Comparative Study of the Use of Aquazol in Paintings Conservation, *e- conservation magazine* 24 (2012) 72; (c) Arslanoglu J, Tallent C, *WAAC Newsletter* Volume 25 (2003) 12.

[40] Camaiti M, Borgioli L, Rosi L, *Science and Technology* (2011) 100.

[41] Ackroyd P, *Rev. Conserv.* 3 (2002) 3.

[42] Orsini S, La Nasa J, Modugno F, Colombini MP, *J. Anal. Appl. Pyrolysis* 104 (2013) 218.

[43] (a) Elias M, de la Rie RE, Delaney J, Charron E, Morales K, *Opt. Commun.* 266 (2006) 586; (b) Berns RS, de la Rie RE, *Stud. Conserv.* 48 (2003) 73; (c) de la Rie ER, *Stud. Conserv.* 32 (1987) 1.

[44] (a) de la Rie ER, Delaney J, Morales KM, Maines CA, Sung L-R, *Stud. Conserv.* 55 (2010) 134; (b) Delaney JK, de la Rie ER, Elias M, Sung L-R, Morales KM, *Stud. Conserv.* 53 (2008) 170.

[45] (a) Maines CA, de la Rie ER, *Prog. Org. Coat.* 52 (2005) 39; (b) Berns RS, de la Rie ER, *Stud. Conserv.* 48 (2003) 73.

[46] (a) Farmakalidis HV, Douvas AM, Karatasios I, Sotiropoulou S, Boyatzis S, Argitis P, Chryssoulakis Y, Kilikoglou V, *Mediterr. Archaeol. Ar.* 3 (2016) 213; (b) Piena H, *J. Am. Inst. Conserv.* 40 (2001) 59; (c) de la Rie RE, Shedrinsky AM, *Stud. Conserv.* 34 (1989) 9.

[47] Dunky M, *Int J. Adhes. Adhes.* 18 (1998) 95.

[48] Arslanoglu J, Learner T, *The Conservator* 25 (2001) 62.

- [49] Cimino D, Chiantore O, de La Rie ER, McGlinchey CW, Ploeger R, Poli T, Poulis JA, *Int. J. Adhes. Adhes.* 67 (2016) 54.
- [50] Stoye D, Freitag W, *Resins for Coating: Chemistry, Properties and Applications*, Hansen Publishers, Munich, 1996.
- [51] (a) Zhang Y, Zeng X, Ren B, *J. Coat. Technol. Res.* 6 (2009) 337; (b) Li H, Zhang Y, Zeng X, *Prog. Org. Coat.* 66 (2009) 167.
- [52] Peris-Vicente J, Baumer U, Stege H, Lutzenberger K, Gimeno Adelantado JV, *Anal. Chem.* 81 (2008) 3180.
- [53] Bonaduce I, Colombini MP, Degano I, di Girolamo F, La Nasa J, Modugno F, Orsini S, *Anal. Bioanal. Chem.* 405 (2012) 1047.
- [54] van Loon A, Genuit W, Pottasch C, Smelt S, Noble P, *Microchem. J.* 126 (2016) 406.
- [55] *Laropal A81* Product Information Sheet, BASF.
- [56] (a) Baglioni P, Chelazzi D, Giorgi R, Poggi G, *Langmuir* 29 (2013) 5110; (b) Natali I, Saladino ML, Andriulo F, Chillura Martino D, Caponetti E, Carretti E, Dei L, *J. Cult. Herit.* 15 (2014) 151; (c) Dei L, Salvadori B, *J. Cult. Herit.* 7 (2006) 110; (d) Ambrosi M, Dei L, Giorgi R, Neto C, Baglioni P, *Langmuir* 17 (2001) 4251.
- [57] (a) Chelazzi D, Giorgi R, Baglioni P, *Macromol. Symp.* 238 (2006) 30; (b) Giorgi R, Chelazzi D, Baglioni P, *Langmuir* 21 (2005) 10744; (c) Baglioni P, Giorgi R, *Soft Matter.* 2 (2006) 293.
- [58] Giorgi R, Dei L, Ceccato M, Schettino C, Baglioni P, *Langmuir* 18 (2002) 8198.
- [59] Natali I, Tempesti P, Carretti E, Potenza M, Sansoni S, Baglioni P, Dei L, *Langmuir* 30 (2014) 660.
- [60] (a) Daniele V, Taglieri G, *J. Cult. Herit.* 13 (2012) 40; (b) Liu T, Zhu Y, Zhang X, Zhang T, Li X, *Materials Letters* 64 (2010) 2575; (c) Daniele V, Taglieri G, *J. Cult. Herit.* 1 (2010) 102; (d) Nanni A, Dei L, *Langmuir* 19 (2003) 933; (e) Fratini E, Page MG, Giorgi R, Colfen H, Baglioni P, Demè B, Zemb T, *Langmuir* 23 (2002) 2330; (f) Salvadori B, Dei L, *Langmuir* 17 (2001) 2371.
- [61] (a) Rodriguez-Navarro C, Suzuki A, Ruiz-Agudo E, *Langmuir* 29 (2013) 11457; (b) Hansen E, Doehne E, Fidler J, Larson J, Martin B, Matteini M, Pardo ES, Price C, De Tagle A, Teutonico JM, Weiss N, *Rev. Conserv.* 4 (2003) 13.
- [62] (a) Wheeler G, *Alkoxysilanes and the consolidation of stone*, The Getty Conservation Institute, Los Angeles, CA, 2005; (b) Tsakalof A, Manoudis P, Karapanagiotis I, Chryssoulakis I, Panayiotou C, *J. Cult. Herit.* 8 (2007) 69; (c) Cnudde V, Dierick M, Vlassenbroeck J, Masschaele B, Lehmann E, Jacobs

P, Hoorebeke LV, *J. Cult. Herit.* 8 (2007) 331; (d) Kim EK, Won J, Do J, Dug Kim S, Soo Kang Y, *J. Cult. Herit.* 10 (2009) 214.

[63] Mosquera MJ, de los Santos DM, Montes A, Valdez-Castro L, *Langmuir* 24 (2008) 2772.

[64] De Ferri L, Lottici PP, Lorenzi A, Montenero A, Salvioli-Mariani E, *J. Cult. Herit.* 12 (2012) 356.

[65] Scherer GW, *J. Non-Cryst. Solids* 107 (1989) 135; (b) Scherer GW, *J. Am. Ceram. Soc.* 73 (1990) 3.

[66] Nanoestel Technical data sheet.

[67] Zornoza-Indart A, Lopez-Arce P, *J. Cult. Herit.* 18 (2016) 258.

[68] Sudarsan V, *Optical materials: fundamentals and applications in Functional materials, preparation, processing and application*, Elsevier, 2011.

[69] For some examples see: (a) Yam VWW, Lo KKW, *Coord. Chem. Rev.* 184 (1999) 157; (b) Beeby A, Botchway SW, Clarkson IM, Faulkner S, Parker AW, Parker D, Williams JAG, *J. Photochem. Photobiol. B: Biol.* 57 (2000) 83; (c) Oshishi Y, Kanamori T, Kitagawa T, Takashashi S, Snitzer E, Sigel GH, *Opt. Lett.* 16 (1991) 1747; (d) Slooff LH, Polman A, Wolbers MPO, van Veggel F, Reinhoudt DN, Hofstraat JW, *J. Appl. Phys.* 83 (1998) 497; (e) Kuriki K, Koike Y, Okamoto Y, *Chem. Rev.* 102 (2002) 2347; (f) Nakamura K, Hasegawa Y, Kawai H, Yasuda N, Kanehisa N, Kai Y, Nagamura T, Yanagida S, Wada Y, *J. Phys. Chem. A* 111 (2007) 3029; (g) Carlos LD, Ferreira RAS, Bermudez VD, Molina C, Bueno LA, Ribeiro SJL, *Phys. Rev. B* 60 (1999) 10042; (h) Moore EG, Samuel APS, Raymond KN, *Acc. Chem. Res.* 42 (2009) 542; (i) Rocha J, Carlos LD, Almeida Paz FA, Ananias D, *Chem. Soc. Rev.* 40 (2011) 926; (l) Armelao B, Quici S, Barigelletti F, Accorsi G, Bottaro G, Cavazzini M, Tondello E, *Coord. Chem. Rev.* 254 (2010) 487; (m) Eliseeva SV, Bünzli J-C, *Chem. Soc. Rev.* 39 (2010) 189; (n) Bünzli J-C, *Chem. Rev.* 110 (2010) 2729; (o) Ma Y, Wang Y, *Coord. Chem. Rev.* 254 (2010) 972; (p) Bünzli J-C, Eliseeva SV, *J. Rare Earths* 28 (2010) 824; (q) Binnemans K, *Chem. Rev.* 109 (2009) 4283; (r) Dos Santos CMG, Harte AJ, Quinn SJ, Gunnlaugsson T, *Coord. Chem. Rev.* 252 (2008) 2512; (r) Bünzli J-C, Comby S, Chauvin A-S, Vandevyver CDB, *J. Rare Earths* 25 (2007) 257; (s) Parker D, Dickins RS, Puschmann H, Crossland C, Howard JAK, *Chem. Rev.* 102 (2002) 1977; (t) Choppin GR, Peterman DR, *Coord. Chem. Rev.* 174 (1998) 283.

[70] (a) Pozza G, Ajò D, Chiari G, De Zuane F, Favaro M, *J. Cult. Herit.* 1 (2000) 393; (b) Yu C, Wang T, Xu K, Zaho J, Li M, Weng S, Zhang J, *Dyes Pigments* 96 (2013) 38; (c) Ooyama HE, Ide T, Yamasaki H, Harada A, Nagahama Y, Ono A, Yoshida K, *Dyes Pigments* 94 (2012) 103; (d) Ammar H, Fery-Forgues S, El-Gharbi R, *Dyes Pigments* 57 (2003) 259; (e) Xianhai H, Zhang X, Liu J, Dai J, *J. Lumin.* 142 (2013) 23; (f) Rauf MA, Graham JP, Bukallah SB, Al-Saedi MAS, *Spectrochim. Acta part A* 72 (2009) 133; (g) Yi X, Yang P, Huang D, Zhao J, *Dyes Pigments* 96 (2013) 104.

- [71] (a) Kunimi S, Fujihara S, *Dyes Pigments* 91 (2011) 49; (b) Sreeram KJ, Aby CP, Nair BU, Ramasami T, *Sol. Energy Mater. Sol. Cells* 92 (2008) 1462; (c) Sabbagh Alvani AA, Moztarzadeh F, Sarabi AA, *J. Lumin.* 114 (2005) 131; (d) Sameie H, Salimi R, Sabbagh Alvani AA, Sarabi AA, Moztarzadeh F, *Physica B* 405 (2010) 4796; (e) Olegário RC, De Souza ECF, Borges JFM, da Cunha JBM, de Andrade AVC, Antunes SRM, Antunes AC, *Dyes Pigments* 97 (2013) 113; (f) Strnadlová L, Šulcová P, Llusar M, *J. Therm. Anal. Calorim.* 102 (2010) 661.
- [72] (a) Gheno G, Ganzerla R, Bortoluzzi M, Enrichi F, *Book of abstract XV Congresso Nazionale della Chimica Italiana, Divisione Chimica dell’Ambiente e dei Beni Culturali, Bergamo, June 14-18, 2015*; (b) Gheno G, Ganzerla R, Bortoluzzi M, Enrichi F, *J. Lumin.* 145 (2014) 963.
- [73] (a) Fricker SP, *Chem. Soc. Rev.* 6 (2006) 524; (b) Beerby A, Bushby LM, Maffeo D, Williams JAG, *J. Chem. Soc. Dalton Trans.* (2002) 48; (c) Wong KL, Kwok WM, Wong WT, Phillips DL, Cheah KW, *Angew. Chem. Int. Ed.* 43 (2004) 4659.
- [74] (a) Pan Z, Jia G, Duan C-K, Wong W-Y, Wong W-T, Tanner P-A, *Eur J. Inorg. Chem.* 5 (2011) 637; (b) Mirochnik AG, Bukvetskii BV, Zhikhareva PA, Karasev VE, *Russ. J. Coord. Chem.* 27 (2001) 443.
- [75] (a) Armelao L, Quici S, Barigelletti F, Accorsi G, Bottaro G, Cavazzini M, Tondello E, *Coord. Chem. Rev.* 254 (2010) 487; (b) Scotognella F, Meinardi F, Ottonelli M, Raimondo L, Tubino R, *J. Lumin.* 129 (2009) 746.
- [76] Taha ZA, Ajlouni AM, Ababneh TS, Al-Momani W, Hijazi AK, Al Masri M, Hammad H, *Struct. Chem.* 28 (2017) 1907.
- [77] Manganelli Del Fà C, *La porosità nei materiali lapidei naturali e artificiali - problematiche di determinazione della porosità. Correlazione tra caratteristiche fisiche dei materiali, porosità, dinamica dei fluidi, degrado e trattamenti conservativi, Supplemento al n. 10 di Geoitalia, Modena, 2002.*
- [78] Maravelaki-Kalaitzaki P, Bertoncetto R, Biscontin G, *J. Cult. Herit.* 3 (2002) 273.
- [79] (a) Maravelaki-Kalaitzaki P, Biscontin G, *Atmos. Environ.* 33 (1999) 1699; (b) A. Paleni, S. Curri, *Biological aggression of works of art in Venice, in Biodeterior. Mater. Vol. 2, 1st ed., Applied Science Publishers, London, 1972, pp. 392.*
- [80] Gheno G, Badetti E, Brunelli A, Ganzerla R, Marcomini A, *J. Cult. Herit.* (2017), <https://doi.org/10.1016/j.culher.2018.02.013>.
- [81] (a) Andradý AL, Hamid SH, Hu X, Torikai A, *J Photochem. Photobiol. B Biol.* 46 (1998) 96; (b) Johnsons BW, McIntyre R, *Prog. Org. Coat.* 27 (1996) 95; (c) McNeill IC, Ahmed S, Memetea L, *Polym. Degrad. Stabil.* 47 (1995) 423.

- [82] (a) ASTM D2244:2011, Standard Practice for Calculation of Color Tolerances and Color Differences from Instrumentally Measured Color Coordinates; (b) Wyszecki G, Color science; concept and methods, quantitative data and formulae, Wiley, New York, 2000.
- [83] (a) Oleari C, Misurare il colore. Fisiologia della visione a colori – Fotometria – Colorimetria e Norme Internazionali, Hoepli Ed., Milano, 2008; (b) Palazzi S, Colorimetria – La Scienza del Colore nella tecnica e nell’arte, Nardini Ed., Firenze, 1995.
- [84] ASTM D4674e89:1989 standard test method for accelerated testing for color stability of plastics exposed to indoor fluorescent lighting and window-filtered daylight.
- [85] (a) ASTM D523:2004, Standard test method for specular gloss; (b) BS EN ISO 2813:2000, Paints and varnishes. Determination of gloss value at 20 degrees, 60 degrees and 85 degrees.
- [86] Campbell D, Pethrick RA, White JR, Polymer Characterization: Physical Techniques (II edition), Stanley Thornes Ltd, United Kingdom, 2000.
- [87] (a) Morancho JM, Salla JM, Ramis X, Cadenato A, Thermochim. Acta 419 (2004) 181; (b) Neag CM, Floyd L, Manzuk S, Polym. Mater. Sci. Eng. 68 (1993) 331; (c) Kissinger HE, Anal. Chem. 29 (1957) 1702.
- [88] Lerche D, J. Dispersion Sci. Technol. 23 (2002) 699.
- [89] Neira-Velásquez MG, Rodríguez-Hernández MT, Hernández-Hernández E, Ruiz-Martínez ARY, Polymer Molecular Weight Measurement in Handbook of Polymer Synthesis, Characterization and Processing, Jhon Wiley and Sons Inc. Publications, New Jersey, 2013.
- [90] (a) Striegel AM, Chromatographia 80 (2017) 989; (b) Oberlerchner JT, Rosenau T, Potthast A, Macromolecules 20 (2015) 10313.
- [91] (a) Sikkema H, Hanner MJ, Brennan DJ, Smith PB, Priddy DB, Polim. Degrad. Stabil. 38 (1992) 119; (b) Kaczmarek H, Kaminska A, van Herk A, Eur. Polym. J. 36 (2000) 767.
- [92] (a) Hayes P, Vahur S, Leito I, Spectrochim. Acta Part A Mol. Biomol. Spectrosc. 133 (2014) 207; (b) Šuštar V, Kolar J, Lusa L, Learner T, Schilling M, Rivenc R, Khanjian H, Koleša D, Polim. Degrad. Stabil. 107 (2014) 341; (c) Pintus V, Schreiner M, Anal. Bioanal. Chem. 399 (2011) 2961; (d) Scilling M, Bouchard M, Khanjian H, Learner T, Phenix A, Rivenc R, Acc. Chem. Res. 43 (2010) 888; (e) Ploeger R, Scalarone D, Chiantore O, Polim. Degrad. Stabil. 94 (2009) 2036; (f) Manzane E, Navas N, Checa-Moreno R, Rodriguez-Simon L, Capitan-Vallvey LF, Talanta 77 (2009) 1724; (g) Doménech-Carbó MT, Anal. Chim. Acta 621 (2008) 109; (h) Scalarone D, Lazzari M, Castelvetro V, Chiantore O, Chem. Mater. 19 (2007) 6107; (i) Miliani C, Ombelli M, Morresi A, Romani A, Surf. Coat. Technol. 151 (2002) 276; (m) Bacci M, UV-VIS-NIR, FT-IR, and FORS Spectroscopies, Modern Analytical

Methods in Art and Archaeology, Wiley-Interscience, New York, 2000; (n) Allen NS, Parker MJ, Regan CJ, *Polim. Degrad. Stabil.* 47 (1995) 117.

[93] (a) Pan Z, Jia G, Duan CK, Wong WY, Wong WT, Tanner PA, *Eur. J. Inorg. Chem.* (2011) 637; (b) Puntus LN, Zolin VF, *Russ. J. Coord. Chem.* 29 (2003) 574; (c) Zeng Y-Q, Zhou L-X, Lin JL, Zhang SW, *Z. Anorg. Allg. Chem.* 627 (2001) 1643; (d) Mirochnik AG, Bukvetskii BV, Zhikhareva PA, Karasev VE, *Russ. J. Coord. Chem.* 27 (2001) 443.

[94] (a) Binnemans K, *Coord. Chem. Rev.* 295 (2015) 1; (b) Bünzli J-C G, Chauvin AS, Kim HK, Deiters E, Eliseeva SV, *Coord. Chem. Rev.* 254 (2010) 2623; (c) Werts MHW, Jukes RTF, Verhoeven JW, *Phys. Chem. Chem. Phys.* 4 (2002) 1542.

[95] Vázquez-Ibar JL, Weinglass AB, Ronald Kaback H, *PNAS* 99 (2002) 3487.

[96] Schubert EF, *Chromaticity (Chapter 17) in Light-Emitting Diodes*, Cambridge University Press, New York, 2006.

[97] Pondelak A, Kramara S, Lesar Kikelj M, Sever Škapin A, *J. Cult. Herit.* 28 (2017) 1.

[98] (a) Mosquera MJ, Pozo J, Silva B, Rivas T, Esquivias E, *J. Non-Cryst. Solid.* 311 (2002) 185–194; (b) Mosquera MJ, Pozo J, Esquivias E, *J. Sol-Gel. Sci. Tech.* 26 (2003) 1227–1231.

[99] For some examples see: (a) Ozcelik Y, Careddu N, Yilmazkaya, *Cold Reg. Sci. Technol.* 82 (2012) 49; (b) Careddu N, Marras G, *Constr. Buil. Mater.* 49 (2013) 828; (c) Eren Sarici D, *Constr. Buil. Mater.* 102 (2016) 416.

[100] For some examples see: (a) Rossi S, Fedel M, Deflorian F, Zanol S, *Mater. Des.* 50 (2013) 332; (b) Johnsons BW, McIntyre R, *Prog. Org. Coat.* 27 (1996) 95; (c) Gheno G, Ganzerla R, Bortoluzzi M, Paganica R, *Prog. Org. Coat.* 101 (2016) 90.

[101] For some examples see: (a) Hu YH, Chen CY, *Polim. Degrad. Stabil.* 82 (2003) 81; (b) Madorsky SL, *J. Polym. Sci.* 11 (1953) 491; (c) Madorsky SL, *J. Polym. Sci.* 11 (1953) 491; (d) Kashiwagi T, Hirata T, Brown JE, *Molecules* 18 (1985) 131; (e) Kashiwagi T, Inaba A, Brown JE, Hatada K, Kitayama T, Masuda E, *Molecules* 19 (1986) 2160; (f) Manring LE, *Macromolecules* 21 (1988) 528; (g) Arisawa H, Brill TB, *Combust Flame* 109 (1997) 514; (h) Bagby G, Lehrle RS, Robb JC, *Polym.* 10 (1969) 683.

[102] (a) Grassie N, McNeill IC, Cooke I, *J. Appl. Polym. Sci.* 12 (1968) 831; (b) McNeill IC, Neil D, *Europ. Polym. J.* 6 (1970) 143; (c) McNeill IC, Neil D, *Europ. Polym. J.* 6 (1970) 569; (d) McNeill IC, Rincon A, *Polim. Degrad. Stabil.* 18 (1987) 99.

- [103] Chelazzi D, Poggi G, Jaidar Y, Toccafondi N, Giorgi R, Baglioni P, J. Colloid. Interfase Sci. 392 (2013) 42.
- [104] Scalarone D, Chiantore O, Learner T, Ageing studies of acrylic emulsion paints. Part II. Comparing formulations with poly (EA-co-MMA) and poly(nBA-co-MMA) binders, Preprint ICOM Committee for Conservation 14th Triennial Meeting, James & James/Earthscan, The Hague, 2005.
- [105] Ho BC, Lee YD, Chin WK, J. Polim. Sci. Part A 30 (1992) 2389.
- [106] Glassner M, D'hooge DR, Young Park J, Van Steenberge PHM, Monnerya BD, Reyniers MF, Hoogenboom R, Europ. Polym. J. 65 (2015) 298.
- [107] Kandelbauer A, Despres A, Pizzi A, J. Appl. Polym. Sci. 106 (2007) 2192.
- [108] Klasek A, Koristek K, Lycka A, Tetrahedron, 59 (2003) 5279.
- [109] Garcia-Torres J, Bosch-Jimenez P, Torralba-Calleja E, Kennedy M, Ahmed H, Doran J, Gutierrez-Tauste D, Bautista L, Della Pirriera M, J. Photochem. Photobiol. 275 (2014) 103.
- [110] Sastri VR, Bünzli JC, Ramachandra R, Rayudu, GVS, Perumareddi JR, Modern Aspects of Rare Earths and their Complexes, Elsevier, Amsterdam, 2003.
- [111] (a) Gorller-Walrand C, Binnemans K, Handbook of the Physics and Chemistry of Rare Earths, Elsevier, Amsterdam, 1996; (b) Binnemans K, Gorller-Walrand C, J. Rare Earths 14 (1996) 173.